Signal development in silicon sensors used for radiation detection

Dissertation
zur Erlangung des Doktorgrades
des Department Physik
der Universität Hamburg

vorgelegt von
Julian Becker
aus Hamburg

Hamburg
2010

This thesis was supported by the Helmholtz Alliance "Physics at the Terascale" and the European XFEL.

Gutachter der Dissertation:

- Prof. Dr. Robert Klanner, Institute of Experimental Physics, University Hamburg, Luruper Chaussee 149, 22761 Hamburg, Germany
- Dr. Heinz Graafsma, Deutsches Elektronen-Synchrotron (FS-DS), Notkestr. 85, 22607 Hamburg,
- Dr. Helmuth Spieler, Lawrence Berkeley National Laboratory, 1 Cyclotron Road, 94720 Berkeley, California, USA Germany

Gutachter der Disputation:

- Prof. Dr. Robert Klanner, Institute of Experimental Physics, University Hamburg, Luruper Chaussee 149, 22761 Hamburg, Germany
- Dr. Erika Garutti, Deutsches Elektronen-Synchrotron (FLC), Notkestr. 85, 22607 Hamburg, Germany

Datum der Disputation: 06.08.2010
Vorsitzender des Prüfungsausschusses: Dr. Georg Steinbrück
Vorsitzender des Promotionsausschusses: Prof. Dr. Joachim Bartels
Leiterin des Departments Physik: Prof. Dr. Daniela Pfannkuche

Abstract in English language

This work investigates the charge collection properties in silicon sensors.

In order to perform the investigations a setup for measurements utilizing the Transient Current Technique (TCT) has been designed and built. Optical lasers with different wavelengths and short pulses (FWHM < 100 ps) have been used to create charge carriers in the sensor volume.

A new parameterization of charge carrier mobilities in bulk silicon as function of electric field and temperature was derived for two different crystal orientations from investigations on pad sensors with low charge carrier densities.

In the course of these investigations a simulation program for current pulses was developed. The program simulates current pulses, which are induced by drift and diffusion of charge carriers for pad sensors, and approximately for strip and pixel sensors.

The simulation program could be used to describe the current pulses of irradiated sensors. Additionally, using the simulation program, it was shown that impact ionization is a possible reason for the recently reported charge multiplication effects in highly irradiated sensors.

The central topic of this work is the investigation of effects of high charge carrier densities, so called plasma effects. In this work plasma effects were created by focusing the lasers.

The measurements of the plasma effects on pad sensors were used as reference measurements for simulations performed by WIAS in Berlin. It was shown that using charge transport models accepted in literature, the observed plasma effects cannot be described.

Measurements on strip sensors were performed with regards to the detector development for the European XFEL.

Measurements of peak currents and charge collection times as function of photon intensity and applied bias voltage allowed the determination of optimum operation parameters of the Adaptive Gain Integration Pixel Detector (AGIPD), which will be used at the European XFEL.

Utilizing position sensitive measurements on strip sensors, the spatial distribution of charge clouds with high charge carrier densities could be determined. These distributions allowed estimations of the influence of plasma effects on the charge sharing behavior of two different pixel sizes for the AGIPD.

Abstract in German language

In dieser Arbeit werden die Ladungssammlungseigenschaften in Siliziumsensoren untersucht.

Für die Untersuchungen wurde ein Messstand für Messungen mittels der Transient Current Technique (TCT) entworfen und aufgebaut. Es wurden optische Laser verschiedener Wellenlängen mit einer kurzen Pulsdauer (FWHM < 100 ps) verwendet, um Ladungsträger im Sensorvolumen zu erzeugen.

Untersuchungen an Pad-Sensoren mit niedriger Dichte erzeugter Ladungsträger ermöglichen die Bestimmung von Ladungsträgermobilitäten im Silizium-Volumenmaterial als Funktion des elektrischen Felds und der Temperatur für zwei unterschiedliche Kristallrichtungen.

Im Rahmen der Untersuchungen wurde ein Simulationsprogramm für Strompulse entwickelt. Das Programm ermöglicht die Simulation der durch Drift und Diffusion von Ladungsträgern induzierten Strompulse für Pad-Sensoren, sowie Näherungen für Streifen- und Pixelsensoren.

Dieses Simulationsprogramm konnte verwendet werden um die Strompulse von bestrahlten Sensoren zu beschreiben. Zusätzlich konnte mittels des Simulationsprogramms gezeigt werden, dass Stoßionisation eine mögliche Ursache für den kürzlich entdeckten 'charge multiplication' Effekt in extrem hoch bestrahlten Sensoren ist.

Der Schwerpunkt dieser Arbeit ist die Untersuchung von Effekten hoher Dichte erzeugter Ladungsträger, sogenannter Plasmaeffekte. In dieser Arbeit wurden Plasmaeffekte durch eine Fokussierung der verwendeten Laser erzeugt.

Die Messungen des Plasmaeffekts in Pad-Sensoren wurden als Referenzmessungen für Simulationen des Plasmaeffekts verwendet, welche vom WIAS in Berlin durchgeführt wurden. Es wurde gezeigt, dass mit den in der Literatur akzeptierten Ladungstransportmodellen die beobachteten Plasmaeffekte nicht beschrieben werden kann.

Insbesondere im Hinblick auf die Detektorentwicklung für den Europäischen Röntgen-Laser (XFEL) wurden Messungen an Streifensensoren durchgeführt.

Die Messung von Spitzenströmen und Ladungssammlungszeiten als Funktion von Photonenintensität und angelegter Spannung ermöglichte die Bestimmung optimaler Betriebsparameter für den Adaptive Gain Integration Pixel Detector (AGIPD), welcher am Europäischen XFEL zum Einsatz kommen wird.

Positionsabhängige Messungen an Streifensensoren ermöglichten zudem die Bestimmung der räumlichen Verteilungsfunktion von Ladungswolken mit hohen Ladungsträgerdichten. Diese Verteilungen ermöglichen Abschätzungen der Auswirkungen von Plasmaeffekten auf das Ladungsteilungsverhalten für zwei unterschiedliche Pixelgrößen für den AGIPD.

Contents

1 Introduction **1**
1.1 LHC upgrade (sLHC) . . . 1
1.2 The European XFEL . . . 2

2 Silicon material properties **3**
2.1 Band structure . . . 3
2.2 Charge carrier density . . . 5
2.3 p-n junction . . . 5
2.3.1 Capacitance of the p-n junction . . . 7
2.4 Charge carrier transport . . . 8
2.4.1 Drift . . . 8
2.4.2 Diffusion . . . 9
2.5 Radiation damage . . . 9

3 Interactions with radiation **11**
3.1 Charged particles . . . 11
3.1.1 Minimum ionizing particles . . . 13
3.1.2 Heavy ions . . . 13
3.1.3 Electrons . . . 13
3.2 Neutral particles . . . 14
3.2.1 Photons . . . 14
3.2.2 Optical photons . . . 16
3.2.3 X-rays . . . 17
3.2.4 γ-rays and higher energy photons . . . 18
3.2.5 Neutrons . . . 18

4 Silicon sensors for radiation detection **19**
4.1 Planar diodes (pad sensors) . . . 19
4.2 Strip sensors . . . 20
4.3 Pixel sensors . . . 21
4.4 Other silicon sensors . . . 22
4.4.1 Silicon drift detectors . . . 22
4.4.2 3D sensors . . . 22
4.4.3 pn-CCD sensors . . . 22
4.4.4 DEPFET sensors . . . 24
4.5 Other sensor materials . . . 25

4.5.1 Other semiconductor materials . . . 25
4.5.2 Diamond . . . 26

5 Current and capacitance measurements 29
5.1 I/V Measurements . . . 30
5.2 C/V Measurements . . . 31

6 Transient current technique 33
6.1 Experimental setup . . . 33
6.1.1 Substrate . . . 34
6.1.2 Mounting . . . 35
6.1.3 Sample enclosure . . . 36
6.1.4 Cooling system . . . 36
6.1.5 Translation stages . . . 37
6.1.6 Electronic appliances . . . 37
6.1.7 Data acquisition and control . . . 38
6.2 Laser system . . . 39
6.2.1 Laser pulse properties . . . 40
6.2.2 Stability of the laser . . . 42
6.3 Summary . . . 43

7 Signal simulation 45
7.1 Electric field . . . 46
7.2 Initial distribution . . . 47
7.3 Ramo's theorem . . . 47
7.3.1 Weighting potential . . . 48
7.4 Drift and diffusion of charge carriers . . . 50
7.5 Mobility model . . . 52
7.6 Charge carrier trapping and multiplication . . . 52
7.6.1 Trapping . . . 52
7.6.2 Multiplication . . . 53
7.7 Pulse shape modifications . . . 54
7.7.1 Pulse structure of the laser light . . . 55
7.7.2 Readout circuit . . . 56
7.8 Summary . . . 57

8 Measurements on pad sensors with low charge carrier densities 59
8.1 Investigated sensors . . . 59
8.2 Measurements . . . 60
8.3 Results . . . 60
8.3.1 Fitted mobility parameters . . . 62
8.4 Discussion and Conclusions . . . 65

9 Comparison of simulations and measurements on pad sensors 67

9.1 Field dependent trapping and double junction effect 67
9.2 Multiplication in highly irradiated diodes 71
9.3 Summary 73

10 Measurements on pad sensors with high charge carrier densities 75
10.1 Investigated sensor 75
10.2 Simulations 76
10.3 Comparison of simulations and measurements 77
10.3.1 Junction side illumination 77
10.3.2 Illumination opposite to the junction 78
10.4 Discussion and Conclusions 80
10.5 Summary 86

11 Transient measurements on strip sensors 87
11.1 Investigated sensors 87
11.2 Transients for rear side illumination 91
11.3 Transients for rear side illumination with different focusing 92
11.4 Transients for front side illumination 94
11.5 Relevance for XFEL sensors 95
11.5.1 Peak currents 96
11.5.2 Increase of the charge collection time 97
11.5.3 Pile-up effects 98
11.6 Summary 98

12 Position sensitive measurements on strip sensors 101
12.1 Measurement procedure 101
12.2 Fit procedure to derive the point spread function 101
12.3 Fit results 105
12.4 Point spread function 110
12.5 Modulation transfer function 112
12.6 Summary 112

13 Comparison of simulations and measurements on strip sensors 115
13.1 Investigated sensor 115
13.2 Simulations 115
13.3 Comparison of simulations and measurements 117
13.4 Summary 118

14 Considerations influencing the sensor design of the AGIPD 121
14.1 The readout circuit of the AGIPD 121
14.2 Relevant detector specifications 122
14.3 Input protection 123
14.4 Pile-up 123
14.5 Integration time 124

14.6 Sensor polarity . . . 124
14.7 Lateral spread . . . 125
14.7.1 200 µm pixels . . . 128
14.7.2 100 µm pixels . . . 128
14.8 Summary . . . 131

15 Summary and Conclusions 133
15.1 Setup . . . 133
15.2 Simulation program . . . 133
15.3 Investigations on pad sensors . . . 133
15.3.1 Measurements with low charge carrier densities . . . 134
15.3.2 Comparison of simulations and measurements . . . 134
15.3.3 Measurements with high charge carrier densities . . . 134
15.4 Investigations on strip sensors . . . 134
15.4.1 Transient measurements . . . 134
15.4.2 Position sensitive measurements . . . 135
15.4.3 Comparison of simulations and measurements . . . 135
15.5 Implications for the AGIPD sensor design . . . 136

A Appendix 137
A.1 List of investigated sensors . . . 137
A.2 Optical components used to build the setup . . . 137
A.3 Experiments with irradiated strip sensors . . . 139

B List of publications 141
B.1 List of publications as corresponding author . . . 141
B.2 List of publications as contributing author . . . 141

List of Figures

2.1 Band structure of silicon at $T = 300$ K. 4
2.2 A p-n junction in thermal equilibrium with zero bias voltage applied. . . 6
2.3 Examples of lattice defects in silicon. 10

3.1 Energy loss of charged particles as function of momentum. 12
3.2 Absorption coefficient μ in silicon as function of photon energy. 14
3.3 Attenuation length in silicon as function of photon energy. 16
3.4 Quantum efficiency of silicon sensors with different thicknesses as function of photon energy. 17

4.1 Sketch of a pad diode. 19
4.2 Sketch of a strip sensor. 20
4.3 Sketch of a bump bonded pixel sensor. 21
4.4 Simplified sketch of a 3D sensor. 23
4.5 Simplified sketch of a pn-CCD sensor. 24
4.6 Simplified sketch of a DEPFET sensor cell. 25
4.7 Dominant interaction of photons as function of energy and atomic number. 26

5.1 Schematic drawing of the setup used for current and capacitance measurements 29
5.2 I/V measurement of CG1017. 30
5.3 C/V measurement of CG1017. 31

6.1 Photograph of the setup. 34
6.2 Photograph of the interior of the setup. 35
6.3 Sketch of the front side of the substrate. 36
6.4 Schematic drawing of the arrangement of the optical components used. . 39
6.5 Photocurrent measurements. 41
6.6 Photocurrent of the reference diode as function of time for three different laser heads. 42

7.1 Different parameterizations of the electric field. 46
7.2 Weighting potentials for different geometries. 49
7.3 Simplified scheme of one transport step. 51
7.4 Exemplary current pulses simulated for 660 nm light and 1015 nm light. . 54
7.5 Effect of laser pulse structure and external circuit. 55
7.6 Time structure of the laser pulse. 56

7.7 Transfer function derived from the SPICE simulations for 9.2 pF capacitance. 57
7.8 Equivalent circuit for SPICE simulations. 58

8.1 Comparison of simulated pulses and measurements at T=30°C. 61
8.2 Comparison of different parameterizations of the saturation velocity. . . . 63
8.3 Comparison of different parameterizations of the mobility and drift velocities at T = 300 K. 64
8.4 Difference between mobilities determined in this work and those of [55] at T = 300 K. 65

9.1 Overview of the field distribution inside the 150 µm epitaxial sensor. . . 68
9.2 Overview of the distribution of electrons inside the simulation volume at different times. 69
9.3 Comparison of simulations and measurements for an irradiated 153 µm epitaxial sensor. 70
9.4 Comparison of simulations of the CCE of a 75 µm epitaxial diode. 71
9.5 Pulse structure and parameter distribution of the 75 µm epitaxial sensor. 72
9.6 Overview of the simulation process of the 75 µm epitaxial sensor. 72
9.7 Comparison of measured and simulated pulses for different voltages. . . . 74

10.1 Evolution of a plasma cloud in space and time. 76
10.2 Results for junction side illumination using defocused laser light to avoid plasma effects. 78
10.3 Results for junction side illumination using focused laser light. 79
10.4 Results for illumination opposite to the junction using defocused laser light to avoid plasma effects. 80
10.5 Results for injection opposite to the junction using focused laser light. . . 81
10.6 Effects of different parameters on the simulated current pulses for 1×10^6 electron hole pairs at 200 V applied voltage. 84
10.7 Effects of different parameters on the simulated current pulses for 11×10^6 electron hole pairs at 200 V applied voltage. 85

11.1 Microscope pictures of the investigated strip sensors. 87
11.2 C/V and I/V measurement of PSI1mm. 88
11.3 Transients obtained with focused light of 660 nm and 1015 nm wavelength. 89
11.4 Transients obtained with focused light of 660 nm and 1015 nm wavelength. 91
11.5 Current pulses measured and integrated charge for light of 1015 nm wavelength and different focusing. 93
11.6 Transients obtained after front side illumination with focused light of 660 nm and 1015 nm wavelength. 94
11.7 Peak current measured as function of the number of created electron hole pairs. 96
11.8 Charge collection time of the 450 µm sensor as function of bias for different intensities of 660 nm and 1015 nm light. 97

11.9 Charge pulses of the 450 μm sensor as function of the applied voltage for the high and medium intensities of 1015 nm light. 99

12.1 Illustration of the charge collection of a charge distribution in a segmented sensor. 102
12.2 Charge collected on one strip of the 450 μm sensor as function of injection location; 660 nm light. 103
12.3 Charge collected on one strip of the 450 μm sensor as function of injection location; 1015 nm light. 104
12.4 Fit results for N_p and μ as function of voltage. 106
12.5 Fit results for N_p and μ as function of voltage. 107
12.6 Fit results for r_0 and σ_p as function of voltage. 108
12.7 Fit results for r_0 and σ_p as function of voltage. 109
12.8 Fit results for the radial point spread function. 111
12.9 Modulation transfer functions. 113

13.1 Comparison of simulations and measurements for 0.21×10^6, 0.85×10^6 and 2.15×10^6 electron hole pairs. 116
13.2 Comparison of simulations and measurements for 8.55×10^6 electron hole pairs. 117
13.3 Comparison of the fraction of collected charge in simulations and measurements. 119
13.4 Comparison of the total collected charge in simulations and measurements. 120

14.1 Block diagram of the readout ASIC of the AGIPD. 122
14.2 Simulated current pulses for different layouts of 200 μm pixels. 125
14.3 Fraction of charge collected within a 200 μm pixel as function of impact position. 126
14.4 Fraction of charge collected within a 100 μm pixel as function of impact position. 127
14.5 Collected charge within a 200 μm and 100 μm pixel. 129
14.6 Fraction of the pixel area without charge sharing for 200 μm and 100 μm pixels. 130

A.1 Performance of plano-convex and achromatic lenses, reproduced from [82]. 139
A.2 Current and capacitance measurements on irradiated strip sensors 140

List of Tables

8.1 Parameters for the field dependent mobility at 300 K. 62
8.2 Temperature parameters α_i for the field dependent mobility reduction. . 62

10.1 Pulse durations for all measurements presented in this chapter compared to their simulations. 82

11.1 Table of the investigated intensities for each sensor. 90

A.1 List of all sensors investigated in this work. 138
A.2 List of optical components. 138

1 Introduction

Silicon is used as a material for the detection of radiation since decades. It is a very versatile material which can be manufactured to application specific demands in large quantities.

Silicon sensors are built as p-n junctions operated under reverse bias. Electron hole pairs are created by ionization or direct excitation and induce a current in the electrodes when drifting in the electric field until the charge carriers reach a contact.

In modern day experiments, like the Large Hadron Collider (LHC) and the European X-ray Free Electron Laser (XFEL), silicon sensors are used in a very challenging environment requiring excellent knowledge of their behavior.

The silicon sensors in use at the LHC and its future upgrade the super LHC (sLHC) are operated in a very harsh radiation environment. The enormous amount of radiation damage influences the operating conditions of the sensors.

Experiments at the XFEL will push the performance limits of the detectors. In order to operate these detectors under optimum conditions the precise behavior of the silicon sensor has to be known.

In order to investigate sensor materials, the Transient Current Technique (TCT) was used. In this work a TCT setup, which allows the investigation of structured silicon devices with focused laser light was built. It is constructed in a versatile way, which allows to investigate the effects of radiation damage and to simulate to actual operating conditions of experiments at the European XFEL.

1.1 LHC upgrade (sLHC)[1]

After approximately 10 years of operation, an upgrade of the LHC to a tenfold luminosity of 10^{35} cm^{-2}s^{-1} is under discussion. This will lead to very high radiation levels, especially in the innermost tracking region where a 1 MeV neutron equivalent fluence of $\Phi_{eq} = 1.6 \times 10^{16}$ cm^{-2} is expected [2]. Thus silicon detectors as used today will suffer from severe damage caused by radiation-induced defects. A strong degradation of the signal-to-noise ratio (SNR) will occur due to an increasing depletion voltage (U_{dep}) at high fluences, higher leakage currents (I_{rev}) and trapping of charge carriers.

Trapping reduces the charge collection efficiency (CCE) significantly and is considered to be the most limiting factor at sLHC fluences. Recently CCE values larger than 1 were reported for highly proton-irradiated thin epitaxial (EPI) diodes at high voltages [3, 4] indicating charge multiplication.

[1] Text partly reproduced from [1]

1.2 The European XFEL

The European XFEL [5] will push the limits of brilliance further than any light source today. The design of silicon sensors and front end electronics for detectors at the European XFEL is a challenge, as the expected dynamics in the experimental data ranges from single photons to 10^5 12 keV photons per pixel per pulse. The Adaptive Gain Integrating Pixel Detector (AGIPD) is a detector, which is designed to cope with the challenges at the European XFEL [6, 7, 8, 9, 10].

At the European XFEL the photon energy will be tunable from 0.8 keV to 12.4 keV. The XFEL pulses will be of short duration ($<$ 100 fs) and have a bunch repetition rate of 4.5 MHz (222 ns bunch spacing). A super-cycle of 2700 bunches is followed by 99.4 ms idle time (10 Hz) [11].

X-ray photons are detected when they create electron hole pairs in the sensor material. At the x-ray energies of the European XFEL charge carriers will be dominantly created by the photoeffect, in which the x-ray photon is absorbed in the sensor material.

When the created charge carrier densities are sufficiently high to modify the electric field in the sensor, significant changes, compared to the situation with low charge carrier densities, are noticed (so called plasma effects). These effects have been observed in the detection of heavily ionizing particles and with high intensity laser light.

Plasma effects are also expected for experiments at x-ray free electron lasers. This work aims at understanding plasma effects for experiments at the European XFEL.

The plasma formed by the high densities of electrons and holes dissolves slowly. The plasma boundaries effectively shield its inner region from the electric field created by the external bias, thus altering the induced current pulse and increasing the charge collection time [12]. Plasma effects decrease as the electric field increases [13]. Using incident ions of different masses and energies, the influence of material properties on plasma effects has been studied in detail in [14].

The plasma effects change the charge collection process. Carriers will drift apart laterally due to two processes: Diffusion and electrostatic repulsion. At first diffusion is the dominant process as electrons and holes are not separated. Once the charges are separated mutual electrostatic repulsion, which increases with charge carrier density, increases the lateral spread.

These two effects will result in an increased lateral spread of the collected charge and thus in increased charge sharing between pixels, as shown in [15] for α-particles.

All measurements in this work have been performed using light with perpendicular incidence. Results for oblique incidence are expected to show less plasma effects and asymmetric charge spreading as shown in [16] for light ions.

2 Silicon material properties

In order to understand the fundamental properties of silicon it is essential to understand the physics of radiation detection using silicon sensors. Silicon is a semiconductor, its properties are well known and modern advances in silicon processing technology make using silicon as detector material relatively easy.

2.1 Band structure

Being determined by its band structure, it is necessary to examine the formation and impact of the band structure on the electric properties of silicon.

When many atoms form a crystal lattice their individual wave functions overlap and interact. The individual energy levels of the atoms become degenerate, forming many energy levels which are separated by very small energies. Due to the very large number of individual atoms, these close-by energy states effectively form continuous bands.

The highest energy band which has occupied states is called valence band, the lowest completely unoccupied band is called conduction band. Depending on the energetic gap between valence and conduction band, a solid state body is considered either as conductor, insulator or semiconductor. The region between the valence and conduction band is called band gap or forbidden band.

In a conductor both bands are energetically adjacent or overlap or there are free states in the valence band[1]. Thus, if an external field is applied, electrons can move freely.

In an insulator there are no free states in the valence band and the band gap is several eV large. As there are no states to which the electrons can move, no charge is transported and the material acts as an insulator. It should be noted that under special circumstances (e.g. large external fields) electrons can gain enough energy to reach states in the conduction band, this phenomenon is called dielectric breakdown.

A semiconductor has separated bands, but the separation energy is small enough that conduction band states can be reached by thermally exited electrons. Due to the occupation of conduction band states, the conductivity of semiconductors increases as function of temperature in contrast to the conductivity of conductors, which decreases as function of temperature.

The band structure of silicon as function of crystal orientation is shown in Figure 2.1. It can be seen that silicon has a so called indirect band gap ($E_g = 1.12$ eV at 300 K), meaning that the maximum of the valence band and the minimum of the conduction band are at different momenta $\vec{k}$ of the electrons. Momentum conservation results in

[1] In a conductor, a valence band with free states can also be called conduction band.

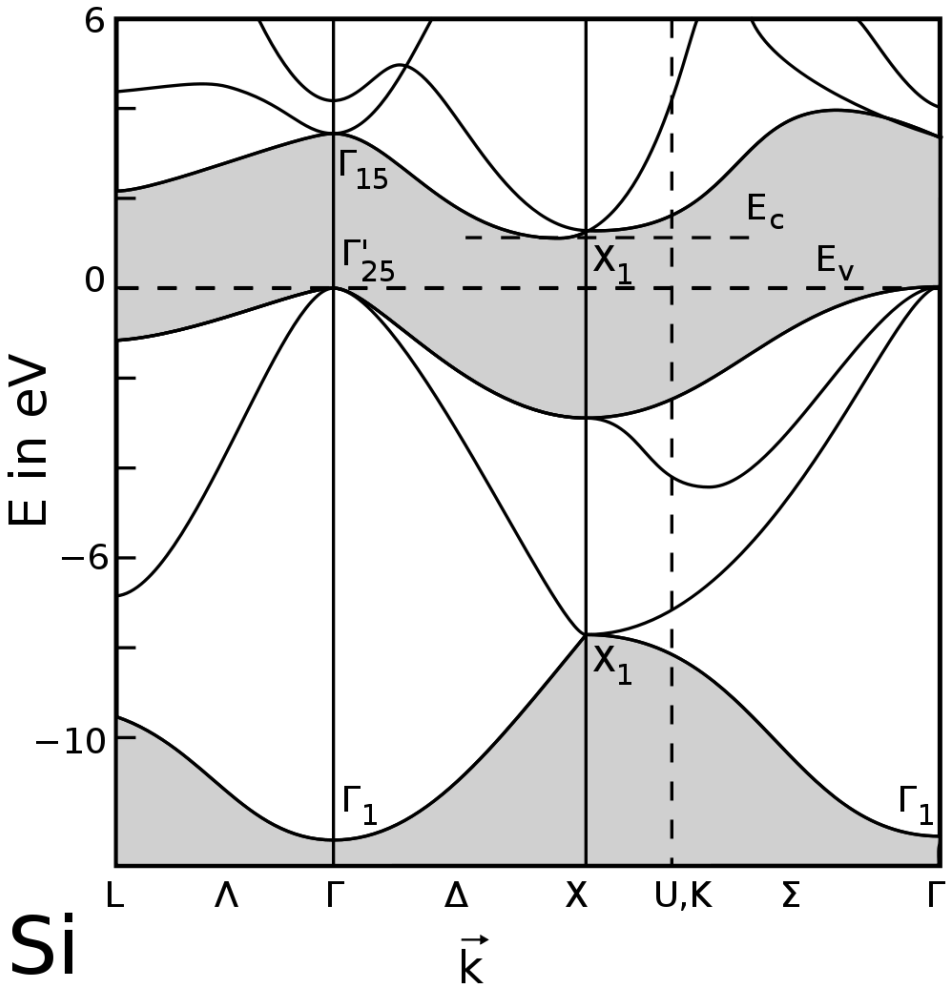

Figure 2.1: Band structure of silicon at $T = 300$ K. Per definition the upper edge of the valence band is at 0 eV. The energetic difference between the lower edge of the conduction band (at X) is separated by 1.12 eV from the upper edge of the valence band (at Γ). The band gap is marked in grey. Reproduced from [17].

the need of phonons (lattice vibrations) to excite electrons from the valence band to the conduction band. At the temperatures investigated in this work there are always enough phonons present in the crystal to allow the excitation of electrons to the conduction band.

If cryogenic temperatures are considered, there are not enough phonons present to conserve the crystal momentum, thus optical photons must excite electrons directly requiring a higher photon energy. The direct band gap energy of silicon is 3.6 eV, thus silicon is transparent to optical light at cryogenic temperatures.

2.2 Charge carrier density

When bulk silicon material at a given, non-vanishing temperature T is considered, the Fermi-Dirac distribution of electrons $f(E)$ for this thermal energy extends into the conduction band. The density of electrons is given as

$$n_e = 2 \int_{E_c}^{\infty} D_e(E) f(E)\, dE \tag{2.1}$$

with $D_e(E)$ being the density of states in the conduction band. The factor of 2 is introduced as electrons have a spin of $^1/_2$, which allows each state to be occupied by two electrons.

Each excited electron leaves a so called hole in the valence band, which is a positive charge carrier and can move in the crystal lattice. Due to charge conservation the number of electrons and holes, and therefore their density, is equal[2].

The intrinsic charge carrier density n_i is defined as:

$$n_i = \sqrt{n_e n_h} \propto e^{E_g/(2k_B T)} \tag{2.2}$$

The resulting value of n_i for T=300 K is approximately 10^{10} cm^{-3}. This relation is also valid when dopants are introduced to the silicon lattice.

When controlled impurities (so called dopants) are incorporated into the silicon lattice, additional levels are created inside the band gap. This process is called doping. Common doping materials include phosphorus (donor) and boron (acceptor). These dopants create shallow levels close to the conduction or valence band which are completely ionized even at low temperatures. This results in additional free charge carriers and therefore the charge carrier concentration in presence of only one type of dopant is equal to the dopant concentration ($n_e = N_D$ or $n_h = N_A$). In general the material is called n-type silicon when $N_D > N_A$, and p-type silicon when $N_A > N_D$, with $N_{eff} = |N_D - N_A|$ being the so called effective doping concentration for both types of silicon.

2.3 p-n junction

A p-n junction is created when a piece of p-type silicon and a piece of n-type silicon are joined together. Free electrons and holes will diffuse towards each other and recombine, leaving behind the immobile donor and acceptor ions, which in turn constitute a so called space charge region. This space charge region creates an electric field that compensates the diffusion of charge carriers and a steady state is reached. A sketch of a typical p-n junction is shown in Figure 2.2.

The situation inside the diode can be described by the Poisson equation.

[2] Although the total number of electrons and holes is equal their energy distributions $n_e(E)$ and $n_h(E)$ are not. This is due to their different effective masses, which in turn leads to the Fermi energy (or, more correctly, chemical potential) not being in the middle of the band gap at non-vanishing temperatures.

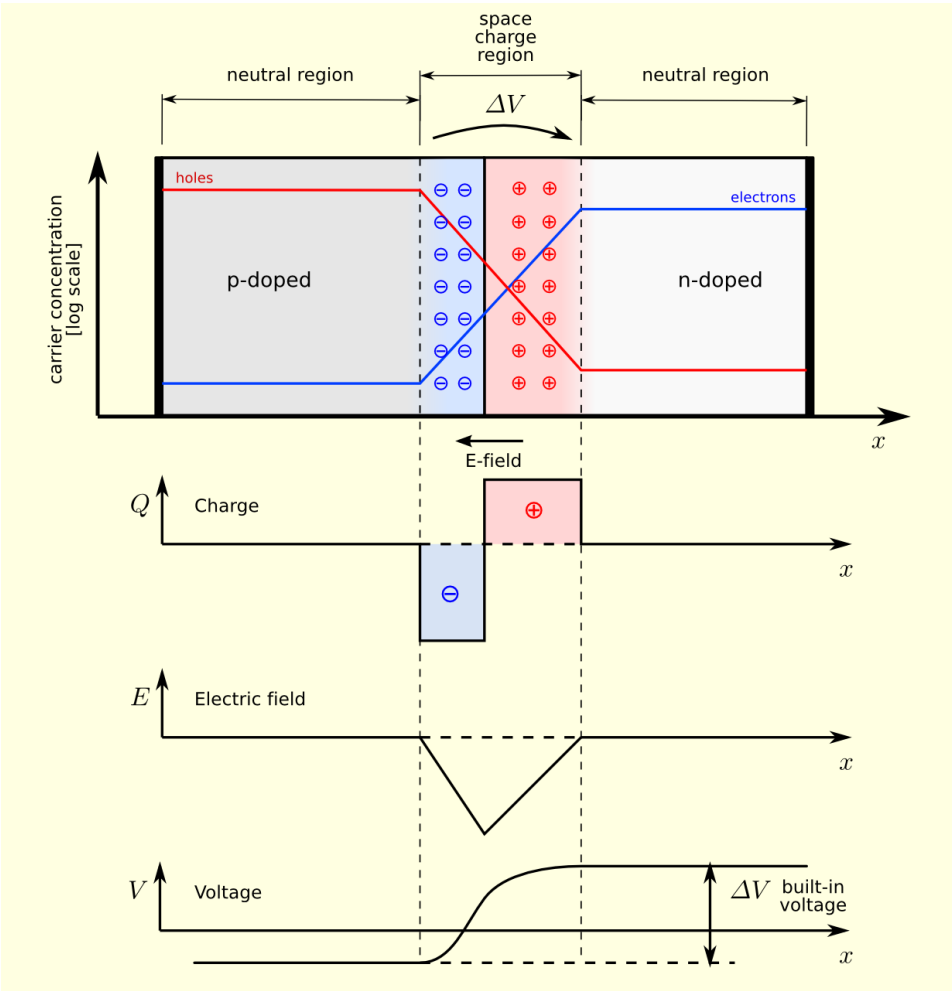

Figure 2.2: A p-n junction in thermal equilibrium with zero bias voltage applied. Electron and hole concentrations are shown with blue and red lines, respectively. Gray regions have no net charge. The red zone is positively charged, the blue zone is negatively charged. Beneath the junction, graphs for charge density, electric field and voltage are shown. Reproduced from [17].

$$\triangle\phi = \frac{\rho}{\epsilon\epsilon_0} = \frac{e_0}{\epsilon\epsilon_0}\left(N_A - N_D\right) \tag{2.3}$$

With ϕ being the electrostatic potential, ϵ the dielectric constant of silicon, ϵ_0 the vacuum permittivity and e_0 the elementary charge.

Charge neutrality requires the number of positive charges to be equal to the number of negative charges, thus charge density multiplied by the length of the space charge region must be equal for both sides.

$$N_A l_p = N_D l_n \tag{2.4}$$

Resulting in the total width w of the space charge region being $w = l_p + l_n$.

Using this relation and the assumption of $N_D = 0$ if $N_A > 0$ and vice versa, the built-in potential difference U_{bi} can be expressed as

$$U_{bi} = \frac{e_0}{2\epsilon\epsilon_0}\left(N_D l_n^2 + N_A l_p^2\right) \tag{2.5}$$

or, in the more commonly used form, as

$$U_{bi} = \frac{k_B T}{e_0} \ln\left(\frac{N_A N_D}{n_i^2}\right) \tag{2.6}$$

Typical built-in voltages are in the region between 0.5 V and 1 V.

In typical sensor applications one side of the junction has a very high (so- called p^+ or n^+) dopant concentration, while the other one has a very low one[3]. Taking this into account and replacing the low doping concentration with the effective doping concentration on the lowly doped side, the junction width can be approximated as:

$$w = \sqrt{\frac{2\epsilon\epsilon_0 U_{bi}}{e_0 N_{eff}}} \tag{2.7}$$

Applying an external voltage to the p-n junction either increases or decreases the width of the space charge region. Below the reverse bias case (increasing the width of the space charge region) is discussed. A p-n junction in the forward bias case behaves distinctively different than in the reverse bias case.

The space charge region is also called depleted region, as it is devoid of free charge carriers. If the applied voltage U is large compare to the built-in voltage (which is usually the case) the width of the depletion region is:

$$w = \sqrt{\frac{2\epsilon\epsilon_0 U}{e_0 N_{eff}}} \tag{2.8}$$

At a certain voltage the depletion region reaches the full thickness d of the diode. This voltage is called depletion voltage U_{dep} and can be expressed as:

$$U_{dep} = \frac{e_0 d^2 N_{eff}}{2\epsilon\epsilon_0} \tag{2.9}$$

Charge carriers which are created inside the depleted region either by thermal excitation or external stimuli are subjected to the charge carrier transport mechanisms explained below.

2.3.1 Capacitance of the p-n junction

The depleted region inside the silicon volume can be seen as a capacitor. The capacitance of a p-n junction can be defined as:

$$C(U) = \frac{dQ}{dU} = \frac{dQ}{dw}\frac{dw}{dU} \tag{2.10}$$

[3] In this way the width of the depletion zone w can be approximated by the length of the space charge region on the lowly doped side.

The space charge of the diode can be defined as $Q = e_0 A N_{eff} w$, with A being the area of the diode. Assuming an applied voltage $U_{dep} > U \gg U_{bi}$ the diode is depleted up to the width w as given in Equation 2.8 and $\frac{dw}{dU} = \sqrt{\frac{\epsilon\epsilon_0}{2e_0 N_{eff} U}}$.

When edge effects are neglected the diode behaves like a parallel plate capacitor ($C = \epsilon\epsilon_0 A/w$) and the capacitance of the diode is:

$$C(U) = \begin{cases} \epsilon\epsilon_0 A/w = A\sqrt{\frac{\epsilon\epsilon_0 e_0 N_{eff}}{2U}} & \text{if } U < U_{dep} \\ \epsilon\epsilon_0 A/d & \text{if } U \geq U_{dep} \end{cases} \tag{2.11}$$

2.4 Charge carrier transport

Being caused by moving charge, the transport of charge carriers (e.g in a semiconductor) creates a current. When an electric field is applied to a solid state body with free electrons, the electrons do not accelerate indefinitely, but undergo scattering processes at crystal impurities or with lattice vibrations (phonons). These scattering processes can be understood as a friction term compensating the acceleration of the charge carriers, resulting in a constant drift velocity (Drude model [18]). The resulting current density $\vec{j}$ is proportional to the electric field $\vec{E}$. The proportionality constant σ is called conductivity.

$$\vec{j} = \sigma \vec{E} \tag{2.12}$$

According to the Drude model, which is valid at non-cryogenic temperatures and over distances of more than a few 100 nanometers, the conductivity can be described by the product of the elementary charge e_0, the charge carrier density and the mobility μ of the charge carriers.

$$\sigma = e_0 n \mu \tag{2.13}$$

When both electrons and holes contribute to the current both contributions are summed up.

$$\sigma = e_0(n_e \mu_e + n_h \mu_h) \tag{2.14}$$

For high electric fields the mobility is a function of the electric field, its dependence is investigated in Chapter 8.

A detailed simulation of the charge carrier transport processes is used in Chapter 7.

2.4.1 Drift

Charge drift is an average process with an average velocity which is the product of mobility and electric field. The drift velocity saturates for high fields.

$$\vec{v}_{dr} = \pm \mu \vec{E} \tag{2.15}$$

The sign of the drift velocity is defined by the sign of the charge of the charge carrier (q/e_0).

2.4.2 Diffusion

Even when no electric field is applied charge carriers constantly undergo a random walk process due to their non-vanishing thermal energy.

In one dimension an initial delta distribution of N_0 charge carriers in space at $t = t_0$ and $x = x_0$ can be described by a Gaussian distribution for $t > t_0$, with $D = \mu \frac{k_B T}{e_0}$ being the diffusion constant according to the Einstein relation.

$$N(x) = \frac{N_0}{\sqrt{4\pi D(t - t_0)}} exp(-\frac{(x - x_0)^2}{4D(t - t_0)}) \tag{2.16}$$

2.5 Radiation damage

Radiation damage in silicon sensors can be separated into two categories. Surface damage, which is created by ionization in silicon-dioxide and at the Si-SiO_2 interface, and lattice defects in the silicon bulk which is created by radiation with energy above certain energy thresholds.

Surface damage can further be separated into two kinds of damage: Oxide charges and interface traps. Both kinds of damage influence the electronic properties of the sensor.

Different kinds of lattice defects are shown in Figure 2.3. The most common lattice defects are missing lattice atoms (vacancies).

The introduction of additional defects after irradiation is dependent on the type of irradiation, its fluence, its energy and the silicon material itself, especially the amount of impurities. Lattice defects are created by non-ionizing energy loss (NIEL), especially the primary silicon recoil ions are of importance [20, 21].

Lattice defects effectively introduce new levels in the band gap. Depending on the lattice temperature these levels can be (partly) ionized and thus contribute to the effective doping concentration, increase the leakage current by Shockley-Read-Hall generation act as recombination centers or act a trapping centers of charge carriers. Any combination of these effects is possible.

Changes of the effective space charge result in changes of the electric field in depleted diodes, which in turn influences the drift velocity of the charge carriers.

SRH generation causes an increased leakage current in the silicon bulk due to a higher probability to thermally create electron hole pairs.

Trapping effectively reduces the amount of drifting charge in the silicon bulk. Eventually these charges will be released from the traps (detrapped) and contribute to the current again.

Defects can migrate in the silicon lattice. The activation energy of this migration is different for each defect, leading to the possibility to influence defects by annealing (tempering) the silicon material. Defects can also interact with each other forming new defects or vanishing (e.g. vacancies and interstitials).

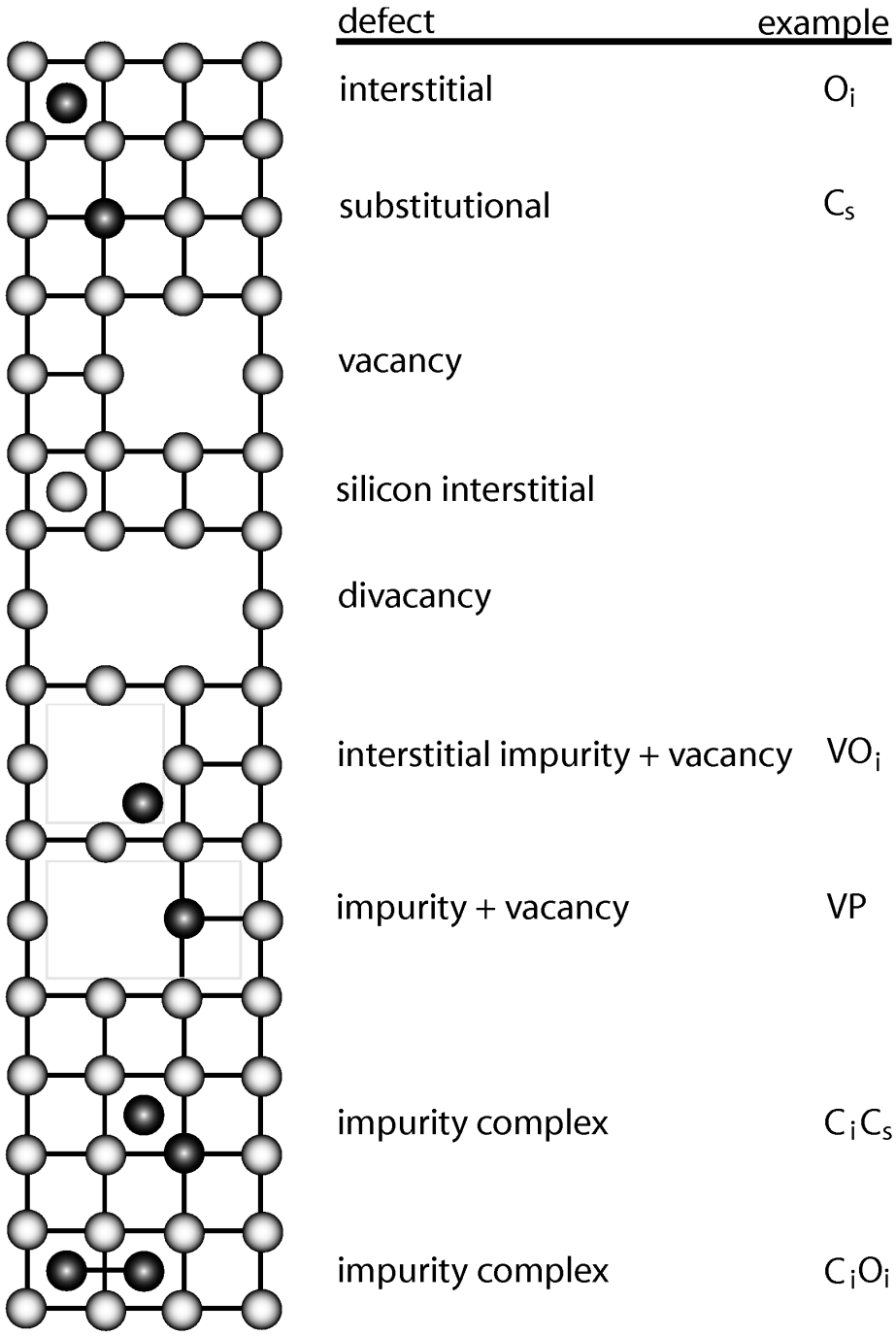

Figure 2.3: Examples of lattice defects in silicon. Figure provided by [19].

3 Interactions with radiation

In order to use silicon as a sensor material it has to be understood how the radiation interacts with silicon material.

The dominant mechanism used for the detection of radiation is ionization. Electron hole pairs are created by the ionization process inside the sensor volume, which are in turn detected.

Above a threshold of a few tens of eV, the number of electron hole pairs created in the silicon lattice is proportional the energy absorbed by the silicon. Being a statistical process the creation of electron hole pairs is associated with corresponding fluctuations. On the average one electron hole pair is created for every 3.6 eV deposited in the crystal lattice. The difference of this energy to the band gap energy of silicon (≈ 1.12 eV at room temperature) is dispersed as phonons. The associated production of electron hole pairs and phonons results in a reduced statistical variance of the number of created electron hole pairs. The reduction factor is called Fano factor and has been experimentally determined to be around 0.1 for silicon.

3.1 Charged particles

When charged particles traverse matter they can undergo the following processes:

1. Elastic collisions with shell electrons.
2. Elastic collisions with nuclei or entire atoms, where a part of the kinetic energy is transferred to the recoiling atom or nucleus.
3. Inelastic collisions with shell electrons, where the released energy is used for ionization or excitation.
4. Inelastic collisions, where due to the deceleration of the particle in the Coulomb field of nucleus or electrons energy is released in form of bremsstrahlung.
5. Collisions with nuclei that excite the nucleus or initiate nuclear reactions.
6. Emission of light when the velocity of the passing particle is larger than the speed of light in this medium (Cherenkov radiation).

The domination of certain processes is strongly dependent on the particle type and the particle energy.

The mean energy loss of charged particles follows the Bethe-Bloch formula describing the energy transfer to shell electrons of the matter:

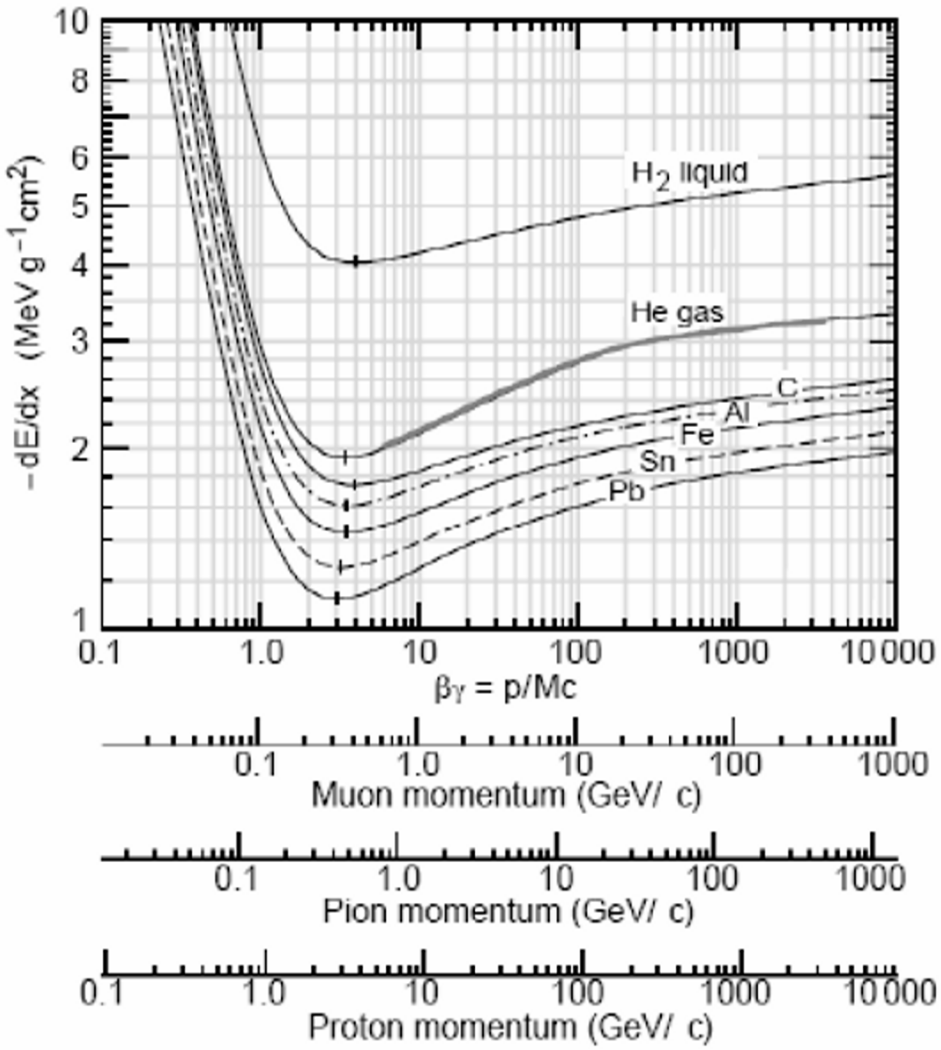

Figure 3.1: Energy loss of charged particles as function of momentum. Reproduced from [22].

$$-\left(\frac{dE}{dx}\right) = \frac{Z^2 e^4 n_e}{8\pi\epsilon_0^2 v^2 m_e}\left\{\ln\frac{2m_e v^2}{\langle E_B^{(e)}\rangle(1-\beta^2)} - \beta^2 - \frac{\delta}{2}\right\} \tag{3.1}$$

The following definitions are used when calculating energy losses of charged particles: $\beta = v/c$ being the velocity in units of the speed of light, the rest mass of the electron m_e, the mean binding energy of an electron to its atom[1] $\langle E_B^{(e)}\rangle = 13.5Z$ and $n_e = \frac{Z}{A}\rho N_A$, the electron density of the matter. With ρ being the mass density of the matter and N_A the Avogadro number.

[1]There is more accurate data available, tabulated for each element [22].

The energy loss as function of momentum is depicted in Figure 3.1. For low velocities ($\beta \ll 1$) the energy loss per unit path length decreases like $1/\beta^2$ with increasing momentum until reaching a minimum at $\beta\gamma \approx 3$. Particles with this momentum are called minimum ionizing particles. Further increase of the momentum increases the energy loss (called relativistic rise) until reaching a saturation value for very high momenta ($\beta \approx 1$).

When the energy loss in a single interaction is large enough to liberate a shell electron, the liberated electron is called δ- or knock-on electron. δ-electrons may carry a significant amount of energy, resulting in the need to consider them as secondary particles, which can ionize the sensor material.

3.1.1 Minimum ionizing particles

In silicon sensors of common thicknesses (< 1mm) the energy loss of minimum ionizing particles (mips) is small compared to the particle energy. Thus mips traverse the commonly used silicon sensors. The distribution of electron hole pairs in sensors which are small compared to the radiation length of the mip follows the Vavilov distribution (modified Landau distribution taking the escape of δ-electrons into account). The resulting charge carrier densities are usually small compared to the bulk doping.

3.1.2 Heavy ions

The energy loss for heavy ions is proportional to Z^2 of the ion, as seen from Equation 3.1. As a consequence of the behavior of the energy loss as function of the particle momentum (shown in Figure 3.1), a heavy particle looses most of its energy at the end of its trajectory, causing the so called Bragg peak.

Thus when heavy ions are stopped within the silicon lattice they deposit a large fraction of their energy locally. Stopped heavy ions cannot be considered as mips, as the large energy deposition gives rise to localized areas with high charge carrier densities and thus plasma effects.

The effects of these so called plasmas are investigated in this work.

3.1.3 Electrons

Due to their low mass the total energy loss for electrons consists of two components, the energy loss due to collisions and the energy loss due to radiation.

$$\left(\frac{dE}{dx}\right) = \left(\frac{dE}{dx}\right)_{col} + \left(\frac{dE}{dx}\right)_{rad} \tag{3.2}$$

Collision (ionization) energy losses of electrons deposit energy to the silicon lattice directly while radiative losses produce bremsstrahlung, which may escape the sensor.

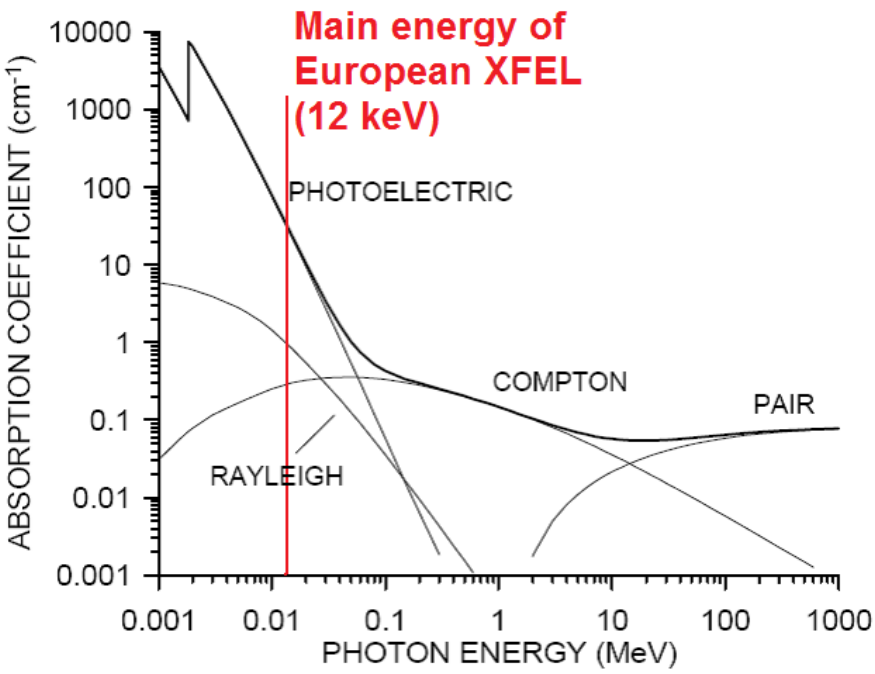

Figure 3.2: Attenuation coefficient in silicon as function of photon energy. Reproduced from [23] and modified.

3.2 Neutral particles

3.2.1 Photons

Photons can interact via the electromagnetic force with shell electrons, nuclei or other electromagnetic fields either elastically or inelastically.

Elastic reactions are dominant at low photon energies and include the recoil free absorption and emission of photons in nuclei (Mössbauer effect), the resonant excitation of shell electrons (Thomson scattering), coherent scattering (Rayleigh) and interference in solid state bodies (Bragg diffraction).

Inelastic scattering includes the Compton effect[2] (scattering at a quasi free shell electron or nucleus), scattering at a nucleus with excitation, incoherent scattering at single nucleons in the nucleus, etc.

Photons can also be absorbed by a shell electron (photo effect), the nucleus (photonuclear effect) or in a particle production process (electron-positron pairs or mesons).

Instead of continuously loosing energy, like charged particles, the number of photons (flux) is decreasing continuously with the path x and the number of photons.

$$d\Phi = -\mu\Phi dx \tag{3.3}$$

$$\Phi(x) = \Phi_0 e^{-\mu x}, \tag{3.4}$$

[2]which is an elastic interaction of electron and photon

where Φ_0 is the initial flux and μ is the linear absorption coefficient. It is a product of atomic concentration (N_V) and effective absorption cross-section (σ_a), which is the sum of the cross-sections for the photo effect, Compton effect and pair production (the cross section of other effects is small compared to the cross sections of these three effects).

The linear absorption coefficient μ of silicon as function of photon energy is shown in Figure 3.2.

Photo effect

The photo effect liberates a shell electron from its atom. The resulting kinetic energy of the photoelectron is

$$E_e = E_\gamma - E_B^{(i)}, \tag{3.5}$$

where E_γ is the photon energy and $E_B^{(i)}$ is the binding energy of the electron of the (i)-th shell. Energy and momentum conservation require the presence of a nucleus that absorbs a part of the momentum.

The photo effect cross-section shows characteristic peaks at $E_\gamma = E_B^{(i)}$ and is decreasing with increased energy. When electrons from inner shells are liberated characteristic x-rays (fluorescence photons) are produced by the refilling of the vacant shells from the outer shells.

Compton effect

In the laboratory system, the Compton effect is a scattering process that transfers a part of the photon energy to the electron. Although the electron is bound to the atom it can be considered free and at rest ($E_\gamma \gg E_B^{(i)}$). The kinematics of the Compton effect can be deduced from energy and momentum conservation. The energy of the scattered photon ($E_{\gamma'}$) and electron (E_e) is

$$E_{\gamma'} = E_\gamma \frac{1}{1+\epsilon(1-\cos\theta)} \tag{3.6}$$

$$E_e = E_\gamma \frac{1-\cos\theta}{1+\epsilon(1-\cos\theta)}, \tag{3.7}$$

where θ is the angle between the undisturbed photon direction and the scattered photon direction and $\epsilon = E_\gamma / m_e c^2$.

Compton scattering of photons at atomic nuclei can be neglected as the electromagnetic radius of the nucleus is small compared to that of the electron.

Pair production

Pair production is the process of emission of positron and electron due to absorption of a photon in the Coulomb field of an atomic nucleus or electron. Pair production in the Coulomb field of a nucleus has a threshold energy of $E_{th} = 2m_e c^2 = 1.02\ MeV$, which is the combined rest mass of electron and positron.

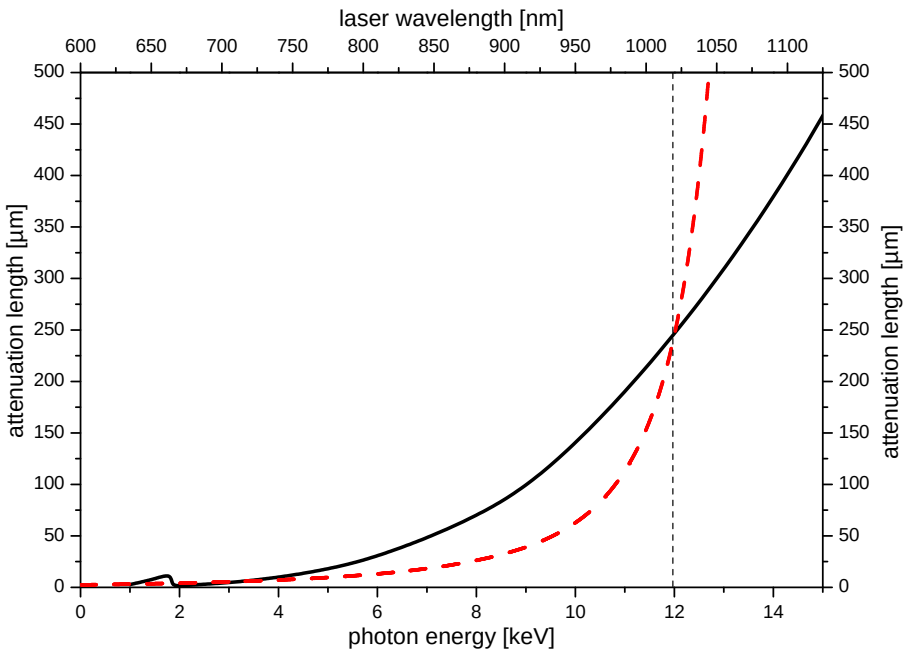

Figure 3.3: Attenuation length in silicon as function of photon energy for optical photons and x-ray photons. Values for optical photons (dashed red line) are calculated according to [24]. Values for x-rays (solid black line) are calculated according to [25]. Light of 660 nm and 1015 nm is used in this work, as the attenuation length of these wavelengths corresponds to the attenuation length of 1 keV and 12 keV x-rays.

3.2.2 Optical photons

Optical photons are a special case, as they do not ionize the silicon lattice and their wave character is dominant. If the photon energy is below the band gap energy of silicon, electron hole pairs cannot be excited directly. However electron hole pairs can be created by second order effects.

If the photon energy exceeds the band gap energy, electron hole pairs can be excited and additional energy of the optical photon is dissipated to the lattice as phonons. The lasers used in this work produce photons with energies exceeding the band gap energy. The attenuation length of optical photons as function of wavelength is compared to the attenuation length of x-ray photons in Figure 3.3.

Once the photon energy exceeds multiples of the band gap energy additional effects, like the excitation of multiple electron hole pairs are possible.

It should be noted that the aforementioned mechanisms are approximately true at room temperature, at cryogenic temperatures a wealth of spectroscopic possibilities exist that allow resonant production of bound electron hole pairs (excitons) and various excited states states of electrons and holes.

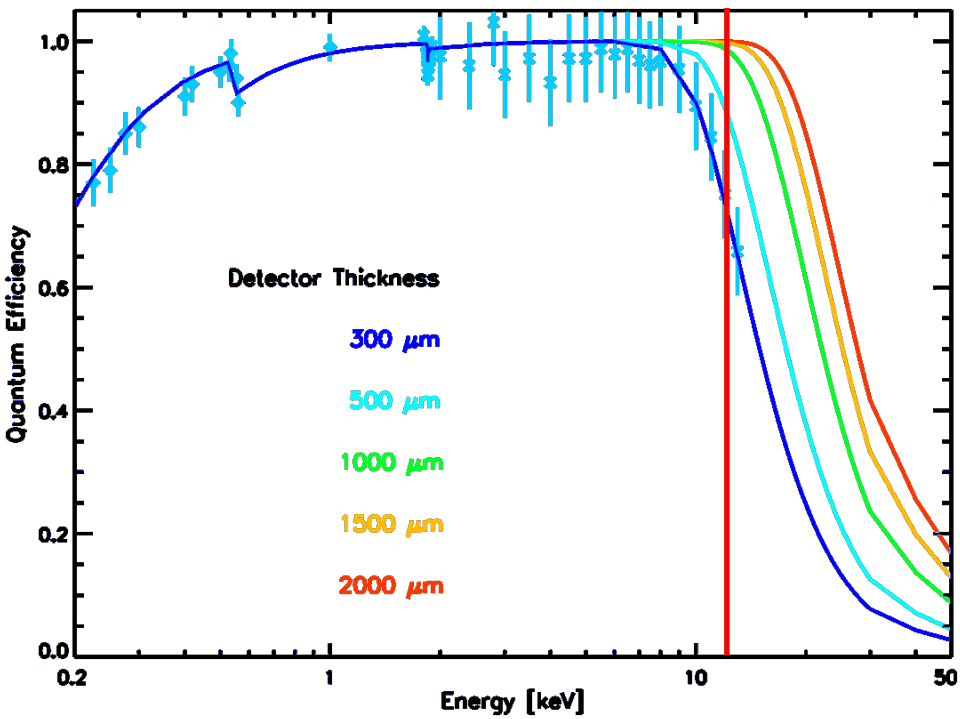

Figure 3.4: Quantum efficiency of silicon sensors with different thicknesses as function of photon energy. At 12 keV (marked, as it is the main energy of the European XFEL) the quantum efficiency is a function of the sensor thickness. Reproduced from [26].

3.2.3 X-rays

X-rays carry enough energy to ionize the silicon lattice once they are absorbed. X-rays can interact with silicon in multiple ways, however they carry not enough energy to produce electron positron pairs. For low energies, like 12 keV, the main energy of the European XFEL, photoabsorbtion is the dominant process. The photon is absorbed directly by the lattice, creating electron hole pairs locally. Compton scattering is possible, but not dominant at low energies. When a photon undergoes Compton scattering, as explained above, the photon transfers part of its energy to an electron of a silicon atom. The scattered photon can undergo additional scattering and absorption processes. The secondary electron is an ionizing particle and transfers its energy to the lattice in the usual way.

It should be noted that the absorption of primary x-rays (attenuation) may follow a different distribution than the energy absorbed by the lattice, as energy can be transported by secondary particles like fluorescence photons, Compton scattered photons and secondary electrons.

Figure 3.4 shows the quantum efficiency (probability to detect a photon) as function of photon energy for different thicknesses of silicon.

3.2.4 γ-rays and higher energy photons

At energies beyond the x-ray regime additional interactions with matter are possible. If the photon energy exceeds twice the electron mass, pair production is possible, as explained above. The photon is converted into an electron and a positron, any energy in excess of twice the electron mass is transfered to the particles as kinetic energy. Electron and positron are charged particles and interact with silicon in the above mentioned way.

3.2.5 Neutrons

Although neutrons of enough energy can produce silicon recoils that deposit their energy by ionization, most commonly indirect methods are used to detect neutrons.

For some applications (mostly low energy neutron detection) neutron converters like ^{3}He, ^{6}Li or ^{10}B are used. These isotopes have a high cross section for interactions with low energy neutrons and produce densely ionizing particles, which in turn are detected.

In other applications hydrogen rich moderators, like plastic, are used. These moderators contain a high amount of hydrogen, which produces proton recoils with an average energy of half of the neutron energy. Being charged particles the recoil protons can then be detected.

4 Silicon sensors for radiation detection

Silicon sensors detect radiation by detecting the charge carriers created due to interactions of the radiation with the sensor material.

Although there are certain applications where timing is not critical (e.g. astronomy) and charge is collected slowly, the majority of applications utilizes an electric field inside the sensor volume to quickly drift charges to the readout electrodes.

The drifting charge induces a current signal on the readout electrodes which can be integrated to yield the collected charge. Some sensor types, like CCDs, pn-CCDs or DEPFET sensors, do not evaluate this induced current, but store the generated charge in potential minima, which can be manipulated to read out the sensor signal.

All sensor types presented in this chapter use the drift approach, although they differ in geometry, drift direction, read out scheme and sensor material.

4.1 Planar diodes (pad sensors)

Due to their simple geometrical layout, planar diodes (also called pad diodes or pad sensors) are commonly used as test structures to investigate material properties. They can be reasonably well approximated with simple assumptions. This facilitates the calculation of certain quantities necessary for transport simulations and offers the possibility to study certain aspects of the material with a well defined geometry.

A sketch of a typical pad diode is shown in Figure 4.1.

During the course of this work pad diodes have been used extensively to study the

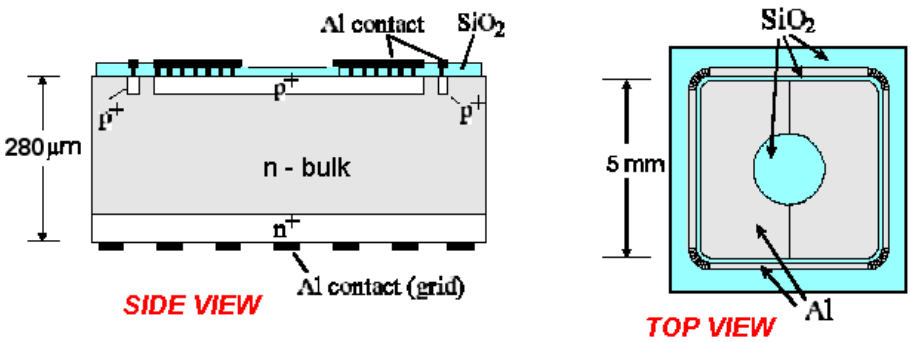

Figure 4.1: Sketch of a pad diode. Reproduced from [27] and modified.

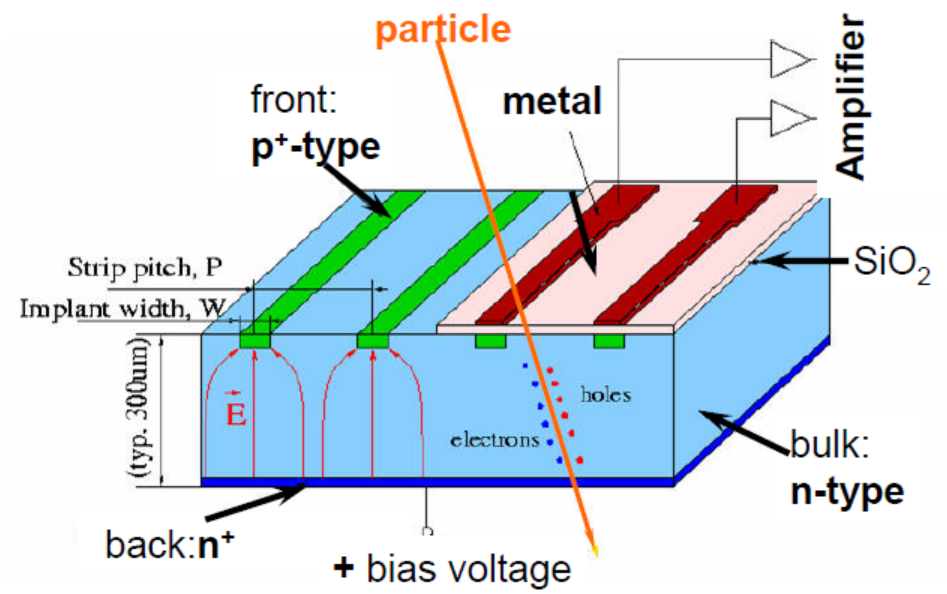

Figure 4.2: Sketch of an AC coupled strip sensor. Reproduced from [28].

bulk mobilities of electron and holes in detail (presented in Chapter 8). Additionally, plasma effects in pad diodes have been studied in Chapter 10.

4.2 Strip sensors

Strip sensors allow to gain information on the position of an impinging particle perpendicular to the strips. In order to reconstruct both coordinates from a mip[1] perpendicular to the sensor depth, two strip sensors tilted with respect to each other can be used. However if more than one particle is detected during the readout cycle of both sensors the impinging positions can not be unambiguously determined without additional information.

The periodicity of a strip sensor (e.g. distance between the center of two strips) is called pitch. The ratio of implant width over pitch is usually about 0.25.

Silicon strip sensors can be thought of as pad sensors in which one of the electrodes is divided into slices. However in the region between the strips the situation deviates from the situation in a planar diode.

The electric field of a strip sensor is similar to that of a planar diode, except for small regions in between and close to the strips, but the weighting potential (explained in Chapter 7) of a strip sensor differs from the weighting potential of a planar diode, resulting in different pulse shapes for identical initial distributions of charge carriers.

A sketch of a typical strip sensor is shown in Figure 4.2. The readout of a strip sensor can either happen with a direct connection between implantation and readout electronics

[1] or any other charged particle which is not stopped within the sensor material

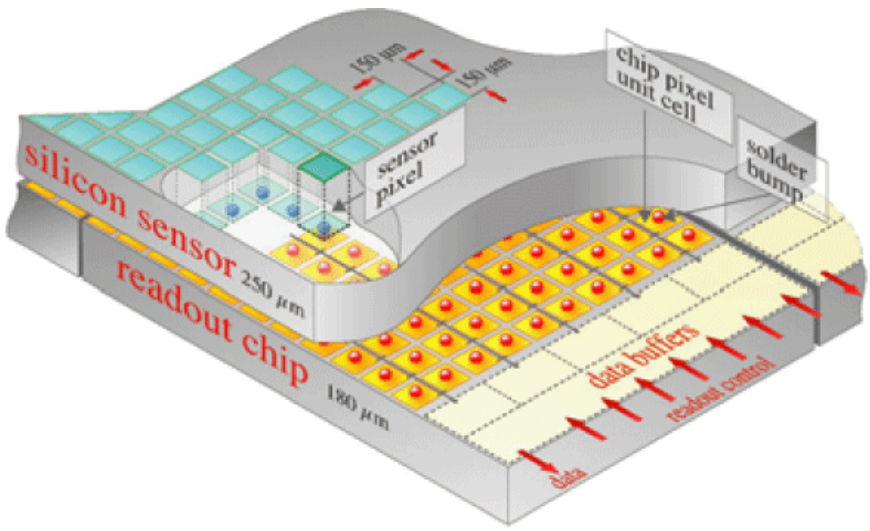

Figure 4.3: Sketch of a bump bonded pixel sensor. Reproduced from [29].

(so called DC coupling) or by contacting a metal layer on top of an insulating layer (so called AC coupling, shown in Figure 4.2). AC coupling allows to protect the input of the readout electronics from the leakage current of the sensor, however it requires a separate way to keep the implants at a constant potential (i.e. sink the current).

In this work strip sensors have been used to gain position information of charge clouds. The results of these investigations are presented in Chapter 11.

4.3 Pixel sensors

Pixel sensors behave similar to strip sensors except for the readout electrode being divided in two dimensions. This allows the determination of x and y coordinate of an ionization event with only one detector. In contrast to the assembly of two strip detectors, which are tilted with respect to each other, pixel detectors have no ambiguity when more than one particle is detected per readout cycle.

A common way to read out a pixel sensor is to bump bond a readout chip to it, thus creating a so called hybrid. Using bump bonding techniques has the advantage of avoiding additional signal routing layers, thus reducing the cross talk and the capacitance of a pixel.

A sketch of a typical pixel sensor bump bonded to a readout chip is shown in Figure 4.3. Like strip sensors, pixel sensors can be operated both with AC and DC coupling. In case of AC coupling an elaborate biasing scheme is needed, which is indicated in Figure 4.3 by the thin black lines connecting always two pixel cells.

4.4 Other silicon sensors

Modern day silicon processing technology allows to manufacture silicon sensors with more complex geometries than typical pad, strip or pixel sensors. Some examples of different types of silicon sensors are explained below.

4.4.1 Silicon drift detectors

Silicon drift detectors are commonly used in applications which require large sensitive areas and low noise.

Different layouts of silicon drift detectors are possible. All of them have one feature in common: they drift the created charge carriers laterally. This results in longer charge collection times (namely the drift time) in contrast to the 'standard' sensors explained above.

Drift detectors usually deplete laterally and thus have smaller capacitances than comparable strip sensors, which in turn results in better noise performance.

Due to the longer drift time compared to 'standard' silicon detectors the maximum count rate of drift detectors is lower, as multiple interactions within the maximum drift time cannot be distinguished.

When the time of interaction with the sensor is externally provided, the drift time can be used to determine the distance to the readout electrode in which the charge was created. Combining this information with position information from a structured readout electrode, both coordinates of an impinging particle can be reconstructed.

4.4.2 3D sensors

So called 3D sensors utilize the same principle as drift detectors, namely drifting the charge carriers laterally instead of along the thickness of the device. In contrast to silicon drift detectors, the drift path in 3D detectors is intended to be as short as possible to reduce possible trapping effects introduced by radiation damage.

3D sensors are discussed as possible technology for future sensors in high energy physics (sLHC) as they disentangle the amount of created charge (proportional to the device thickness) from the drift distance (proportional to the column separation).

A sketch of a typical 3D sensor is shown in Figure 4.4.

4.4.3 pn-CCD sensors

CCD stands for Charge Coupled Device and describes a readout technique that differs in the signal generation compared to the readout technique described above for the 'standard' silicon sensors.

In a CCD, the charges, created by the radiation, are stored in potential minima inside the CCD, constituting pixel cells, and are transfered to a readout-node when the readout takes place. Thus the charge collection process and the charge readout are

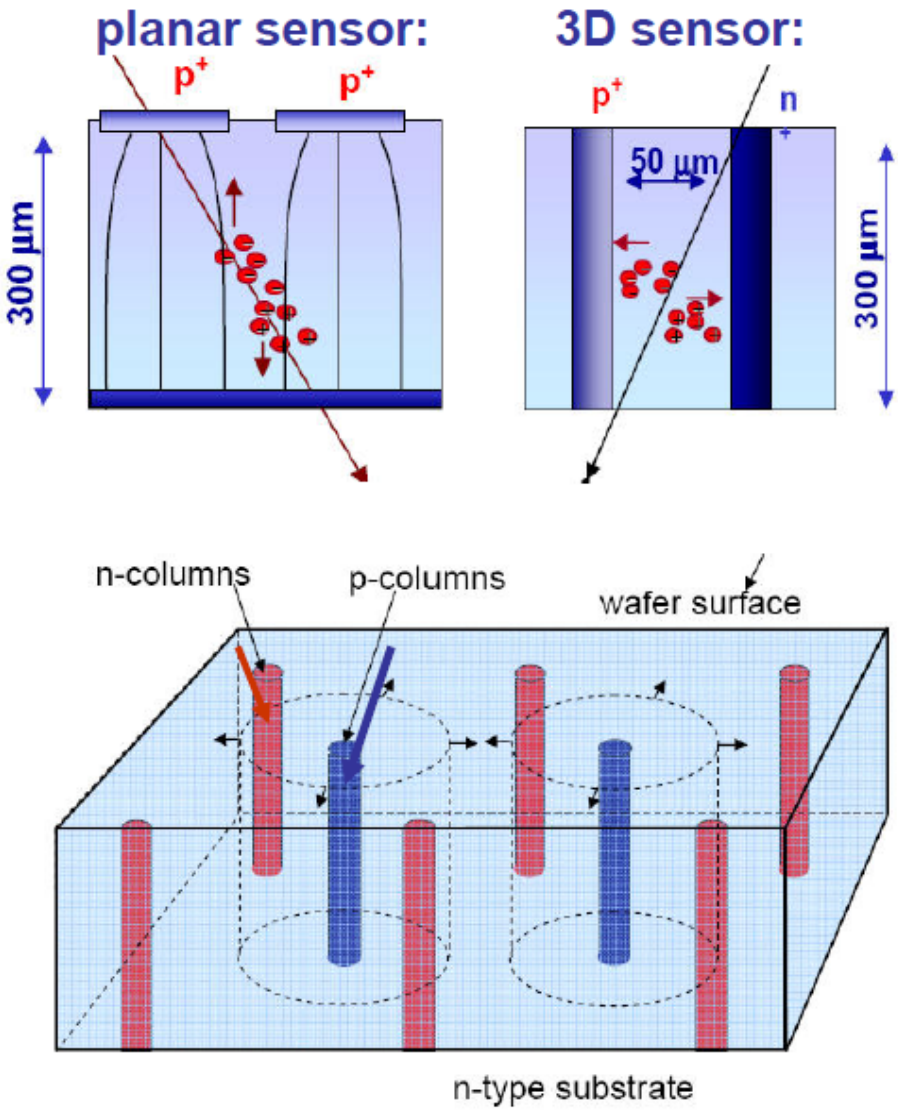

Figure 4.4: Simplified sketch of a 3D sensor. Reproduced from [28].

performed separately, allowing very long integration times (also called illumination time or acquisition time) compared to 'standard' silicon sensors and a low noise readout.

The in-sensor charge transfer allows to read out the sensor with a single on chip amplifier, without the need of routing layers. The signals of each row are shifted to the readout column, which is read out sequentially. In this way a pixel structure can be read out sequentially without the need to bump bond a specialized readout chip. As the readout circuit usually consumes most of the power of a detector assembly, pn-CCD sensors, having only one readout circuit for the whole pixel matrix, are suited for environments where low power consumption is mandatory, e.g. space missions.

However such a readout scheme also limits the readout speed of the detector, as signals

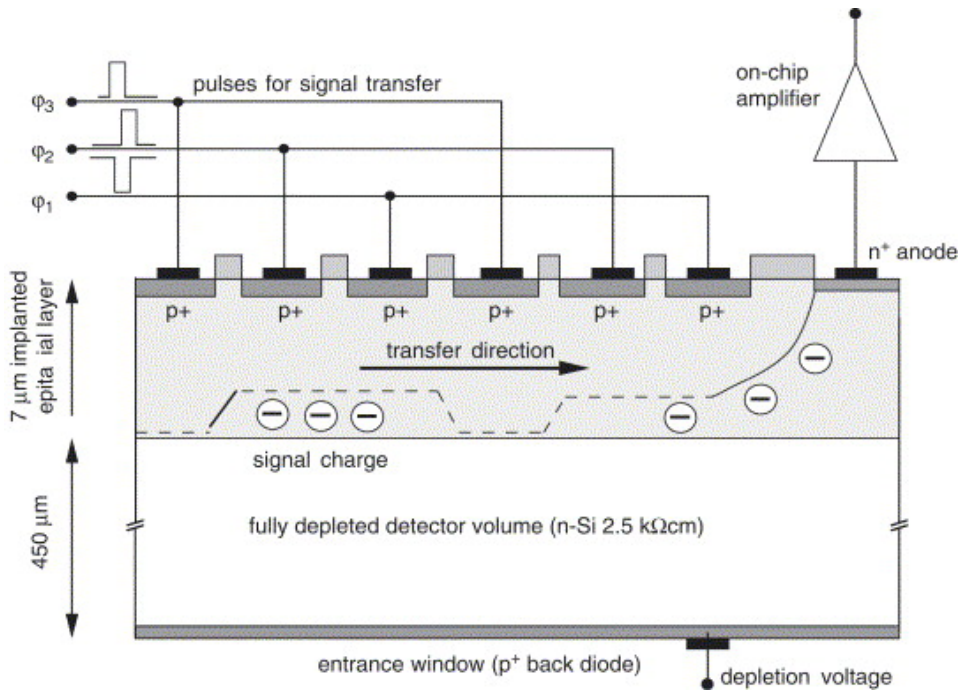

Figure 4.5: Simplified sketch of a pn-CCD sensor. Reproduced from [30].

are not processed in parallel. A further problem develops when signals occur during the readout cycle, as they would be attributed to a wrong pixel. In order to avoid this, shutter techniques have to be used.

A sketch of a typical pn-CCD sensor is shown in Figure 4.5.

When the sensor material suffers from bulk damage certain defects trap charge carriers. Depending on the properties of the defects and their detrapping time, the trapped charge is released to the sensor volume again. This will create a memory effect in the sensor, i.e. a pixel will generate charges on its own (due to the release of trapped charge carriers) and thus fake a signal, although it has already been read out and should not contain charges (similar to blooming or smearing effects known in digital photography).

Depending on the ratio of detrapping time and readout cycle time this effect may either be not observed at all, appear as a 'tail' of the hit pixel along the readout direction or increase the leakage current of the sensor.

4.4.4 DEPFET sensors

DEPFET stands for Depletion Field Effect Transistor and is a further evolution of the CCD principle. While charge is generated and stored in the same way as in CCDs, the potential minimum is located beneath the conducting channel of a transistor. Thus the collected charge modulates the source-drain current of this transistor, which in turn is the first, low noise amplification process of the readout chain.

In contrast to a CCD device the charge is not transfered between the potential minima, thus requiring a DEPFET for each pixel cell. In between two data acquisitions, the

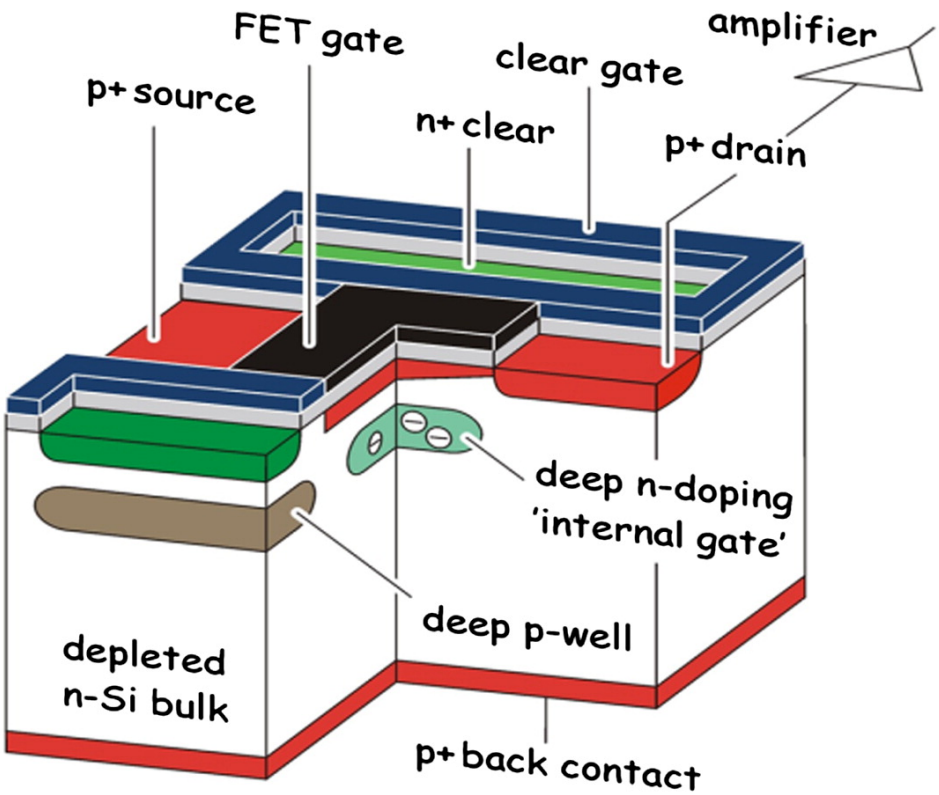

Figure 4.6: Simplified sketch of a DEPFET sensor cell. Reproduced from [31].

charge in the internal gate of the DEPFET needs to be removed, thus introducing a dead time of the sensor.

As charge is not transfered between pixel cells, there are no blooming or smearing effects when charges are trapped in damaged bulk material.

A sketch of a typical DEPFET sensor cell is shown in Figure 4.6.

4.5 Other sensor materials

Although silicon is a common sensor material, there are certain limitations inherent to the silicon material, which prohibit its use in certain applications.

One of this limitations is the relatively low atomic number Z = 14, which strongly reduces the quantum efficiency of silicon sensors for x-ray energies above a few ten keV (shown in Figure 3.4).

4.5.1 Other semiconductor materials

A photon which does not interact with the sensor material is not detected. Thus, in order to increase the detection probability in the sensor material, a sensor material with

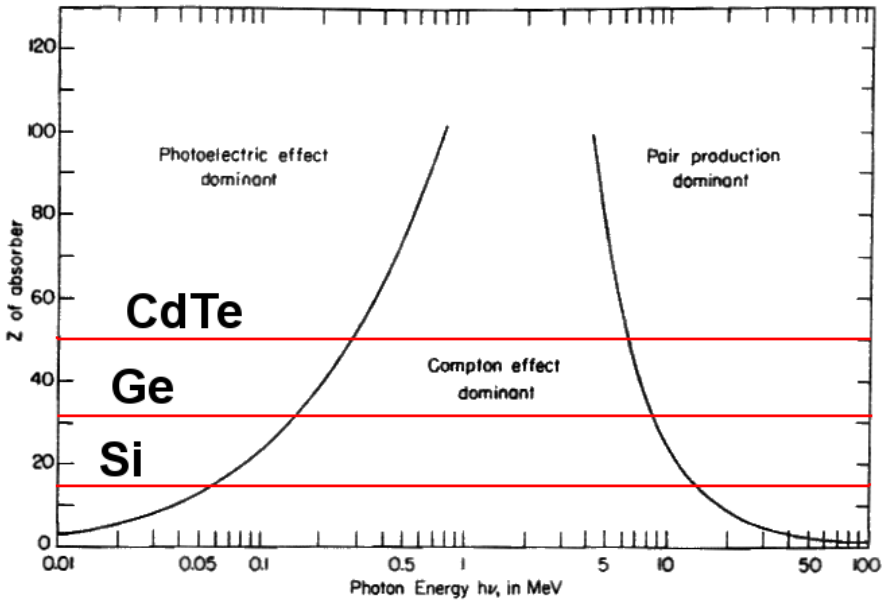

Figure 4.7: Dominant interaction of photons as function of energy and atomic number. Reproduced from [32] and modified.

a higher atomic number can be chosen. The probability of photoabsorption scales with approximately Z^5.

An overview of the dominant process as function of photon energy and atomic number of the sensor material is shown in Figure 4.7.

To overcome the limitation of the low atomic mass of silicon other semiconductors can be used to construct the same sensor types as mentioned above. Especially the hybrid technology (bump bonding the sensor material to a readout chip) allows an easy substitution of the sensor material, as only limited processing is needed on the sensor material.

Most alternative materials suffer from less developed processing techniques compared to silicon, limited availability with sufficient quality (e.g CdTe), and additional limitations imposed by the sensor material (e.g. Germanium needs cooling with liquid nitrogen).

4.5.2 Diamond

In high energy physics a contrary limitation of silicon is observed. A precise tracking of charged particles is desired, requiring the detector to have a small mass to reduce multiple scattering of the charged particles. Simultaneously neutral particles (especially photons) should be disturbed as little as possible. As mentioned in Chapter 3, high energy photons undergo pair production, the relevant parameter is the radiation length[2],

[2] which can also be used to estimate the amount of multiple scattering

which is the 7/9 of the mean free path of a photon before undergoing pair production.

As the cross section of pair production scales with approximately Z^2 a material with a lower atomic number is favorable over a material with a high atomic number. Comparing carbon to silicon increases the radiation length per unit path length almost by a factor of two [33].

Being an insulator, diamond has intrinsically no leakage current and thus no need for sensor cooling. This reduces the total mass which has to be used in the tracking region of a high energy physics experiment, thus reducing the multiple scattering of charged particles.

Diamond can be used as a sensor material for radiation detection without a p-n junction, as its intrinsic charge carrier concentration is very low ($< 10^3$ cm^{-3}). It has a large bandgap of ≈ 5.5 eV and 13 eV of energy are needed to create an electron hole pair. Thus the expected signal created by a mip in a diamond detector is less than the expected signal of a mip in a silicon sensor of identical thickness. Once electron hole pairs are created the drift and diffusion processes observed in silicon are also applicable for diamond. Additionally the mobilities of electrons and holes in diamond are larger than in silicon (≈ 1900 cm^2/Vs for electrons and ≈ 2300 cm^2/Vs for holes) allowing a faster readout of the detector (diamond data quoted from [34]).

5 Current and capacitance measurements

In order to understand basic properties of the investigated sensors, current and capacitance of the sensors have been measured as function of voltage.

Current versus voltage (I/V) and capacitance versus voltage (C/V) measurements are a common tool to characterize sensor materials.

A schematic drawing of the setup used to measure I/V and C/V characteristics is shown in Figure 5.1.

All sensors investigated in the course of this work have been characterized by measuring the I/V and the C/V behavior, however unless it deviates strongly from the expectations for the given geometry the characteristics will not be reproduced here.

The measurements were performed in a probe station, which contacts the sensor with manually adjustable needles. The probe station is enclosed in a light tight metal casing, which acts as a Faraday cage. All signals which leave the enclosure are on the inner conductors of RG-58 cables with BNC connectors, the outer conductors are grounded and thus act as a shield.

The measurements were controlled by a custom written LabView software on a per-

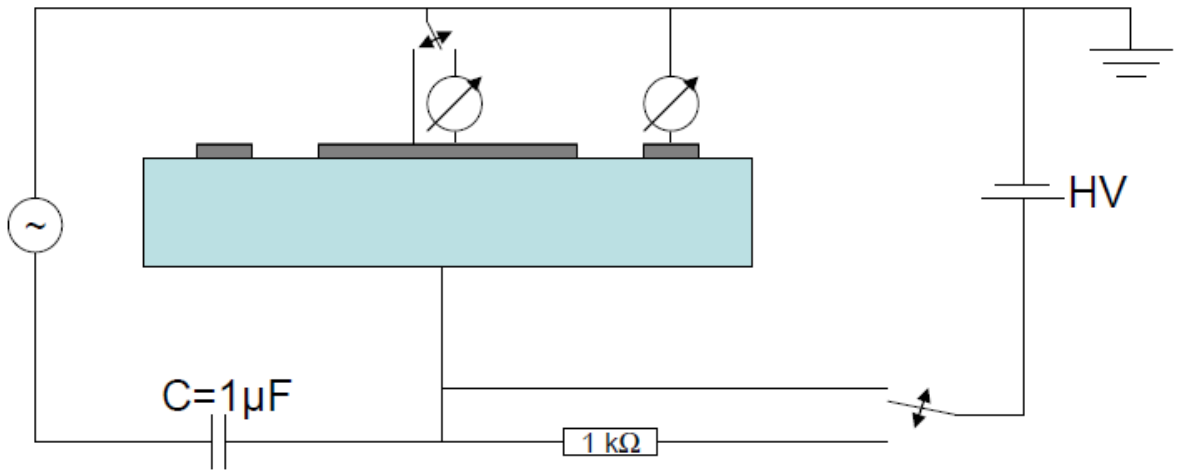

Figure 5.1: Schematic drawing of the setup used for current and capacitance measurements. The two switches are connected and allow to chose between I/V and C/V measuring mode. The LCR meter is drawn as an AC source, the high voltage source as a battery.

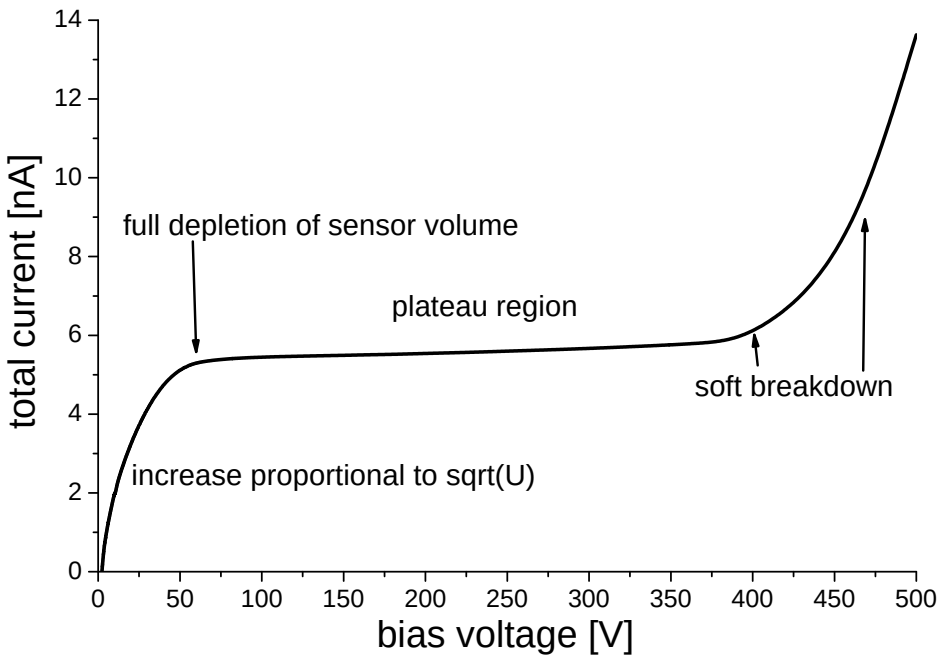

Figure 5.2: I/V measurement of the strip sensor CG1017. All strips were measured in parallel, contacting the bias ring of the sensor. The guard ring was grounded separately, its current is not shown here.

sonal computer which also stores the measurement data to the storage disk.

Although most of the measurements in this work have been done using the transient current technique (explained in Chapter 6) I/V and C/V characteristics have been measured to gather fundamental information on the sensors.

5.1 I/V Measurements

I/V measurements are done by applying a selected DC voltage to the sensor and measuring the DC current. In case of a pad diode, pad current and guard ring current are measured with different devices to separate the current generated in the bulk silicon and the current generated at the surface and cut edges.

On strip sensors such an approach is only possible when the sensor is AC coupled. In this case bias ring and guard ring are contacted separately. In case of DC coupled sensors no bias ring exists. Thus the properties of a single strip were measured by contacting it directly. All other strips are biased by a punch through mechanism from the guard ring. The punch through mechanism results in a small potential difference between guard ring and biased strips. An I/V measurement of the AC coupled strip sensor CG1017 is shown in Figure 5.2.

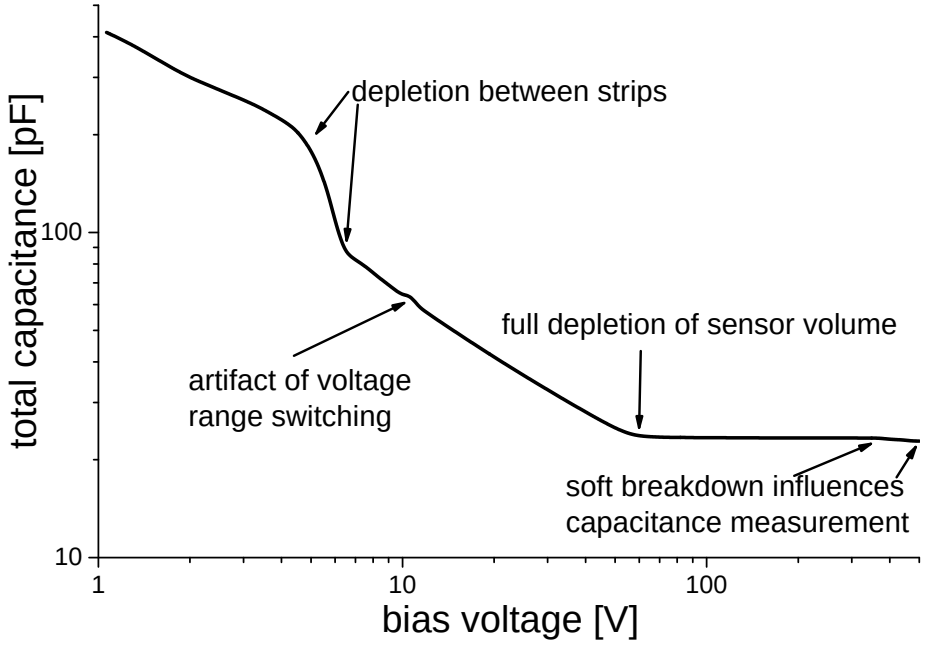

Figure 5.3: C/V measurement of the strip sensor CG1017. All strips were measured in parallel with 10 kHz frequency. The guard ring was grounded separately.

5.2 C/V Measurements

Measuring the capacitance as function of voltage is a bit more complicated than measuring the I/V characteristics. The sensor is still biased with a DC voltage but additionally an LCR meter adds an AC voltage to the bias voltage (shown in Figure 5.1). The LCR meter then measures amplitude and phase shift of the AC current (complex current) and calculates the capacitance from the imaginary part of the current. For the calculation the LCR meter either assumes a parallel or series circuit of a resistor and a capacitor.

In order to account for unwanted capacitances (of setup and guard ring) a zero adjustment is performed before each measurement. The zero adjustment is performed with the sensor connected to the setup on all contacts except the contact to the capacitance under investigation.

The LCR meter then evaluates the difference in the complex current between the zero adjustment and the measurement with the investigated capacitance connected.

The measurement results for the aforementioned strip sensor CG1017 (details of the sensor are found in Table A.1) are shown in Figure 5.3.

6 Transient current technique

The Transient Current Technique[1] (TCT) is a well established technique to determine effective trapping times in irradiated silicon diodes [35], [36]. It can also be used to determine the field distribution in these devices [37]. TCT utilizes the drift of electron hole pairs created inside a reverse biased diode either by ionizing radiation or laser light. These charge carriers drift under the influence of the electric field and induce a current in the readout circuit. The current pulse contains information about the amount of drifting charge and its drift velocity.

6.1 Experimental setup

In order to study the impact of electron hole plasmas on the current pulses of segmented sensors a multi channel Transient Current Technique (mTCT) setup was built. The required high number of charge carriers were created with sub-ns lasers and the time resolved current pulses of the investigated sensors were read out by a Tektronix DPO 7254 2.5 GHz oscilloscope (4 channels simultaneously).

Photographs of the setup used in this work are shown in Figures 6.1 and 6.2.

The setup was designed to be very versatile. The following features were required:

- Light injection from both sides.
- High intensity laser light; focused to a small spot in order to create the charge densities required to study plasma effects.
- Large dynamic range in the laser power.
- Large dynamic range in the readout circuit in order to investigate very high intensities and very low intensities with the same setup.
- High bandwidth of the readout circuit in order to sample the fast transients correctly.
- Bias voltage applied to the rear side.
- Remote positioning of the sensor with respect to the laser beam; position error smaller than laser beam diameter.

[1] TCT is sometimes called Time Of Flight (TOF) method as well. However TOF just evaluates the pulse width, whereas TCT evaluates the whole pulse structure.

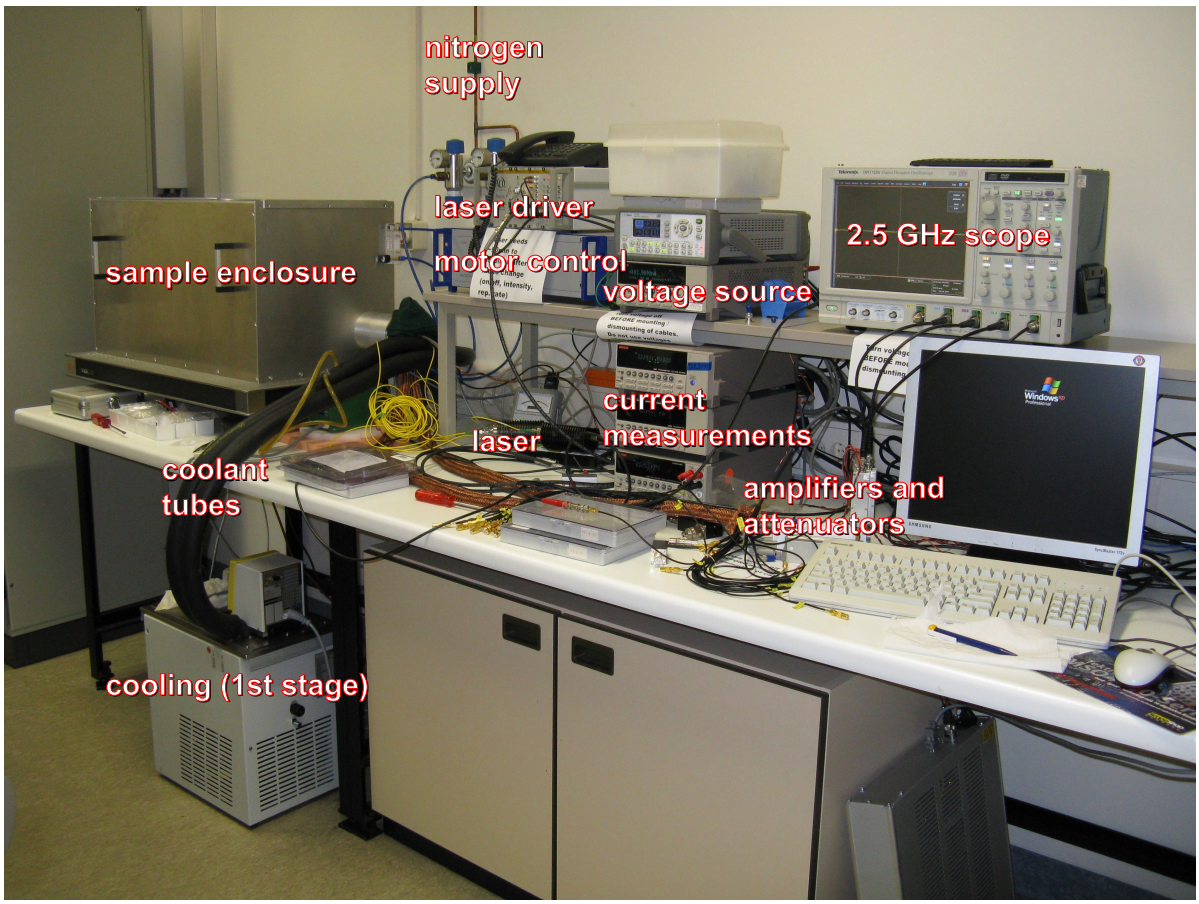

Figure 6.1: Photograph of the setup.

- Stable temperature (± 0.1 K (rms)) in the range from 240 K to 340 K.
- Read out channels selectable without remounting of the sensor.
- Sensors exchangeable without rebonding of readout channels.
- Shielding against ambient light and RF noise.
- As much automation as possible.

In order to fulfill these requirements it was decided to separate the sample holder into substrate and mounting.

6.1.1 Substrate

The sensor is glued to the substrate and the investigated channels are bonded to selectable readout channels. A sketch of the substrate is shown in Figure 6.3. The substrate features a central hole, which allows light injection from the rear side. The bias

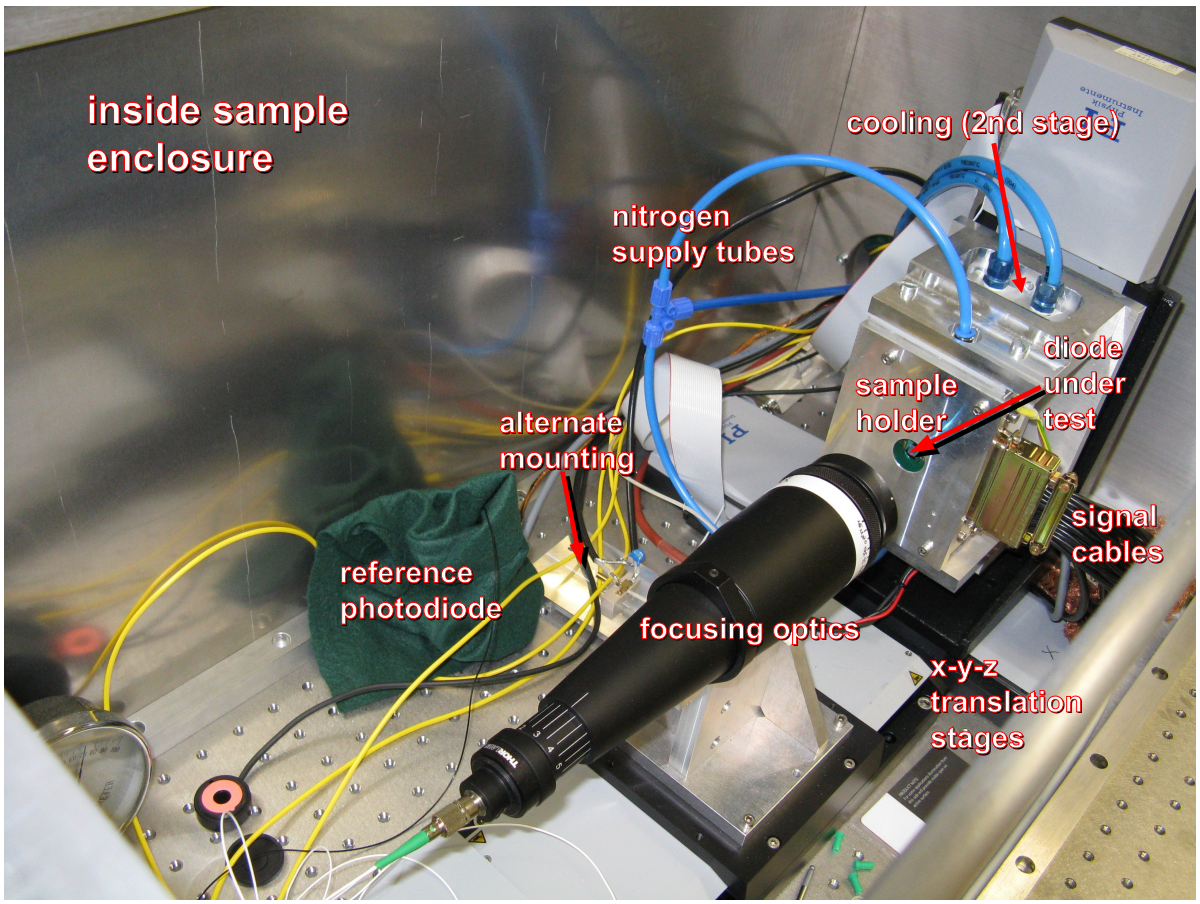

Figure 6.2: Photograph of the interior of the setup.

voltage of the sensor is provided via an H-like structure on the rear side of the substrate. All pads are connected to identical pads on the other side of the substrate with vias. This allows to mount the substrate 'upside down' and thus provides the required possibility to illuminate from both sides.

The substrate was manufactured from ceramics (Al_2O_3) by CeramTec [38], it is 0.3 mm thick. The routing lines are a sandwich structure (from bottom to top) of copper (9-25 µm), nickel (≈ 4-6 µm) and a thin gold passivation. The width of the routing lines (200 µm) on the ceramics has been chosen to have an impedance of 50 Ω.

6.1.2 Mounting

In order to provide the required temperature stability the mounting was designed as a large cold mass. Additionally it houses the electronic parts which contact the pads of the substrate and connects them to the signal cables. The bias voltage is filtered by an RCR network inside the mounting. The bias line is decoupled by a 1 kΩ resistor and the CR circuit consists of a 1 nF capacitor and a 10 Ω resistor. The 10 Ω resistor dampens electronic oscillations of the system.

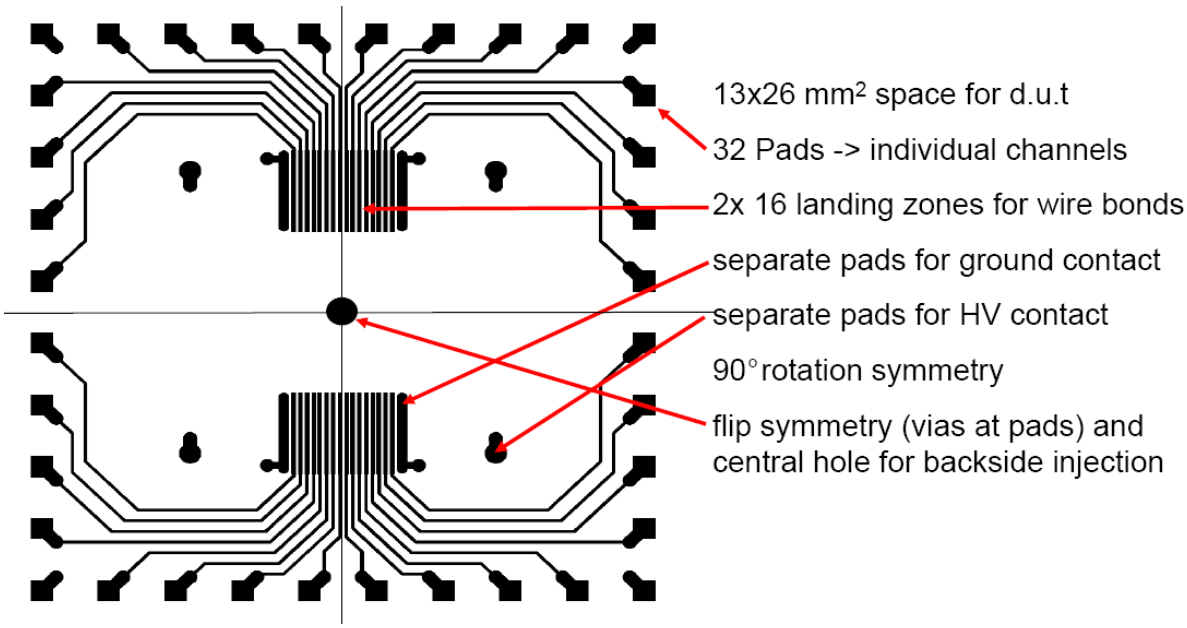

Figure 6.3: Sketch of the front side of the substrate. The rear side features an H-like structure to provide the bias voltage to a metalization around the central hole. A different metalization serves as a ground plane for the routing lines on the front side.

The mounting features a system of feedthroughs which guide an external nitrogen flow to all electronic parts and the sensor in order to avoid condensation of humidity on sensitive parts of the setup.

In order to measure pad diodes without bonding, an alternate mounting is available. The alternate mounting does not have any provision for gas flow and connects one RG-174 cable to the diode without additional filtering. The inner conductor of the cable is connected to the pad, the outer conductor (ground) is connected to the rear side of the diode.

6.1.3 Sample enclosure

The sample enclosure is manufactured from aluminum and acts as a light shield and Faraday cage at the same time. There is one outlet for all relevant cables. The setup can be manually opened and closed. It features tightening screws, however it was observed that the light shielding is sufficient without the screws.

6.1.4 Cooling system

The mounting is connected to a DA-120-24-00 Peltier assembly from Supercool [39], which in turn is connected to a LAUDA Ecoline Staredition RE 210 liquid chiller [40]. The sensor temperature is assumed to be identical with the mounting temperature,

which is monitored by a Pt100 temperature sensor, which is read out by a Keithley 2700 digital multimeter [41]. The DC current needed to drive the Peltier element is provided by a Hameg HMP2020 [42] current source. The entire temperature control chain is computer controlled by a custom written LabView software. Depending on the ambient temperature, sensor temperatures as low as -35°C have been achieved.

Temperature stability ($\Delta T < 0.1$ K) is reached after 10 to 15 minutes, depending on the difference between intended sensor temperature and ambient temperature and the difference to the last stable sensor temperature. If the temperature is kept stable for more than one hour the stability improves to $\Delta T < 1$ mK.

A temperature range of -30°C to +60°C has been achieved regularly and reliably in the course of this work.

In principle there is no upper limit on the temperature range, but there are some limiting factors. The Lauda chiller cannot heat the liquid to more than +40°C (firmware limitation of the device, can be changed). The chilling liquid evaporates at +60°C, but it could be replaced with a liquid with a higher boiling point. Finally the Peltier assembly cannot produce temperature differences of more than 40 K reliably when it is used in heating mode, leading to a theoretical upper limit of $\approx$ 80°C with the current chilling liquid ($\approx$ 140°C with water as chilling liquid).

6.1.5 Translation stages

The mounting is fixed on an x-y assembly (plane perpendicular to optical axis) of translation stages from Physik Instrumente [43]. The laser optics is mounted on a third translation stage, which acts as a z stage (along the optical axis). The x and y stage are M510.12 stages with a bi-directional repeatability of 0.1 µm, the z stage is a M511.DG stage with 0.2 µm bi-directional repeatability. All stages are connected to a C-844 motor controller, which is controlled by the data acquisition PC.

6.1.6 Electronic appliances

The bias voltage is provided by a Keithley 6517A electrometer [41]. The voltage source provides up to 1 mA current at voltages of up to 1000 V. The bias line is decoupled from the setup by an RCR filter (2 kΩ each, 100 nF) to which a current meter, monitoring the total current, is connected. To measure currents the Keithley 6517A can be used, additionally a Keithley 6485 picoamperemeter and a Keithley 6487 are available for current measurements.

Observations revealed an irritation of the automated range switching of the Keithley 6517A by signal transients, sometimes causing wrong measurements. The Keithley 6485 was best suited to measure currents with signal transients. Disabling the automated range switching solves this problem, but requires a priory knowledge of the expected maximum current.

In order to provide the high dynamic range in the read out chain, it consisted of Agilent 8496G attenuators [44], Miteq AM-1309 wideband amplifiers [45] and a Tektronix DPO 7254 2.5 GHz oscilloscope [46]. The attenuators have a bandwidth of DC to 4 GHz,

the oscilloscope of DC to 2.5 GHz and the amplifiers of 10 kHz to 1 GHz. The nominal impedance of all elements is 50 Ω, however strong reflections of the signal transients have been observed caused by the amplifier. When the attenuator is set to a non-vanishing attenuation it serves as an impedance matcher and the reflections vanish.

The attenuators are controlled by an Agilent 11713C driver, which is remote controlled by the PC. The attenuators can be set to discrete attenuation values between 0 dB and 120 dB in steps of 10 dB (factor of $\sqrt{10}$ in transients, adding dB values multiplies attenuation factors).

The Miteq AM-1309 wideband amplifiers [45] feature an amplification of ≈ 54 dB, which corresponds to a factor of ≈ 500 for transients. The linear regime of the amplifiers ranges to ≈ 0.7 V on the output (1.4 mV on the input). Input signals with higher amplitudes have to be attenuated in order to be sampled correctly. The input of the amplifier is equipped with a limiter, protecting the amplifier from damage by voltage spikes.

Other amplifiers are available for measurements. Two Phillips Scientific wideband amplifiers with a bandwidth of 100 kHz to 1.8 GHz and an amplification of 20 dB (factor 10) or 40 dB (factor 100) can be used. However the DC resistance of them is > 50 Ω, which introduces an additional voltage drop in presence of large DC currents. Both amplifiers tolerate voltage spikes. Additionally four Femto HSA-X-40 amplifiers are available with a bandwidth of 10 kHz to 2 GHz and an amplification of 40 dB (factor 100). Not having any input protection, these amplifiers are damaged by voltage spikes > ±4 V. The use of these amplifiers has been discontinued as the absence of voltage spikes > ±4 V could not be guaranteed.

The Tektronix DPO 7254 2.5 GHz oscilloscope [46] samples the output of the amplifiers. The high bandwidth of 2.5 GHz is available when the input is DC coupled with an impedance of 50 Ω and the vertical setting is ≥ 10 mV/Div. Reducing the vertical setting to ≥ 5 mV/Div, reduces the bandwidth to 2.0 GHz, a lower vertical setting reduces the bandwidth to 100 MHz.

In case of operation without amplifiers the inputs of the oscilloscope have to be protected from voltage spikes > ±24 V[2] (tolerated maximum). In order to achieve this, four RF-limiters with a bandwidth of DC to 1.8 GHz are available. They limit any transients to amplitudes of ≤ 0.5 V.

The alternate mounting supplies the bias voltage to the front side of the diode by using a 5531 Picosecond Pulse Labs bias-T [47] for decoupling the high voltage (1.5 kV max) from the signal transients. The bias-T has a bandwidth of 750 kHz to 10 GHz, the decoupling capacitance is 2.2 nF, which introduces distortions in the signal transients.

6.1.7 Data acquisition and control

The entire setup is controlled by a custom written LabView software for data acquisition and control. The software is modular, allowing to control the standard TCT setup and the multi channel TCT setup used in this work. All appliances can be selected in any

[2] Micro-discharges may produce such voltage spikes

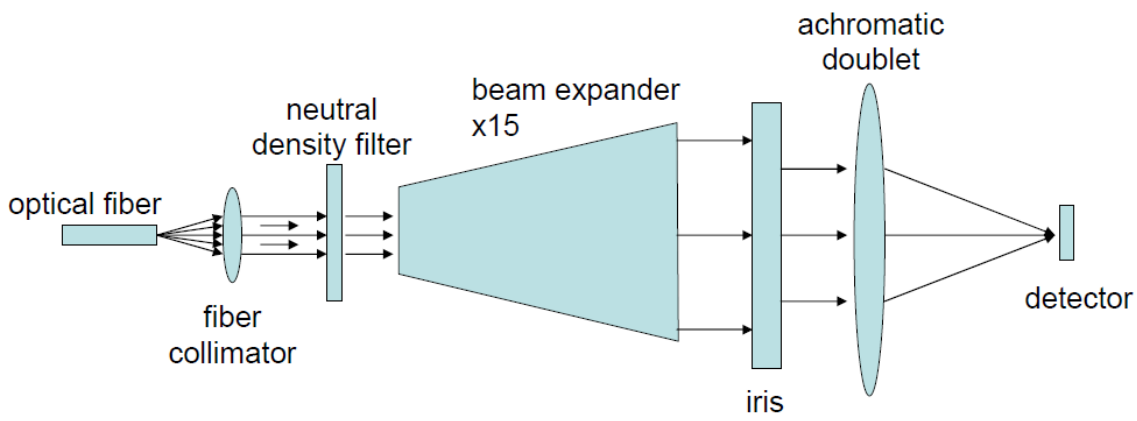

Figure 6.4: Schematic drawing of the arrangement of the optical components used.

function for maximum versatility. All functions of the appliances, except for the bias voltage, are reset at the beginning of the measurement. In this way any manual changes to the device settings are ignored. In the mTCT mode the user can select whether position scans at each bias voltage shall be done or voltage scans at each position. Additionally it can be selected whether the x-coordinate is scanned at each y-coordinate or vice versa.

The software features an adaptive scaling mode which scales the oscilloscope and attenuator settings to an optimal setting of the analog-digital-converter (ADC) of the oscilloscope. However the use of this feature is not recommended, as it was observed that the inaccurateness of the necessary fine tuning of the vertical setting is larger than the inaccurateness introduced by the sub-optimal use of the ADC.

The user can select whether the data acquisition should be triggered by the laser driver or by the signal itself (selectable by choosing 'alpha' as radiation type). Self-triggering is preferable when radioactive sources are used or special features of the diode (e.g. micro-discharges) shall be investigated.

The measurement data is stored to a measurement data file in ASCII format. The data file contains a header with all the settings of the appliances used. The measurement data is stored in rows. Each row has its own header identifying the individual measurement. Storing the data row wise is advantageous as each measurement point can be appended to the data file without resorting its contents. Additionally, in case of a sudden data stream loss (e.g. power failure, manual stop of the experiment) the measurement data acquired so far has already been stored to disk.

6.2 Laser system

The laser system was manufactured by Picoquant GmbH [48] and emits short and intense light pulses with a FWHM < 100 ps. The time resolved pulse structure was provided by the manufacturer (shown in Figure 7.6).

The laser system consists of a laser driver (Sepia II), a laser emitting diode assembled into a so called laser head and optics, feeding the laser pulse into an optical fiber. Laser driver and laser head are enclosed systems, while the optics of the laser head can be adjusted to achieve maximum coupling efficiency between laser head and optical fiber.

The laser system can be programmed to arbitrary pulse sequences on a user selectable clock of 80 MHz, 64 MHz or 50 MHz and provides a trigger signal to the oscilloscope. Alternatively the laser can be driven by an external trigger signal. The repetition frequency of the laser was chosen as 1 kHz and the data acquisition was triggered by the laser driver.

6.2.1 Laser pulse properties

For this study laser light with a wavelength of 660 nm (± 2 nm) and 1015 nm (± 6 nm) was used. The maximum pulse energy is 140 pJ and 260 pJ for the 660 nm and 1015 nm laser, respectively. Optical attenuators, which have no effect on the time structure of the pulses, were used when a reduced laser intensity was necessary, e.g. when plasma effects had to be avoided.

Laser light was used to simulate x-ray photons. In silicon the number of optical and x-ray photons decreases exponentially as function of depth in the silicon material. At 20°C the attenuation length of 660 nm light and 1 keV photons is 3 µm. 1015 nm light and 12 keV photons have an attenuation length of roughly 250 µm (calculated from the mass energy absorption coefficient of 12 keV photons). The mass energy absorption coefficient describes the energy deposited in the silicon lattice by many photons. It takes secondary interactions like fluorescence, Compton scattering and bremsstrahlung production of secondary electrons into account [25]. The attenuation length of light and x-ray photons as function of energy is shown in Figure 3.3.

It should be noted that x-ray photon absorption is a statistical process involving secondary processes like Compton scattering and fluorescence. Thus only the average energy transfered to the silicon lattice (and therefore the initial electron hole distribution) can be described by an exponential function. However the statistical fluctuations of deposited energy per unit path length become negligible when a few hundred photons are absorbed simultaneously. So lasers can be used to simulate the energy distribution of many x-ray photons, not the absorption of individual x-ray photons.

The optical fiber transports the laser pulse to the setup enclosure. The optical fiber is a special single mode fiber provided by the laser manufacturer. The single mode fiber is needed in order to select the main lasing mode of the laser head. Any higher order modes of the laser are filtered this way. Inside the sample enclosure the optical fiber is coupled to a fiber splitter in order to divert a part of the pulse to a reference photodiode.

The arrangement of the optical components used to build the setup is shown schematically in Figure 6.4. A list of the part numbers of the components is found in Table A.2 in the appendix. The laser light is emitted from the fiber as a divergent beam. Afterwards the beam is converted to a parallel beam, which in turn is expanded by a telescope. In order to filter out remaining higher orders and to define the laser beam on the lens, an iris is inserted between the telescope and the lens.

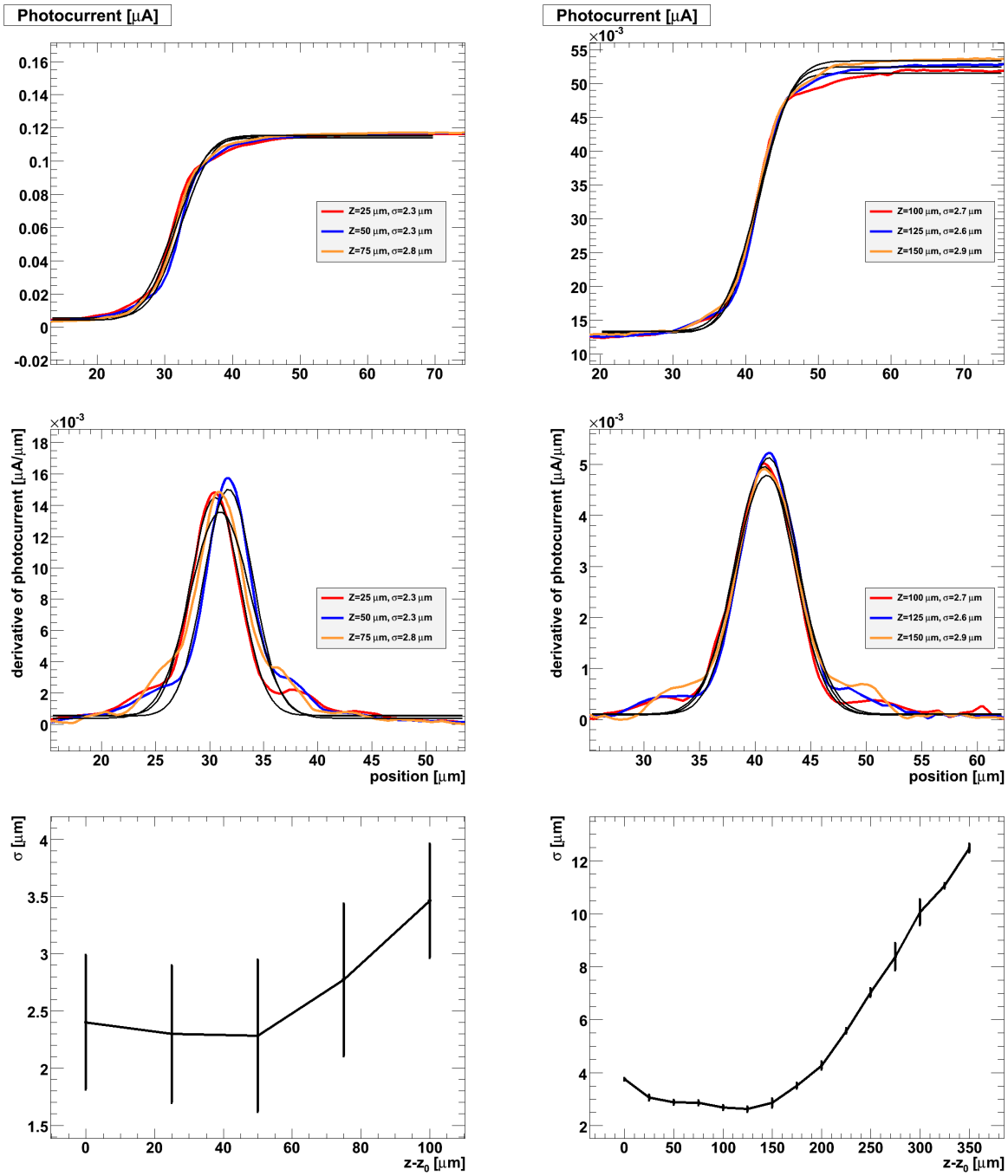

Figure 6.5: The first row shows the photocurrent profile of a reference diode as function of position along the edge of a metalization. The second row shows the laser beam profile, derived from the derivative of the photocurrent profile. The third row shows the rms width, σ, of the fit of the beam profile as function of focus position. The left column was measured for 660 nm light, the right column for 1015 nm light. Black lines show the fits of error functions (photocurrent) or Gaussian functions (beam profile) to the measured profiles.

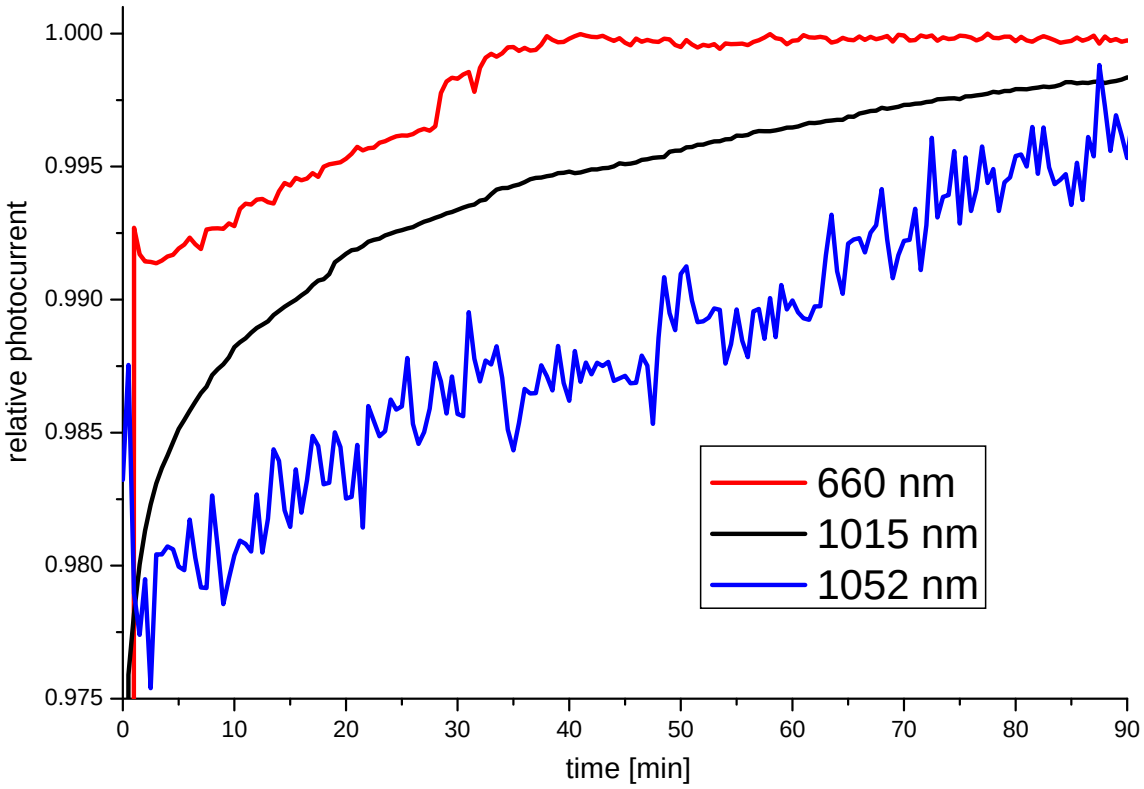

Figure 6.6: Photocurrent of the reference diode as function of time for three different laser heads.

The laser beam was used defocused or focused to a spot with Gaussian profile with $\sigma = 10$ µm or $\sigma \leq 3$ µm. In air the Rayleigh length (distance from focal point to the point where the beam radius increases by $\sqrt{2}$) is approximately 90 µm. This guarantees a focused laser beam for 1015 nm light through the entire thickness of the silicon sensors used in this work, as the high refractive index of silicon effectively increases the Rayleigh length inside the silicon by a factor of approximately 3.6.

The spot size was measured by recording the photocurrent of a test diode while performing a position scan along the edge of the metalization of the diode. Examples for measured photocurrents and the derived spot sizes are shown in Figure 6.5.

6.2.2 Stability of the laser

The laser head of the system is temperature stabilized for maximum stability of the light output. While the 660 nm laser head could be operated stable at all driving intensities, the 1015 nm laser head could only be operated stable at 100 % driving intensity. Below this intensity significant variations in the pulse height of individual pulses were observed.

Both laser heads need a warm up time of approximately 90 minutes. This warm up

time should be taken into account after each operation mode change, especially when changing the repetition frequency. At typical evolution of the photocurrent as function of time for three laser heads is shown in Figure 6.6. After the warm up time the typical deviations in the pulse intensity are significantly below 1 %.

6.3 Summary

A multi channel Transient Current Technique (mTCT) setup was built. It provides a versatile way to investigate silicon sensors. It features a laser system with very intense pulses, which allow to create charge clouds with charge carrier densities large enough to study plasma effects.

The created charge carrier density can be varied by using neutral density filters to attenuate the laser beam. The laser beam can be focused to spot sizes of ≈ 3 µm. Three different lasers with different wavelengths are available to simulate 1 keV or 12 keV photons and mips.

A special mounting and substrate were developed allowing light injection from both sides of the sensor. The high voltage is provided to the rear side of the sensor, up to 32 channels can be bonded for readout and the temperature can be controlled in the range from -30°C to +60°C.

7 Signal simulation

Signal simulation is an essential way to understand the properties of the investigated sensors. While in certain situations the experimental situation is sufficiently well defined to directly interpret the results, many experimental situations require simulations in order to disentangle the many effects, which play a role in charge transport.

The simulations were done in two steps. At first the expected current pulse was calculated using a custom written transport code, assuming a constant potential on the electrodes and an instantaneous charge deposition. Afterwards the resulting current pulse was convoluted with the time structure of the light pulse and with the transfer function of the readout circuit. Effects of high charge carrier densities (plasma effects) cannot be simulated this way, as this approximation is only valid as long as the interactions of charge carriers with other charge carriers are negligible.

The custom transport code used for the simulations takes charge drift, diffusion, charge trapping and multiplication into account. It is a 1D calculation on a grid with a selectable cell size (Δx) and a selectable time step (Δt).

It should be noted that, in order to achieve reliable results, Δx and Δt should be chosen in such a way, that $v_{dr}\Delta t > \Delta x/2$ for the whole detector volume. The code checks this condition and if $\Delta x > \sqrt{2D\Delta t}$ (cell size larger than one sigma of the diffusion spread) and prints a warning if potentially dangerous cells are found.

Further notice should be paid to the fact that it is a 1D simulation, thus simulations for two or three dimensional geometries (e.g. strip and pixel layouts) do not take diffusion perpendicular to the drift direction into account.

In order to avoid problems with charge carriers leaving the simulation volume ($x < 0$ or $x > d$) and diffusing back into it, a charge carrier which reaches the last grid point along the drift direction is stopped at the volume boundary and removed from the simulation between the transport steps.

The numerical stability of the simulation has been checked by varying the grid size between 10 nm and 1 µm and the time step between 1 ps and 25 ps. No effect on the pulse shape was observed when multiplication effects were turned off. Due to the exponential nature of charge multiplication the grid size needs to be reduced to 10 nm or less to get approximately correct results. Charge conservation was checked for situations without trapping and multiplication and no charge loss or gain was found.

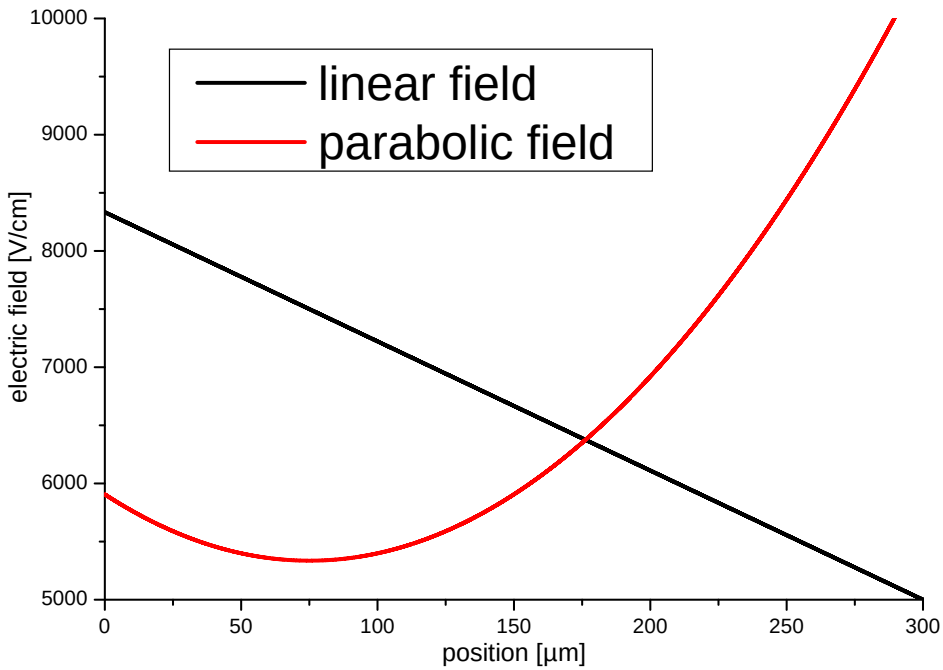

Figure 7.1: Different parameterizations of the electric field for 200 V applied bias on a sensor of $d = 300$ µm thickness. For the linear field a depletion voltage of 50 V ($N_{eff} = 7.3 \times 10^{11}$ cm^{-3}) was assumed. The parabolic field was parameterized as in Equation 7.2, with $\overline{N_{eff}} = -1 \times 10^{12}$ cm^{-3} and $\Delta N_{eff} = 2 \times 10^{12}$ cm^{-3}.

7.1 Electric field

For non irradiated sensors above full depletion the absolute value of the electric field[1] inside a sensor is approximately linear[2], with its highest value at the p$^+$n-junction ($x = 0$) and described by the following equation:

$$E(x) = \frac{1}{d}\left(U_{bias} + U_{dep} - \frac{2x}{d}U_{dep}\right) \tag{7.1}$$

Where x is the position inside the sensor (center of the corresponding cell), d the sensor thickness, U_{bias} the applied bias voltage and U_{dep} the depletion voltage of the sensor.

For irradiated sensors the electric field may follow a different function. Assuming a linear dependence of the effective doping ($N_{eff}(x) = \overline{N_{eff}} + \Delta N_{eff} - \frac{2x}{d}\Delta N_{eff}$) [37], leads to a parabolic electric field which is parameterized as follows:

[1]The simulation always uses the absolute value of the electric field. The sign of the electric field in p-type and n-type silicon devices is opposite, which is accounted for by the different drift directions in these devices.

[2]For strip and pixel geometries this is not true close to the surface, as it is not homogeneously implanted. However for most of the sensor volume the assumption of a linear field is valid.

$$E(x) = x^2 \frac{e_0 \Delta N_{eff}}{\epsilon\epsilon_0 d} - x \frac{e_0 \left(\overline{N_{eff}} + \Delta N_{eff}\right)}{\epsilon\epsilon_0} + C \tag{7.2}$$

Where $\overline{N_{eff}}$ is the average effective doping concentration, ΔN_{eff} the maximum change in N_{eff}, and C a constant with following properties:

$$C = \frac{U_{bias}}{d} - \frac{e_0}{d\epsilon\epsilon_0} \left(\frac{1}{2}\overline{N_{eff}} + \frac{1}{6}\Delta N_{eff}\right) \tag{7.3}$$

The constant ensures $\int_0^d E(x)\, dx = U_{bias}$.

Examples of resulting linear and parabolic electric fields are shown in Figure 7.1.

The transport simulation does not assume the electric field to follow any distribution, instead the electric field is assumed to have a constant value for each cell. Thus the electric field for the cell center is calculated according to one of the distributions mentioned above and assumed for the entire cell.

7.2 Initial distribution

The actual charge creation process is not simulated. Instead, an arbitrary distribution is processed as starting point of the simulations. The initial number of electrons and holes can be specified for each cell.

To facilitate the specification of the initial charge carrier distribution the user can select the automatic generation of a delta function of electrons and holes at a given location inside the sensor volume or an exponential function. An exponential distribution of charge carriers is generated by laser light.

The normalized exponential charge carrier distribution $N_{e,h}(x, t = 0) = \frac{\Delta x}{\lambda_{abs}} e^{-x^*/\lambda_{abs}}$ has a user selectable attenuation length λ_{abs}. Depending on the (user selectable) illumination side $x^* = x$ for front side illumination or $x^* = d - x$ for rear side illumination.

The code assumes the initial distribution of electrons and holes to be identical. This is a reasonable assumption as electrons and holes are created in pairs. Changing the code to process different initial distributions to be would only require minor changes and additional input parameters.

7.3 Ramo's theorem

The induced current is calculated according to the Ramo theorem [49]. The induced current (normalized to the elementary charge e_0) can be approximated by:

$$I(t + \Delta t) = \sum_x \left[I_e(x, t + \Delta t) - I_h(x, t + \Delta t)\right] \tag{7.4}$$

$$I_e(x, t + \Delta t) = \phi_w(x) \frac{e_0}{\Delta t} \left(N_e(x, t + \Delta t) - N_e(x, t)\right) \tag{7.5}$$

$$I_h(x, t + \Delta t) = \phi_w(x) \frac{e_0}{\Delta t} \left(N_h(x, t + \Delta t) - N_h(x, t)\right) \tag{7.6}$$

Where $I_{e,h}(x,t)$ is the current induced by the electrons (e) or the holes (h) of the cell at x at the time t, $N_{e,h}(x,t)$ denotes the number of electrons or holes in the cell at x at the time t. $\phi_w(x)$ denotes the weighting potential for the cell at x, which is explained below.

This approximation is only valid when charge is conserved in the transport step between t and $t + \Delta t$. Any change of the number of drifting charge carriers is accounted for before starting the next transport step.

All weighting potentials ($\phi_w(x)$) can be reversed with respect to the detector depth (effectively exchanging x with $d - x$) and thus account for situations where the readout electrode is opposite to the junction (e.g. n-in-n devices).

Although the pulses resulting from n-type readout have a negative polarity, the simulation calculates them as positive transients to facilitate the comparison of different device types.

7.3.1 Weighting potential

In order to calculate the induced charge on the readout electrode the weighting potential $\phi_w(x)$ has to be known. It can either be calculated numerically or in a limited number of cases analytically. The weighting potential for the ideal pad, strip and pixel geometry can be calculated analytically as explained below. The calculation of the weighting potential assumes the sensors to be fully depleted.

The analytic solutions calculate the charge induced on the readout electrode by the mirror charge method. The weighting potential is normalized to the elementary charge. Examples for different weighting potentials are shown in Figure 7.2. The weighting field is the derivative of the weighting potential.

pad sensor

The weighting potential of an ideal planar diode is given by the induced charge on one of the planes of an infinite parallel plate capacitor as function of the distance to it. It is linear and can be calculated as:

$$\phi_w(x) = 1 - x/d \tag{7.7}$$

strip sensor

For a strip sensor the weighting potential can be approximated by calculating the induced charge on a parallel plate capacitor limited in one dimension, for a given position in the other dimension. The approximation assumes a homogeneous metalization on the sensor surface with an infinitely small gap between the strips. This approximation is valid for most of the sensor volume, except close to the surface. The resulting weighting potential (according to [50]) is:

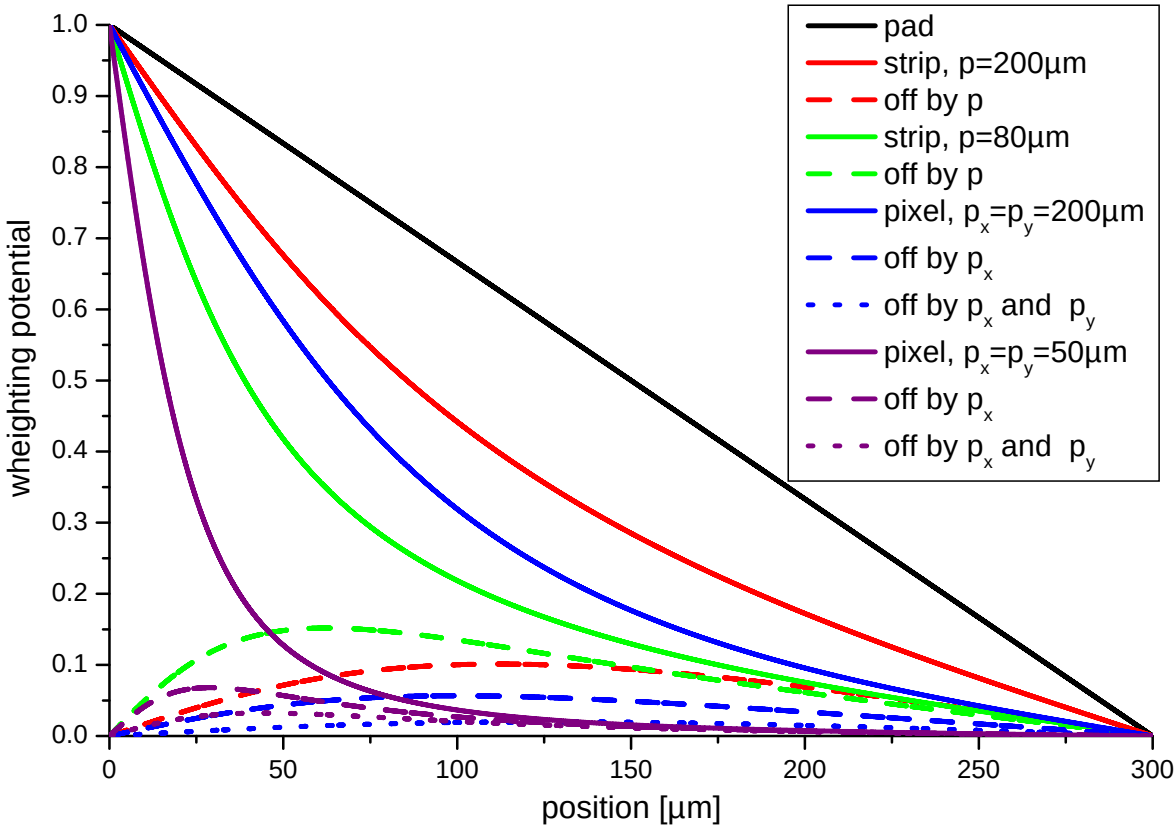

Figure 7.2: Weighting potentials for different sensor geometries of $d = 300$ µm thickness. Dashed lines indicate the same geometry as the solid lines but show the weighting potential for charges centered beneath the neighbor electrode. Dotted lines show the weighting potential for charges centered beneath the electrode which touches the pixel at the corner.

$$\phi_w(x,y) = 1 - \frac{1}{\pi}\left[\operatorname{atan}\left(\frac{\tan\frac{\pi x}{2d}}{\tanh\frac{\pi(p/2-y)}{2d}}\right) - \operatorname{atan}\left(\frac{\tan\frac{\pi x}{2d}}{\tanh\frac{\pi(-p/2-y)}{2d}}\right)\right] \tag{7.8}$$

Where p is the strip pitch and y is the position perpendicular to the strip.

pixel sensor

For a pixel sensor the situation resembles an ideal parallel plate capacitor which is limited in two dimensions. In contrast to the strip sensor case the resulting infinite sum does not have an analytic expression.

A pixel sensor has two pitches p_y and p_z along the y-axis and z-axis, correspondingly y and z are the coordinates along these axes, which are perpendicular to each other and to the x-axis along the thickness. According to [51] the following equations are valid:

$$\phi_w(x,y,z) = -\frac{1}{2\pi}\left[\phi_w^*(x,y,z)\sum_{i=1}^{\infty}(\phi_w^*(2id+x,y,z)-\phi_w^*(2id-x,y,z))\right] \quad (7.9)$$

$$\phi_w^*(x,y,z) = \mathrm{atan}(A1)-\mathrm{atan}(A2)-\mathrm{atan}(A3)+\mathrm{atan}(A4) \quad (7.10)$$

$$A1 = \frac{(p_y/2-y)(p_z/2-z)}{x\sqrt{(p_y/2-y)^2+(p_z/2-z)^2+x^2}} \quad (7.11)$$

$$A2 = \frac{(-p_y/2-y)(p_z/2-z)}{x\sqrt{(-p_y/2-y)^2+(p_z/2-z)^2+x^2}} \quad (7.12)$$

$$A3 = \frac{(p_y/2-y)(-p_z/2-z)}{x\sqrt{(p_y/2-y)^2+(-p_z/2-z)^2+x^2}} \quad (7.13)$$

$$A4 = \frac{(-p_y/2-y)(-p_z/2-z)}{x\sqrt{(-p_y-y/2)^2+(-p_z/2-z)^2+x^2}} \quad (7.14)$$

As shown by [52] this infinite sum can be approximated by the finite sum to the number n and adding the following six correction terms:

$$C1 = -\frac{1}{4}\phi_w^*(2nd-x,y,z) \quad (7.15)$$

$$C2 = \frac{1}{4}\phi_w^*(-2(n-1)d-x,y,z) \quad (7.16)$$

$$C3 = -\frac{x}{4d}\phi_w^*((2n-1)d,y,z) \quad (7.17)$$

$$C4 = \frac{x}{4d}\phi_w^*((-2n+1)d,y,z) \quad (7.18)$$

$$C5 = \frac{1}{4}\phi_w^*(2nd,y,z) \quad (7.19)$$

$$C6 = -\frac{1}{4}\phi_w^*(-2(n-1)d,y,z) \quad (7.20)$$

7.4 Drift and diffusion of charge carriers

The charge drift and diffusion was simulated using the following basic equations:

$$\delta x(x) = \pm\overline{\mu_{e,h}}(x)\overline{E}(x)\Delta t \quad (7.21)$$

$$\sigma_{e,h}^*(x) = \sqrt{2\overline{\mu_{e,h}}(x)\frac{kT}{e_0}\Delta t} \quad (7.22)$$

$$N_{e,h}(x,t+\Delta t) = \sum_{x^*} N_{e,h}(x^*,t)C(x,x^*) \quad (7.23)$$

$$C(x,x^*) = \frac{1}{2}\left[A(x,x^*)-B(x,x^*)\right] \quad (7.24)$$

$$A(x,x^*) = erf\left(\frac{x^*+\delta x(x)-x+0.5*\Delta x}{\sqrt{2}\sigma_{e,h}^*(x)}\right) \quad (7.25)$$

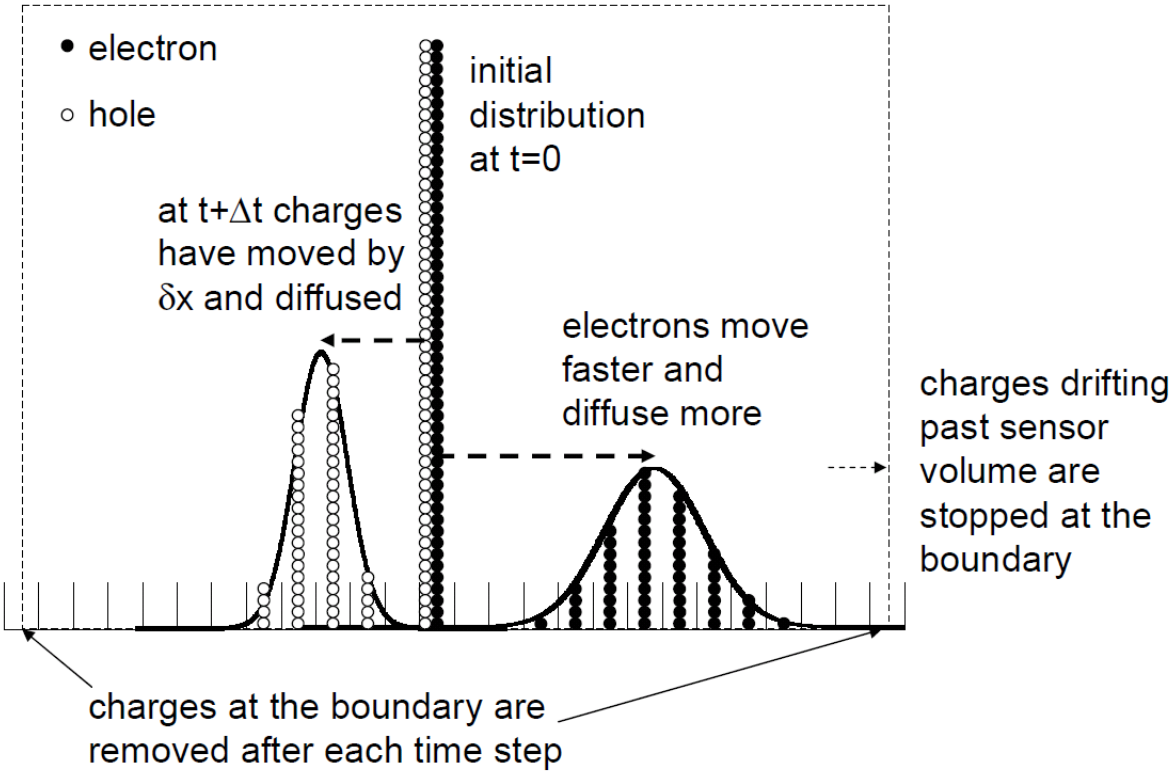

Figure 7.3: Simplified scheme of one transport step.

$$B(x, x^*) \quad = \quad erf\left(\frac{x^* + \delta x(x) - x - 0.5 * \Delta x}{\sqrt{2}\sigma^*_{e,h}(x)}\right) \tag{7.26}$$

Where $\delta x(x)$ is the distance traveled within one time step (Δt). It is negative for holes as they drift into the opposite direction of electrons. Average values (e.g. $\overline{\mu_{e,h}}(x)$) have been calculated by adding the values for the transversed cells and dividing by the number of cells traveled ($\pm 1/\delta x^* \sum_x^{x+\delta x^*}$, for δx^* is δx rounded to nearest cell center). δx was determined by adding the drift times for each cell until the total drift time (t_{drift}) exceeded the time step when n_{cell} cells have been transversed, then calculating $\delta x = \frac{n_{cell} * \Delta x}{t_{drift}} \Delta t$. Diffusion is simulated using the Einstein relation ($D_{e,h} = \overline{\mu_{e,h}}(x) \frac{kT}{e_0}$).

The number of charge carriers at each grid cell is calculated as the integral of a Gaussian function shifted by δx with $\sigma = \sqrt{2D\Delta t}$ from $x - \frac{\Delta x}{2}$ to $x + \frac{\Delta x}{2}$ (beginning of cell to end of cell).

These shifted Gaussian functions are calculated for each grid cell and summed over all grid cells. A schematic drawing of a simulation step is shown in Figure 7.3.

As this calculation is a 1D simulation along the depth of the device, lateral diffusion (perpendicular to the drift path) is not taken into account. Thus results calculated for strip and pixel structures are only approximations, especially for calculations in between strips or pixels.

The simulation allows the user to reverse the drift directions of electrons and holes,

which is necessary when p-type bulk material is investigated.

7.5 Mobility model

The field dependence of the mobility was parameterized in the following way:

$$\mu_{e,h}(x) = \frac{\mu^0_{e,h}}{\left(1 + \left(\frac{\mu^0_{e,h} E(x)}{v^{sat}_{e,h}}\right)^{\beta_{e,h}}\right)^{1/\beta_{e,h}}} \tag{7.27}$$

Where $\mu_{e,h}(x)$ is the mobility of electrons or holes for a given grid cell at x with the electric field $E(x)$, $\mu^0_{e,h}$ the ohmic mobility (also called low field mobility), $v^{sat}_{e,h}$ the saturation velocity and $\beta_{e,h}$ a parameter describing the transition between ohmic behavior and saturation velocity.

The temperature dependence of these parameters was modeled using a simple exponential law:

$$Parameter_i(T) = Parameter_i(300K)\left(\frac{T}{300K}\right)^{\alpha_i} \tag{7.28}$$

Values for the mobility parameters have been determined in Chapter 8 and are summarized in Table 8.1 and Table 8.2.

7.6 Charge carrier trapping and multiplication

The simulation process assumes charge carrier trapping and multiplication to be independent processes. Thus both processes are simulated separately.

The approximations used to calculate the induced current (Equation 7.4 to 7.6) require charge conservation during the drift and diffusion simulation step (Equation 7.23). Thus any change in the number of charge carriers is accounted for between two transport steps, modifying $N_{e,h}(x)$ for a given time step.

7.6.1 Trapping

Trapping is included into the simulation by reducing the number of drifting charge carriers. Once a charge carrier is trapped it is removed from the simulation. Detrapping of charge carriers (release after a certain emission time) is not included into the simulations, which is a justified approximation as long as the emission time is large compared to the pulse duration. Detrapping could be easily included into the simulations, but would require a parameterization of the detrapping time, which in turn could be different for every cell (e.g. due to dependence on the electric field).

Trapping is approximated by removing charge carriers with a certain trapping time constant τ.

$$dN_{e,h}(x,t) = -N_{e,h}(x,t)\frac{1}{\tau(x)}dt \tag{7.29}$$

The trapping constant may depend on the external bias, as motivated in [53].

$$\tau(x) = \tau_0 + \tau_1 U \tag{7.30}$$

Alternatively, the trapping constant may depend on the electric field and thus on the position, as motivated in [37].

$$\tau(x) = \tau_0 + \tau_1 \overline{E}(x) \tag{7.31}$$

τ_0 is the constant part of the trapping time, specified by the user, τ_1 a user defined parameter which specifies the voltage or field dependence of the trapping time ($\tau_1 = 0$ specifies a constant trapping time). Whether Equation 7.30 or Equation 7.31 is used in the simulation process is selected by the user.

Presently the code uses identical trapping parameters for electrons and holes. The trapping of electrons and holes is already handled separately by the code (due to the different average electric fields encountered during the drift), thus having different trapping parameters would require only minor changes in the code and additional input parameters.

7.6.2 Multiplication

In the presence of high electric fields charge carriers can gain enough energy to create secondary electron hole pairs. This process is called impact ionization. It can be described as

$$dN_{e,h} = (\alpha_{e,h} N_{e,h} + \alpha_{h,e} N_{h,e})\, dx \tag{7.32}$$

where $\alpha_{e,h}$ is the so called impact ionization coefficient. When simulating impact ionization special care has to be taken, as secondary electrons and holes can multiply as well. Thus the simulation uses:

$$dN_{e,h}(x,t) = N_{e,h}(x,t) \prod_{x^*=x\mp\delta x}^{x} \alpha_{e,h}(x^*)\Delta x \tag{7.33}$$

Using this equation, secondary charge carriers are deposited at the end of the drift path, i.e. they 'drift along' with the primary charge carriers. The charge spread by diffusion is ignored in this derivation.

Secondary charge carriers of the opposite type (note the exchanged subscript in the next equation) are created along the drift path of the primary charge carriers. It can be approximated for the corresponding cells (i runs from 0 to the rounded up integer value of $|\delta x/\Delta x|$) in the following way:

$$dN_{h,e}(x \pm i\Delta x, t) = \left(N_{e,h}(x,t) \prod_{x^*=x}^{x\pm i\Delta x} [1 + \alpha_{e,h}(x^*)\Delta x] \right) \alpha_{e,h}(x \pm i\Delta x)\Delta x \tag{7.34}$$

In contrast to the secondary charge carriers of the same type, the secondaries of the opposite type are not 'drifted along', but deposited in the cell of their creation.

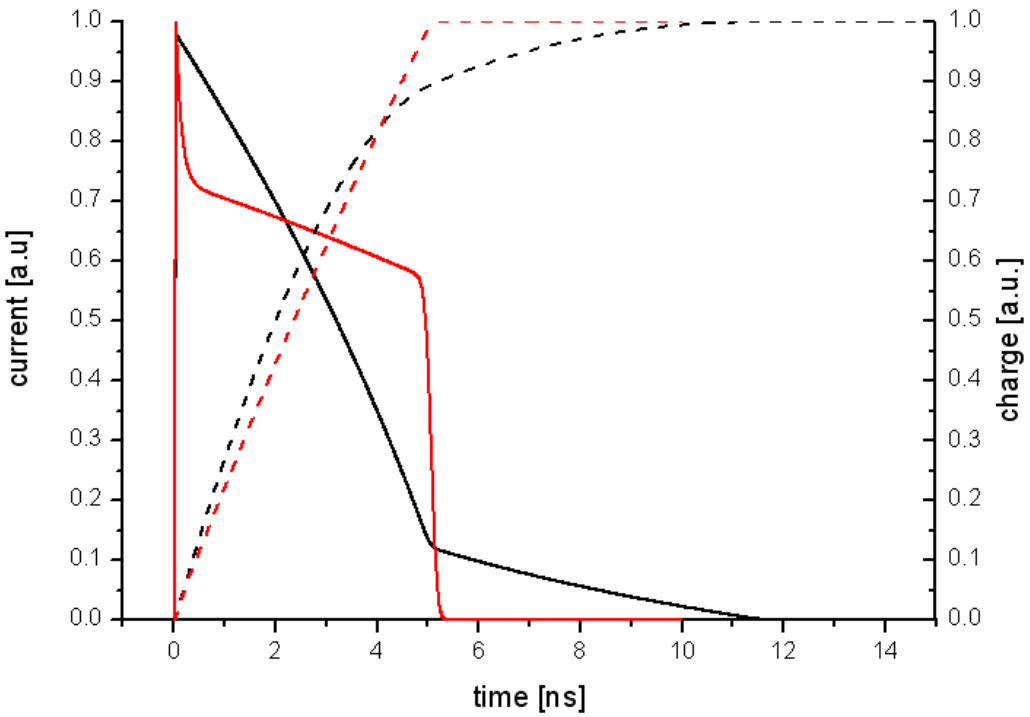

Figure 7.4: Exemplary current pulse simulated for 660 nm light (red) and 1015 nm light (black). The sensor thickness is 280 µm, the depletion voltage is 50 V and the applied voltage is 200 V. For comparison the integrated pulses (charge pulses) are shown with dashed lines.

7.7 Pulse shape modifications

Exemplary current pulses are shown in Figure 7.4. It shows simulated pulses for a 280 µm sensor with 50 V depletion voltage and 200 V applied bias illuminated from the front side. Depending on the penetration length of the laser light ($\approx$ 3 µm for 660 nm light, $\approx$ 250 µm for 1015 nm light) the pulse shapes differ.

In order to create pulses which are dominated by either electron drift or hole drift, electron hole pairs can be created by injecting laser light either from the p^+ or from the n^+ side of the sensor. When the penetration depth of the light is short compared to the thickness of the investigated sensor (e.g. in case of 660 nm light), one type of charge carrier dominates the current pulse, as the other type is collected very quickly (within approximately 200-300 ps in this case).

The effect of certain modifications on the current pulse is shown in Figure 7.5. How these effects are calculated and accounted for is explained below.

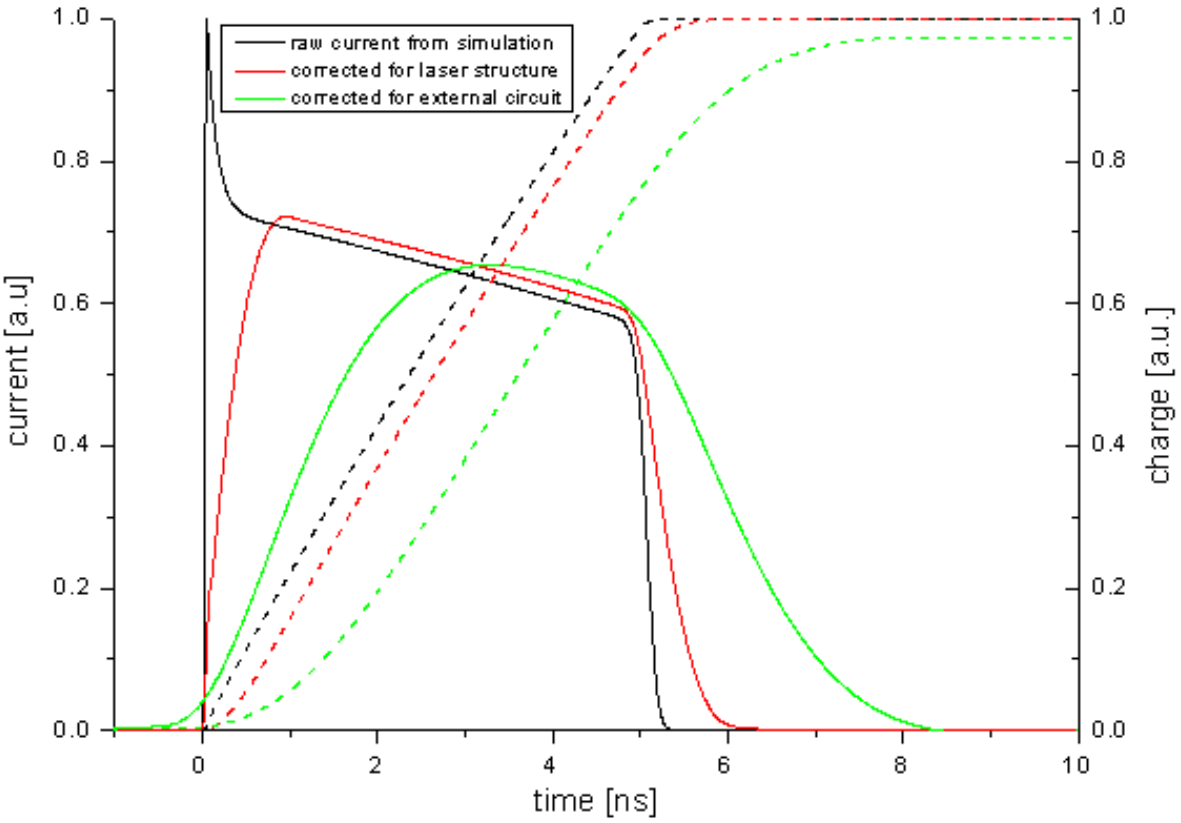

Figure 7.5: Effect of laser pulse structure and external circuit. For comparison the integrated pulse (charge) is shown with dashed lines. The integrated pulse after the circuit correction increases slowly after 8 ns until it reaches 1.0 at approximately 35 ns. The time offsets of laser structure and external circuit simulation have been removed to facilitate comparison.

7.7.1 Pulse structure of the laser light

The simulation assumes that there are no interactions between charge carriers. Thus any modulation of the input source (in this case the laser light) can be simulated by calculating the current pulse for a delta function in time (instantaneous deposition of charge carriers) and convoluting the simulated current pulse with the time structure of the source.

In this work the pulse structure of the laser light (shown in Figure 7.6) was interpolated to the same time steps as the simulation and normalized. The resulting time structure was then convoluted with the current pulse from the simulation.

All laser pulses shown in Figure 7.6 have been included into the simulation program, as well as a δ-pulse in time and the possibility to provide user defined laser pulse structures. The user can select which pulse to use for convolution (selecting the δ-pulse effectively does no convolution at all). Most measurements in this work have been done with the maximum laser intensity for the corresponding wavelength, as they proved to be most

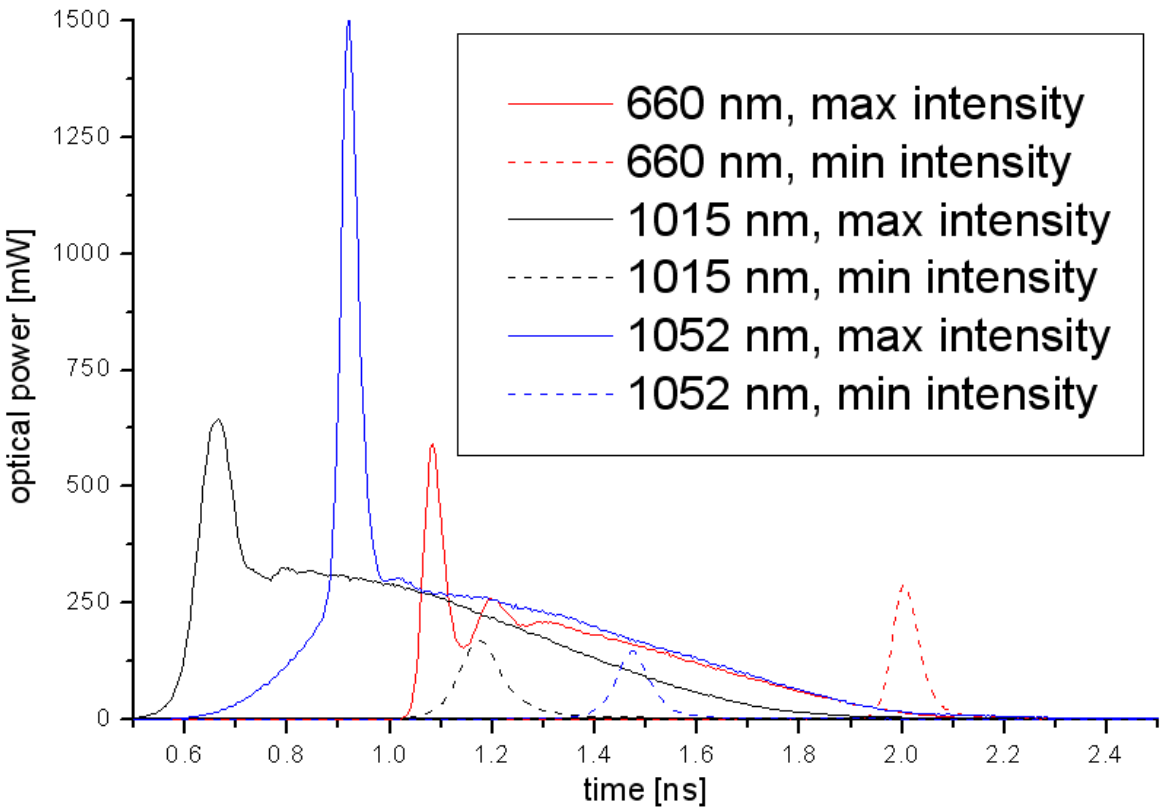

Figure 7.6: Time structure of the laser pulse. Minimum and maximum intensity indicate the corresponding setting of the laser driver. The laser pulse can be attenuated externally without influencing the time structure. The data was provided by the manufacturer [48].

stable (explained in Chapter 6). Simulations compared to these measurements have been convoluted with the corresponding laser pulse structure.

7.7.2 Readout circuit

To simulate the pulse modifications of the setup an external SPICE simulation was used. The SPICE simulation has been used to calculate the step response of the system. The transfer function of the system is the derivative of this step response and shown in Figure 7.7.

Similar to the procedure for the simulation of the laser pulse structure the transfer function was interpolated to the time step size of the transport simulation and convoluted with the current pulse.

For the simulations of strip sensors no correction due to the external circuitry was done. As shown below, the detector capacitance dominates the behavior of the system. The strip capacitance is very low compared to the capacitance of a pad diode, thus reducing the influence of the external circuit.

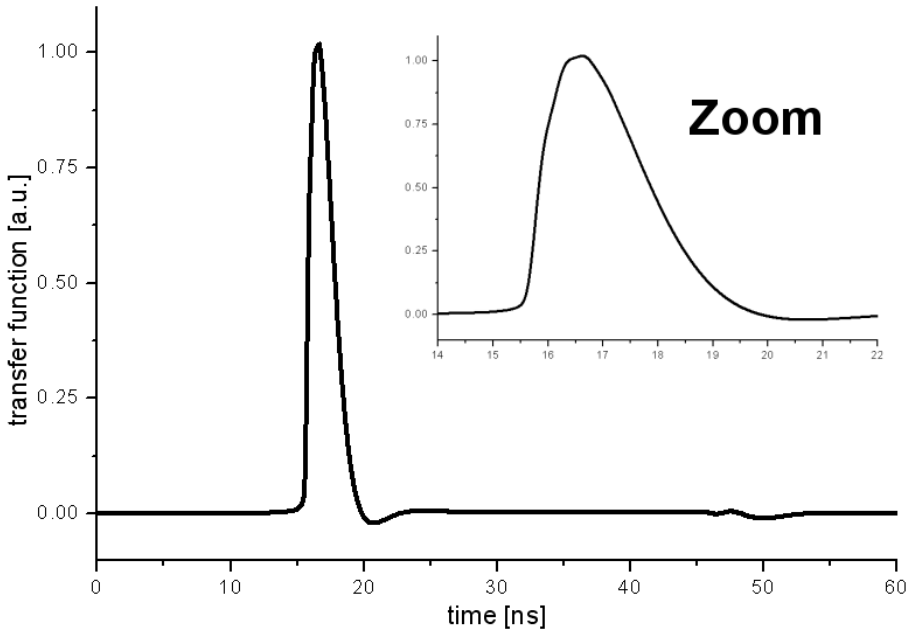

Figure 7.7: Transfer function derived from the SPICE simulations for 9.2 pF capacitance. A similar transfer function was calculated for 9.4 pF capacitance, however the deviations are too small to be seen on this scale. The inset shows a zoom of the peak structure of the transfer function using the same units on the x- and y-axis.

Equivalent circuit for SPICE simulations

An equivalent circuit of the setup was used for SPICE simulations (see Figure 7.8). In the equivalent circuit detector capacitance (9.2 pF or 9.4 pF), signal cable length (3.05 m), bandwidth of the amplifier (1 GHz) and imperfections of the setup (inductances and capacitances) were taken into account.

The lossy transmission line used in the simulation implements the following frequency dependent parameters per meter of cable (s is the complex frequency parameter used in the Laplace transform): $R = (0.783 + 5.723 \times 10^{-5}\sqrt{s/Hz})\ \Omega$, $C = 100$ pF, $L = 250$ nH and $G = (4 \times 10^{-14} + 5.183 \times 10^{-13}|s/Hz|)$ S, which were derived from literature data on RG-174 cables.

7.8 Summary

A simulation program for current pulses of silicon sensors has been developed. Assuming no charge carrier interactions (no plasma effects), current pulses for sensors with pad, strip and pixel geometries can be calculated.

The simulation is grid based and allows arbitrary definitions of the initial charge carrier distribution, electric field and weighting potential. The transport code calculates

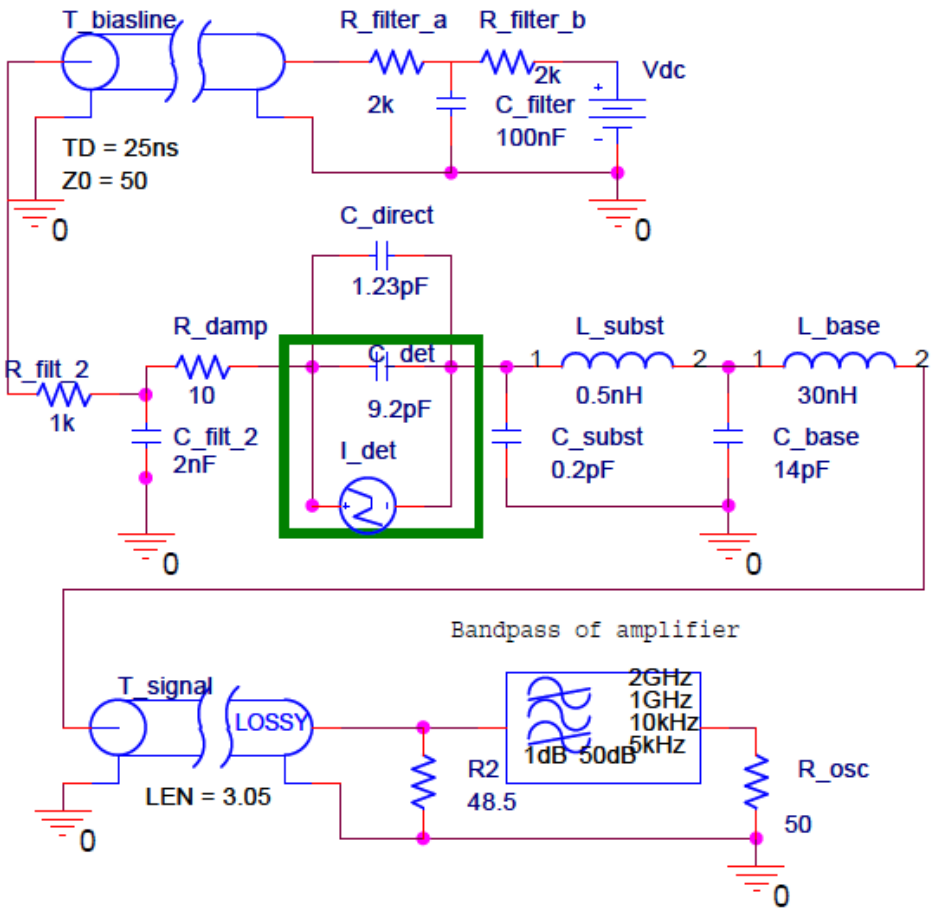

Figure 7.8: Equivalent circuit for SPICE simulations. Dominant elements are the diode capacitance (only 9.2 pF shown) in parallel to the current source (marked by the rectangle), the system inductance (30 nH) the lossy transmission line (3.05 m RG-174 cable) and the band pass filtering properties of the amplifier.

drift and diffusion of both charge carrier types, taking the mobility reduction due to high electric fields, trapping and multiplication into account.

As the simulation code is limited to one dimension, diffusion perpendicular to the drift direction is not taken into account and results for strip and pixel sensors are only approximations.

The simulation program is used intensively for the investigations presented in the following chapters.

8 Measurements on pad sensors with low charge carrier densities

The measurement setup has been used to study the transport properties of bulk silicon. Precise knowledge of the transport properties is important, as in applications with large drift distances, e.g. radiation sensors, even small uncertainties in the drift velocities can have noticeable effects.

Comparing measurements to simulations it was possible to determine a parameterization of the charge carrier mobilities as function of temperature and electric field for different crystal orientations. Parameterizations of charge carrier mobilities can be found in the literature, however the most recent measurements using the time of flight technique have been performed by Canali et al. in 1971 [54]. There have been quite a few reviews of this data, the one by Jacoboni et al. [55] is especially useful, as it provides a temperature dependent parameterization of the drift velocity in <111> direction. No parameterization for the <100> direction is given. There have been other reviews incorporating other measurements and proposing different parameterizations [56, 57, 58, 59], however either temperature dependence or anisotropy are neglected.

In this chapter measurements of pulse shapes of p^+nn^+ diodes in the temperature range between -30°C and 50°C with different applied bias voltages are compared to simulations in order to determine a set of parameters, describing the mobility as function of electric field and temperature, for two crystal orientations.

8.1 Investigated sensors

The investigated sensors[1] were planar p^+nn^+ diodes fabricated by CiS Forschungsinstitut für Mikrosensorik und Photovoltaik GmbH [60]. They are labeled CG1215 and CC1604. The silicon used is high resistivity n-type diffusion oxygenated float zone silicon with <100> and <111> orientation manufactured by Siltronic [61]. The effective doping of the <100> and <111> sensors is $8.2\text{x}10^{11}$ cm^{-3} and $1.1\text{x}10^{12}$ cm^{-3}. The resulting depletion voltages are 49 V and 63 V with dark currents at the depletion voltage of 0.72 nA and 1.64 nA, respectively. The sensors have very low concentrations of lattice defects, leading to life times in the order of milliseconds, which is many orders of magnitude larger than the longest pulse duration recorded in this work (approximately 35 ns). Thus any trapping effects have been considered negligible.

From the measured pad capacitance of 9.23 pF and the pad area of $(4.95\ \text{mm})^2$ a thickness of 280 µm is obtained using the standard formula for a parallel plate capacitor

[1] Details on all sensors investigated in this work are found in Table A.1.

without edge effects. The corresponding numbers for the <111> diode are 9.42 pF, $(4.93\ \text{mm})^2$ and 272 μm. For the measurement of the pad capacitance the capacitance of the guard ring to the backplane and the sensor edge is subtracted by the zero adjustment of the LCR meter. The remaining effect of the guard ring is estimated to be well below 1 %. The estimated uncertainty of the diode thickness is ± 2 μm.

Mechanical measurements of the thickness yield somewhat higher values but include 'dead' layers like the n^+ and p^+ implantations, passivations and aluminizations. The accuracy of the final capacitance has the biggest influence on the determination of the thickness, as a change of 0.1 pF changes the measured thickness by approximately 3 μm.

The sensors feature an opening on the junction side and a grid like aluminum layer on the opposite side to allow light injection. The gap between the metalization of diode guard ring is 20 μm wide, the distance between the corresponding implantations is 10 μm. A sketch of the sensor is shown in Figure 4.1.

8.2 Measurements

Measurements have been performed for junction side illumination (electron signal) and illumination opposite to the junction (hole signal) with an attenuated and defocused laser beam. Bias voltages of 100 V, 200 V and 500 V were applied and these measurements were done in temperature steps of 10 K in the range between -30°C and 50°C (243.15 K and 323.15 K). A set of measurements and corresponding simulations are shown in Figure 8.1.

To evaluate whether high density effects (also called plasma effects) were present, the diameter of the laser spot on the sensor was changed by focusing and defocusing. As no changes in the recorded current pulses were observed, high density effects can be considered negligible. Plasma effects in pad diodes are investigated in Chapter 10.

To reduce the random noise component of the system, 4096 pulses were averaged. The remaining noise is no longer random and has an rms value of $\sigma_I < 0.4$ μA.

8.3 Results

Using the simulation code explained in Chapter 7, current pulses have been calculated for different mobility parameters. To determine the free parameters of the mobility model a modified χ^2 procedure is used. At first current pulses for all measurements were simulated and the squares of the difference between measurement and simulation were summed up.

$$\chi^2 = \frac{1}{(\sigma_I n_s n_U n_T n_i)^2} \sum_s \sum_U \sum_T \sum_i \left(I_{meas}(i) - I_{sim}(i)\right)^2 \tag{8.1}$$

With $n_s = 2$ being the number of sensors (<111> and <100> orientation), $n_U = 3$ the number of compared bias voltages (100 V, 200 V and 500 V), $n_T = 9$ the number

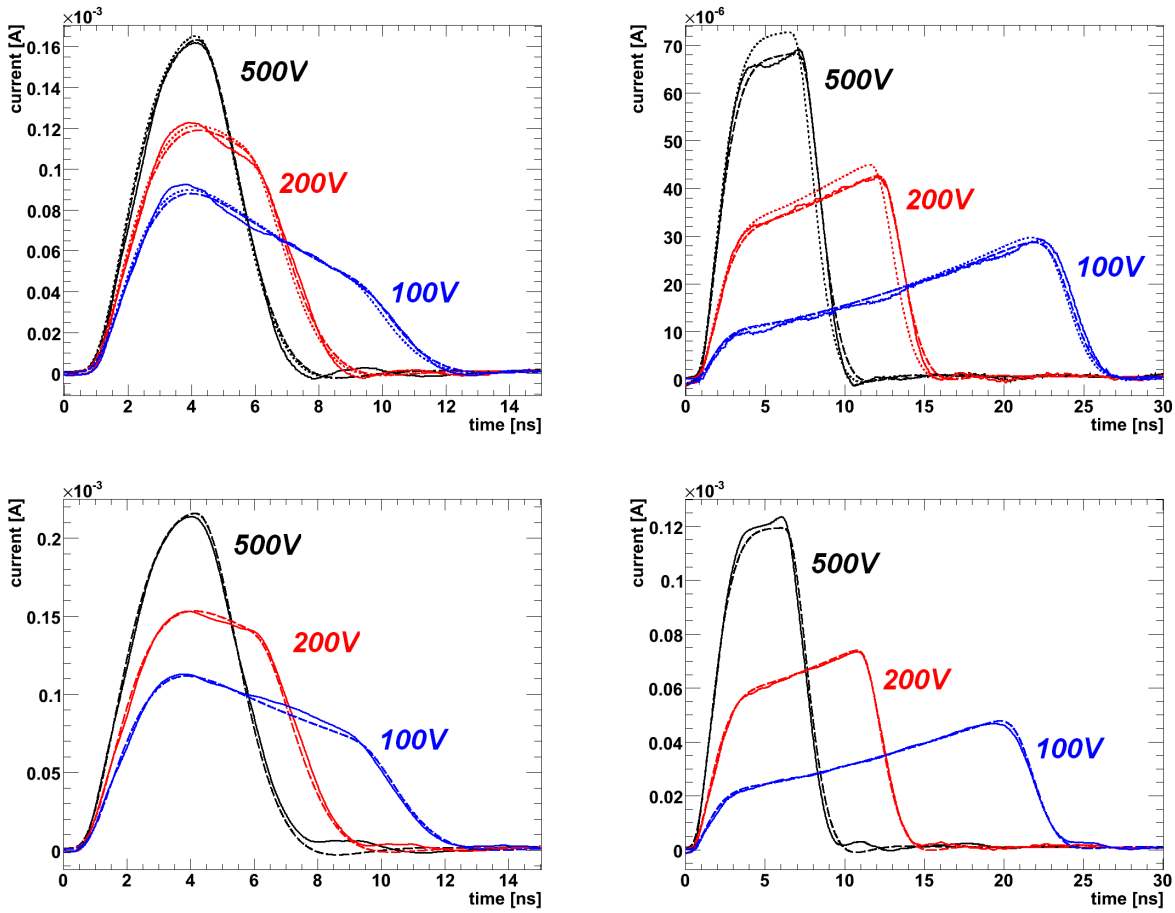

Figure 8.1: Comparison of simulated pulses and measurements at T=30°C. The upper row shows pulses for <111> orientation, the lower for <100> orientation; The left column shows electrons, the right column shows holes. The measured pulses (solid lines) are generally well reproduced by the simulations (dotted: using the mobility parameters of Jacoboni et al. [55], dashed: using the mobility parameters of this work), although some small ringing features are not correctly reproduced by the SPICE simulation. For electrons the simulated pulses of both models differ only slightly, while for holes a difference in pulse height and length is observed.

of compared temperatures (-30°C to 50°C in steps of 10 K) and n_i the number of compared sampling points on the current pulse (1300 for electrons, 2600 for holes). I_{meas} is the measured pulse and I_{sim} is the simulated current pulse for a given set of mobility parameters. For the normalization σ_I was assumed to be 0.4 µA. The normalization is only an approximation, as the sampling points are correlated by the external circuit and the noise is not random.

The χ^2 sum was calculated for every set of parameters and the parameters with the smallest χ^2 are presented in Tables 8.1 and 8.2. Errors have been calculated by using

	μ^0 [cm^2/Vs]	v^{sat} [cm/s]	$\beta^{<100>}$	$\beta^{<111>}$
electrons	1440±15	(1.054±0.038)×10^7	0.992±0.004	1.075±0.004
holes	474±10	(0.940±0.027)×10^7	1.181±0.003	0.924±0.002

Table 8.1: Parameters for the field dependent mobility at 300 K.

	μ^0	v^{sat}	$\beta^{<100>}$	$\beta^{<111>}$
electrons	-2.260±0.007	-0.602±0.003	0.572±0.003	0.220±0.001
holes	-2.619±0.007	-0.226±0.002	0.644±0.003	0.550±0.002

Table 8.2: Temperature parameters α_i for the field dependent mobility reduction.

the Minuit fitting program [62] of the ROOT package [63]. Transients calculated with this set of parameters are shown in Figure 8.1.

The errors given in Tables 8.1 and 8.2 have been determined by Minuit, taking all cross-dependencies of parameters (co-variances) into account. The errors are only approximations, as the system is highly non-linear.

To evaluate the influence of systematic uncertainties in the thickness and depletion voltage the same set of measurements was fitted but assuming ± 1 % difference in thickness or ± 5 % difference in depletion voltage. The difference in the resulting mobility parameters is within the range of the errors calculated by Minuit.

The attenuation length of 660 nm light changes by about 50 % in the investigated temperature range. Comparison of simulations with the longest and shortest penetration depth and otherwise unchanged parameters showed no significant change in the overall pulse shape, thus the simulation neglected the temperature dependence of the penetration depth.

Optical photons of 660 nm wavelength (1.87 eV) produce so called hot charge carriers as the band gap of silicon is approximately 1.12 eV at room temperature. The simulation assumes charge carriers in thermal equilibrium with the crystal lattice. This is considered to be a good approximation as the thermalization of the hot carriers is usually very fast compared to the pulse duration.

8.3.1 Fitted mobility parameters

The fitted values of the ohmic mobilities at 300 K reproduce the accepted values [64] within the quoted errors. For the temperature coefficients reported values range from -2.3 to -2.6 for electrons and -2.2 to -2.8 for holes [64]. The best fit value of holes lies within the quoted interval, while the electron value of this work lies just outside the quoted interval (rounded to the second digit it would be -2.3 and thus at the edge of the quoted interval), although it is lower than the value of -2.0 which has been reported by [57].

Saturation velocity parameterizations as function of temperature have been provided by many authors [55, 65, 66], however the reported values differ by about 20 %. The

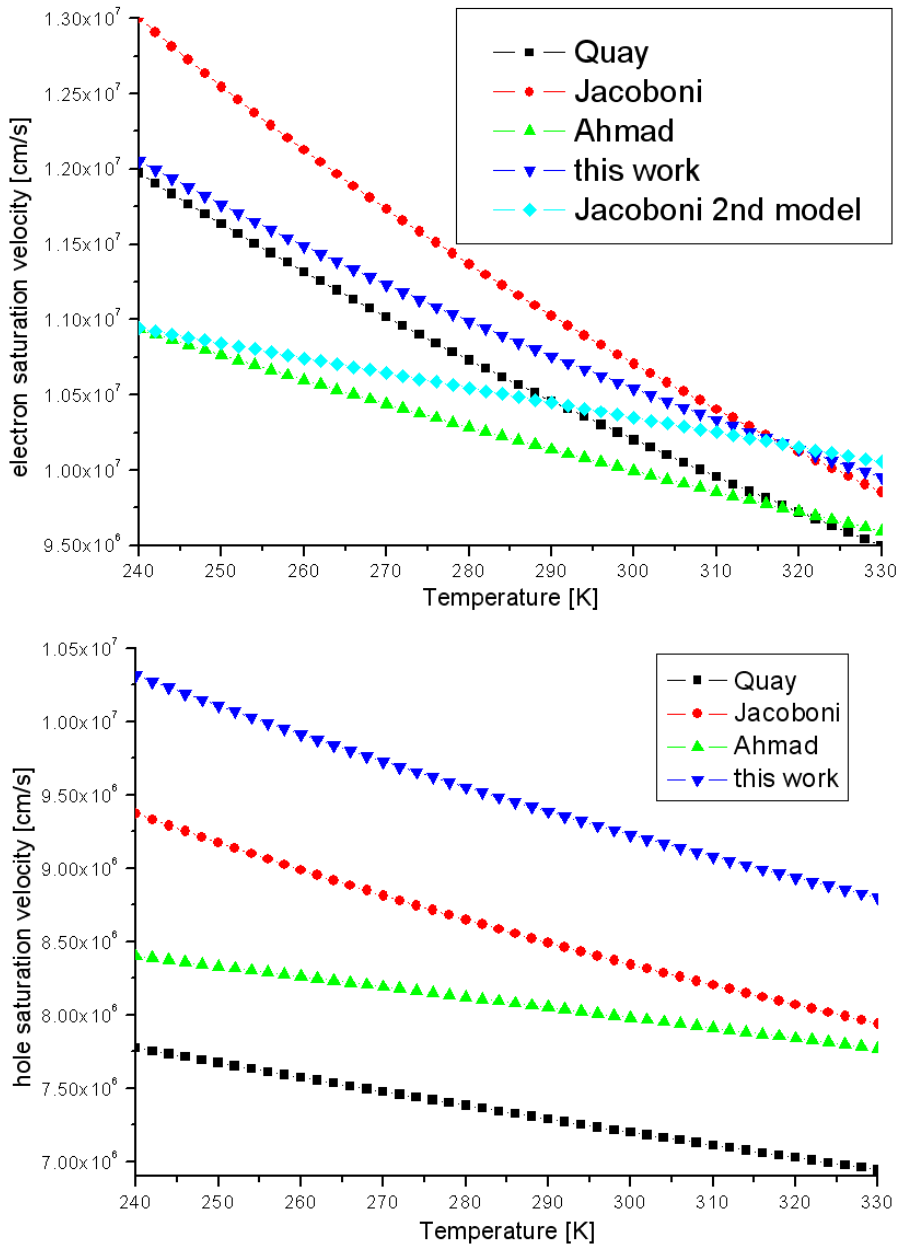

Figure 8.2: Comparison of different parameterizations of the saturation velocity proposed by other authors. In the publication of Jacoboni et al. [55] two parameterizations are given. The one parameterizing the electron saturation velocity directly has been labeled '2nd model'.

values for electrons of this work are in the range of values proposed by others, while the values for holes are higher than reported by [55, 65, 66], however values as high as 0.96×10^7 cm/s at 300 K have been found by Smith and Frey [67], which is even larger than the value determined in this work. A comparison is shown in Figure 8.2.

Except for the value for <111> orientation [55], no parameterizations of β values as

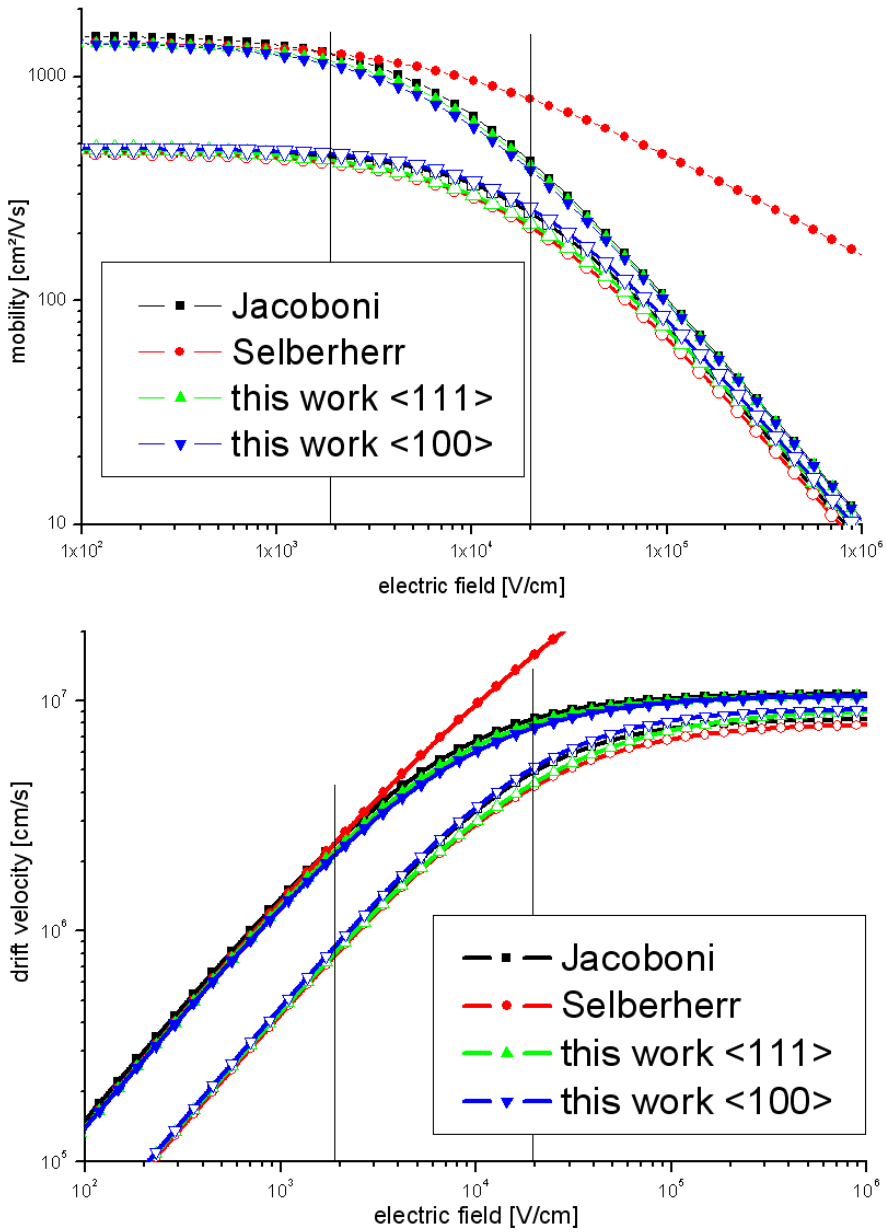

Figure 8.3: Comparison of different parameterizations of the mobility and drift velocities at T = 300 K. Electrons are marked by the full symbols, holes by the open symbols. Vertical black lines indicate the approximate minimum and maximum field encountered in the measurements of this work. Both electrons and holes show an anisotropy. Comparing <111> to <100> orientation the electron drift velocity and mobility decreases, while the hole drift velocity and mobility increases.

function of temperature and crystal orientation are available.

A comparison of mobilities and resulting drift velocities determined in this work with

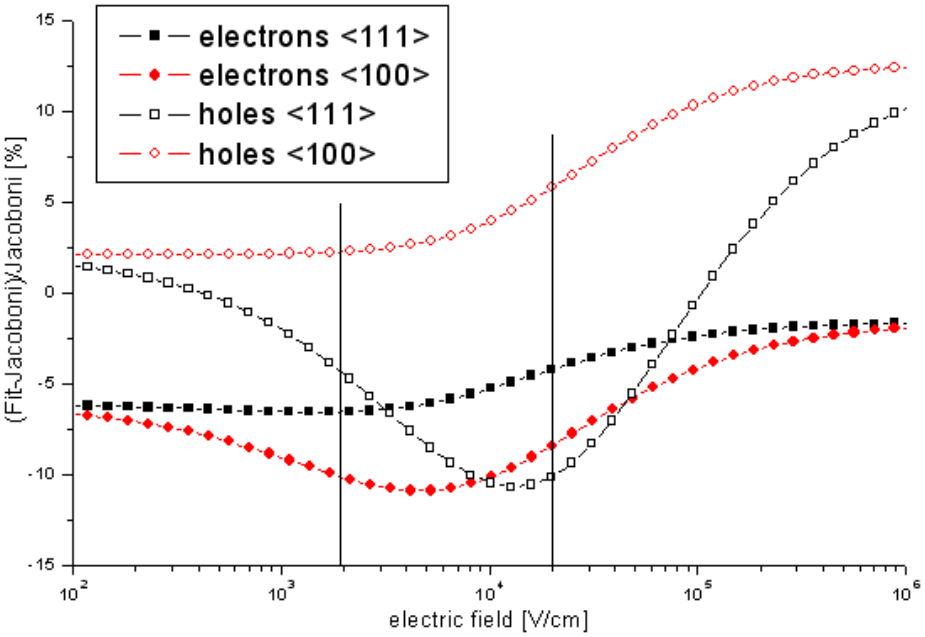

Figure 8.4: Difference between mobilities determined in this work and those of [55] at T = 300 K. Vertical black lines indicate the approximate minimum and maximum field encountered in the measurements of this work. Maximum deviations at this temperature are ± 12%.

those proposed by other authors is shown in Figure 8.3.

8.4 Discussion and Conclusions

A new parameterization of the field and temperature dependence of electron and hole mobilities in bulk silicon was presented for <111> and <100> crystal orientation.

The differences between the values derived from the parameterization presented here and the parameterization of Jacoboni et al. [55] are approximately ± 15% in the investigated temperature regime. The difference as function of electric field for T=300 K is shown in Figure 8.4. While the parameterizations for electrons in the <111> direction show an almost constant difference of - 5% the other parameterizations show distinctive differences.

No sensors of <110> orientation were available, thus no parameters for this direction could be determined. The electron parameters for this orientation provided by Castoldi and Rehak [68] (μ_e^0 = 1394 cm^2/Vs, v_e^{sat} = 1.85×10^6 cm/s, $\beta_e^{<110>}$ = 2.51, T = 300 K) differ greatly from the parameters presented here. However they have been obtained with very low fields (up to 700 V/cm), in which case the simple parameterization used in this work might need some corrections.

9 Comparison of simulations and measurements on pad sensors

In order to validate the assumptions on trapping and charge multiplication presented in Chapter 7, simulations were compared with selected measurements performed by others [37, 1]. The simulation code explained in Chapter 7 was used to do transport simulations and to calculate current pulses based on the parameters determined by others.

The mobility values determined in Chapter 8 were used in the simulation process. The measurements have been performed on so called epi material. Epi material denotes a thin (25 µm-150 µm) layer of epitaxial silicon, which has been grown on a highly doped ($> 10^{17}$ cm^{-3}) Czochralski (Cz) silicon substrate. For the simulations the Cz layer is assumed to be a perfect conductor, i.e. it is ignored in the simulation, the sensor volume ends at the epi-Cz interface.

The measurements have been performed on the 'standard' TCT setup. The 'standard' TCT setup is similar to the mTCT setup explained in Chapter 6, but was constructed having the investigation of pad diodes in mind. The sensors are not bonded but connected by a needle (allowing an easy exchange of sensors). The connection scheme is similar to the alternate mounting explained in Chapter 6. The rear side of the device is grounded and the high voltage is supplied to the front side. In order to decouple the high voltage and the measured signal a bias-T is used. The readout uses a Phillips Scientific amplifier and a Tektronix DPO 4104 Oscilloscope with 1 GHz bandwidth and 5 GS/s.

The 'standard' TCT setup can be flushed with nitrogen and thus allows temperature controlled measurements below the dew point. The temperature is controlled by a liquid chiller identical to the one explained in Chapter 6. The setup has been recently equipped with a Peltier element to improve the temperature range and stability, however the measurements presented here have been acquired before.

9.1 Field dependent trapping and double junction effect

In order to investigate the validity of assumptions on field dependent trapping and the double junction effect in the simulations, measured current pulses of an epitaxial diode of 153 µm thickness at a temperature of 20°C were compared to corresponding simulations. The sensor was heavily irradiated with neutrons ($\Phi_n = 2 \times 10^{15}$ cm^{-2}) and the current pulse shows a double peak structure for applied bias voltages between 250 V and 300 V (as shown in Figure 9.3).

A detailed investigation of the trapping probability as function of the electric field for

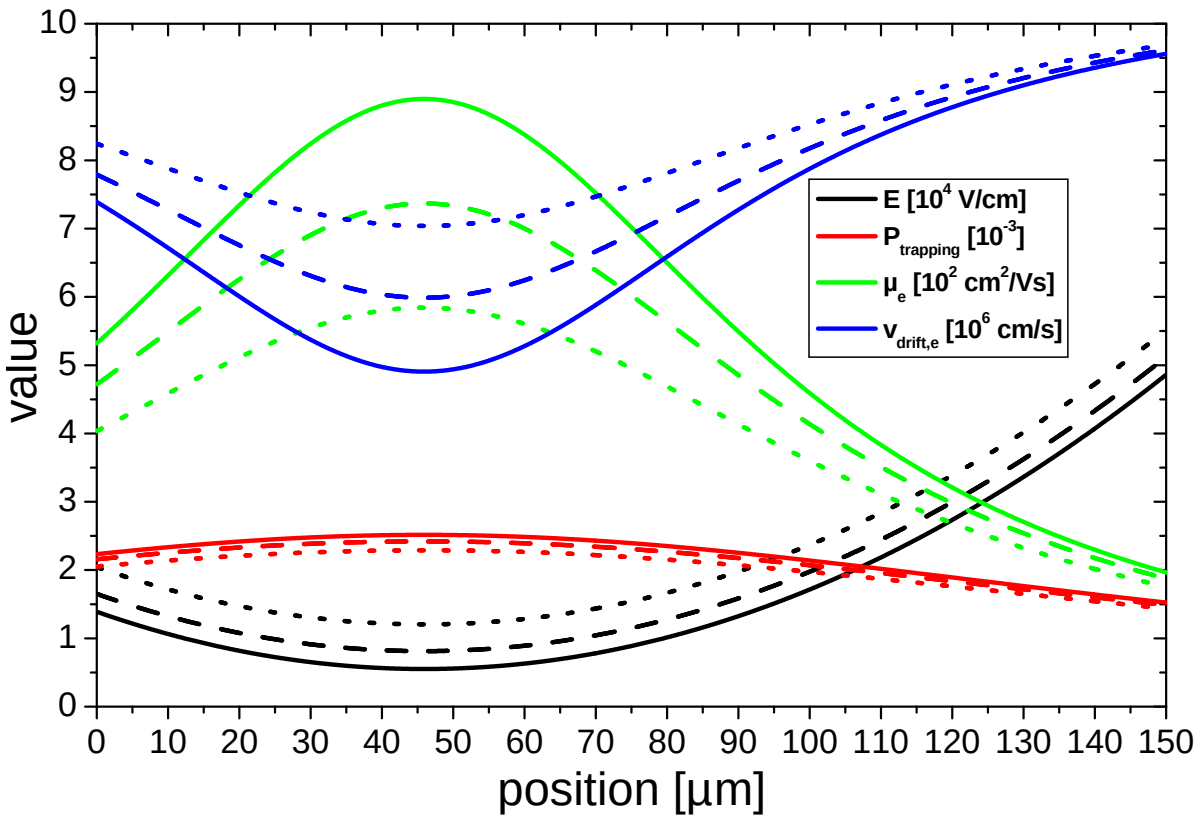

Figure 9.1: Overview of the simulation process of the 153 µm epitaxial sensor. Solid lines represent the situation for 260 V bias, dashed lines for 300 V and dotted lines for 360 V. The graph shows the distribution of electric field, trapping probability within the simulated timestep (Δt = 5 ps), mobility and drift velocity inside the simulation volume. The diffusion constant is proportional to the mobility.

this sensor was done by [37] finding the following parameters: $\tau_0 = 1.82$ ns, $\tau_1 = 0.30$ ns$\frac{\mu m}{V}$ (used in Equation 7.31) as well as $\overline{N_{eff}}$ = -16×10^{12} cm^{-3} and ΔN_{eff} = 40×10^{12} cm^{-3} (used in Equation 7.2).

To account for the pulse shape distortions of the 'standard' TCT setup used for the measurements, the same equivalent circuit as used by [37] has been employed.

Figure 9.1 shows the electric field, the trapping probability for one timestep ($\Delta t = 5$ ps), mobility and drift velocity inside the simulation volume for three different voltages. The minimum of the electric field is located at approximately one third of the sensor depth. At this location the trapping probability and the mobility are highest and the drift velocity is lowest.

Figure 9.2 shows the distribution of electrons inside the sensor volume for selection of times and voltages after illumination with 660 nm light. Although the effect of the diffusion cannot be observed in the current pulse, the broadening of the charge

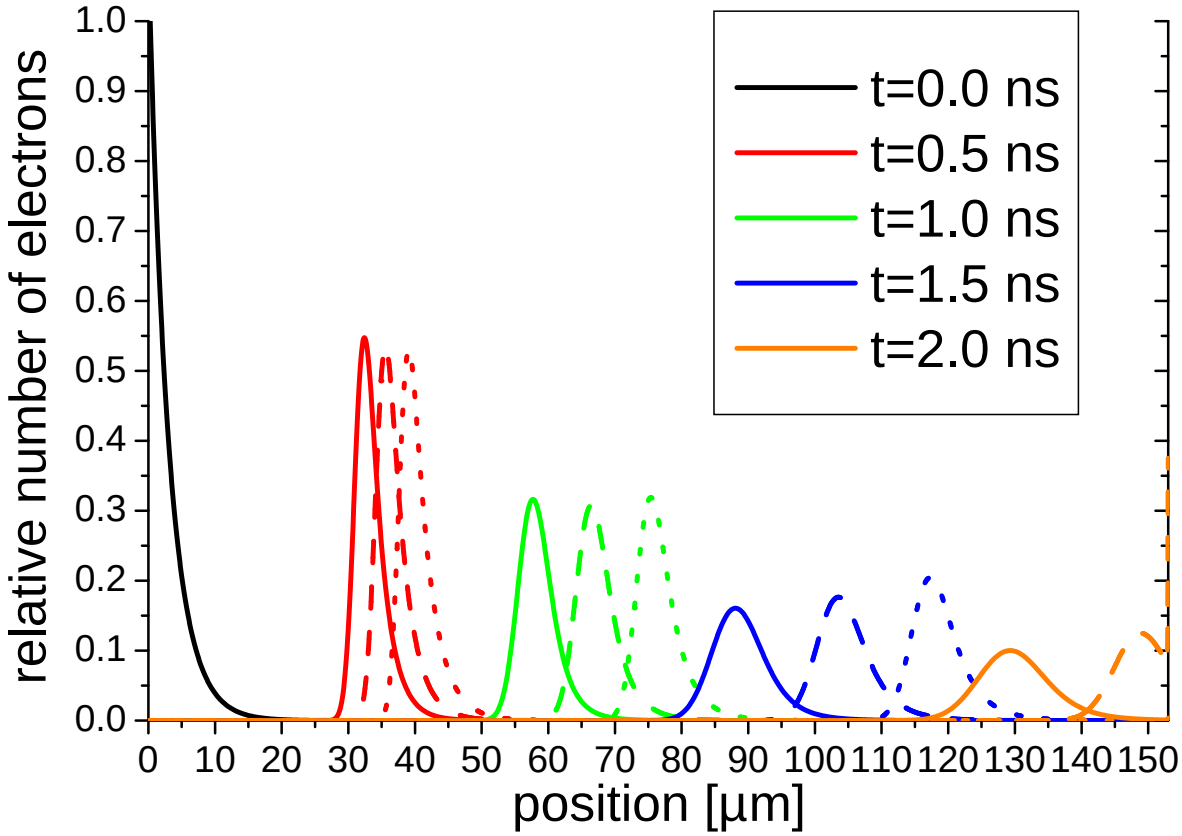

Figure 9.2: Overview of the distribution of electrons inside the simulation volume at different times. Solid lines represent the situation for 260 V bias, dashed lines for 300 V and dotted lines for 360 V. For $t = 2$ ns and 300 V applied voltage the effect of the charge carriers being stopped at the sensor boundary can be observed.

carrier distribution inside the sensor volume is clearly seen. From the Einstein relation ($D = \mu k_B T/e_0$) the diffusion constant is expected to be lower for higher applied voltages, as the average electric field is higher, reducing the mobility. A corresponding behavior is seen in Figure 9.2, the charge cloud, e.g. at $t = 1.5$ ns, is broader at lower voltages.

Figure 9.3 shows a comparison of transients for three different voltages. The measured transients are qualitatively reproduced, however discrepancies of up to 10 % remain. In the region below 0.3 ns the measured current increases while the simulation does not show such a behavior. Around 1 ns the peak value of the measured current is not reproduced exactly, the simulated values are lower. Between 2.5 ns and $\approx$ 4 ns the decrease of the current is less than simulated and the undershoot introduced by the external circuit simulation is stronger than observed.

All these deviations can be explained by inaccuracies in the equivalent circuit. The deviation in the rising slope is similar to an artifact commonly observed when modeling lossy transmission lines. This 'pre-rise' is the result of the so-called skin-effect in

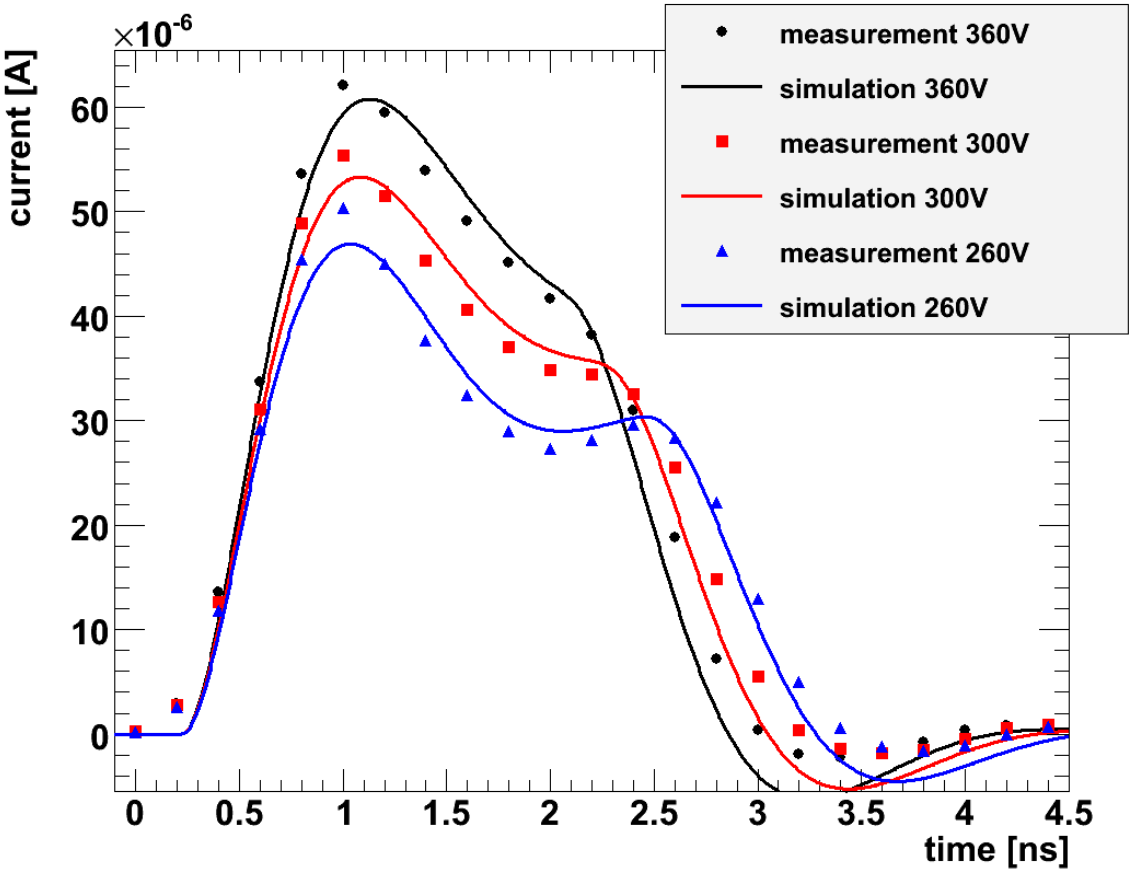

Figure 9.3: Comparison of simulation and measurements for an irradiated 150 µm epitaxial sensor for three different voltages after illumination with 660 nm light. Simulations are shown as solid lines, the sampling points of the measurements are shown as markers.

cables, resulting in a higher attenuation for higher frequency components of the signal. This effect also produces a corresponding 'late-rise', i.e. an additional delay until the maximum value is reached, if a step function is transmitted via the transmission line.

The other two effects can be explained by the LCR network of the equivalent circuit. If the effective capacitance is too high this will result in an increased rise time and thus reduced sensitivity to fast changes in the input signal. Additionally if the inductance is not well matched the ringing behavior of the system might not be correctly modeled. To accurately model the observed deviations several LCR circuits would have to be combined and the frequency dependence of all components had to be known very precisely.

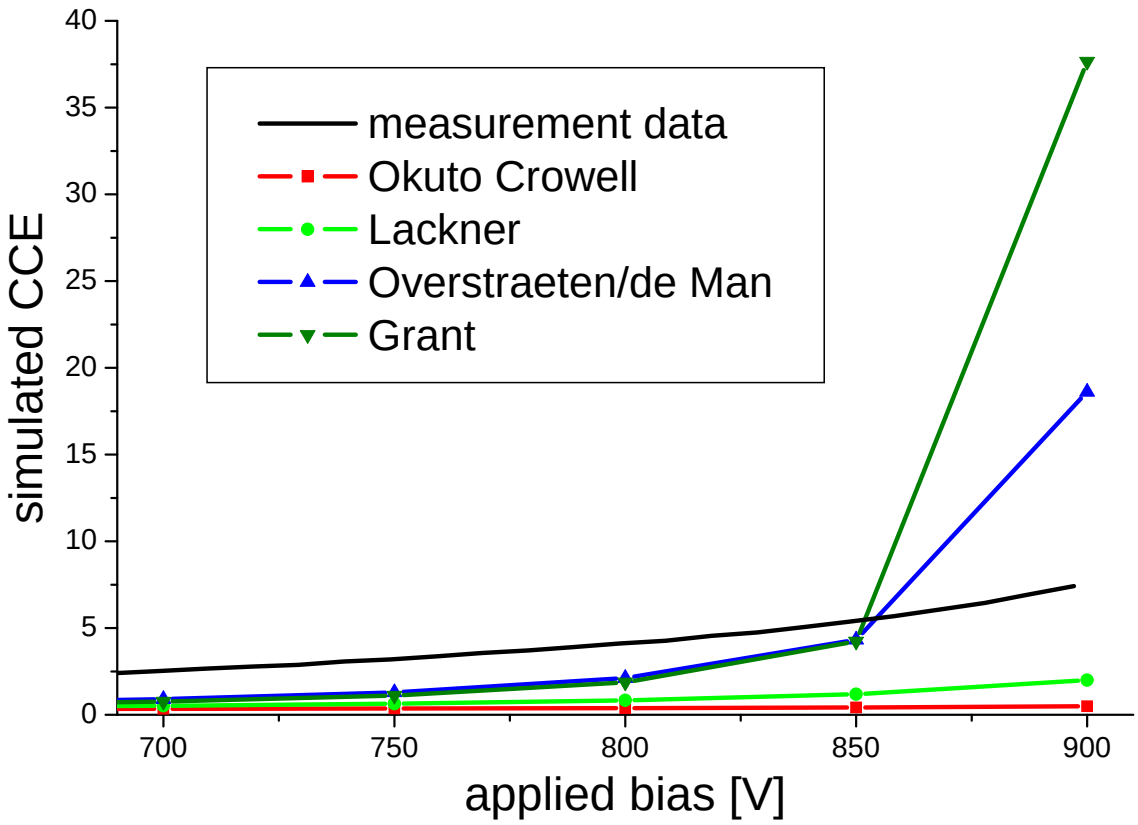

Figure 9.4: Comparison of simulations of the CCE of a 75 µm epitaxial diode after illumination with 660 nm light. Different parameterizations of the impact ionization coefficients have been used while keeping all other parameters unchanged. Measured CCE values range around 7 at 900 V applied bias.

9.2 Multiplication in highly irradiated diodes

Recent investigations showed the onset of charge multiplication in heavily irradiated sensors [1]. Simulations were performed in order to interpret the observed results qualitatively. A 75 µm epitaxial diode irradiated with 24 GeV/c protons up to an equivalent fluence of $\Phi_{eq} = 1 \times 10^{16}$ cm^{-2} was used for the comparison.

The experimental situation after such high irradiations is not as well defined as in the non-irradiated case. Certain assumptions, motivated by [1] were made. The electric field was assumed to be linear with a depletion voltage of $U_{dep} = 750$ V and the trapping time was assumed to be independent of the electric field $\tau_0 = 0.2$ ns. During the measurements the sensor temperature was kept constant at T = -10°C.

Being normalized to the elementary charge, the integration of the simulated pulse shape yields the Charge Collection Efficiency (CCE). Thus the CCE of the simulation was determined directly. For the measurements the CCE was determined by integrating the current pulse and dividing it by the charge collected in a non irradiated diode of the

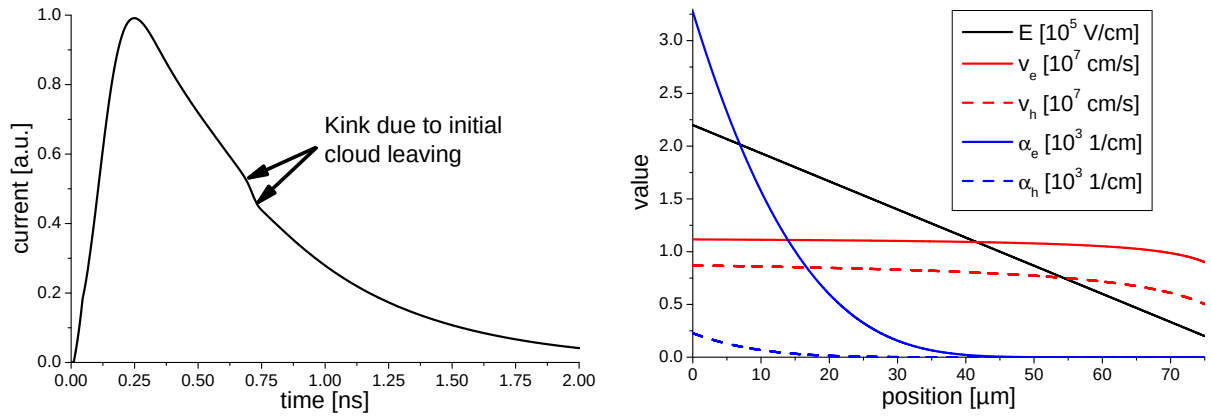

Figure 9.5: Pulse structure (left) and parameter distribution of the 75 µm epitaxial sensor (right).

same type for voltages above depletion.

The simulations have been performed for different applied voltages with different parameterizations [69, 70, 71, 72] of the impact ionization coefficient α. The results are shown in Figure 9.4.

A different slope of the CCE curve is observed and the increase in the charge collection efficiency is only qualitatively reproduced. In the measurements the CCE for voltages below 850 V is systematically higher than in the simulation, for voltages above 850 V the simulated CCE is too high. This is possibly due to the use of very simple approximations for the electric field and trapping probability in the simulations.

For the detailed simulations shown in Figure 9.5 and Figure 9.6 the same simple approximations and the impact ionization coefficient parametrization by Overstraeten

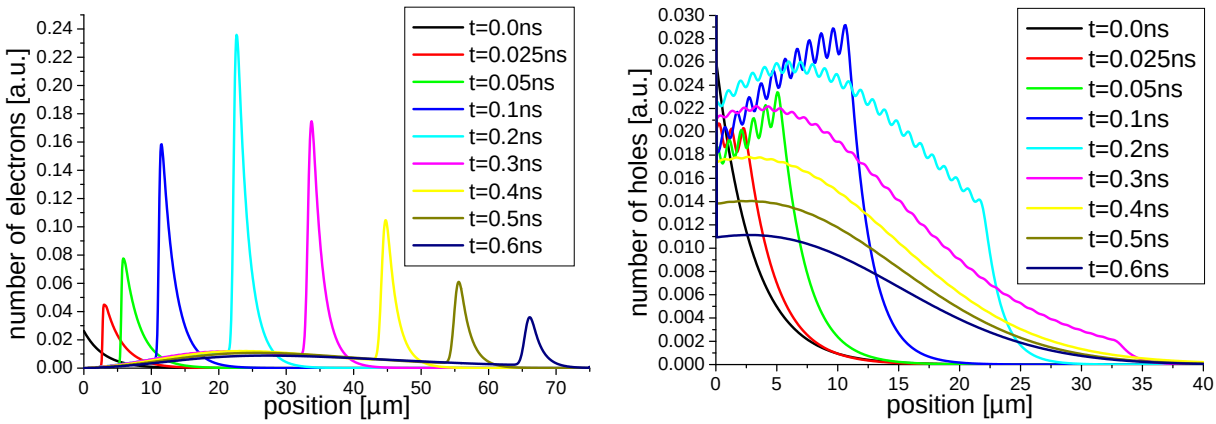

Figure 9.6: The left graph shows the electron distribution inside the diode at selected times. The right graph shows the hole distribution at the same times. The arbitrary units for electrons and holes are identical. The scaling of x-axis and y-axis is different for both graphs.

and de Man [70] was used.

Figure 9.5 shows the simulated current pulse for 900 V applied voltage as well as the electric field, the drift velocities of electrons and holes and the impact ionization parameters for electrons and holes as function of position inside the diode. The current pulse is not corrected for the distortion introduced by the external circuit. The observed rise of the current pulse is due to the continuous multiplication of charge carriers close to the junction. Once the main electron cloud has left the multiplication region (see Figure 9.6) the current starts to decline. Around 0.7 ns the charge cloud leaves the sensor volume (observed as a kink in the current pulse) and a continuous distribution of electrons and holes remains, which is steadily decreasing, as trapping dominates over the charge multiplication process.

Figure 9.6 shows the distribution of electrons and holes inside the sensor for selected times. The oscillations in the hole distribution are artifacts of the simulation process. Decreasing the time step size (Δt) and cell size (Δx) of the simulation reduces these artifacts, but increases the calculation time of the simulation.

It can be seen that the total number of electrons is increasing up to $t = 0.2$ ns - 0.3 ns, which can also be observed as a rise in current. After this time the main charge cloud has left the multiplication regime of electrons (extending approximately 30 µm from the junction) and the number of electrons is continuously reduced due to trapping. There is a small multiplication zone of holes close to the junction. Thus secondary holes created by the multiplication of electrons, create 'tertiary' electrons close to the junction. These electrons are again multiplied when drifting through the multiplication zone for electrons and so on. This behavior is similar to avalanche breakdown[1], but quenched by the trapping.

Figure 9.7 compares simulated pulses (corrected for an external circuit shown in Figure 7.8, but increasing the detector capacitance to 36 pF) and measured pulses at different voltages. None of the features observed in the current pulse without circuit correction can be observed as the detector capacitance is too large. The pulses have been scaled such that the peak values of simulation and measurement at 900 V are similar. Additionally the pulses are scaled with respect to each other, which is noted in the legend of the Figure. The decrease of the simulated pulses is too slow compared to the measurement, indicating a mismatch of capacitances in simulation and measurement.

9.3 Summary

Simulations of irradiated epitaxial diodes have been performed. One of the sensors has a thickness of 153 µm and shows a double peak structure and field dependent trapping. It was shown that an agreement between simulation and measurement can be achieved when the parameterizations described in Chapter 9 are used.

The other investigated sensor has a thickness of 75 µm and shows charge multiplication after heavy proton irradiation. Using different parameterizations of the impact ionization

[1] without trapping electrons and holes multiply indefinitely

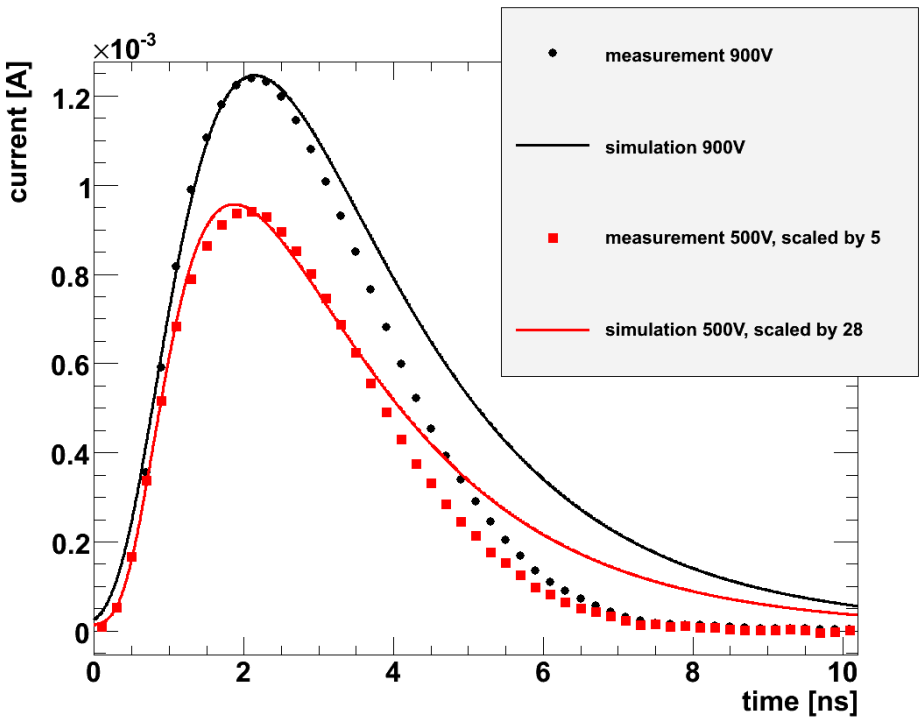

Figure 9.7: Comparison of measured and simulated pulses for different voltages. Any information of the pulse structure is lost due to the high capacitance of $\approx$ 36 pF. The decrease of the simulated current pulses is too long due to an incorrect modeling of the readout circuit.

coefficient the general behavior of the sensor could be reproduced. The simulation allowed to investigate the charge transport inside the sensor showing that predominantly electron but also hole multiplication play a role in the charge collection process.

10 Measurements on pad sensors with high charge carrier densities

When the created charge carrier densities are sufficiently high to modify the electric field in the sensor, significant changes, compared to the situation with low charge carrier densities (investigated in Chapter 8 and Chapter 9), are observed (so called plasma effects). These effects have been observed in the detection of heavily ionizing particles and with high intensity laser light.

Plasma effects are also expected for experiments at X-ray free electron lasers. The studies presented here aim at a quantitative understanding of the plasma effects for experiments at the European XFEL [5].

For high charge carrier densities the electrons and holes form a so called plasma, which dissolves slowly. The plasma boundaries effectively shield its inner region from the electric field created by the external bias, thus altering the induced current pulse and increasing the charge collection time [12]. Plasma effects decrease as the electric field increases [13]. Using incident ions of different masses and energies, the influence of material properties on plasma effects has been studied in detail in [14].

Figure 10.1 shows simulations of the time evolution of the hole density for 11×10^6 electron hole pairs in a 280 μm thick p^+n diode biased to 200 V. The electron hole pairs are created by laser light of 660 nm wavelength focused to 10 μm, injected opposite to the p^+n junction.

From the drift-diffusion calculations (performed by K. Gärtner from WIAS [73]) it is concluded, that the plasma cloud does not expand, instead charge carriers are continuously released from the plasma region and thus form a conductive channel connecting both electrodes.

Electrostatic repulsion effects in the conducting channel result in an increased lateral spread of the collected charge and thus in increased charge sharing between pixels, as shown for α-particles in [15].

The effects on silicon sensors for the European XFEL are investigated in Chapter 11 using a focused high intensity laser to simulate x-rays.

In this chapter simulation results are compared to measured current pulses showing plasma distortions after illumination with focused laser light of high intensity.

10.1 Investigated sensor

The investigated sensor is labeled CG1215, which is the same as used in Chapter 8. In order to investigate plasma effects the laser beam was focused to a spot with a Gaussian

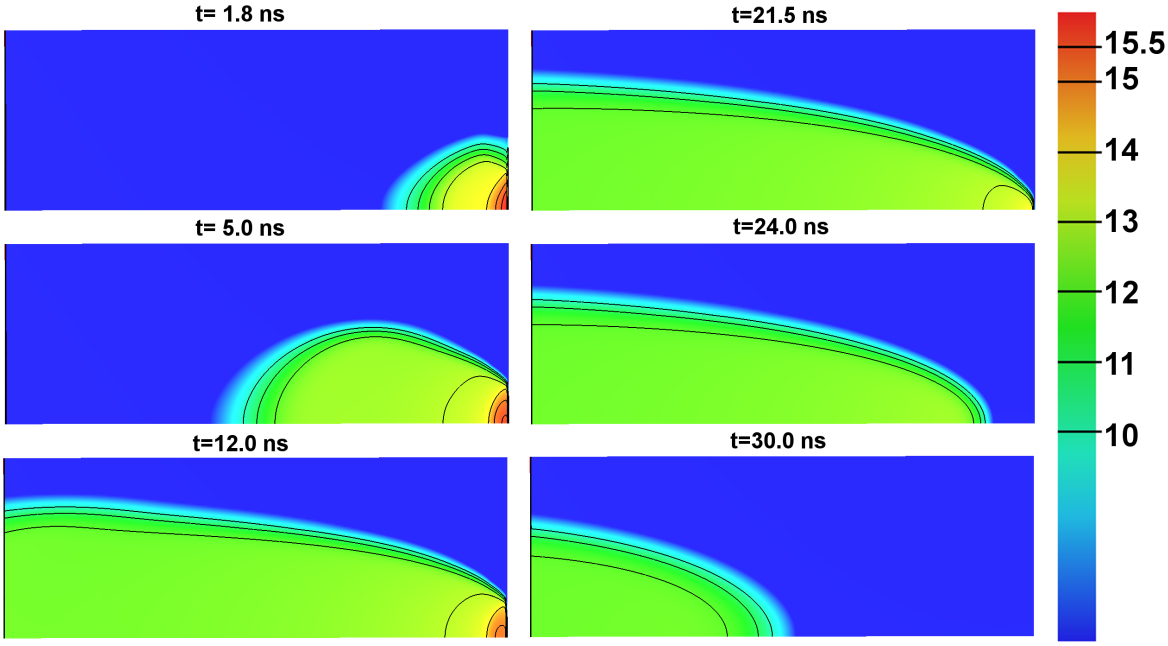

Figure 10.1: Evolution of a plasma cloud in space and time. The logarithm to the base of ten of the hole density is color-coded for a cut along the y axis. The simulation volume is 100 µm high (top to bottom) and 280 µm wide (left to right). 11×10^6 electrons and holes are created on the right side (opposite to the junction) and holes drift to the left. A bias of 200 V is applied.

profile with $\sigma = 10$ µm. A constant lateral beam profile was assumed for the entire absorption process.

10.2 Simulations

The transport simulations have been performed by K. Gärtner from WIAS [73].

For the transport simulations the classical van Roosbroeck equations are used [74]. The van Roosbroeck equations are differential equations describing drift and diffusion of charge carriers.

The lifetime of the plasma cloud is determined by the emission of carriers into the surrounding volume with low charge carrier density. A slow movement of the center of the plasma cloud results from the different probability to emit an electron or a hole from different parts of the plasma, depending on the distance to the closest electrode.

The charge carrier transport outside of the plasma happens almost exclusively in the low doped silicon bulk material[1]. Dominating influences in the simulation are the initial cloud size and the field induced mobility reduction.

As explained in Chapter 7 the readout circuit introduces distortions. To account for

[1]Charge carriers in the highly doped implant regions recombine almost immediately.

these distortions all simulations performed by WIAS have been convoluted with the transfer function of the setup shown in Figure 7.7.

Results presented here are based on charge carrier mobilities reported in literature [75], but using $\beta_n = 1$ (instead of $\beta_n = 2$) for the field dependent mobility reduction ($\mu_0^h = 495\frac{cm^2}{Vs}(\frac{T}{300K})^{-2.23}$, $\mu_0^e = 1448\frac{cm^2}{Vs}(\frac{T}{300K})^{-2.33}$, $v_{sat}^h = 0.95 \times 10^7\frac{cm}{s}$, $v_{sat}^e = 1.1 \times 10^7\frac{cm}{s}$, $\beta^h = \beta^e = 1.0$) and are labeled literature mobility. For comparison two other models have been used as well. The second model is the same as mentioned above but without field dependent mobility reduction (labeled constant mobility). The third model uses the same models for lattice, ionized and unionized impurity scattering as well as the same model for carrier-carrier scattering, but the field dependent parameters for <100> crystal orientation described in Chapter 8 ($\mu_0^h = 474\frac{cm^2}{Vs}(\frac{T}{300K})^{-2.619}$, $\mu_0^e = 1440\frac{cm^2}{Vs}(\frac{T}{300K})^{-2.26}$, $v_{sat}^h = 0.94 \times 10^7\frac{cm}{s}(\frac{T}{300K})^{-0.226}$, $v_{sat}^e = 1.054 \times 10^7\frac{cm}{s}(\frac{T}{300K})^{-0.602}$, $\beta^h = 1.181(\frac{T}{300K})^{0.644}$, $\beta^e = 0.992(\frac{T}{300K})^{0.572}$) were used (labeled fitted mobility).

10.3 Comparison of simulations and measurements

Electron hole pairs have been created with 660 nm laser light of different intensities. The field dependent mobility reduction is dominant for pulses recorded with low intensity laser light. For high intensity illuminations plasma effects dominate experimental results and simulations.

10.3.1 Junction side illumination

Injection on this side allows to check the transport properties of electrons separately from those of holes, as holes reach the close by electrode quickly.

Increasing the number of created carriers increases the plasma effects. Inspection of the simulations shows peak values of $np/n_i^2 \approx 10^{10}$ in the plasma cloud for the case of 97×10^6 generated charge carriers.

Figures 10.2 and 10.3 show the comparison of simulated and measured currents for junction side illumination.

Simulations and measurements for low density clouds are very similar and acceptable agreement between simulation and measurement is observed for 1×10^6 electron hole pairs. Thus it can be concluded that the low density transport properties of electrons are reasonably well modeled. At higher charge carrier densities the current pulse shapes deviate from the low density case due to the lifetime of the plasma cloud. The current is determined by the release of charge carriers from the plasma cloud. The deviation between measurements and simulations increases with increasing plasma density.

As seen in Figure 10.3, the current rises slowly at the beginning of the pulse for 97×10^6 electron hole pairs in simulation and measurement. The rise is followed by an approximately constant current, until the final decrease shows a similar time constant as in the 10×10^6 electron hole pairs case.

In the simulations the peak at the beginning is due to the removal of the low density periphery of the cloud. The remaining high density core has an ellipsoid shape and is

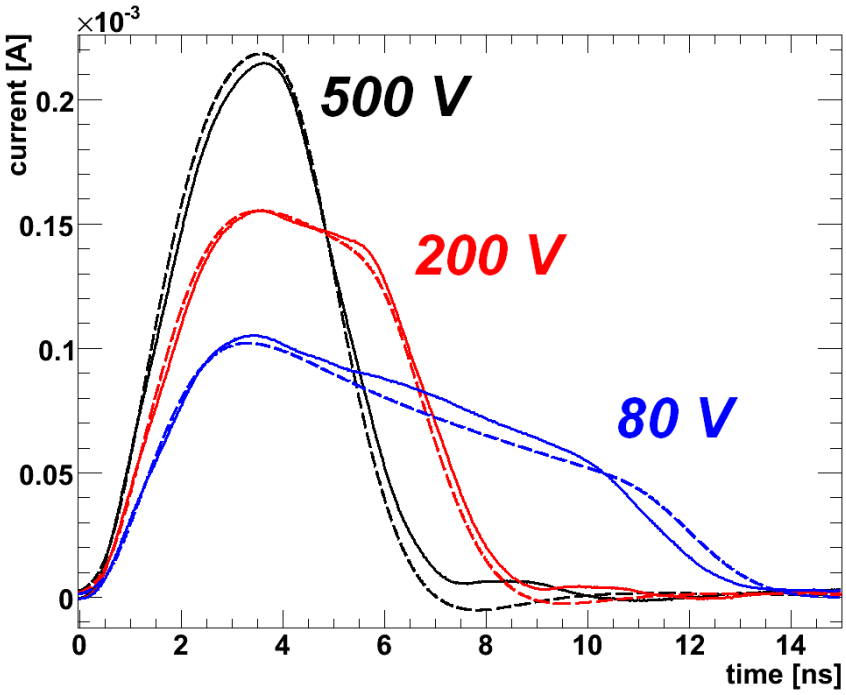

Figure 10.2: Results for junction side illumination using defocused laser light to avoid plasma effects. Simulations with literature mobility are shown as dashed lines and measurements as solid lines.

shrinking with time as well as the maximum density in the plasma (see Figure 10.1). The barycenter of the plasma is slowly moving away from the junction.

Using a constant mobility speeds up the release of charge carriers from the plasma and their drift in the rest of the sensor volume. Thus pulses calculated using the constant mobility are systematically too short, except for the pulse obtained for 97×10^6 electron hole pairs at 100 V bias, which is too long by 4% of the pulse length.

10.3.2 Illumination opposite to the junction

This situation allows to study the transport properties of the holes. Contrary to electrons, holes move towards the high field region (junction). Figures 10.4 and 10.5 show the comparison of simulated and measured currents for this case.

A qualitative agreement between simulation and measurement is observed for the measurement with defocused laser light and 1×10^6 electron hole pairs. However the simulated pulses are systematically too long.

For 11×10^6 electron hole pairs the 100 V and 200 V curves show clear deviations, while at 500 V the deviations are at the level observed for 1×10^6 electron hole pairs. The transient behavior between the low density regime and first plasma effects observed for junction side illumination can also be observed in this case.

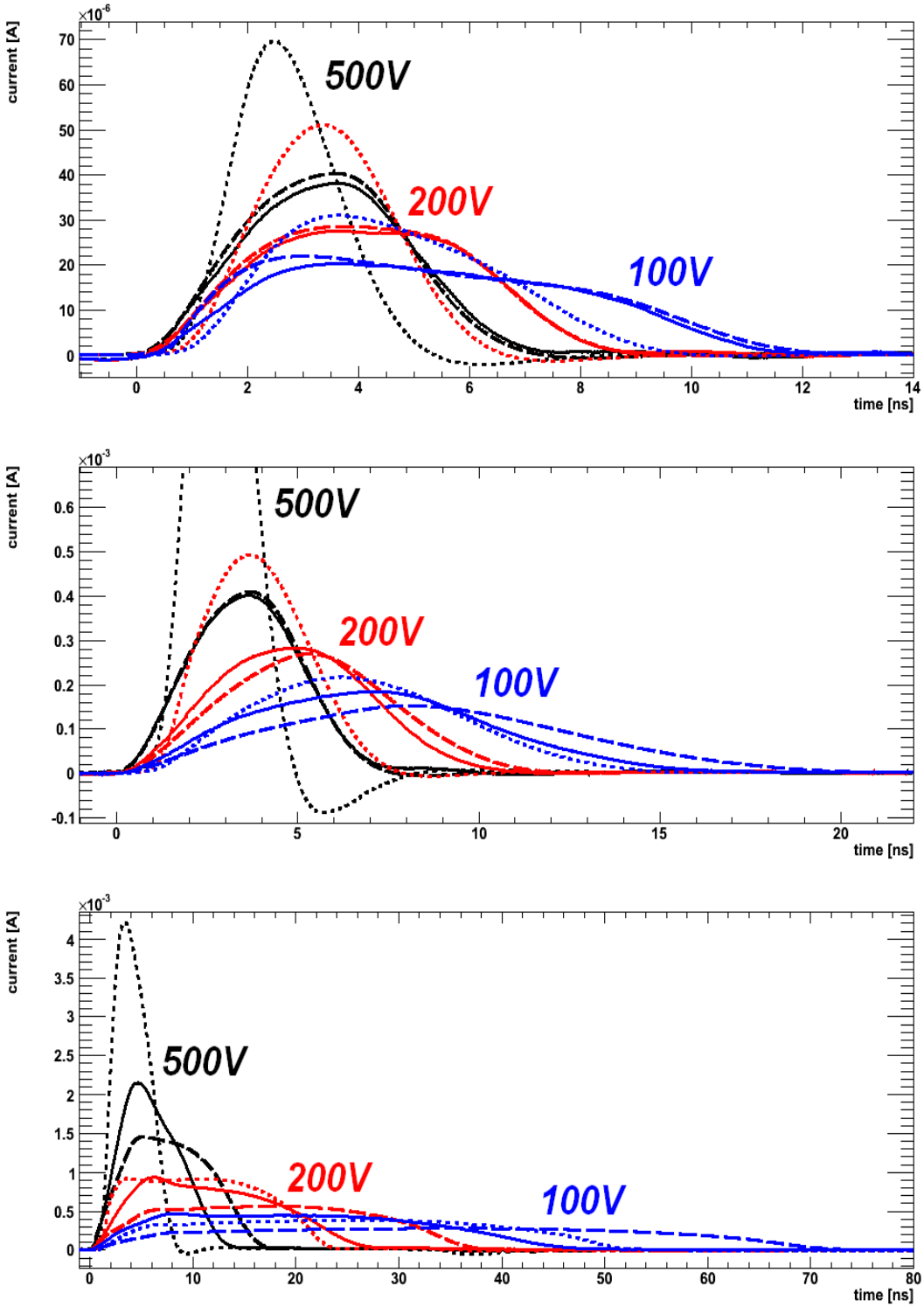

Figure 10.3: Results for junction side illumination using focused laser light. Simulations with literature mobility are shown as dashed lines, with constant mobility as dotted lines and measurements as solid lines. The number of electron hole pairs created is 1×10^6, 10×10^6 and 97×10^6, from top to bottom. While acceptable agreement can be observed for low densities, high densities show a shorter pulse duration than the simulations. Note the different scale on the time axis.

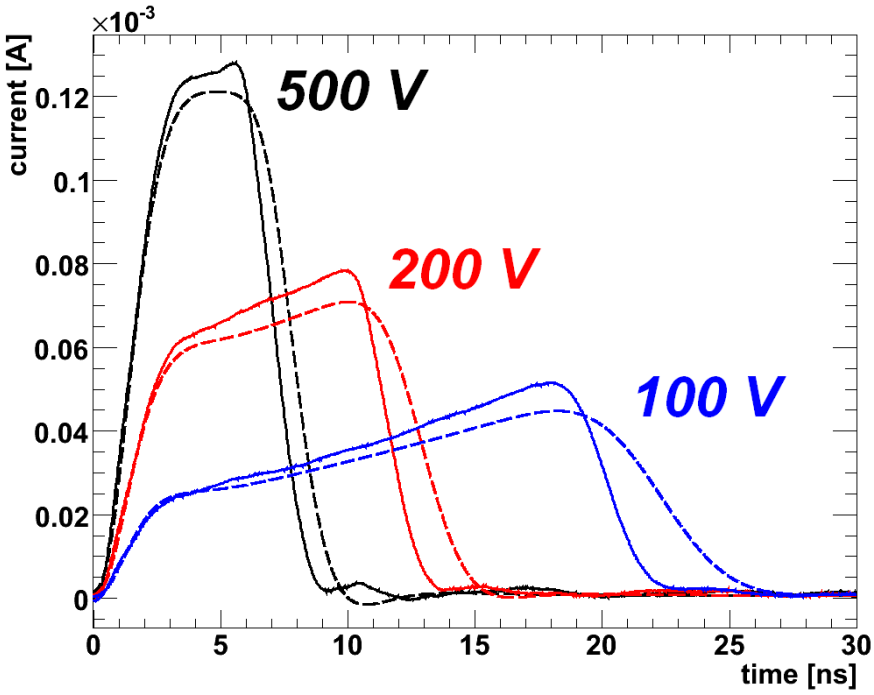

Figure 10.4: Results for illumination opposite to the junction using defocused laser light to avoid plasma effects. Simulations with literature mobility are shown as dashed lines and measurements as solid lines.

When 103×10^6 electron hole pairs were created both simulated and measured current pulse become very long compared to the current pulses observed for low densities. While qualitatively the simulations produce pulses with similar durations, the simulated pulses are systematically too long.

As in the case of illumination on the junction side, using a constant mobility speeds up the release of charge carriers from the plasma and their drift in the rest of the sensor volume. Thus pulses calculated using the constant mobility are systematically too short as well, except for the pulse obtained for 11×10^6 electron hole pairs at 100 V bias (2.4% too long) and 103×10^6 electron hole pairs at 100 V (5.6% too long) and 200 V bias (25.9% too long).

10.4 Discussion and Conclusions

Discrepancies between measurements and simulations are observed. For high charge carrier densities the simulated pulses using the literature mobilities are systematically too long. While the agreement with junction side illumination of low intensity (electron properties dominant) is satisfactory, simulations for illumination opposite to the junction are too long for low densities as well. This may indicate a problem in the modeling of

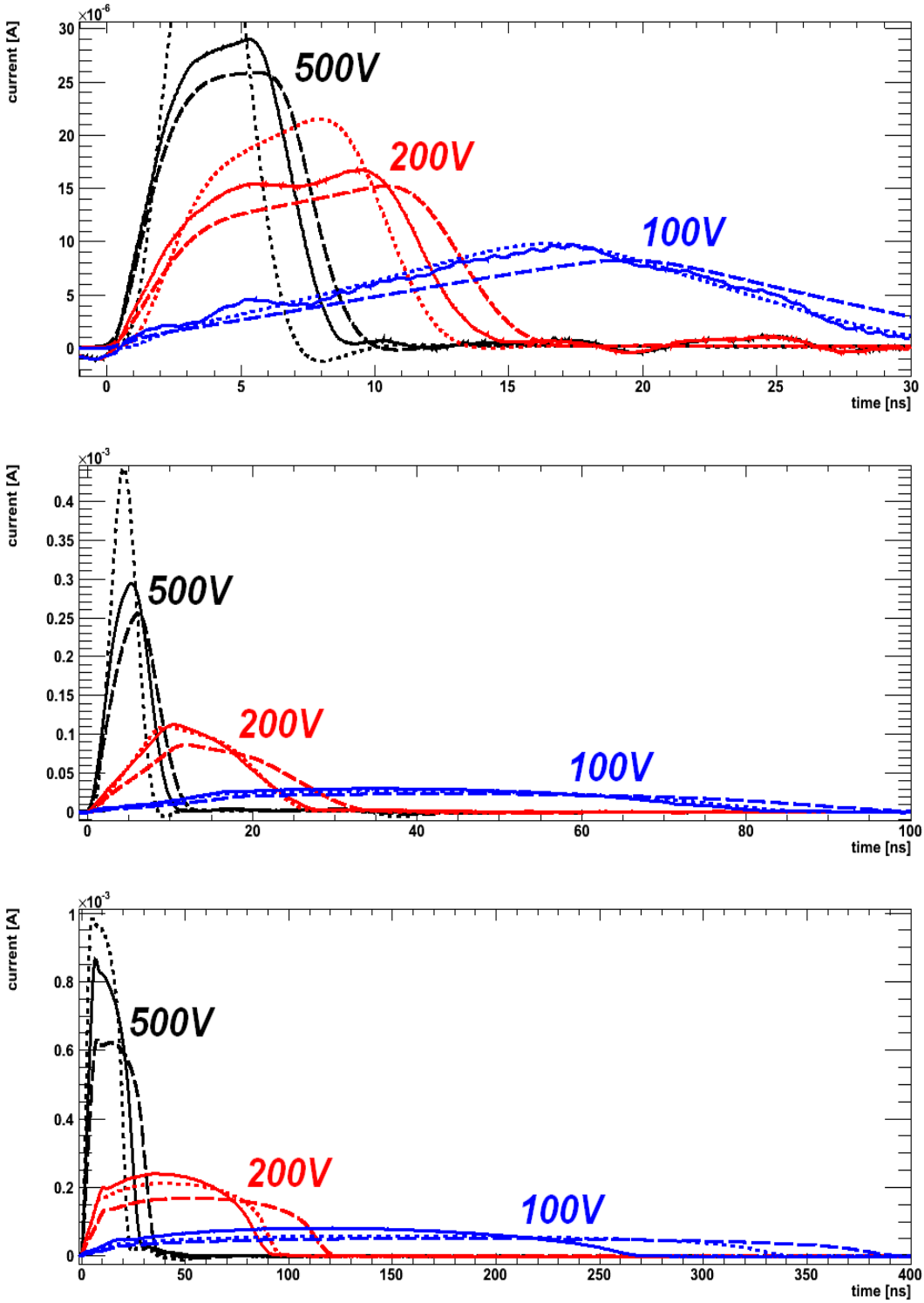

Figure 10.5: Results for injection opposite to the junction using focused laser light. Simulations with literature mobility are shown as dashed lines, with constant mobility as dotted lines and measurements as solid lines. The number of electron hole pairs created is 1×10^6, 11×10^6 and 103×10^6, from top to bottom. Measurements systematically show a shorter pulse duration than the simulations. Note the different scale on the time axis.

Illumination	$N_{e,h}$ [10^6]	U_{bias} [V]	duration [ns]	difference
junction side	-	500	∅/7.0/6.8	∅ / -2.9%
junction side	-	200	∅/8.5/8.4	∅ / -1.2%
junction side	-	80	∅/13.0/13.5	∅ / 3.8%
opp. to junction	-	500	∅/9.0/10.0	∅ / 11.1%
opp. to junction	-	200	∅/13.5/15.0	∅ / 11.1%
opp. to junction	-	100	∅/23.0/27.0	∅ / 17.4%
junction side	1	500	5.0/7.0/7.0	-28.6% / 0.0%
junction side	1	200	6.5/9.0/9.0	-27.8% / 0.0%
junction side	1	100	10.0/12.0/12.3	-16.7% / 2.5%
junction side	10	500	5.0/7.0/7.0	-28.6% / 0.0%
junction side	10	200	8.0/11.0/12.0	-27.3% / 9.1%
junction side	10	100	15.0/17.0/20.0	-11.8% / 17.6%
junction side	97	500	8/14/18	-42.9% / 28.6%
junction side	97	200	24/28/38	-14.3% / 35.7%
junction side	97	100	52/50/75	4.0% / 50.0%
opp. to junction	1	500	7.0/9.0/10.0	-22.2% / 11.1%
opp. to junction	1	200	13/15/17	-13.3% / 13.3%
opp. to junction	1	100	31/31/38	0.0% / 22.6%
opp. to junction	11	500	9/12/14	-25% / 16.6%
opp. to junction	11	200	27/28/35	-3.6% / 25.0%
opp. to junction	11	100	87/85/100	2.4% / 17.6%
opp. to junction	103	500	25/30/35	-16.7% / 16.7%
opp. to junction	103	200	95/90/120	5.6% / 33.3%
opp. to junction	103	100	340/270/390	25.9% / 44.4%

Table 10.1: Pulse durations for all measurements (t_{meas}) presented in this chapter compared to their simulations with the literature mobility model (t_{lit}) and the constant mobility model (t_{const}). The column labeled $N_{e,h}$ lists the number of created electron hole pairs; a '-' indicates the low density measurement and simulation. The column labeled U_{bias} lists the applied bias voltage. The column labeled duration lists $t_{const}/t_{meas}/t_{lit}$. The column labeled difference lists $(t_{const} - t_{meas})/t_{meas}$ and $(t_{lit} - t_{meas})/t_{meas}$. A '∅' indicates that no corresponding simulation was performed. The measurements have been performed with 660 nm light focused to a Gaussian spot with $\sigma_{laser} = 3$ µm on a p^+nn^+ diode with a thickness of 280 µm and an effective doping of 8.2×10^{11} cm^{-3}.

the cloud separation at low fields or with the low density transport properties of holes.

Simulated pulses using a constant mobility are systematically too short (except for the highest intensity and low bias voltage). However both models can be used to estimate an interval in which the measured pulse duration is found. Table 10.1 summarizes these results.

To estimate the effect of having an initial charge carrier distribution which is different from the light profile, simulations with different widths of the initial charge carrier distribution and absorption lengths have been done for 1×10^6 and 11×10^6 electron hole pairs created opposite to the junction. The results for 200 V applied bias are presented in the upper graphs of Figure 10.6 and 10.7, showing that an increase in width by 50 % or an increase in absorption length by 100 % is not sufficient to produce a pulse which is as short as the measurement. However the combination of increased attenuation length, initial width and constant mobility might be sufficient to produce pulses which are shorter than the measurements even for the highest intensity at low bias voltage.

Based on literature data the low density limit for holes (Figure 10.4) could not be reproduced, indicating the need for changes in the mobility parameterizations. Using the fitted mobility parameterization for holes the current pulse for 1×10^6 electron hole pairs could be reproduced well (Figure 10.6, bottom). The effect of assuming a constant mobility model is presented in Figures 10.3 and 10.5, as well as in the lower graphs of Figures 10.6 and 10.7, indicating that the release of charge carriers from the plasma cloud can be significantly accelerated when the diffusion parameter does not decrease with increasing field as obtained from the Einstein relation. In combination with the faster drift velocity of the charge carriers this results in almost all cases in current pulses which are shorter than the measurements.

In the simulations peak densities of $np/n_i^2 \approx 10^{10}$ are observed. At this density charge neutrality is governing the emission of the less likely emitted carrier type[2] and carrier-carrier scattering is of small influence. Simulations without mobility reduction due to carrier-carrier scattering showed the same pulse durations and are not presented here. Strong carrier-carrier scattering increases the pulse duration as expected, while the measurements show shorter pulses than the simulations.

The van Roosbroeck equations used in the simulations describe the situation in the diode for low density clouds well, however in situations with high densities gradients may violate assumptions made in the derivation of the drift-diffusion approximation (compare [75] for discussion).

The possible effects of Fermi-Dirac statistics (see [76], [77]) were estimated by K. Gärtner and the expected influence on the pulse length is weak, however the Einstein relation ($D = \mu k_B T/e_0$) would be replaced by a density dependent one. Especially [77] shows larger diffusion constants compared to the Einstein relation.

Optical photons of 660 nm wavelength (1.87 eV) produce so called hot charge carriers, as the band gap of silicon is approximately 1.12 eV at room temperature. The simulation assumes charge carriers in thermal equilibrium with the crystal lattice, which is justified, as the thermalization of the hot carriers is usually very fast compared to the pulse duration.

The uncertainties in the thickness of the diode and the SPICE model are considered to be small as the measured pulses for low densities of electrons agree with the simulations.

[2] One a charge carrier is 'released' from the plasma, the plasma is no longer charge neutral and attracts the 'released' carrier again. The carrier is only emitted when the attraction is overcome by diffusion or the plasma 'releases' an other charge carrier of opposite sign.

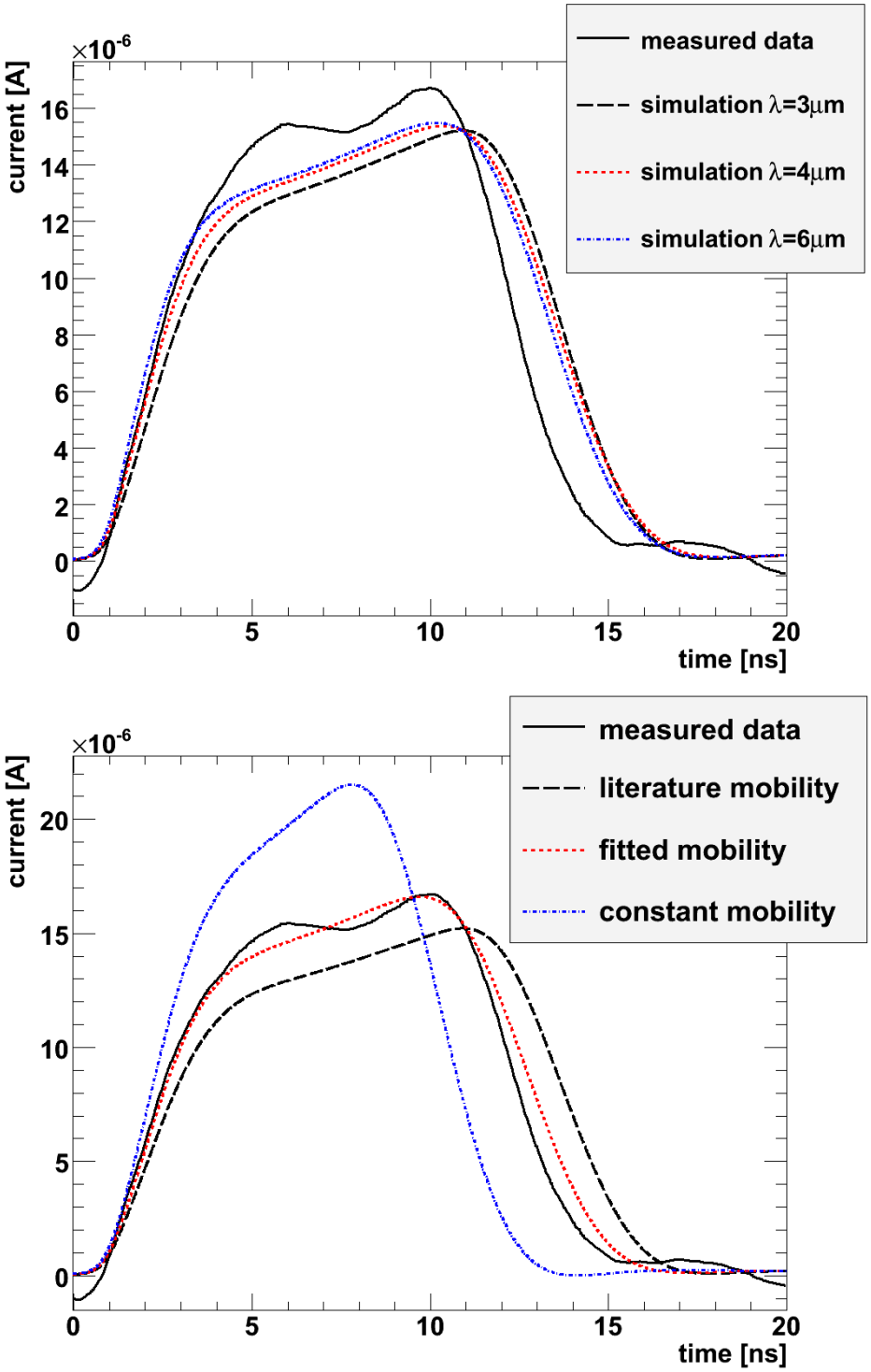

Figure 10.6: Effects of different parameters on the simulated current pulses for 1×10^6 electron hole pairs at 200 V applied voltage. The upper graph shows the influence of the initial distribution. The lower graph shows the influence of different mobility models. Although lower density clouds dissolve faster, the effects of different initial distributions are small compared to the effects of the constant mobility model.

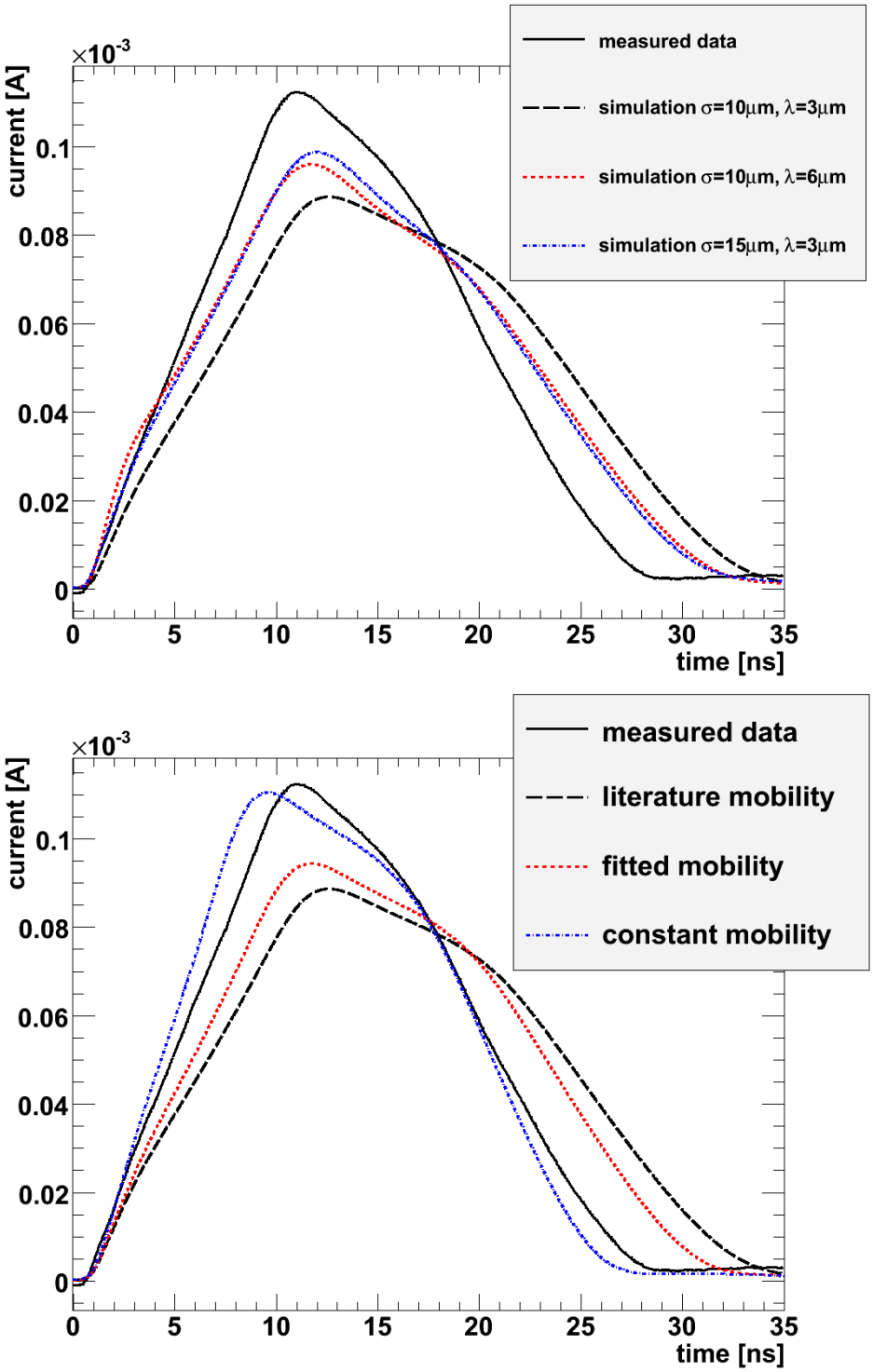

Figure 10.7: Effects of different parameters on the simulated current pulses for 11×10^6 electron hole pairs at 200 V applied voltage. The upper graph shows the influence of the initial distribution. The lower graph shows the influence of different mobility models. Although lower density clouds dissolve faster, the effects of different initial distributions are small compared to the effects of the constant mobility model.

10.5 Summary

A simulation program was developed to study the transport of charge carriers with high densities in silicon sensors with emphasis on the development of detectors for experiments at the European XFEL.

The numerical stability and applicability for sensor design purposes has been demonstrated.

As a result of the comparison of measurements and simulations it is concluded that the observed plasma effects cannot be described by using the mobility and diffusion models in literature. It is shown that, except for the highest intensity, two different sets of mobility models can be used to simulate pulses which are either systematically longer or systematically shorter than the measurements and thus allow to minimum/maximum pulse duration estimations.

In spite of the discussed discrepancies the simulation program is a valuable tool for the design and optimization of sensors and readout electronics for the European XFEL.

Combining the effects of Fermi-Dirac statistics in the diffusion process, variations in the parameters of the initial distribution of charge carriers and an optimized mobility model it seems possible to provide simulations which reproduce the measurements reasonably well for all intensities with a single, unified set of parameters.

11 Transient measurements on strip sensors

In this chapter transient measurements on strip sensors are presented. Three different strip sensors were available for investigation. Their layout is described below.

The equivalent circuit applicable when investigating strip sensors is different from the one used when investigating pad sensors. The capacitance to the backplane of the read out strip is much lower than the capacitance of a pad diode[1]. Thus distortions of the current pulse are much smaller.

Measurements in this chapter were done with lasers focused to a Gaussian spot with a σ_{laser} of ≈ 3 µm, unless mentioned otherwise.

11.1 Investigated sensors

Three microstrip sensors have been investigated. The overall size (substrate) of each microstrip sensor was 10 mm x 10 mm, the strip length about 8 mm. All sensors are p-in-n sensors (structured p+ implant (front) in n-type silicon (bulk), continuous n+ implant (rear)). Each sensor is surrounded by a guard ring[2] to collect currents generated at the surface and at the cut edges.

[1] Additionally coupling capacitances to other strips are introduced.

[2] Every sensor features a different arrangement of structures to decrease the potential in a well defined way. The arrangements usually consist of multiple guard and potential rings of which only the innermost ring is connected to ground potential. The entire arrangement is called 'guard ring' in this work for the sake of simplicity.

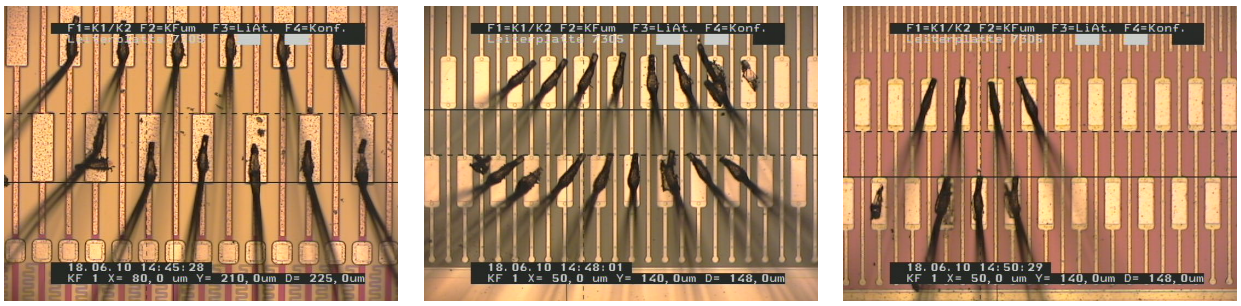

Figure 11.1: Microscope pictures of the investigated strip sensors. From left to right: CG1017, PSI02, PSI1mm. For every second strip of the PSI1mm sample the bond pad is locate at the other end of the strip metalization.

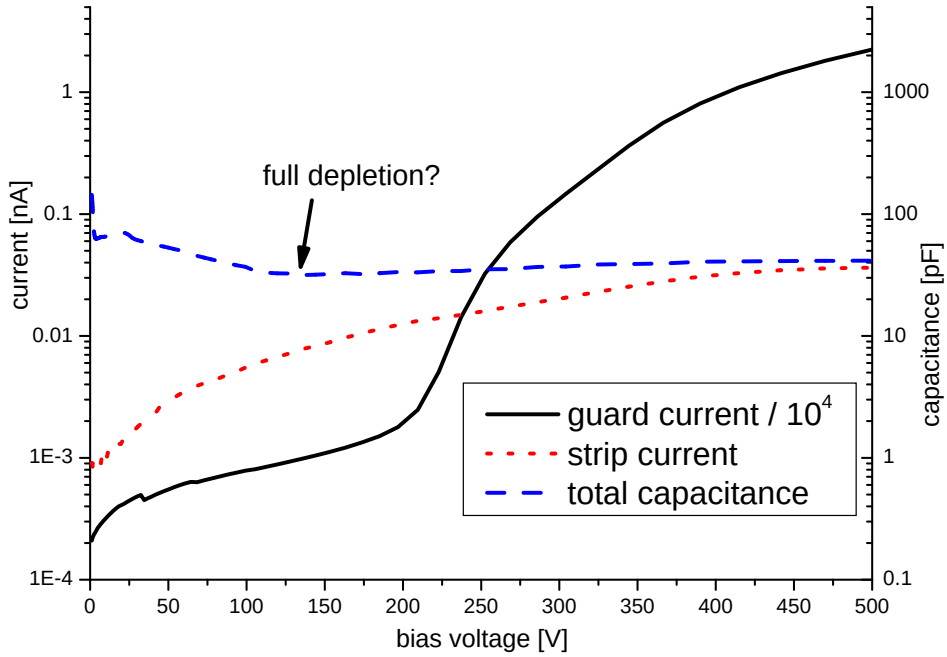

Figure 11.2: C/V and I/V measurements of the sensor labeled PSI1mm. No well defined saturation of either current or capacitance is observed. For the I/V measurement one individual strip and the guard ring are connected. For the C/V measurement only the guard ring is connected. Connecting the guard ring measures all strips in parallel, as they are punch trough biased from the guard ring. The total capacitance decreases until reaching a minimum at 130 V and slowly increases again. From transient measurements the depletion voltage is estimated to be between 150 V - 200 V.

The investigated sensors are labeled CG1017, PSI02 and PSI1mm. The sensors differ in thickness and pitch. A summary of the sensors and their properties is found in Table A.1 in the appendix.

The first sensor (CG1017) has a thickness of 280 µm and a pitch of 80 µm. The sensor features a grid like metalization on the rear side, allowing light injection. The crystal orientation is <100>. Like the pad diode CG1215, the sensor was processed by CiS [60] on material provided by Siltronic [61]. The effective doping, determined from a diode test structure on the wafer is $8x10^{11}$ cm^{-3}. The depletion voltage is 63 V. The strips of this sensor are AC coupled, thus the sensor features a bias ring to which each individual strip implantation is connected via an implanted 1 MΩ resistor.

The second sensor (PSI02) has a thickness of 450 µm and a pitch of 50 µm. The metalization on the rear side of the sensor was partly etched away in order to allow light injection. The crystal orientation is <111>. The sensor was processed by Hamamatsu [78]. The depletion voltage for this sensor is 155V. The strips of this sensor are DC coupled, thus there is no bias ring on this sensor.

The last sensor (PSI1mm) has a thickness of 1000 µm and a pitch of 25 µm. The

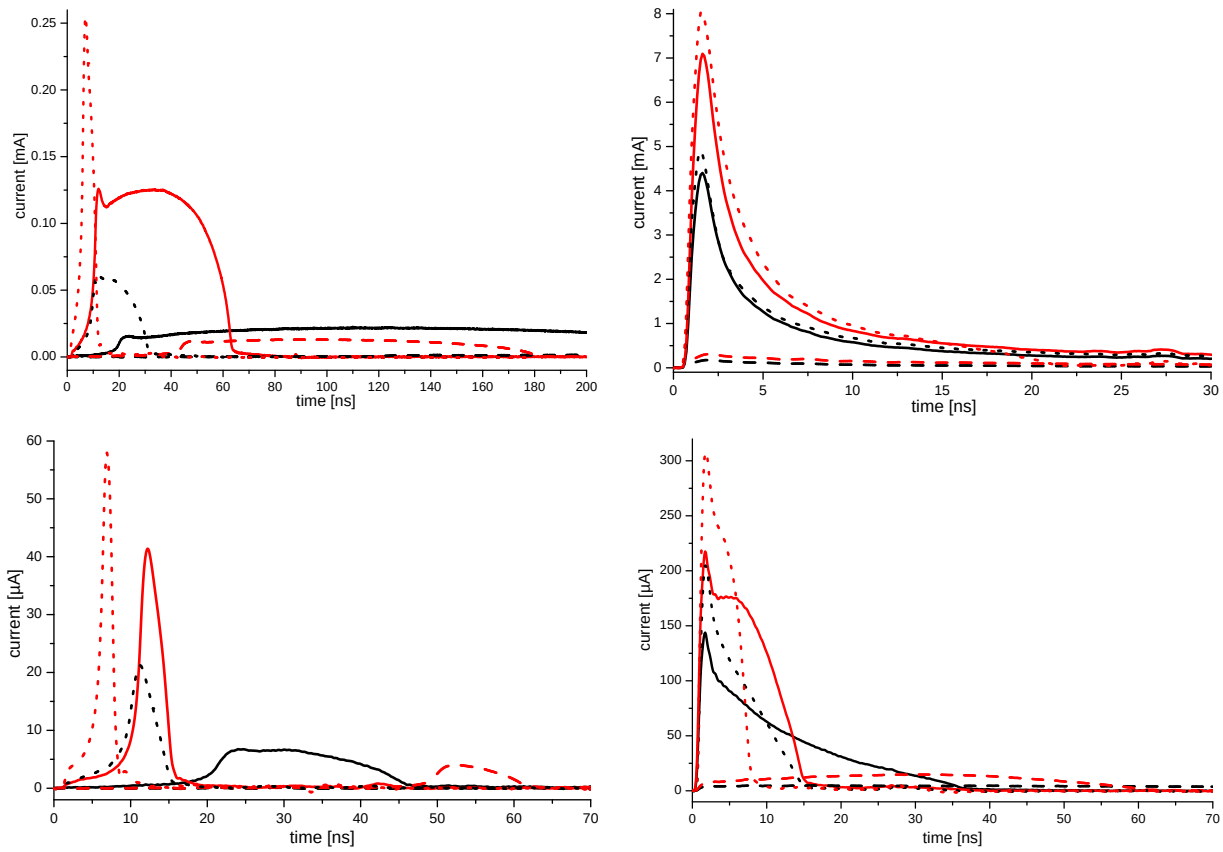

Figure 11.3: Transients obtained with focused light of 660 nm (left column) and 1015 nm wavelength (right column) for high (upper row) and low intensity (lower row) at different voltages (200 V, black, 500 V, red). The 280 µm sensor is shown with dotted lines, the 450 µm sensor with solid lines and the 1000 µm sensor with dashed lines. Charge carriers were created opposite to the readout strip.

metalization on the rear side of the sensor was partly etched away in order to allow light injection. The sensor was processed by Sintef [79]. The depletion voltage of this sensor could not be clearly determined from the C/V and I/V measurements, as shown in Figure 11.2, but was estimated from the transient measurements to be between 150 V and 200 V. This sensor is DC coupled as well.

For all strips the readout electronics was on ground potential. To ensure proper working conditions five strips on both sides of the readout strips were also connected to ground potential. The bias voltage was applied to the rear side.

Intensity	sensor	$N_{e,h}$ [10^6]	λ [nm]	equiv. γ's
high	CG1017	8.55	660	3×10^4 1 keV
medium	CG1017	2.15	660	7740 1 keV
low	CG1017	0.85	660	3060 1 keV
very low	CG1017	0.21	660	756 1 keV
high	CG1017	270	1015	8.1×10^4 12 keV
medium	CG1017	28.5	1015	8550 12 keV
low	CG1017	8.1	1015	2430 12 keV
very low	CG1017	1.6	1015	480 12 keV
high	PSI02	90	660	3.45×10^5 1 keV
medium	PSI02	12	660	4.32×10^4 1 keV
low	PSI02	1.4	660	5040 1 keV
very low	PSI02	0.13	660	468 1 keV
high	PSI02	540	1015	1.62×10^5 12 keV
medium	PSI02	47	1015	1.41×10^4 12 keV
low	PSI02	15	1015	4500 12 keV
very low	PSI02	2.9	1015	870 12 keV
high	PSI1mm	120	660	4.32×10^5 1 keV
medium	PSI1mm	12	660	4.32×10^4 1 keV
low	PSI1mm	1.5	660	5400 1 keV
very low	PSI1mm	0.14	660	504 1 keV
high	PSI1mm	1000	1015	3×10^5 12 keV
medium	PSI1mm	75	1015	2.25×10^4 12 keV
low	PSI1mm	20	1015	6000 12 keV
very low	PSI1mm	4.2	1015	1260 12 keV
high	PSI02	75	660	2.7×10^5 1 keV
medium	PSI02	9.0	660	3.24×10^4 1 keV
low	PSI02	0.8	660	2880 1 keV
very low	PSI02	0.1	660	870 1 keV
high	PSI02	365	1015	1.1×10^5 12 keV
medium	PSI02	38	1015	1.14×10^4 12 keV
low	PSI02	13	1015	3900 12 keV
very low	PSI02	2.5	1015	750 12 keV

Table 11.1: Table of the investigated intensities for each sensor. The procedure to determine the number of created electron hole pairs is presented in detail in Chapter 12. $N_{e,h}$ denotes the number of created electron hole pairs, λ the wavelength of the laser light. The number of equivalent photons has been calculated by dividing the number of created electron hole pairs by 278 (for 660 nm light) or 3333 (for 1015 nm light). Values below the double horizontal line were obtained for front side illumination.

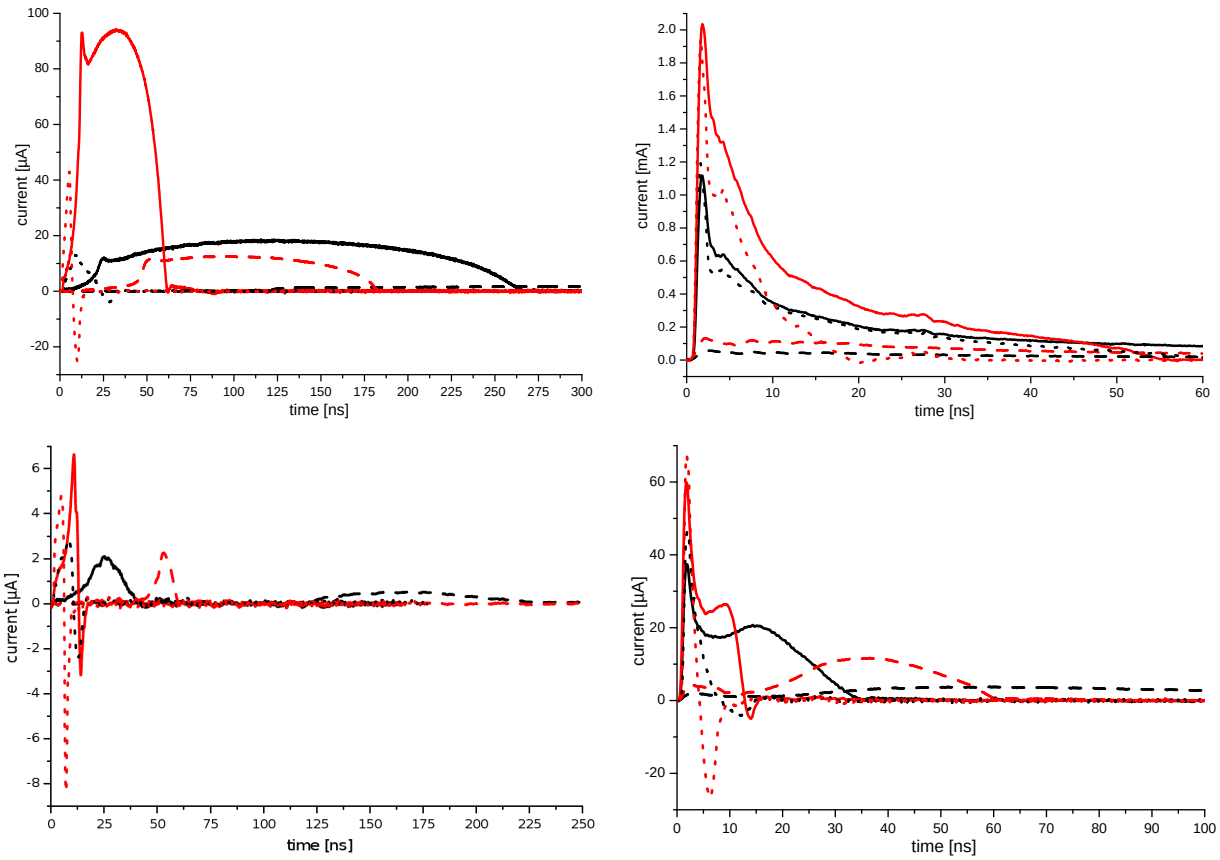

Figure 11.4: Transients obtained with focused light of 660 nm (left column) and 1015 nm wavelength (right column) for high (upper row) and low intensity (lower row) at different voltages (200 V, black, 500 V, red). The 280 µm sensor is shown with dotted lines, the 450 µm sensor with solid lines and the 1000 µm sensor with dashed lines. Charge carriers were created opposite to the neighbor strip for the 280 µm sensor and the 450 µm sensor and opposite to the second neighbor strip for the 1000 µm sensor.

11.2 Transients for rear side illumination

Transients as function of voltage and position have been recorded for selected intensities with two different wavelengths for all three sensors. The corresponding number of created electron hole pairs are listed in Table 11.1. Examples of transients obtained when the point of injection was centered opposite to the read out strip are shown in Figure 11.3.

As expected, at the same applied voltage the pulse length increases for increased thickness of the sensor. Due to the increased thickness the drift distance for the charge carriers is longer and the average electric field (and thus the drift velocity) is lower. This effect is increased in the presence of high charge carrier densities. For the thick sensor and 200 V applied voltage the current pulse is barely visible due to its length.

For high intensities of 1015 nm light (upper right graph in Figure 11.3 and 11.4) the

pulses of CG1017 and PSI02 are very similar. However for 500 V the pulse of CG1017 ends shortly after 20 ns, while the pulse of PSI02 extends to approximately 60 ns. For 200 V applied bias the pulses of both sensors extend beyond 200 ns. The high intensity pulses of PSI1mm do not show a distinctive peak structure and extend for several 100 ns, for low voltages the pulse length significantly exceeds 1 μs.

For the 1000 μm sensor, plasma delays (i.e. the time needed to reach a certain threshold) are clearly visible and decrease for increased voltage. A plasma delay is observed as well for the 450 μm sensor at low voltages.

The current pulses of the 450 μm sensor for high intensity 660 nm light exhibit a local peak around the undisturbed charge collection time, which is caused by the drift of the low density periphery around the dense plasma region.

Transients obtained when the point of injection was centered opposite to the neighbor strip are shown[3] in Figure 11.4. Except for the high intensity of 1015 nm light the transients of the thin sensor show a bipolar structure. The charge clouds in this sensor expand least (for details see Chapter 12) and are created farthest away (pitch of 80 μm). Thus this sensor is expected to show the largest effect of displacement currents[4], which create bipolar pulses. For the high intensity of 1015 nm light (upper right graph of Figure 11.4) the charge cloud has expanded to the read out strip causing a net collection of charge (determined by the integrated transient).

For low intensities the sensor PSI02 shows negative currents between 10-15 ns, the high intensities are completely dominated by the charge sharing between strips due to the expansion of the charge cloud.

For the thick sensor the charge cloud expands to the second neighbor strip, which is shown in Figure 11.4. The large drift distance and the low average electric field result in a significant expansion of the charge cloud for the 1000 μm sensor.

11.3 Transients for rear side illumination with different focusing

Current pulses measured on the central strip and integrated charge for a fixed intensity of 1015 nm light ($\approx 500\times10^6$ electron hole pairs, equivalent to $\approx 1.5\times10^5$ 12 keV photons, in total; the charge collected on the readout strip is a function of voltage and always less than the total charge) have been recorded as function of voltage for different focus sizes for the PSI02 sensor and are shown in Figure 11.5.

The transients were obtained when the center of the point of injection was opposite to the center of the readout strip and varying the distance between optical assembly and sensor (defocusing). For a wider laser spot the created charge is spread over more strips and thus the charge collected on the readout strip decreases. The transients

[3] For the PSI1mm sensor the transients obtained when the laser is centered opposite to the second neighbor strip are shown.

[4] Displacement currents, coupling capacitance and weighting potential with slope change all denote the effects that drifting charges which are not collected on the readout strip induce a bipolar current pulse which integrates to zero.

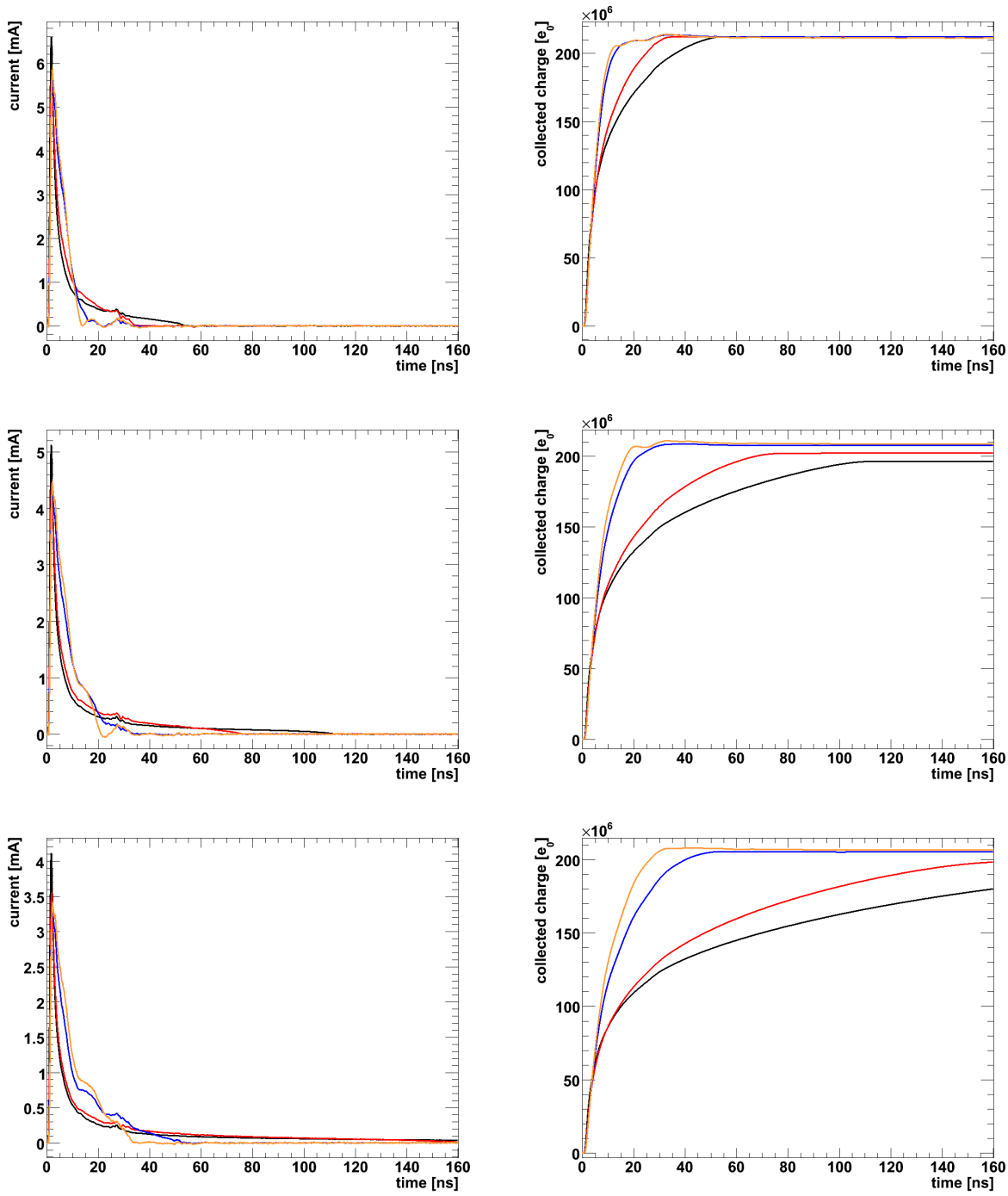

Figure 11.5: Current pulses (left) and integrated charge (right) for light of 1015 nm wavelength and different focusing. The center of the light distribution was aligned opposite to the center of the readout strip. The top row shows 500 V, the center row 300 V and the lower row shows 200 V applied bias. The black lines were obtained for strongest focusing ($\sigma \approx 3$ µm), the red lines for $\sigma \approx 83$ µm, the blue lines for $\sigma \approx 265$ µm and the orange lines for $\sigma \approx 575$ µm. For comparison the red lines were scaled by 1.59, the blue lines by 4.97 and the orange lines by 10.8.

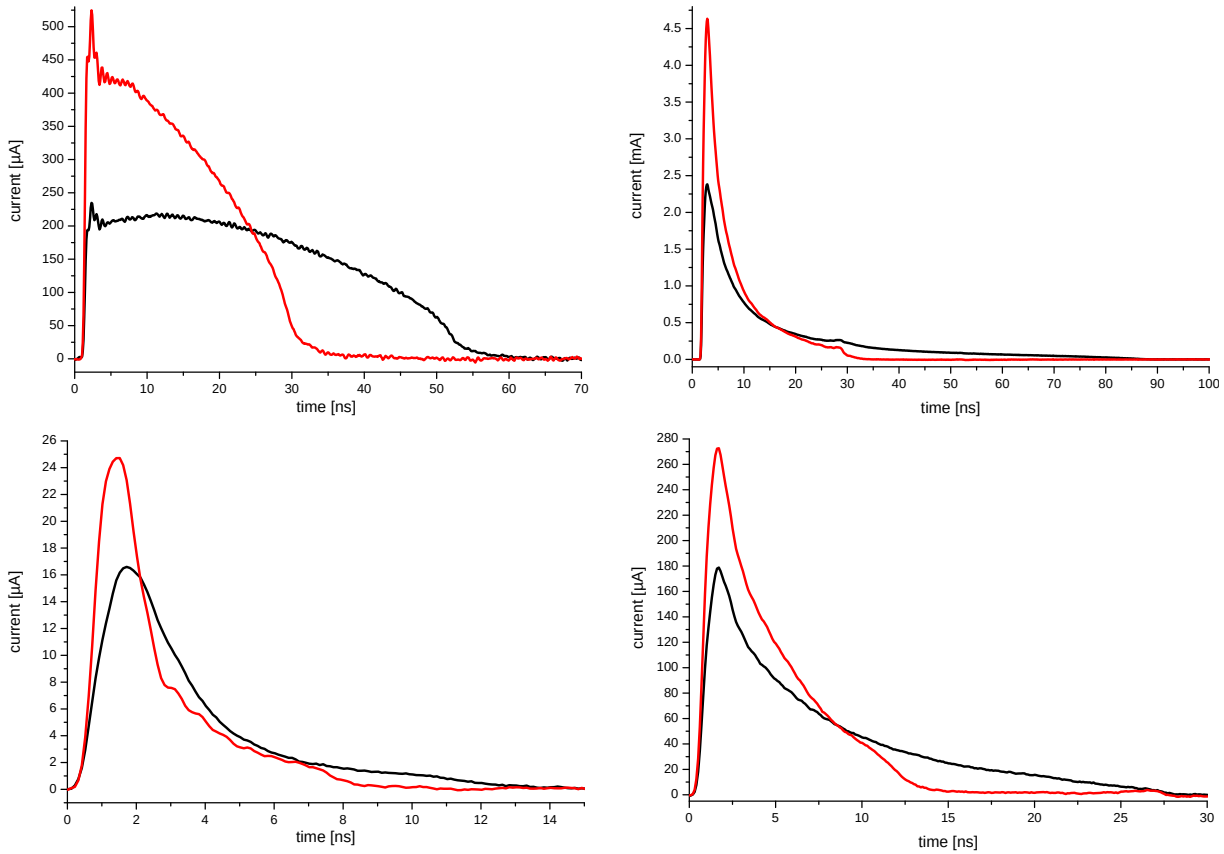

Figure 11.6: Transients obtained after front side illumination with focused light of 660 nm (left) and 1015 nm (right) wavelength for high (top) and low (bottom) intensity at different voltages. Injection was between the readout strip and its neighbor. Black lines were obtained with 200 V applied bias, red lines with 500 V.

shown in Figure 11.5 have been rescaled to equal charge at 500 V applied bias for easier comparison.

Typical spot sizes expected for experiments at the European XFEL have a width with $\sigma \approx 140$ µm, which would be somewhere between the red and the blue line in Figure 11.5. Keeping the bunch spacing of 222 ns in mind, a voltage of at least 300 V applied bias is required in order to avoid pile-up effects.

11.4 Transients for front side illumination

The experimental situation at the European XFEL is such, that photons impinge on the sensor opposite to the readout strip. When the highest charge carrier density shall coincide with the highest electric field the use of n-in-n sensors is mandatory.

For high charge carrier densities the time needed to separate the charge carriers is

dominating the charge collection time. The charge collection in the depleted bulk is fast compared to the separation time. When charges are created at the junction side, the plasma is located where the undisturbed electric field is highest.

Thus high intensity illumination of p-in-n sensors on the front side corresponds to the situation for high intensity illumination on the rear side for n-in-n sensors, where the junction is opposite to the readout side. Thus illumination from the front side can be used to estimate the plasma effects expected for n-in-n devices.

In the case of low charge carrier densities transients obtained for front side illumination are distinctively different from transients in n-in-n devices. While the transients of p-in-n devices are of positive polarity, as holes are collected, n-in-n devices produce transients of negative polarity as electrons are collected. While the pulse duration of both layouts is identical (assuming charge carriers are created along the whole sensor thickness), the pulse shapes differ.

Transients as function of voltage and position for front side illumination have been recorded for selected intensities with two different wavelengths for the PSI02 sensor ($d = 450$ µm).

Transients obtained when the point of injection was between the readout strip and its neighbor are shown in Figure 11.6. These pulses are distinctively different than those shown in Figure 11.3 and 11.4. Charges are created at the high field side and the weighting field decreases along the thickness (drift direction of electrons). As holes are collected quickly (when released from the plasma), the electrons drifting away from the junction induce less and less current with increasing distance to the readout electrode. A corresponding behavior is seen in all transients.

The plasma effects, especially the increase of the charge collection time, are less compared to the effects observed for rear side illumination. The maximum current observed for the high intensity light of 1015 nm (upper right graph of Figure 11.6) is approximately half of the maximum current observed for rear side illumination (upper right graph of Figure 11.3). The factor of two is reasonable, as injection between the strips on the rear side decreases the maximum current by a factor of two as well.

11.5 Relevance for XFEL sensors

In order to estimate the impact of plasma effects for pixel sensors at the European XFEL, the number of created electron hole pairs can be converted into equivalent photons by dividing the number of created electron hole pairs by the number of electron hole pairs created by a photon of 1 keV (278 e,h pairs) for 660 nm light or 12 keV energy (3333 e,h pairs) for 1015 nm light.

Both types of notation are equivalent and are also presented in Table 11.1. When an intensity is given as number of photons in this work the conversion mentioned above was used.

It should be noted, that there is a difference in the number of absorbed and incident 12 keV photons, as the interaction probability of a 12 keV photon within 280 µm, 450 µm and 1000 µm of silicon is roughly 0.73, 0.88 and 0.99, respectively. Additionally energy

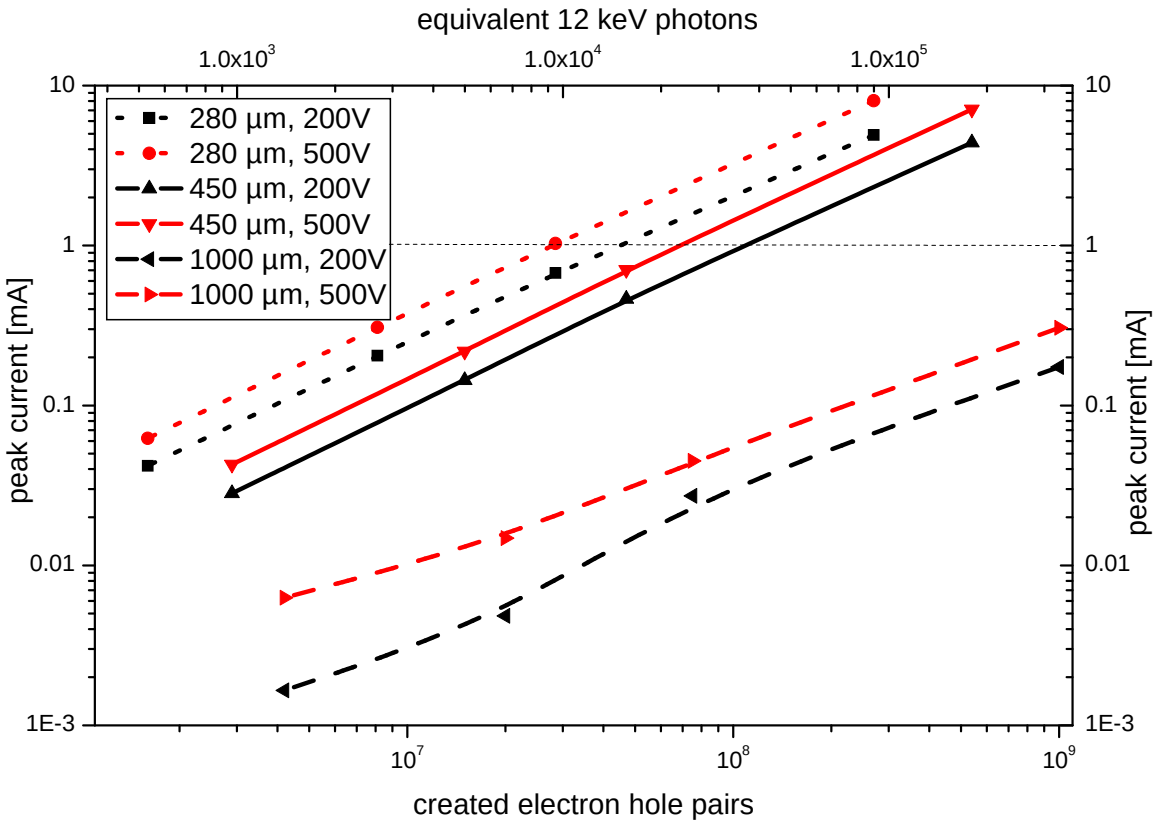

Figure 11.7: Peak current measured as function of the number of created electron hole pairs. For the 280 µm and the 450 µm sensor the current is linearly increasing with increasing density. For the 1000 µm sensor a lower slope is observed. For comparison a line at 1 mA is drawn, as it is a possible current limitation for the AGIPD detector.

might be transported in the silicon lattice, e.g. by fluorescence photons. A detailed description of the possible interactions of photons with silicon is found in Chapter 3.

11.5.1 Peak currents

An investigation of the measured peak currents provides useful information for the design of readout electronics. High current spikes might damage the delicate electronics in the readout circuit and thus require an additional protection measures.

Depending on the actual sensor design, the measured current peaks might not be observed in detectors. The high current could cause a short lived reduction of the bias voltage, if the bias voltage is not stabilized close to the sensor.

As observed for illumination with 660 nm light, plasma effects actually decrease the peak current, as charges are released from the dense plasma region slowly. The current peaks observed for 1015 nm are in the same order as the expected peak currents when

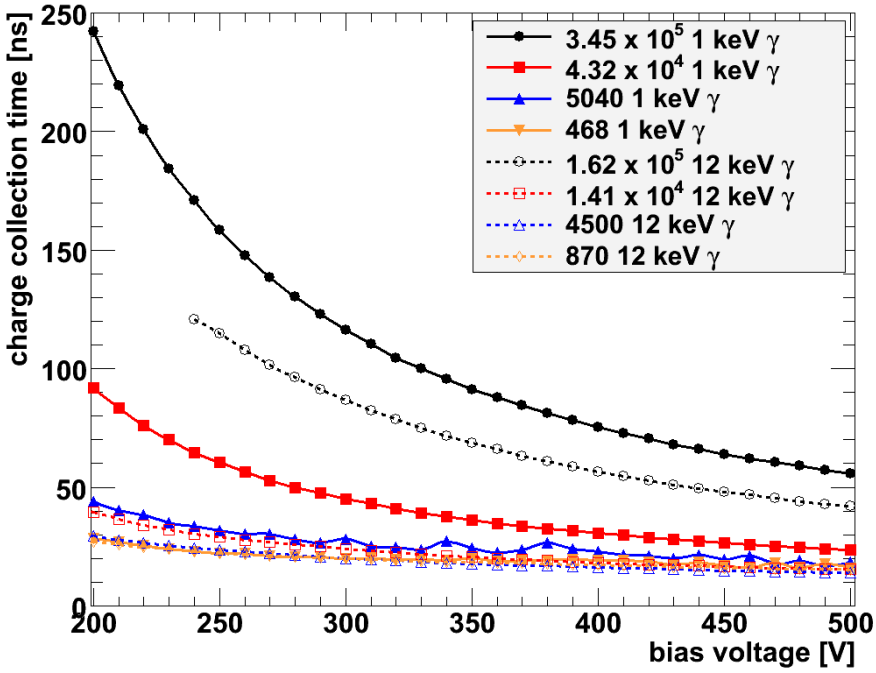

Figure 11.8: Charge collection time of the 450 µm sensor as function of bias for different intensities of 660 nm (1 keV γ) and 1015 nm light (12 keV γ).

plasma effects are neglected.

The peak currents can be estimated in the following way: A deposition of 1×10^5 12 keV photons creates 3.333×10^8 electron hole pairs, corresponding to a charge C of 54 pC ($C = e_0 N_{e,h}$). Assuming a charge collection time t of 20 ns and a rectangular transient, a current I of $I = C/t = 2.7$ mA is expected. When a triangular signal is considered, instead of a rectangular one, the peak current would double to $I_{peak} = 5.4$ mA, which is close to the measured values.

Correspondingly a shorter pulse duration (e.g at increased voltage) results in a larger peak current. Such a behavior is observed in the measurements of sensor CG1017 and PSI02 (shown in Figure 11.7). For the 1000 µm sensor a longer pulse duration is expected due to the longer drift distance an lower average drift velocity. At high intensities plasma effects increase the pulse duration additionally and thus a lower slope of the peak current as function of voltage compared to the other sensors is observed.

11.5.2 Increase of the charge collection time

Charge collection times of the 450 µm sensor as function of applied voltage and charge carrier density are shown in Figure 11.8. The charge collection times is defined as the integration time needed to collect 95% of the total charge. The total charge was determined by integration of the whole transient.

For high densities and low voltages the charge collection time exceeds 222 ns, which is the bunch repetition time of the European XFEL. Thus it is important to carefully match the bias voltage and integration time of the readout electronics to avoid nonlinearities.

The charge collection time obtained with 1015 ns light is less than the charge collection times obtained for 660 nm light for comparable numbers of equivalent photons. This results from the different pulse structure obtained for high intensities (shown in Figure 11.3, upper row). The current pulse obtained for 1015 nm light shows an almost exponential decrease, resulting in a significant amount of time needed to collect the last 5% of charge.

The charge collection time of the 280 μm sensor is less than the charge collection time of the 450 μm sensor. The 1000 μm sensor shows significantly higher charge collection times than the 450 μm sensor, exceeding 1 μs for high intensities and low voltages.

Without plasma effects the charge collection times range from 6 ns to 20 ns (500 V and 100 V, respectively) for the 280 μm sensor and from 12 ns to 30 ns (500 V and 200 V, respectively) for the 450 μm sensor. For low intensities the charge collection time obtained from the measurement is very close to the expected time without plasma effects.

11.5.3 Pile-up effects

Collected charge as function of time for the 450 μm sensor for different applied voltages for high and medium intensities of 1015 nm light are shown in Figure 11.9.

Pile-up effects appear when less than 100% of the charge is collected before a new event occurs. For the European XFEL events can happen in every bunch, thus it is important that all charges are collected within the bunch repitition time of 222 ns.

In order to collect all charges within the bunch repetition time for the highest intensity, at least 300 V should be applied. This results in a charge collection time for medium (and lower) intensities of less than 40 ns.

11.6 Summary

Most of the presented transients have been obtained with very tight focusing ($\sigma \approx 3$ μm). Considering the expected situation at the European XFEL the plasma effects are overestimated. Thus the results presented here should be seen as worst case estimates.

The effect of a relaxed focusing has been investigated for the 450 μm sensor showing that, as expected, plasma effects decrease for reduced densities.

For experiments at the European XFEL spot sizes with $\sigma \approx 140$ μm are expected. It was shown that at these spot sizes plasma effects will be observed.

Transients showing plasma effects were evaluated for all three sensors showing an increase in charge collection time with increased intensity. Using front side illumination the plasma effects expected in n-in-n devices could be estimated, showing that when plasma effects shall be avoided the use of n-in-n devices is favorable.

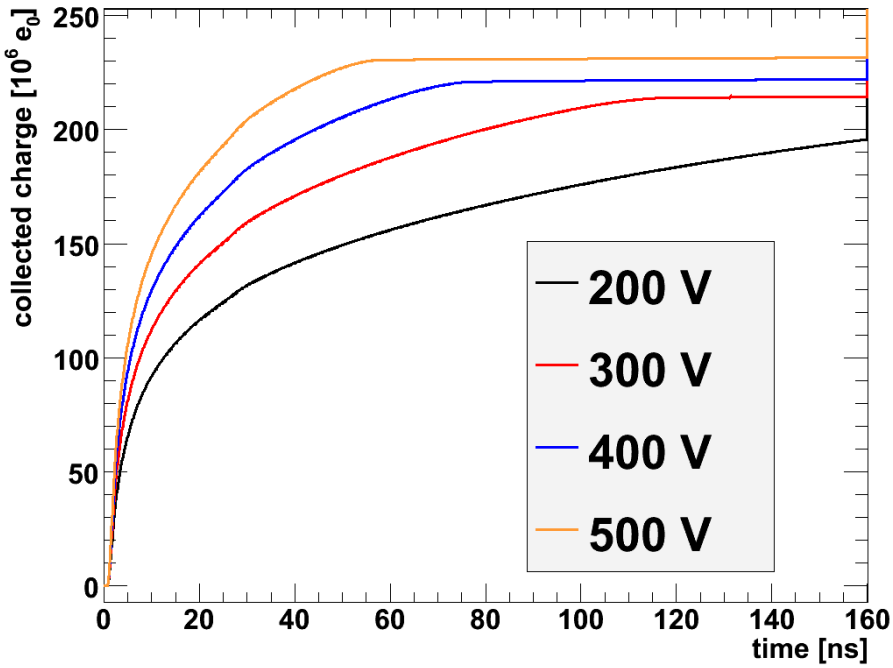

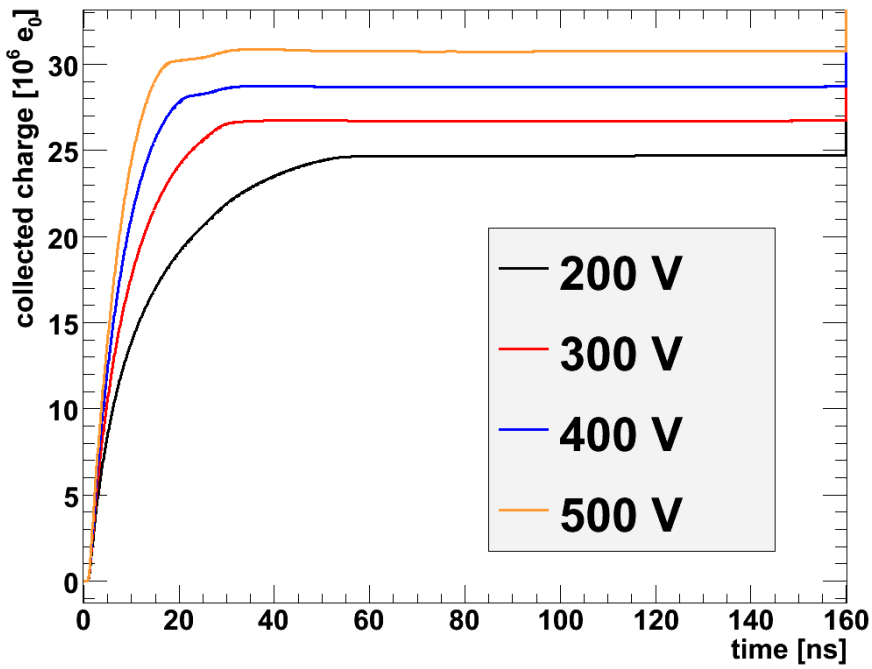

Figure 11.9: Collected charge as function of time for the 450 µm sensor for different applied voltages for high (top graph) and medium (bottom graph) intensities of 1015 nm light. For high intensity and voltages $\geq$ 300 V all charge is within approximately 120 ns. For medium intensity (and all lower intensities) all charge is collected within approximately 30 ns. The total charge collected on the strip is a function of voltage as the size of the charge cloud is a function of voltage.

Peak currents, charge collection times and pile-up effects have been investigated for different intensities and applied voltages with respect to the specifications of the AGIPD for the European XFEL.

A detailed investigation of the impact of the results presented in this chapter on the AGIPD design is presented in Chapter 14.

12 Position sensitive measurements on strip sensors

Measurements of transients obtained from strip sensors have been presented in Chapter 11. Important informations like peak currents and charge collection times have been obtained from the evaluation of transients.

Additional spatial information is available when measurements of structured devices are performed as function of position.

12.1 Measurement procedure

The measurements are performed in the same way and on the same three sensors (CG1017, PSI02, PSI1mm) as explained in Chapter 11. Details of the investigated sensors are found in Table A.1. In order to evaluate the charge collected on the individual strip the recorded transients are integrated. The integration window is selected in such a way, that the entire pulse at 200 V applied voltage is integrated. The integration window is fixed each intensity.

Transients are recorded as function of voltage and position for all sensors and intensities shown in Table 11.1. The step size for the position scan was 2 µm. Due to the integration each transient results in one value for the collected charge.

12.2 Fit procedure to derive the point spread function

The point spread function (PSF) describes the response of an imaging system to a point source or point object. A more general term for the PSF is a systems impulse response.

The collected charge on one strip as function of position (collected charge profile) was used to evaluate the point spread function[1] for a selected intensity and voltage by a fit procedure. The following assumptions were used to evaluate the radial point spread function $PSF(r)$:

The normalized charge cloud distribution (CCD) has radial symmetry and can be approximated by the convolution of a radial function $f(r)$ and a Gaussian distribution:

$$CCD(r) = (f \otimes g)(r) \tag{12.1}$$

$$f(r) = \frac{3}{2\pi r_0^3}\sqrt{r_0^2 - r^2} \quad \text{for } r < r_0, \text{ 0 everywhere else} \tag{12.2}$$

[1] Thus the PSF represents only the charge collected on the readout electrodes (2D), not the distribution of charge carriers inside the sensor (3D).

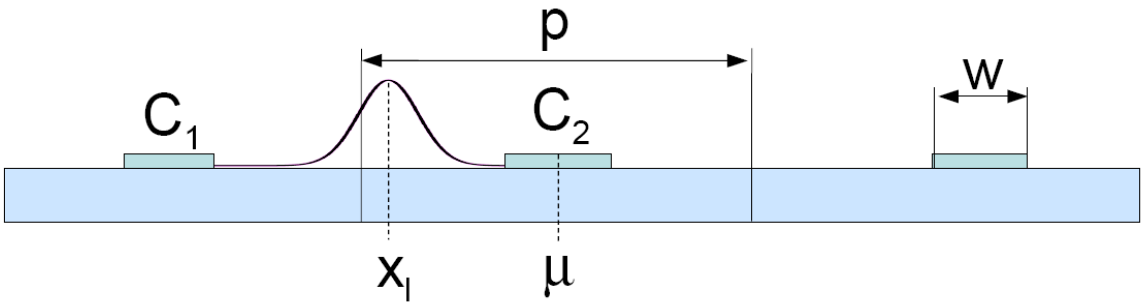

Figure 12.1: Illustration of the charge collection of a charge distribution in a segmented sensor. C_i denotes the charge collected on strip i, μ the center of strip 2, p the strip pitch and x_l the position of illumination. The charge cloud is centered around x_l and the charge collected on strip i is the integral of the charge cloud profile from $\mu - p/2$ to $\mu + p/2$.

$$g(r) = \frac{1}{2\pi\sigma_p^2} exp\left(-\frac{r^2}{2\sigma_p^2}\right) \tag{12.3}$$

When the width of the initial distribution of charge carriers is small compared to the width of the charge cloud distribution the determined distribution corresponds to the point spread function ($CCD(r) = PSF(r)$).

A fit procedure (explained below) is used to determine r_0 and σ_p from the measurements. This parameterization describes the measurements for 660 nm light. To describe the measurements for 1015 nm light an additional reflection term (explained below) is taken into account.

The measurements on strip sensors yield the projection of the charge cloud along the coordinate perpendicular to the strips. Thus we need to obtain the projection (CCP) of the charge cloud distribution, which can also be described by a convolution[2]:

$$CCP(x) = h(x) \otimes k(x) = \int_{-\infty}^{\infty} CCD(r)\, dy \tag{12.4}$$

In order to integrate Equation 12.4 we need to know the antiderivative F with $\mathrm{D}F = f$, D being the differentiation operator and $\mathrm{D}(f \otimes g) = \mathrm{D}f \otimes g = f \otimes \mathrm{D}g$ the derivative rule of the convolution [80]:

$$CCD = \mathrm{D}CCP \tag{12.5}$$
$$f \otimes g = \mathrm{D}(h \otimes k) \tag{12.6}$$
$$f \otimes g = \mathrm{D}h \otimes k \tag{12.7}$$
$$\tag{12.8}$$

Demanding[3] $k = g$, the convolution cancels out and we need to find $f = \mathrm{D}h$, thus

[2] Any function can be described by a convolution. Namely the convolution of itself with the δ-function.

[3] A radial Gaussian distribution can be expressed as the product of a Gaussian distribution in x and y ($g_r(r) = g_x(x)g_y(y)$). Thus the projection of a radial Gaussian distribution is a Gaussian distribution in one dimension.

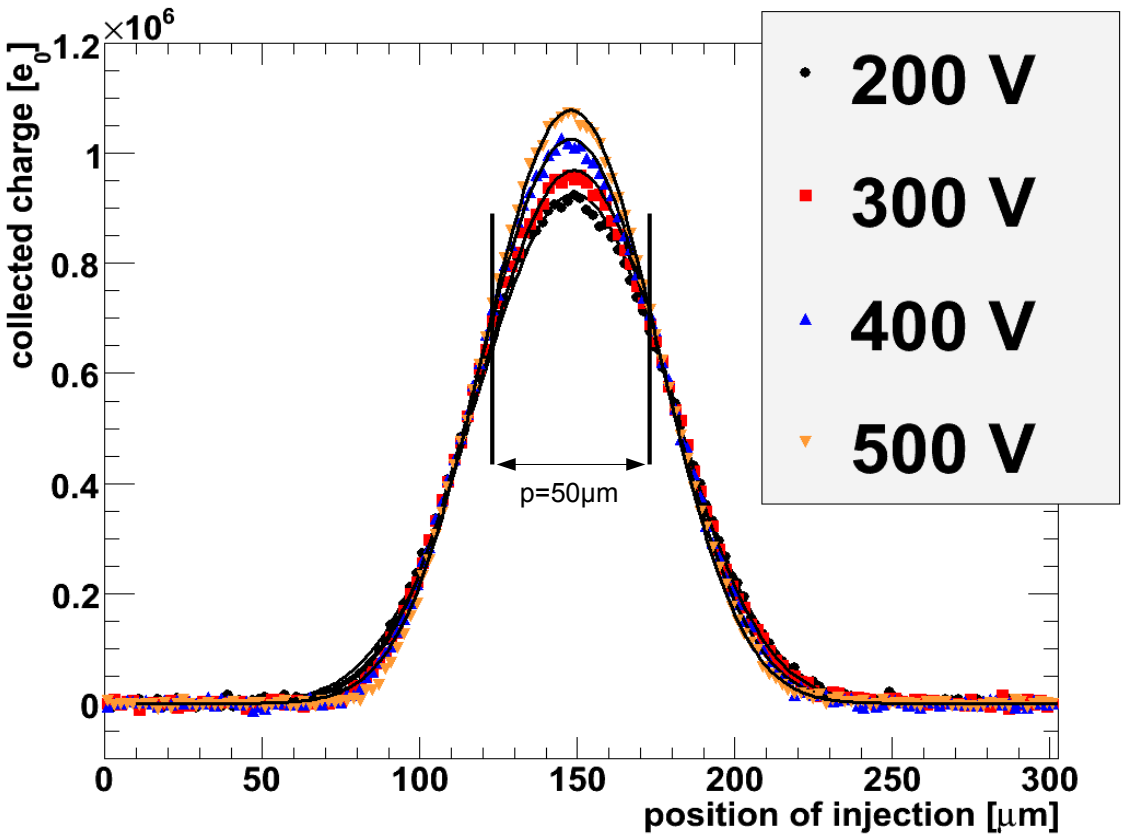

Figure 12.2: Charge collected on one strip of the 450 μm sensor (50 μm pitch) as function of injection location, obtained from position scans with 2 μm step size. Focused 660 nm light (3 μm rms) was used to inject an equivalent of 5040 1 keV photons (1.4×10^6 electron hole pairs). The black lines show the fit to the data.

$h = F$. Consulting [80], F can be expressed as $C_0\,(1-(x^2/r_0^2)) + C_1$, with C_0 and C_1 being constants. Thus the normalized CCP is:

$$CCP(x) = (F \otimes g)(x) \tag{12.9}$$

$$F(x) = \frac{3}{4r_0}\left(1-\frac{x^2}{r_0^2}\right) \quad \text{for } r < r_0,\ 0 \text{ everywhere else} \tag{12.10}$$

$$g(x) = \frac{1}{\sigma_p\sqrt{2\pi}} exp\left(-\frac{x^2}{2\sigma_p^2}\right) \tag{12.11}$$

As schematically shown in Figure 12.1, the charge collected on one strip is determined by the part of the charge cloud profile within $\pm p/2$ of the strip center. Therefore the measurement data $Q(x_l)$ has been fitted using the following equation:

$$Q(x_l) = N_p \int_{\mu-p/2}^{\mu+p/2} CCP(\hat{x}-x_l)d\hat{x} + R(x_l) \tag{12.12}$$

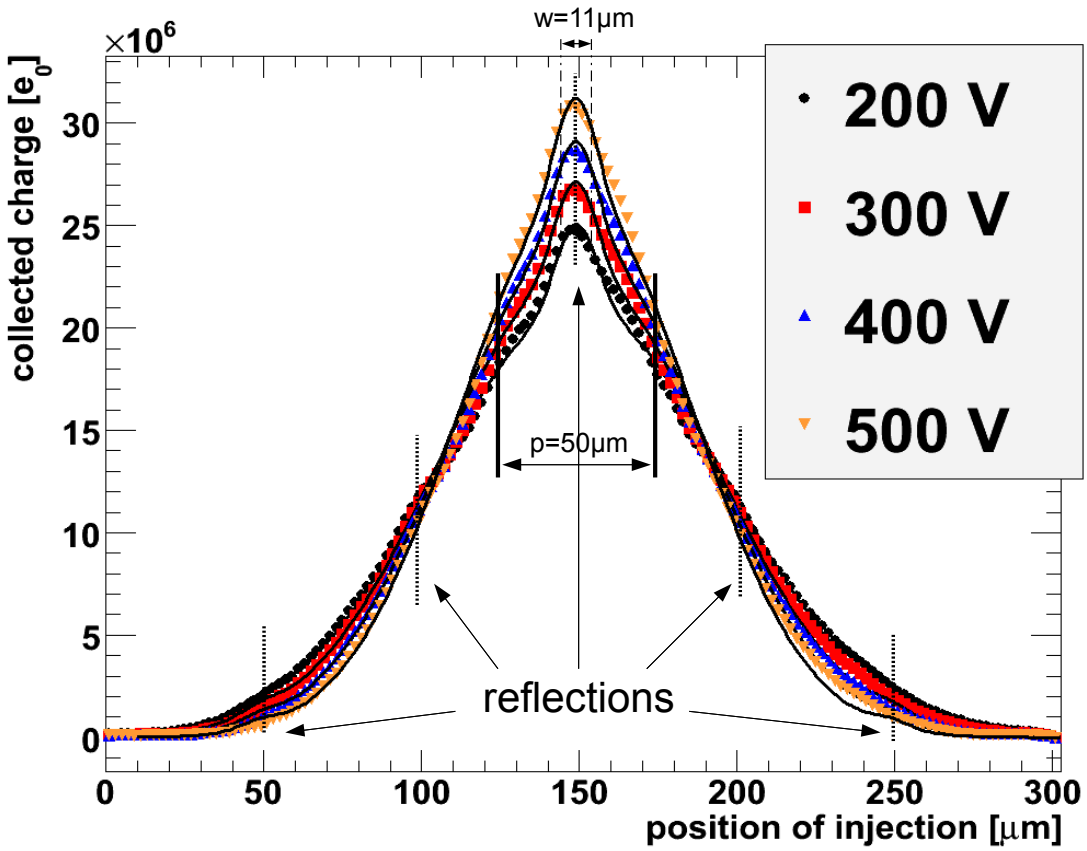

Figure 12.3: Charge collected on one strip of the 450 µm sensor (50 µm pitch) as function of injection location, obtained from position scans with 2 µm step size. Focused 1015 nm light (3 µm rms) was used to inject an equivalent of 1.41x10^4 12 keV photons (47×10^6 electron hole pairs). The black lines show the fit to the data. The increase of collected charge due to light reflection at the strip metalization is visible at the marked locations.

Where Q is the charge collected on the strip, N_p the number of electron hole pairs created by the primary light, μ the strip center position, p the strip pitch, x_l the center of the laser light distribution and $R(x_l)$ a reflection term.

The parameters μ, σ_p, r_0 and N_p are free parameters and determined by the fit.

The reflection term is needed for 1015 nm light in contrast to 660 nm light ($R(x_l) = 0\ \forall x_l$) as not all light is absorbed within the bulk material. Some light reaches the front side and is reflected back into the bulk at the strip metalization. This additional light leads to an apparent "boost" in the collected charge signal (see Figure 12.3).

Additionally the reflected light has its own distribution, which is different from the distribution of the primary light. This distribution was modeled by summing the contributions of read out, first neighbor and second neighbor strips, as a signal boost was also observed when hitting the metalization of the first neighbor and second neighbor

strip. The reflection term was parameterized the following way:

$$R(x) = \sum_{i=-2}^{2} \frac{N_{|i|}}{\sigma_l \sqrt{2\pi}} \int_{x-w/2}^{x+w/2} exp\left(-\frac{(\hat{x} - \mu + ip)^2}{2\sigma_l^2}\right) d\hat{x} \tag{12.13}$$

Where $N_{|i|}$ the number of electron hole pairs created by the reflected light, which is usually two orders of magnitude lower than the number of electron hole pairs created by the primary light and $N_0 \geq N_1 \geq N_2 \geq 0$, w the metal width on top of the p+ implantation and σ_l the standard deviation of the injected laser light. The reflection term (Equation 12.13) is zero for 660 nm light, as no light reaches the strip metalization ($N_0 = N_1 = N_2 = 0$).

The reflection parameters N_0, N_1 and N_2 were determined in the fit procedure as well, increasing the number of free parameters to seven for 1015 nm light.

The collected charge as function of position of injection and corresponding fits are shown in Figure 12.2 and 12.3. The chosen parameterization provides a good description of the data.

12.3 Fit results

The fit has been performed using the Minuit fit program [62] of the ROOT package [63]. Although errors have been determined by Minuit, these errors are not shown here. The errors determined by the fit are too low to be seen as realistic estimates of the uncertainty in the evaluation.

The accuracy of the results is limited by systematic effects. The derivation of the radial charge distribution is empirical, describing the observed results but not the underlying physics. The integration of the transients was assumed to be perfect, i.e the imperfections of the readout circuit were assumed to be negligible. When capacitive coupling of readout channels is not properly taken into account an additional spread of the charge distribution is observed.

The free parameters defining the charge cloud distribution (N_p, r_0 and σ_p) are shown in Figure 12.4 to 12.7. Additionally the lower graphs of Figures 12.4 and 12.5 show the strip center position μ.

Being a free fit parameter, deviations of N_p from the expected constant value indicate problems with the fit procedure.

Below 200 V applied bias the 450 µm sensor shows an increase in N_p for increased voltage. As the integration window of the transients is matched to integrate all of the transient for voltages above 200 V this behavior is expected, as not all charge is integrated. Correspondingly the fit results for r_0 and σ_p are not necessarily correct for voltages below 200 V.

For the very low intensity measurements on the 280 µm sensor a light increase of N_p up to approximately 300 V is observed, which can be explained by the improved signal to noise ratio for higher bias.

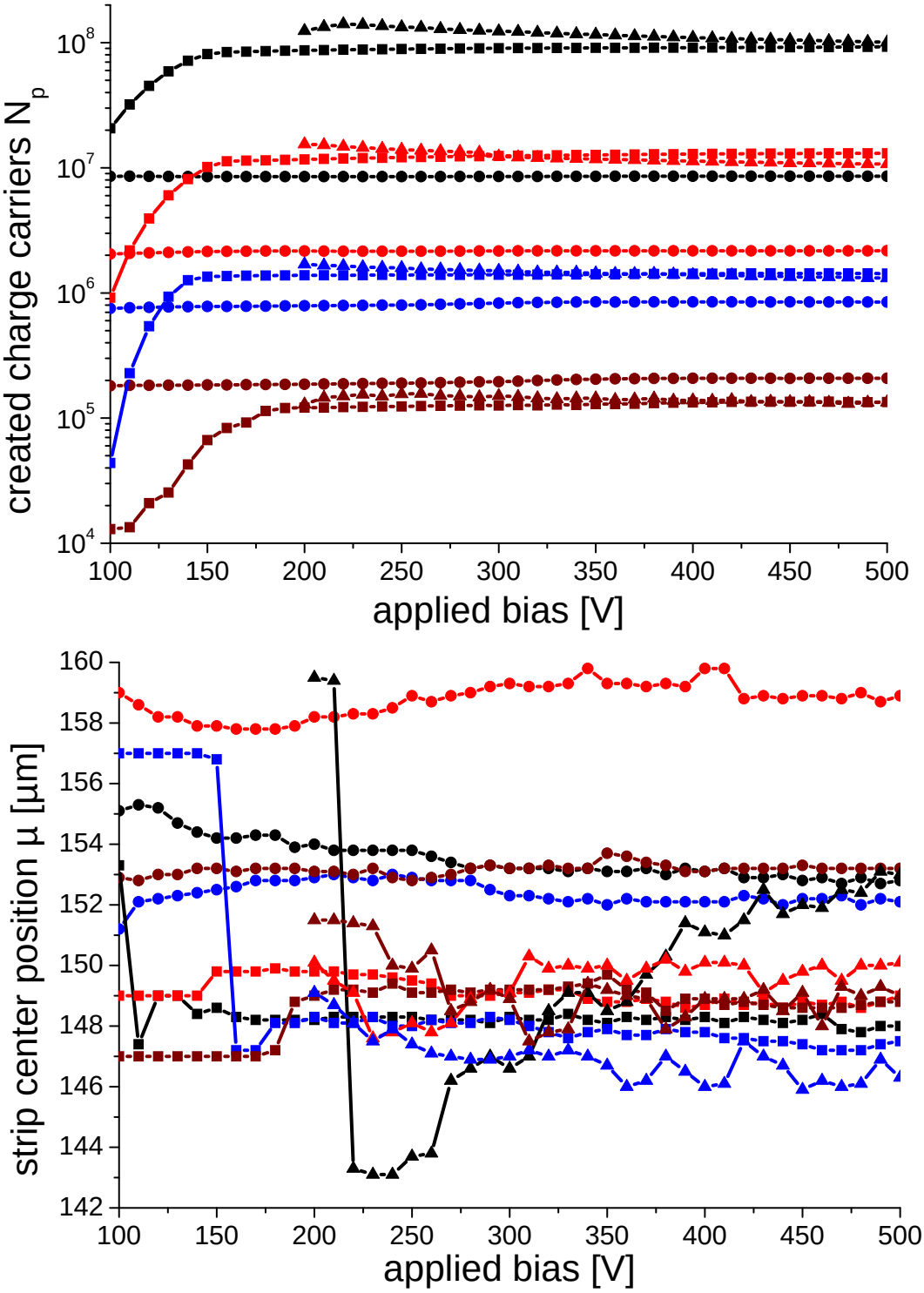

Figure 12.4: Fit results for 660 nm light as function of voltage. The top graph shows N_p, the number of electron hole pairs created by the primary light. The bottom graph shows μ. Black lines show high, red lines medium, blue lines low and dark red lines very low intensity. Circles show the 280 μm sensor, squares the 450 μm sensor and triangles the 1000 μm sensor.

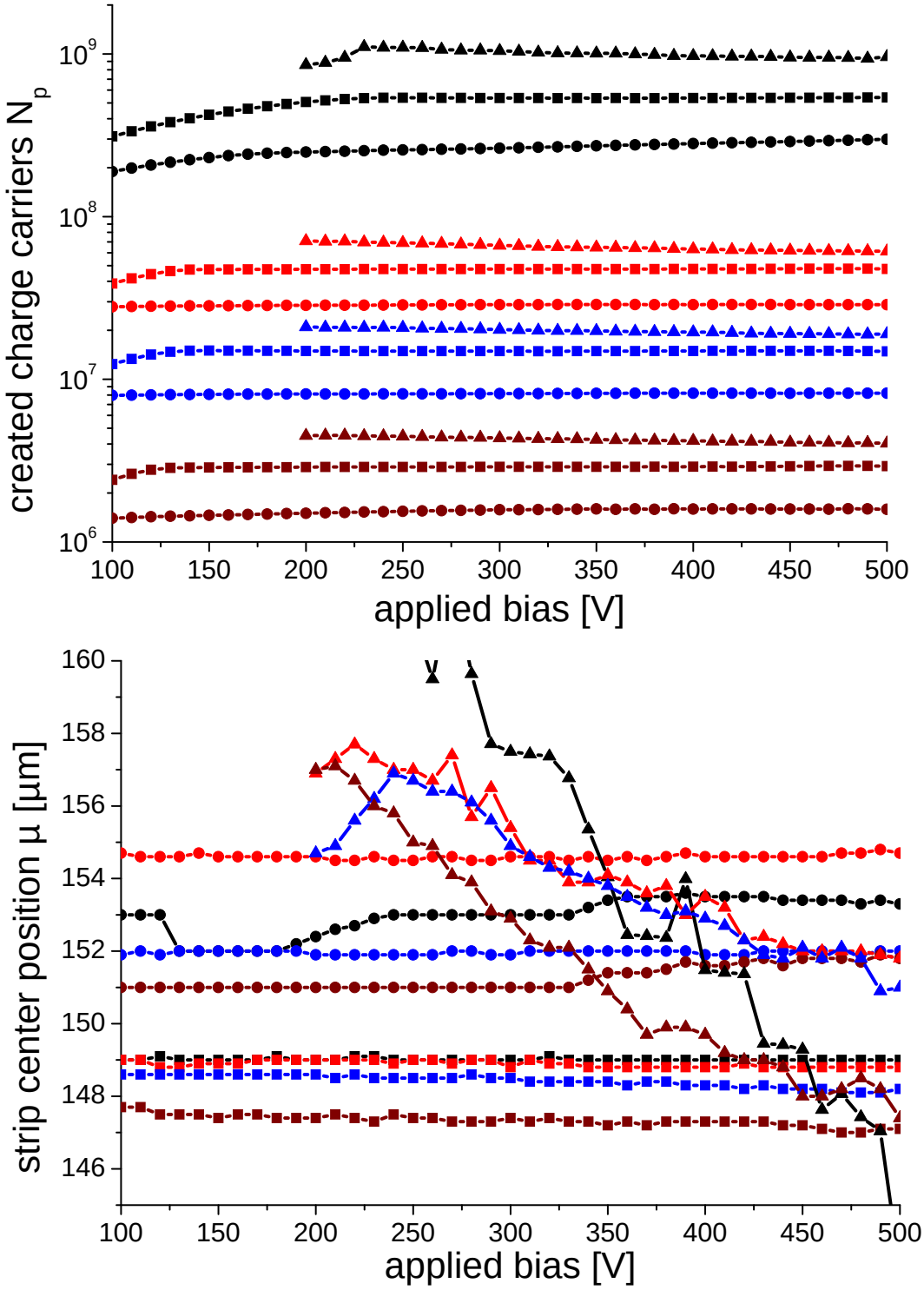

Figure 12.5: Fit results for 1015 nm light as function of voltage. The top graph shows N_p, the number of electron hole pairs created by the primary light. The bottom graph shows μ. Black lines show high, red lines medium, blue lines low and dark red lines very low intensity. Circles show the 280 μm sensor, squares the 450 μm sensor and triangles the 1000 μm sensor.

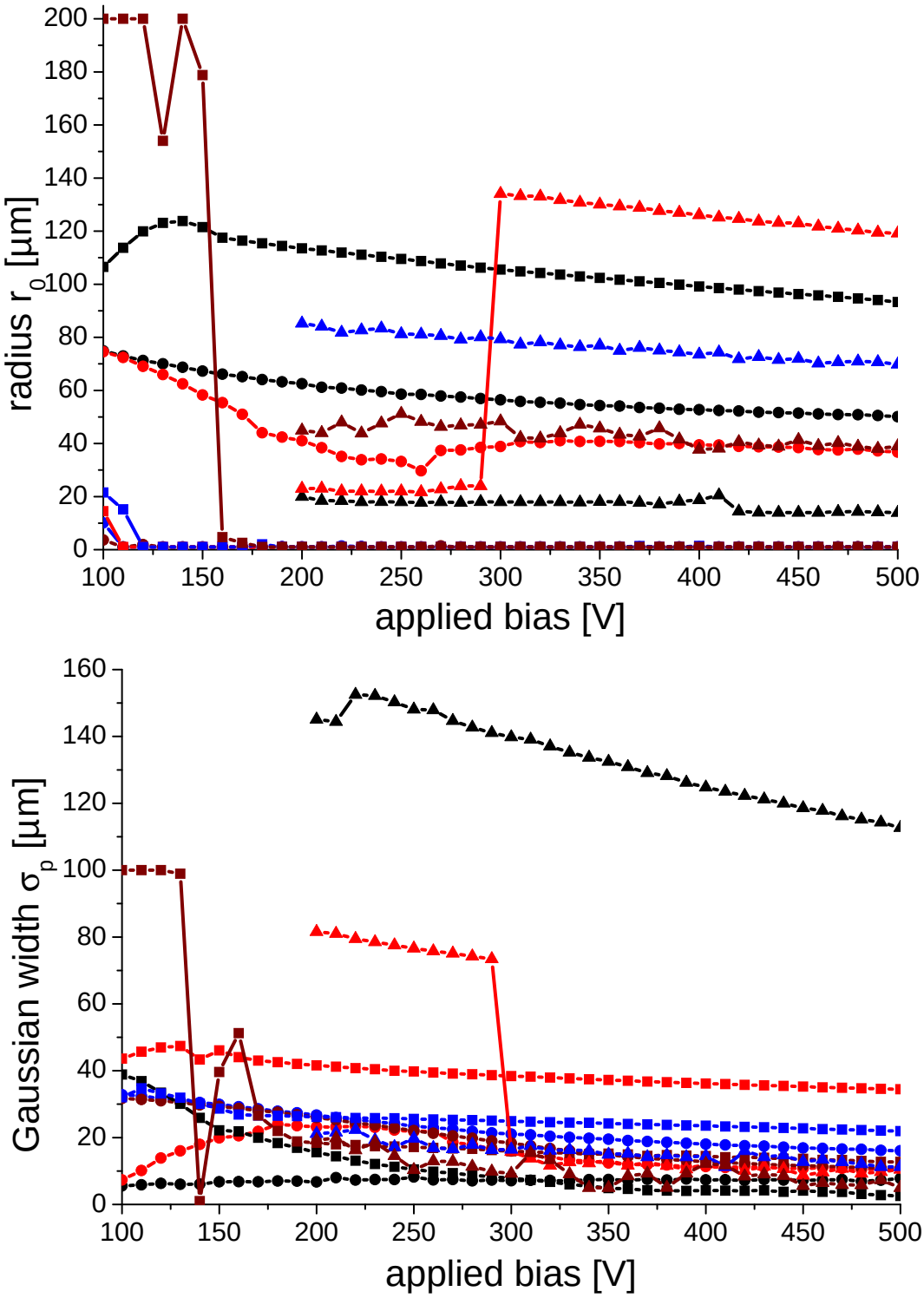

Figure 12.6: Fit results for 660 nm light as function of voltage. The top graph shows r_0, the bottom graph shows σ_p. Black lines show high, red lines medium, blue lines low and dark red lines very low intensity. Circles show the 280 µm sensor, squares the 450 µm sensor and triangles the 1000 µm sensor.

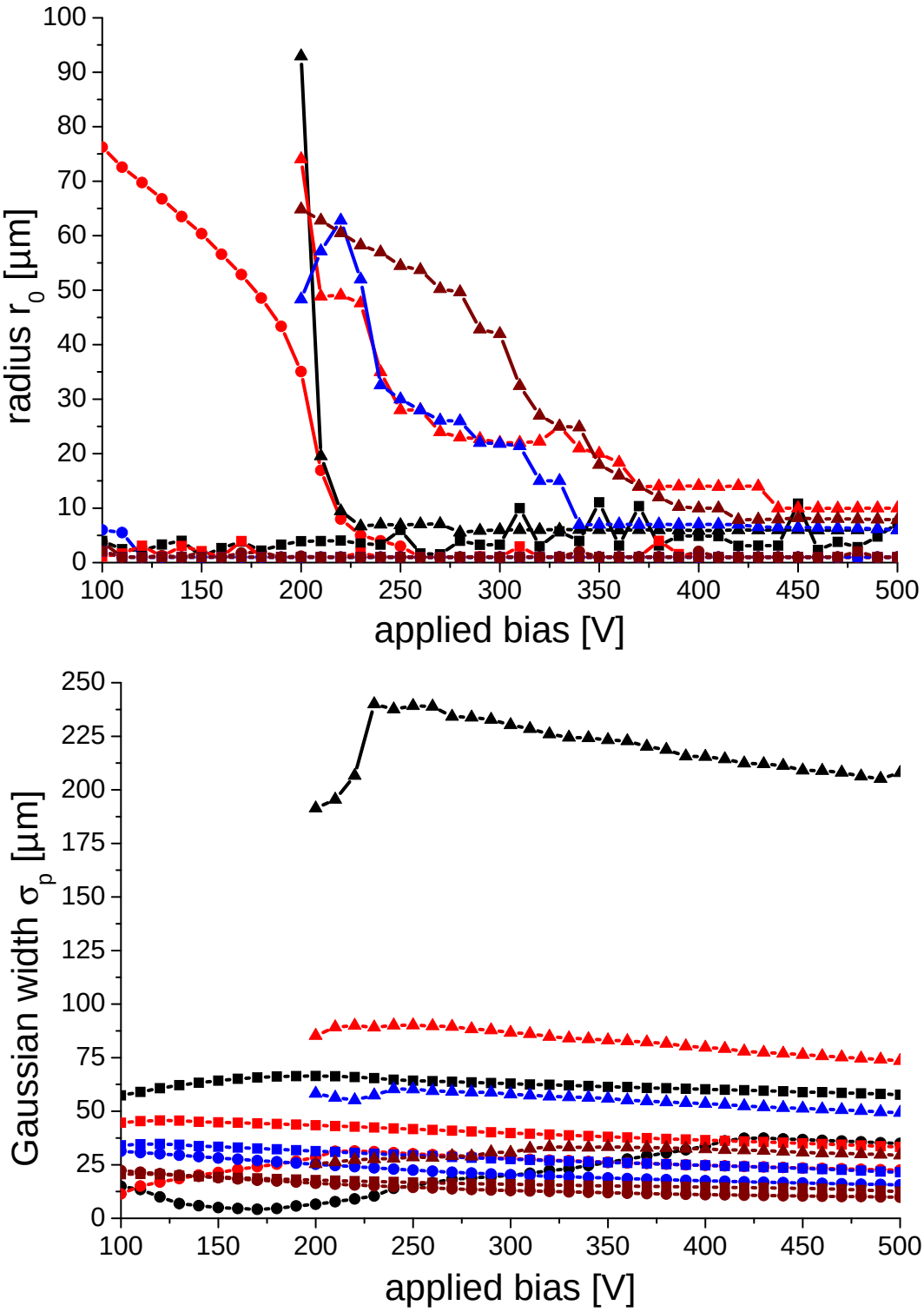

Figure 12.7: Fit results for 1015 nm light as function of voltage. The top graph shows r_0, the bottom graph shows σ_p. Black lines show high, red lines medium, blue lines low and dark red lines very low intensity. Circles show the 280 µm sensor, squares the 450 µm sensor and triangles the 1000 µm sensor.

For the high intensity of 1015 nm light on the 280 µm sensor N_p increases as function of voltage. Inspection of the charge cloud profile shows, that the distribution is not well described for this intensity.

For the 1000 µm sensor all intensities of both wavelengths show as systematic decrease of N_p as function of voltage for voltages above approximately 250 V. Inspection of the charge cloud profile shows a small asymmetry around μ which cannot be described using the fit procedure introduced above. The lower graphs of Figures 12.4 and 12.5 show a dependence of μ on the applied voltage for the 1000 µm sensor (especially for 1015 nm light), which is not observed for the other sensors. This indicates a lateral drift of the charge cloud and thus confirms the known inhomogeneity of the bulk doping of this sensor [81]. Thus results for the lateral spread obtained for the 1000 µm sensor should be seen as approximations.

The parameters of N_p quoted in Table 11.1 are the plateau values of the fit, or, in absence of plateau regions, the average values of N_p for voltages above 250 V.

Fit results for r_0 and σ_p as function of voltage are shown for 660 nm light in Figure 12.6 and for 1015 nm light in 12.7. All values decrease as function of voltage as plasma effects are observed to decrease with increased voltage. There is one exception observed for the 1000 µm sensor at medium intensity of 660 nm light: At 300 V there is an increase in r_0 of approximately 120 µm and a corresponding decrease in σ_p of approximately 60 µm, showing the correlation of both parameters.

For low values of r_0 ($r_0 \ll \sigma_p$), the charge cloud profile can be described by Gaussian distribution. For the 1000 µm sensor the observed spread is very large, especially for high intensities. Thus only a part of the charge cloud distribution is sampled by the measurement and the errors in the determination of r_0 and σ_p increase.

12.4 Point spread function

When the spread of the initial distribution of charge carriers is small compared to the spread of the charge cloud, the PSF can be approximated by the CCD, which is determined by the parameters derived from the CCP.

The measured profiles of the collected charge have been fitted with Equation 12.12 and radius r_0 and sigma σ_p of the point spread function were extracted as function of bias voltage and laser intensity (shown in Figures 12.4 to 12.7).

Using the extracted parameters, the point spread function (PSF), described by the Equations 12.1 to 12.3, was reconstructed. The reconstructed PSFs of all sensors for different applied bias voltages for 660 nm and 1015 nm light of different intensities are shown in Figure 12.8. The width of the PSFs increases with increased intensity and increased sensor thickness. Although the width of the PSF decreases for increased bias voltage, the effect is small compared to the effects of the intensity and the sensor thickness.

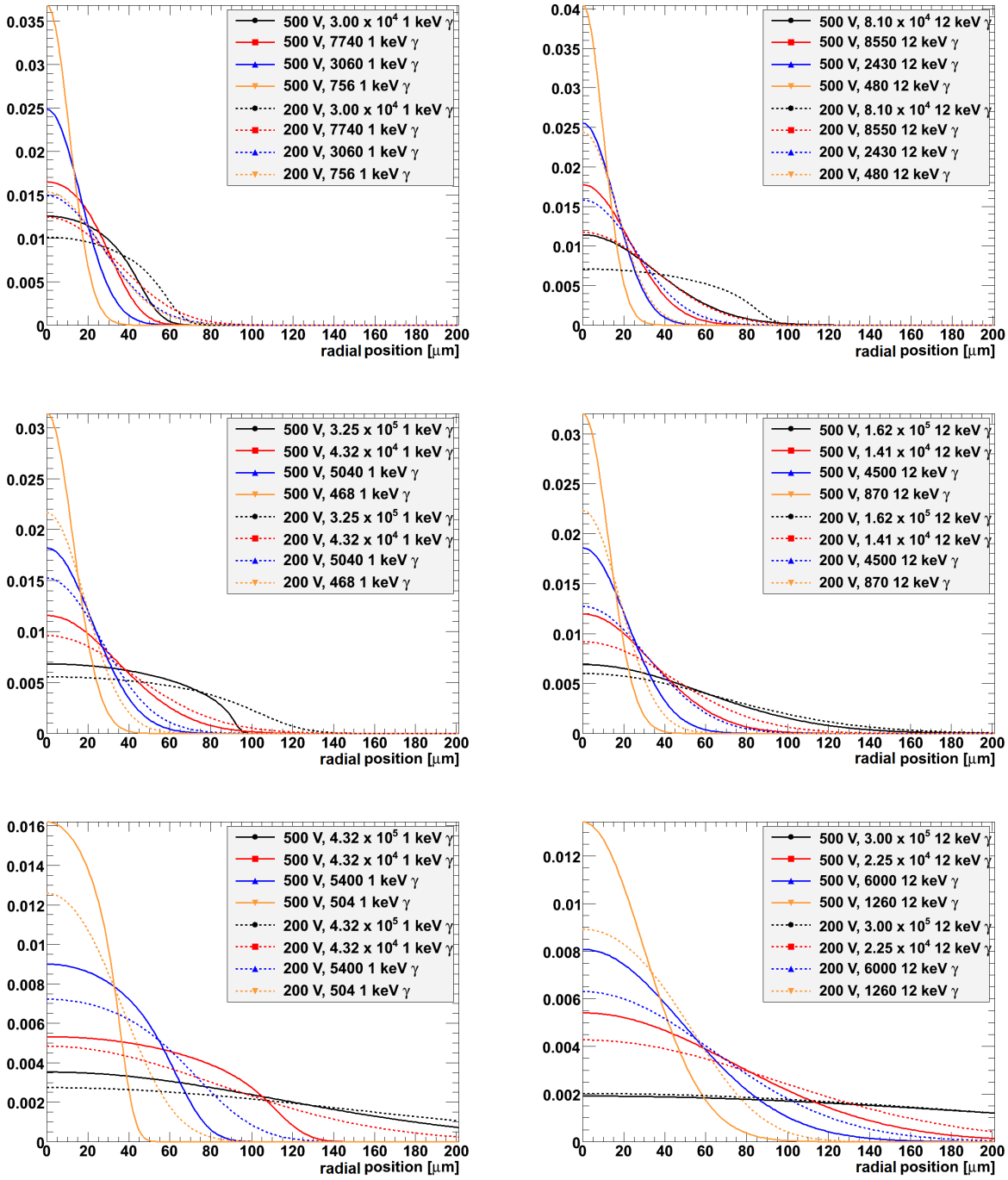

Figure 12.8: Fit results for the radial point spread function for 500 V (solid lines) and 200 V (dashed lines) bias voltage for 660 nm light (left column) and 1015 nm light (right column) and different intensities. The top row shows the 280 μm sensor, the middle row shows the 450 μm sensor and the bottom row shows the 1000 μm sensor. The sigma of the injected light is ≈ 3 μm.

12.5 Modulation transfer function

From determined point spread functions (PSF) modulation transfer functions (MTF) have been calculated for 200 V and 500 V bias voltage. MTFs of all sensors are shown in Figure 12.9 for injection of 660 nm and 1015 nm light.

The MTF is defined as the magnitude of the Fourier transform of the PSF.

A point of special interest on the MTF is the point where the MTF drops to 0.5, which corresponds to the maximal spatial frequency for which images can be resolved. However, distinguishing image points with different intensities requires a higher contrast (value of the MTF).

Additionally the value at the Nyquist frequency (inverse of twice the AGIPD pixel size, 2.5 mm^{-1}) is of importance. It shows the contrast for an alternating black and white line pattern with a line spacing corresponding to the pixel size. At the Nyquist frequency all MTFs are above 0.8 for the 280 µm sensor, above 0.6 for the 450 µm sensor and significantly below 0.5 for the 1000 µm sensor. It is observed that the contrast at a fixed spatial frequency decreases strongly when the charge carrier density is increased and decreases significantly for thicker sensors. An increase of contrast is observed when the applied voltage is increased, however this effect is small compared to the effect of the increased charge carrier density and the increased thickness.

12.6 Summary

The radial distribution of the collected charge has been determined. As the width of the distribution of initial charge carriers was very small, the charge distribution is identical to the Point Spread Function (PSF). From integrated transients (charge) as function of position the PSF for different wavelengths, intensities and voltages has been determined.

For given operating conditions the PSF is a sensor property, which can be used to estimate the imaging performance of a sensor.

The width of the PSFs was observed to increase strongly with increased intensity and increased sensor thickness. A small decrease was observed when the bias voltage was increased.

Using the PSFs the modulation transfer function has been calculated. At the Nyquist frequency the contrast was above 0.8 for the 280 µm sensor, above 0.6 for the 450 µm sensor and significantly below 0.5 for the 1000 µm sensor. Similar to the observations for the PSFs, it was observed that the contrast at a fixed spatial frequency decreases strongly when the charge carrier density is increased and decreases significantly for thicker sensors. An increase of contrast is observed when the applied voltage is increased, however this effect is small compared to the effect of the increased charge carrier density and the increased thickness.

It should be noted that the modulation transfer function is only an indicator for the imaging performance, as it is usually determined from a line pattern and not individual bright spots.

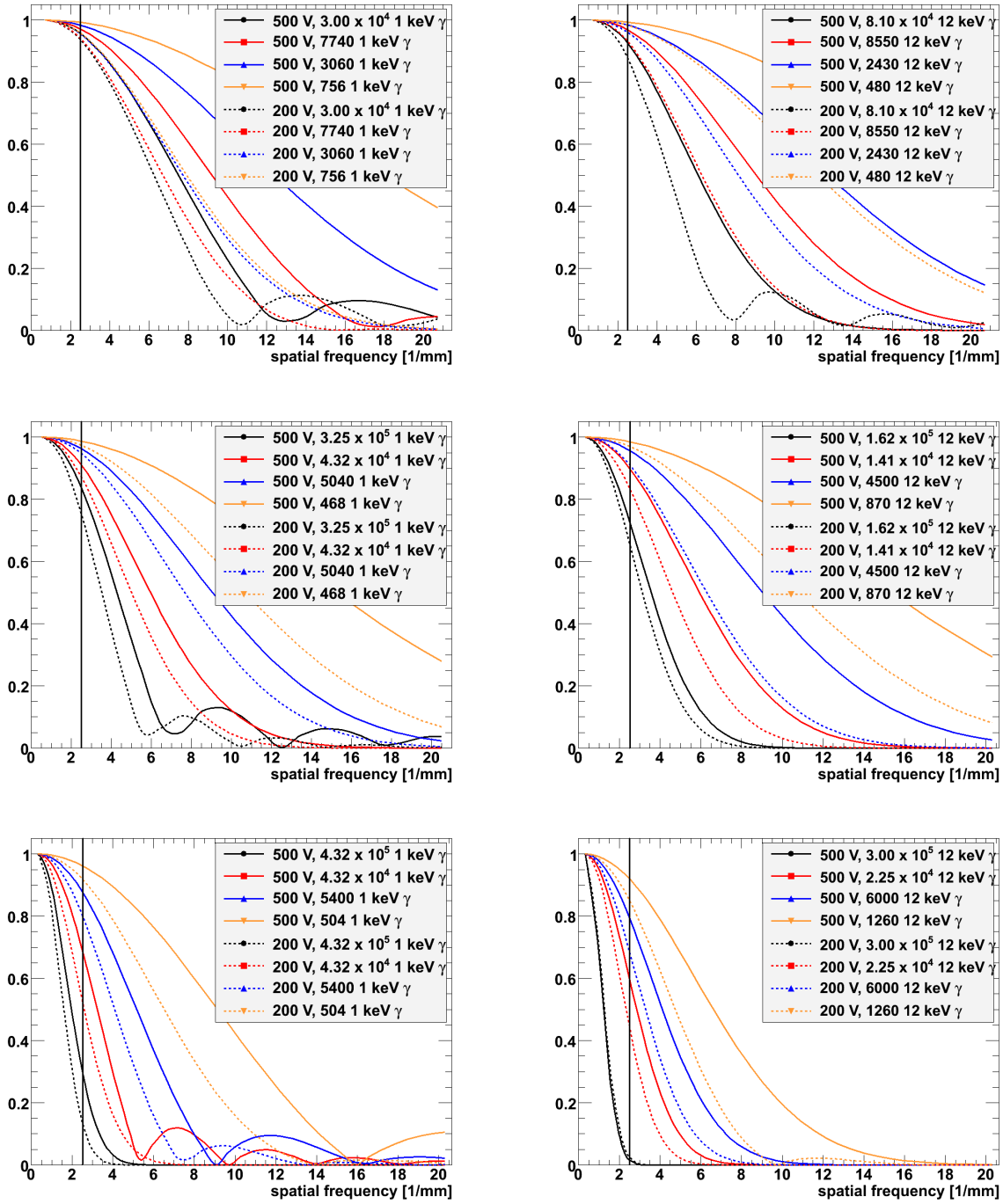

Figure 12.9: Modulation transfer functions for 500 V (solid lines) and 200 V (dashed lines) bias voltage for 660 nm light (left column) and 1015 nm light (right column) and different intensities. The top row shows the 280 µm sensor, the middle row shows the 450 µm sensor and the bottom row shows the 1000 µm sensor. The sigma of the injected light is ≈ 3 µm. The vertical line at 2.5 mm^{-1} spatial frequency indicates the Nyquist frequency (inverse of twice the AGIPD pixel size) for comparison.

13 Comparison of simulations and measurements on strip sensors

Similar to the procedure described in Chapter 10, simulations on plasma effects observed in strip sensors have been performed by WIAS [73].

In this chapter simulation results are compared to measured current pulses of strip sensors showing plasma distortions after rear side illumination with focused 660 nm laser light of high intensity.

13.1 Investigated sensor

The investigated sensor is labeled CG1017 and has a thickness of 280 µm and a pitch of 80 µm (see Table A.1 for details). It is the same used in Chapter 11. In order to investigate plasma effects the 660 nm laser beam was focused to a spot with a Gaussian profile with $\sigma = 3$ µm.

13.2 Simulations

The experimental situation is less well defined than the one in Chapter 10. The charge carrier transport still happens almost exclusively in the low doped silicon bulk material and the dominating influences in the simulation are the initial cloud size and the field induced mobility reduction.

But the experimental determination of the actual spot size and the total number of electron hole pairs created is more difficult than in the diode case. The number of created electron hole pairs is determined by fitting, as explained in Chapter 12. Additionally the spot size was not determined directly, but the laser was moved to the point where the pulse distortions were maximal. At this point the laser spot is smallest and was assumed to have $\sigma = 3$ µm, as this is the smallest spot size determined from the diode measurements.

Compared to diodes the capacitance of individual strips is very low. The diode capacitance is the dominating element in the equivalent circuit of the setup (see Figure 7.8), a reduced capacitance also reduces the distortions. The strip geometry introduces coupling capacitances which dominate the pulse shape. The coupling capacitance can also be understood as the effect of displacement currents or a slope change in the weighting potential. The transfer function of the setup used for strip measurements has been checked and was found to introduce distortions on the sub-ns level, which were considered insignificant.

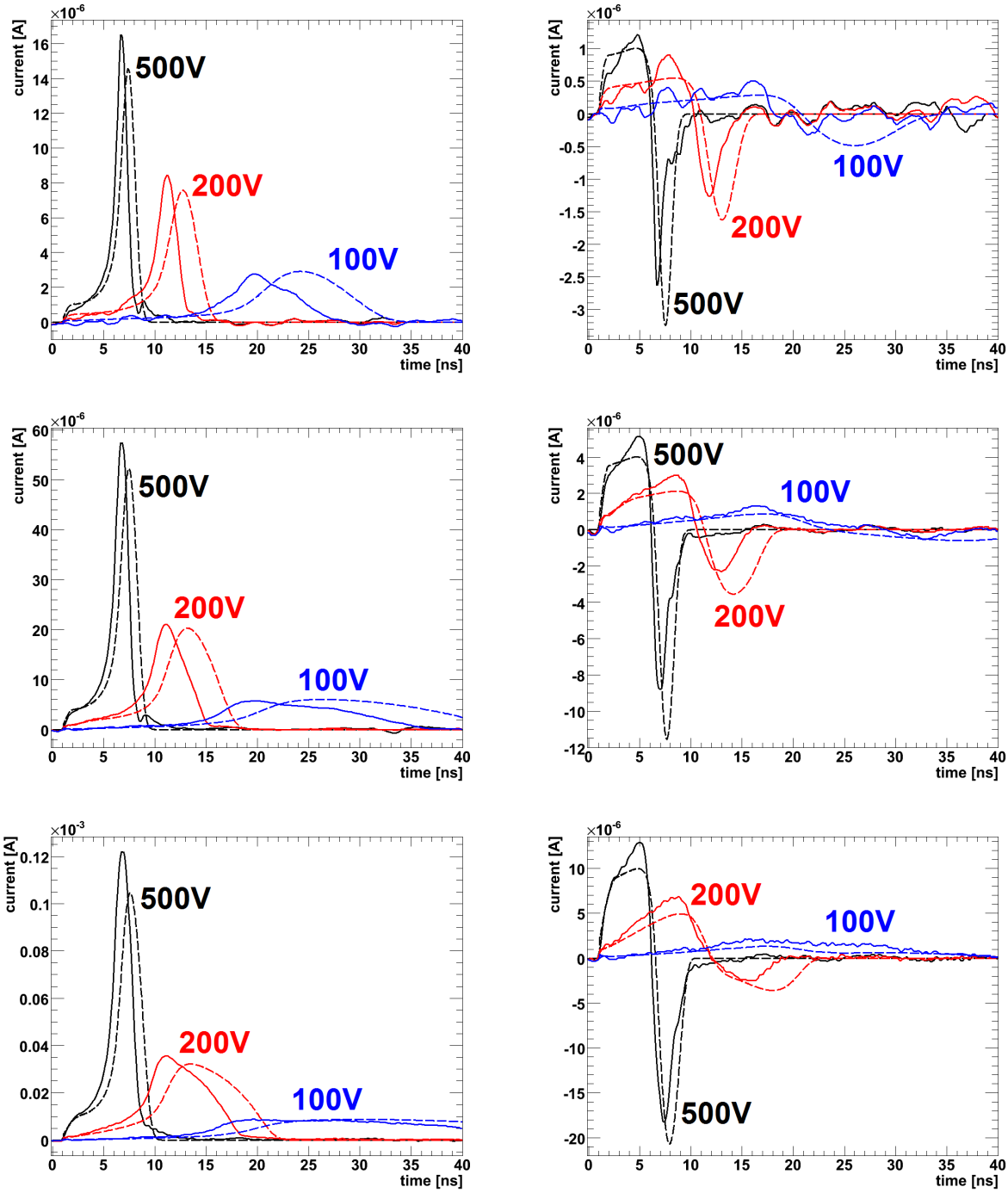

Figure 13.1: Comparison of simulations and measurements for 0.21×10^6, 0.85×10^6 and 2.15×10^6 electron hole pairs (top to bottom). The readout strip is shown in the left column, the neighbor strip in the right column. Measurements are shown with solid lines, simulations with dashed lines.

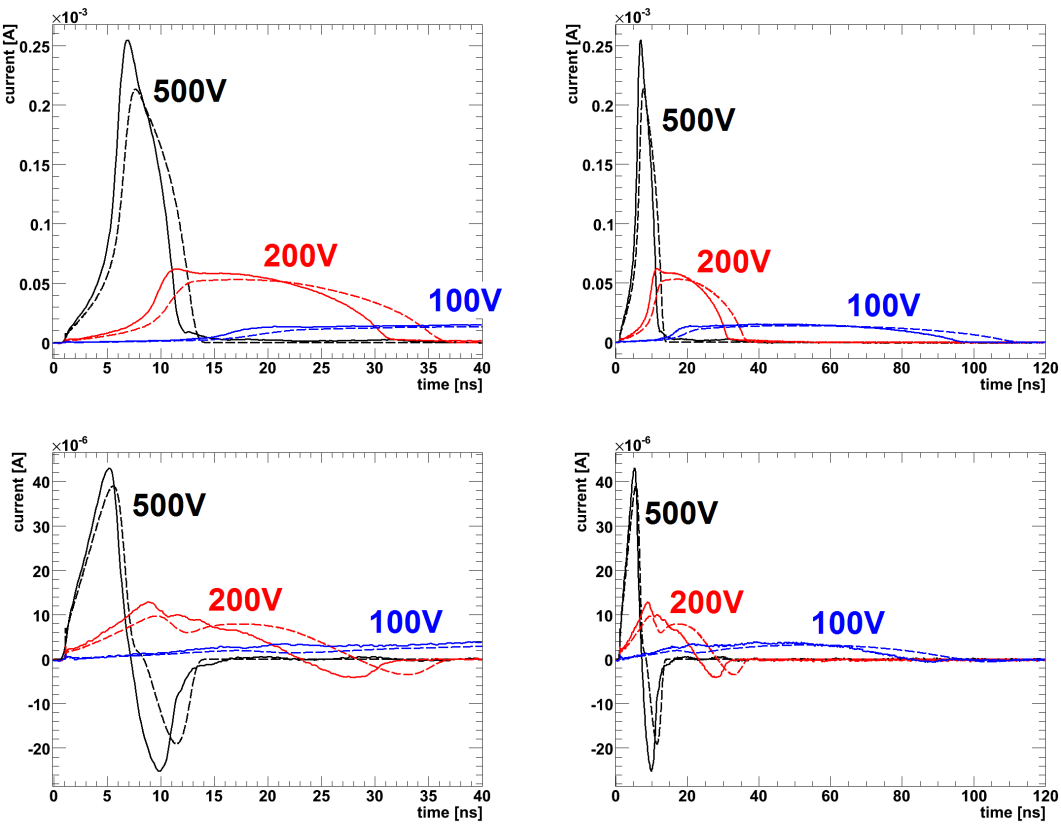

Figure 13.2: Comparison of simulations and measurements for 8.55×10^6 electron hole pairs. The readout strip is shown in the top row, the neighbor strip in the bottom. Measurements are shown with solid lines, simulations with dashed lines. The right column shows the same transients as the left column, but on a larger time scale.

Thus there was no modification of the simulated current pulses.

The simulation program used by WIAS is identical to the program described in Chapter 10 but used a different simulation grid. The mobility model used in the simulations is based on the models in [75] and summarized in Chapter 10 as 'literature mobility'.

13.3 Comparison of simulations and measurements

For the comparison the transients produced when the illuminated spot is centered beneath the readout strip are chosen. Pulses for the readout strip and its neighbor were compared for three different applied voltages and four different intensities. Transients for 0.21×10^6, 0.85×10^6 and 2.15×10^6 electron hole pairs are shown in Figure 13.1. Transients for 8.55×10^6 electron hole pairs are shown in Figure 13.2. Although the general behavior is reproduced well, the simulated pulses are systematically too long. Possible explanations for this are the need for changes in the mobility parameterization of holes

and the release of charge carriers from the plasma cloud. A detailed discussion of these topics is found in Chapter 10.

Figure 13.3 shows a comparison of the integrated current pulses (collected charge) for all compared intensities and voltages.

The shapes of the simulated curves are as expected, as the charge collection time increases with increasing number of created charge carriers. The amount of charge spread to the neighbor strip (due to diffusion and repulsion) increases as well. A higher voltage counteracts this effect, as it reduces the charge collection time.

The behavior of the measurements and its reasons are not obvious. First of all the total charge collected is dependent on the applied voltage, as shown in Figure 13.4. A possible explanation is the noise in the measurements, which is problematic for low and very low intensities. For the neighbor strip noise is even more of a problem, since the current pulse on the neighbor strip is quite low.

However noise cannot explain the almost constant fraction of charge collected on the readout strip. Although the simulation does take coupling capacitances between the strips into account, the grid size of the simulation is limited and the interstrip capacitances and coupling capacitance between a strip and its second neighbor might be wrong. Additionally the simulations are not taking imperfections of the readout circuit into account. Even small resistances in the readout circuit and oscillations in the recorded transients can have an influence. When the transient is disturbed, the large bipolar currents, due to the displacement of charge carriers, do not integrate to zero.

As shown in Figure 12.2 the charge collected on the neighbor strip (identical to charge collected at $\mu \pm p$) is very sensitive to the actual position of injection. The measurement data is acquired in position steps of 2 µm, thus even small uncertainties in the position of laser with respect to the center of the readout strip cause large variations in the charge collected on the neighbor strip. For the investigated sensor the change in collected charge for a position variation of ± 2 µm is about 20%.

Additionally the effect might be caused by charges diffusing into the low field region close to the surface between the readout strips. The time needed to leave this region is long compared to the integration time, thus thus charges located there appear to be 'lost'.

For high intensity the charge obtained from measurements and simulations are approximately similar. Thus the current pulse is determined by charge carriers spreading to the neighbor strips and the influence of distortions in the displacement current is small compared the actual charge spread. For an increased spread, the errors due to the step size are lower as well.

13.4 Summary

Measurements and simulations for one sensor (labeled CG1017) have been compared. The simulations have been performed by WIAS [73]. The general behavior was reproduced, but, especially when comparing the fraction of charge collected on the neighbor strip, discrepancies are observed.

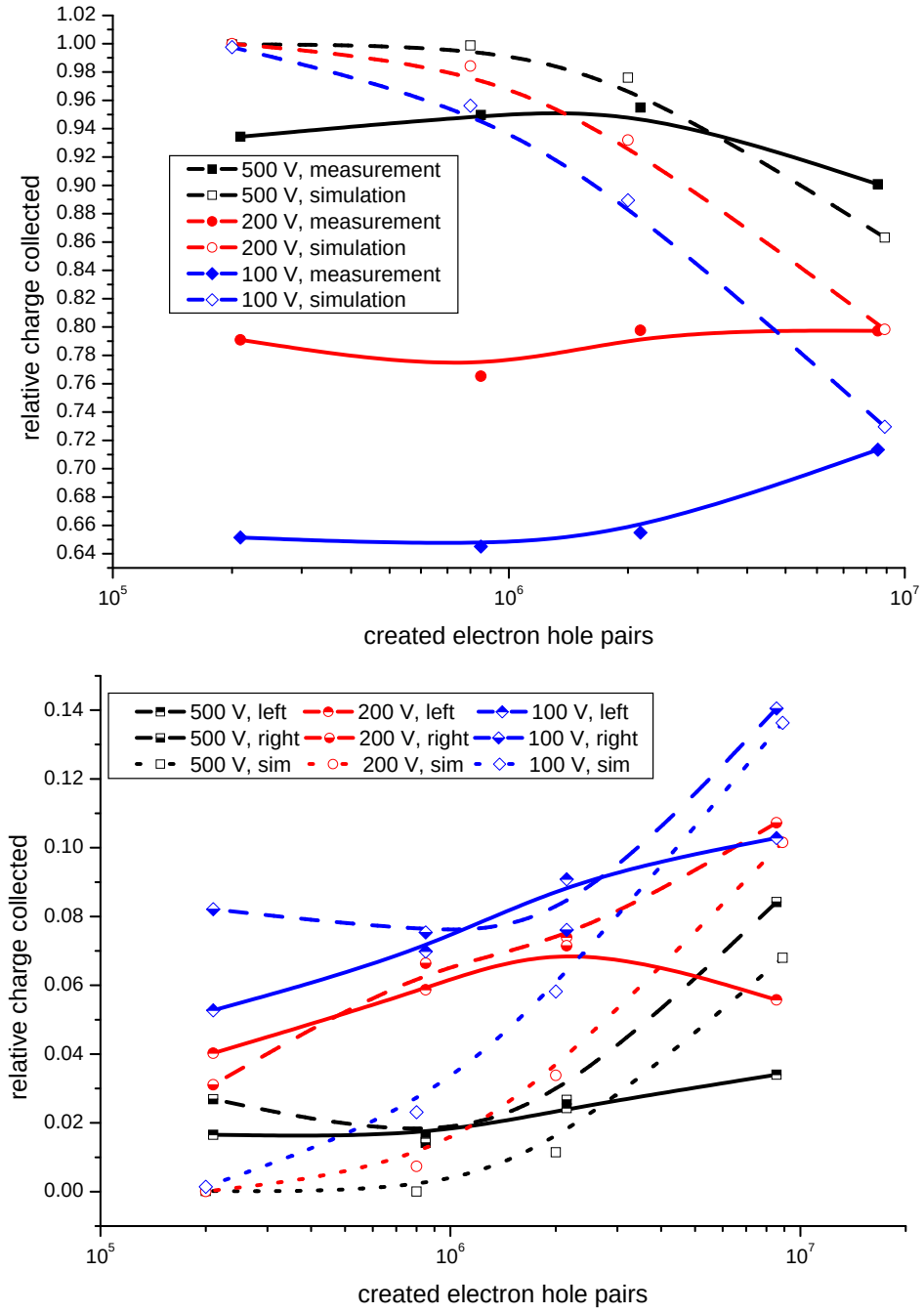

Figure 13.3: Comparison of the fraction of collected charge in simulations (dashed lines, open symbols) and measurements (solid lines and symbols). The charge collected on the readout strip is shown in the upper graph, the charge collected on the left and right neighbor strip in the lower graph.

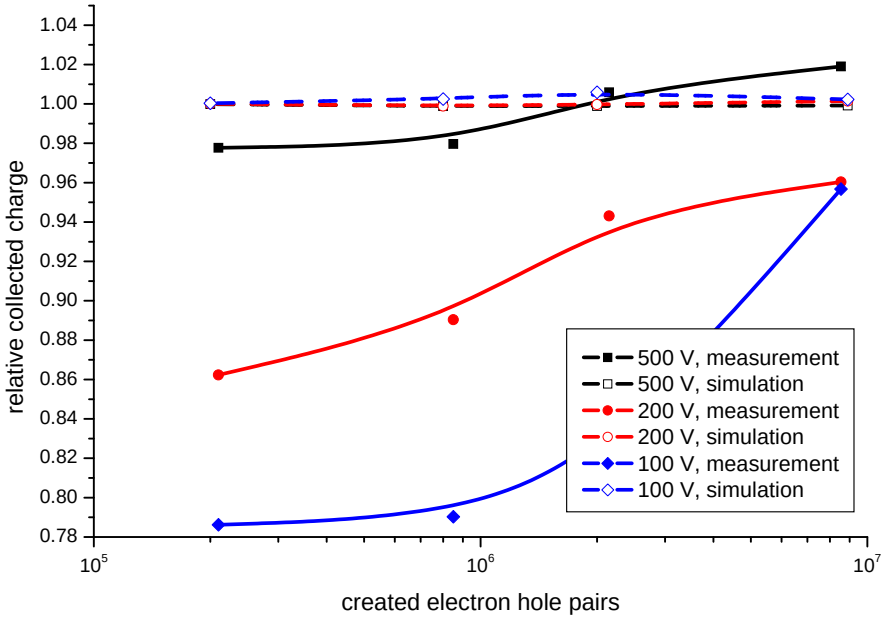

Figure 13.4: Comparison of the total collected charge in simulations (dashed lines, open symbols) and measurements (solid lines and symbols). The total charge was estimated by summing the readout strip and left and right neighbor strip.

The comparison of transient simulations and measurements reveals the same discrepancies discussed in Chapter 10. The strip geometry allows access to additional spatial information by evaluating the fraction of charge collected on the readout strip and its neighbor.

Comparison of the collected charge on readout and neighbor strip reveals strong discrepancies. While for high intensity simulations and measurements are similar, the difference increases with decreasing intensity. Incorrect coupling capacitances, an incorrect sampling of the large displacement currents and incorrect alignment of the laser spot with respect to the strip center have been discussed as possible reasons for the deviations.

It should be noted that a significant error in the sampling of transients dominated by displacement current would influence the sampling on the second neighbor as well. However Figure 12.2 and 12.3 show that for a distance of two pitches the collected charge is $\ll 1\%$ of the total charge, although displacement currents are present. A serious problem with the sampling of the displacement current would lead to collected charges on the second neigbor strip $\gg 1\%$ of the total charge.

As literature data on the diffusion constants perpendicular to the drift direction is sparse it cannot be concluded at this point what the main reasons for the observed discrepancies are. It seems reasonable that the assumptions on the sensor layout for the simulations are not entirely valid, the experimental situation is poorly defined or the experimental errors are too large for comparison with simulations.

14 Considerations influencing the sensor design of the AGIPD

In this chapter the investigations performed in the previous chapters will be evaluated with regard to the Adaptive Gain Integrating Pixel Detector (AGIPD) for the European XFEL.

The AGIPD project is led by DESY and is a collaboration between DESY, PSI, University of Bonn and the University of Hamburg. It is a project to build a pixellated solid state detector for the European XFEL. The goal is a hybrid pixel detector, with 1024 by 1024 pixels with 200 µm pixel pitch and a central hole for the primary beam.

Each pixel contains a charge integrating amplifier which integrates the current generated by x-ray absorption. The gain of the preamplifier is dynamically switched; when the integrated signal rises towards the amplifiers upper limit, the pixel switches to a lower gain setting.

The European XFEL provides up to 2700 photon pulses (bunches) with a repetition frequency of 4.5 MHz (222 ns separation time). The bunch train is followed by 99.4 ms idle time (10 Hz supercycle) during which the images (also called frames), which were stored during the bunch train, are read out.

The dynamic gain switching allows the detector to cope with the large dynamic range of up to 10^4 12 keV photons per pixel in the images produced by the European XFEL, while maintaining single-photon sensitivity in pixels with low illumination. Each pixel has an analog pipeline which allows the detector to store up to 300 images during the bunch train.

The analog signals are then read out and digitized during the intervals between bunch trains.

The baseline sensor design for the AGIPD is a high resistivity n-type material sensor of 500 µm thickness using p-type readout. It provides a sufficiently high quantum efficiency for 12 keV x-rays and will fulfill the requirements imposed by the plasma effect as explained below.

14.1 The readout circuit of the AGIPD

The Application Specific Integrated Circuit (ASIC) implemented in the readout electronics of the AGIPD realizes the design specifications with an adaptive gain switching and analog storage of the image data (more details can be found in [10]). A schematic drawing showing the ASIC is found in Figure 14.1.

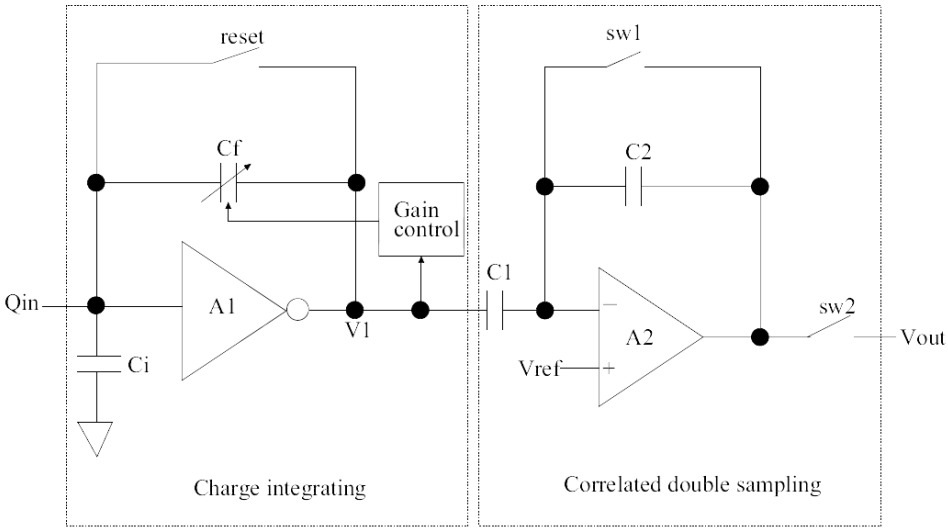

Figure 14.1: Block diagram of the readout ASIC of the AGIPD showing the charge integrating amplifier and the gain switching in the left box and the correlated double sampling in the right box. Reproduced from [10].

In order to understand the ASIC design the sensor can be seen as a current source. The current source is connected to the input of a Charge Integrating Amplifier (CIA). The output of the CIA is a voltage, which is determined by the integrated charge and the feedback capacitance. The relation of the voltage as function of the charge is described by the gain.

The gain of the CIA is determined by the feedback capacitance of the amplifier. The output voltage V_{out} of the CIA can be described by the following equation:

$$V_{out} = \frac{AQ}{C_i + (1+A)C_f} \approx \frac{Q}{C_f} \quad \text{as } C_i \ll C_f \text{ and } A \gg 1 \tag{14.1}$$

with A being the amplification, Q the input charge, C_i the input capacitance including all parasitic capacitances and C_f the feedback capacitance. Depending on the output voltage V_{out} of the CIA additional capacitances are connected in parallel to increase the total feedback capacitance, thus lowering the gain and increasing the dynamic range.

Noise is reduced by the correlated double sampling method ([10] and literature cited therein). The sampled output voltage is stored in an analog storage cell (the gain information is stored digitally) and read out and digitized in between bunch trains.

14.2 Relevant detector specifications

Experiments at the European XFEL are expected to acquire images with a very high dynamic range of up to 10^4 12 keV photons per pixel per pulse, while simultaneously requiring single photon sensitivity in each pixel. The bunch to bunch variation can be

100%, meaning that a very bright image can be followed by a completely dark one, which has to be sampled correctly.

Due to the high number of photons (up to 10^{12}) in a pulse, some pixels of the sensor are expected to see more than 10^5 photons per pulse (e.g. at Bragg peaks or under small angle scattering). Although this high number of photons does not need to be sampled correctly by the readout electronics, the resulting peak currents have to be tolerated.

There is always a certain lateral spread of charge carriers. However at high photon densities this spread increases. Although there is no hard number on the specification of the maximum spread tolerated, it should be small compared to the pixel size. Most of the charges created inside a pixel volume should be collected in this pixel.

14.3 Input protection

In Chapter 11 the peak currents for different sensor types were investigated. For hard x-rays (simulated by 1015 nm light) peak currents in excess of 1 mA have been observed for intensities above some 10^4 12 keV photons.

The CMOS technology, used to fabricate the ASIC, specifies maximum tolerated voltages of 4 V. In order to allow for process variations in the production process, voltage peaks on the input of the amplifier should by limited to $U_{peak} = 1$ V. Assuming a transient impedance of $R = 100\ \Omega$ results in maximum tolerated currents of $I_{peak} = U_{peak}/R = 10$ mA.

Keeping in mind that the investigated maximum intensity in Figure 11.7 is only slightly larger than 10^5 photons and peak intensities of up to 10^6 per pixel are possible for small angle scattering, the expected current could exceed the limit of 10 mA.

Using current limiting diodes across the input of the CIA would protect the ASIC from being damaged. Taking the dynamic range into account the current limit of the diodes should be higher than the peak current when 10^4 photons are absorbed in one pixel. From Figure 11.7 it can be observed that protection diodes with a current limit of 1 mA will not impact on the sampling of up to 10^4 12 keV photons.

For soft x-rays (simulated by 660 nm light) the observed currents are lower and would not require input protection.

14.4 Pile-up

As the number of storage cells is limited not all frames of a bunch can be stored. Due to the image rejection possibility (veto), the analog storage is operated as a random access memory, thus there is no possibility to correct images based on the preceding frame.

Therefore it is important to avoid pile-up effects. Due to the large intensity variations for individual pixels, from 10^5 photons in one frame to 0 or 1 photon in the next frame, even a pile-up of 10^{-5} is not acceptable. Thus the charge collection time for those high intensities has to be less than the bunch repetition time (222 ns). From Figure 11.9 it is

concluded, that at least 300 V have to be applied to the sensor PSI02 in order to fulfill this criterion.

As the AGIPD sensor will be high resistivity n-type material of 500 µm thickness using p-type readout, at least 300 V bias should be applied as well.

14.5 Integration time

As shown in Figure 11.8 the charge collection time is a function of the applied voltage. However the lower bound of the bias voltage is fixed by the considerations of the pile-up effect to 300 V. As the CIA saturates above 10^4 12 keV photons the integration time has to be chosen such that 10^4 are sampled correctly. Higher intensities do not need to be sampled correctly.

Studying Figure 11.8 and 11.9 and allowing for some additional time to collect the final 5 %[1] of charge, an integration time of 60 ns is sufficient.

14.6 Sensor polarity

In order to decide on the readout of holes or electrons (different sensor polarity) several factors have to be balanced.

Using an n-type readout would lead to the situation, where the highest charge carrier density is at the location of the highest electric field, which reduces the observed plasma effects, as shown for front side illumination of sensors with p-type readout.

Collecting electrons on the readout electrode, n-type readout results in transients with negative polarity. Additionally, in the low density case, the charge collection time is determined by the electron mobility. Holes contribute to the current as well, but can be neglected[2] for the determination of the pulse duration as shown in Figure 14.2. The electron mobility is about three times the hole mobility, resulting in pulse durations < 6 ns for a 500 µm sensor with 500 V bias. A negative polarity requires a different type of CIA design, which is known to be slower than the design for positive polarities. This is problematic for the fast gain switching mechanism, which needs to be very fast compared to the pulse duration.

In order to increase the charge collection time, the bias voltage could be reduced to approximately 200 V, resulting in charge collection times of about 15 ns, which corresponds approximately to the charge collection time for p-type readout at 500 V (as shown in Figure 14.2). However, due to the lower voltage, plasma effects are less suppressed and, in the case of low densities, the diffusivity (lateral spread) would increase by approximately 70 % (for same charge collection times the ratio of the lateral spread is proportional to $\sqrt{\mu_e/\mu_h}$).

[1] Figure 11.8 diplays the time needed to collect 95 % of the total charge

[2] The hole contribution cannot be neglected for the determination of the total charge by integration of the current.

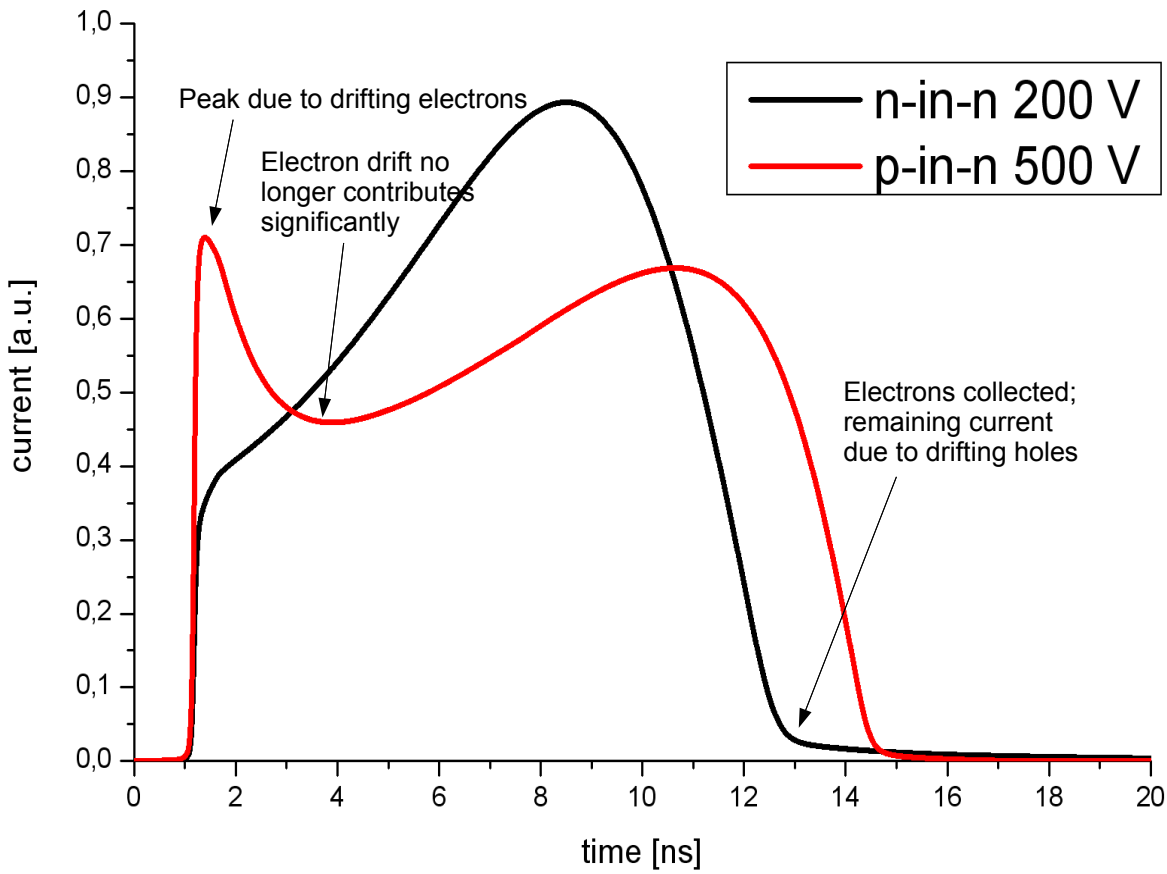

Figure 14.2: Simulated current pulses for different layouts of 200 µm pixels. The sensor is of 500 µm thickness with a depletion voltage of 150 V $N_{eff} = 7.8 \times 10^{11}$ cm^{-3}. Pulses are simulated for a central hit of 12 keV photons neglecting plasma effects at a temperature $T = -20$°C. The absolute value of the current is shown in order to facilitate the comparison.

Thus, as the specifications can be fulfilled by using a sensor design with p-type readout, as shown above, the use of n-type readout should be avoided.

14.7 Lateral spread

The effects of charge sharing due to the increased lateral spread have been estimated using the parameters of the Point Spread Functions (PSF) determined in Chapter 12. The radial PSF has been used to calculate the charge distribution on a square grid. In order to evaluate the spread, the grid points which are inside the pixel area were summed up (numerical integration) and divided by the sum of all grid points, to yield the relative charge collected within the pixel[3].

[3]This assumes no cross-talk between pixels.

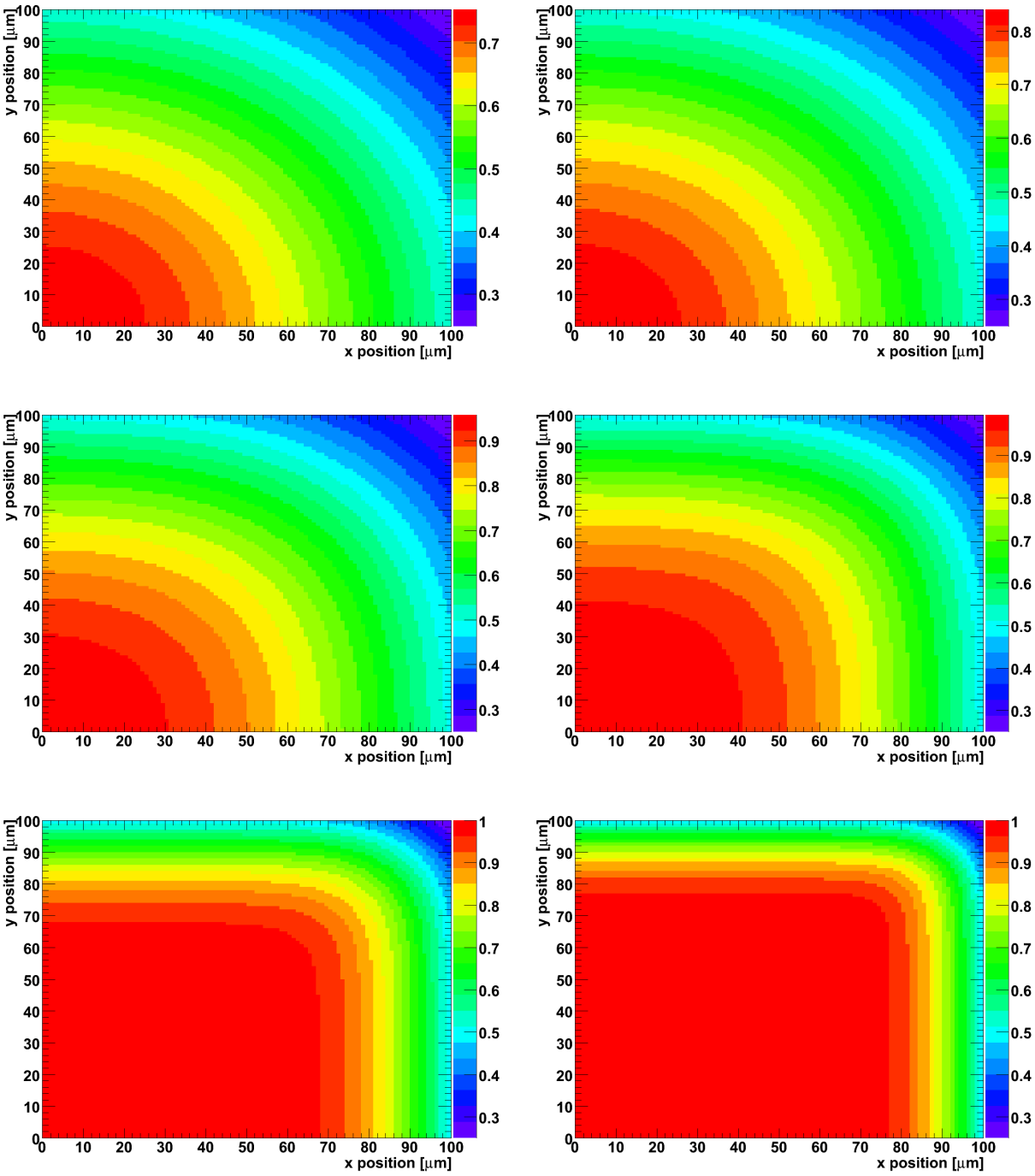

Figure 14.3: Fraction of charge collected within a 200 μm pixel (color coded) as function of impact position. The distribution is calculated from the data obtained from the sensor of 450 μm thickness. The left column shows the distribution for 200 V applied bias, the right column for 500 V. Top row shows the highest intensity (1.62×10^5 12 keV photons), the middle row shows 1.41×10^4 12 keV photons, and the lowest row shows 870 12 keV photons. Note the different color coding for each distribution.

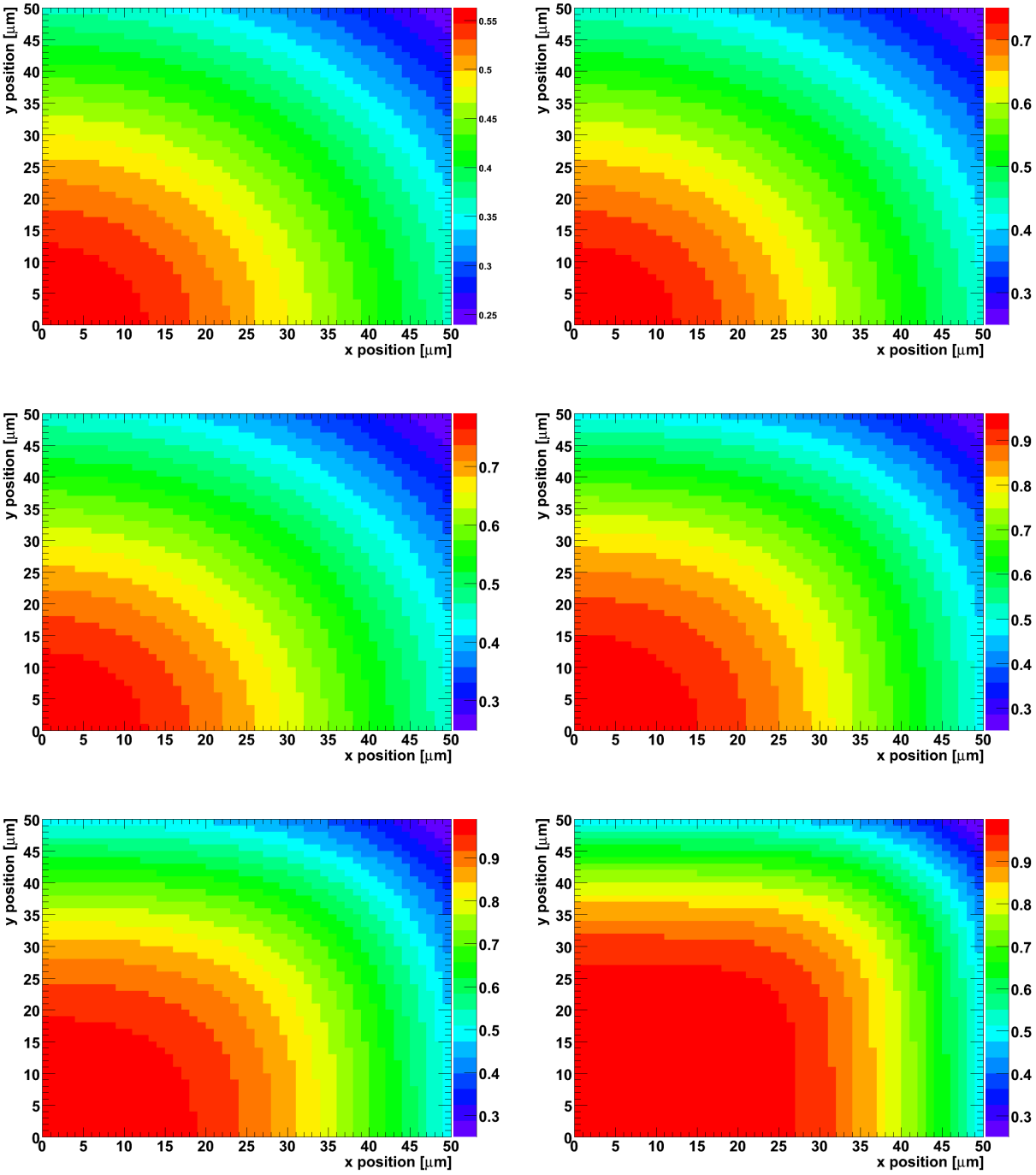

Figure 14.4: Fraction of charge collected within a 100 μm pixel (color coded) as function of impact position. The distribution is calculated from the data obtained from the sensor of 450 μm thickness. The left column shows the distribution for 200 V applied bias, the right column for 500 V. Top row shows 1.41×10^4 12 keV photons, the middle row shows 4.5×10^3 12 keV photons, and the lowest row shows 870 12 keV photons. Note the different color coding for each distribution.

This ratio is calculated as function of the x and y position of the impact point and shown in Figure 14.3 and 14.4 for different pixel sizes, intensities and applied voltages. Additionally the average charge collected and its standard deviation have been calculated and are shown in Figure 14.5 for 200 μm and 100 μm pixels for two different wavelengths as function of intensity for all investigated sensors and two different voltages. The markers are the averages and the error bars show the spread.

Figure 14.6 shows the fraction of the pixel area without charge sharing ($\geq$ 90% charge collected in the pixel) for 200 μm and 100 μm pixels for two different wavelengths as function of intensity for all investigated sensors and two different voltages.

14.7.1 200 μm pixels

Pixels of 200 μm × 200 μm with a sensor thickness of 500 μm are the baseline design of the AGIPD sensor. It is expected that the plasma effects for this layout will be similar to the results obtained from the 450 μm sensor. Within the dynamic range the expected average charge collected within the pixel does not fall below 70% (10^4 12 keV γ, 200 V), which is still acceptable in terms of imaging performance. A higher value (75%) could be obtained with thinner sensors, however the quantum efficiency would be lower, reducing the single photon sensitivity. Thicker sensors, which would be an option if the main energy of the European XFEL would be increased, would suffer even more from plasma effects. The value obtained for the sensor of 1 mm thickness is as low as 50% for 10^4 12 keV photons. Increasing the intensity reduces the value for all investigated sensor types.

Charge sharing will increase with increasing intensity, as shown in the upper graph of Figure 14.6. For 10^4 12 keV photons, the area (and thus the fraction of randomly impacting events) without charge sharing will be below 50%. For the 1000 μm sensor the area is below 20%. Thus image areas with high intensities will show large amounts of charge sharing.

14.7.2 100 μm pixels

Pixels of 100 μm × 100 μm with a thickness of 500 μm are an option for an AGIPD*, which would have less (or no) gain switching stages and less storage cells per pixel. This option is under discussion, as experiments like photon correlation spectroscopy need more spatial resolution but less frames to be recorded per bunch train.

The same investigation as explained above has been carried out, but assuming the smaller pixel size of 100 μm. As seen from Figure 14.4 and the lower graphs of Figure 14.5 and Figure 14.6 the operation with the same dynamic range is not feasible, as the charge collected within the pixel drops to 47% (10^4 12 keV γ, 200 V), which would impact on the imaging performance. However AGIPD* would also have a reduced dynamic range. From the presented data it can be concluded that a dynamic range of up to 10^3 12 keV photons would not suffer more from plasma effects than 200 μm pixels (average collected charge = 70%).

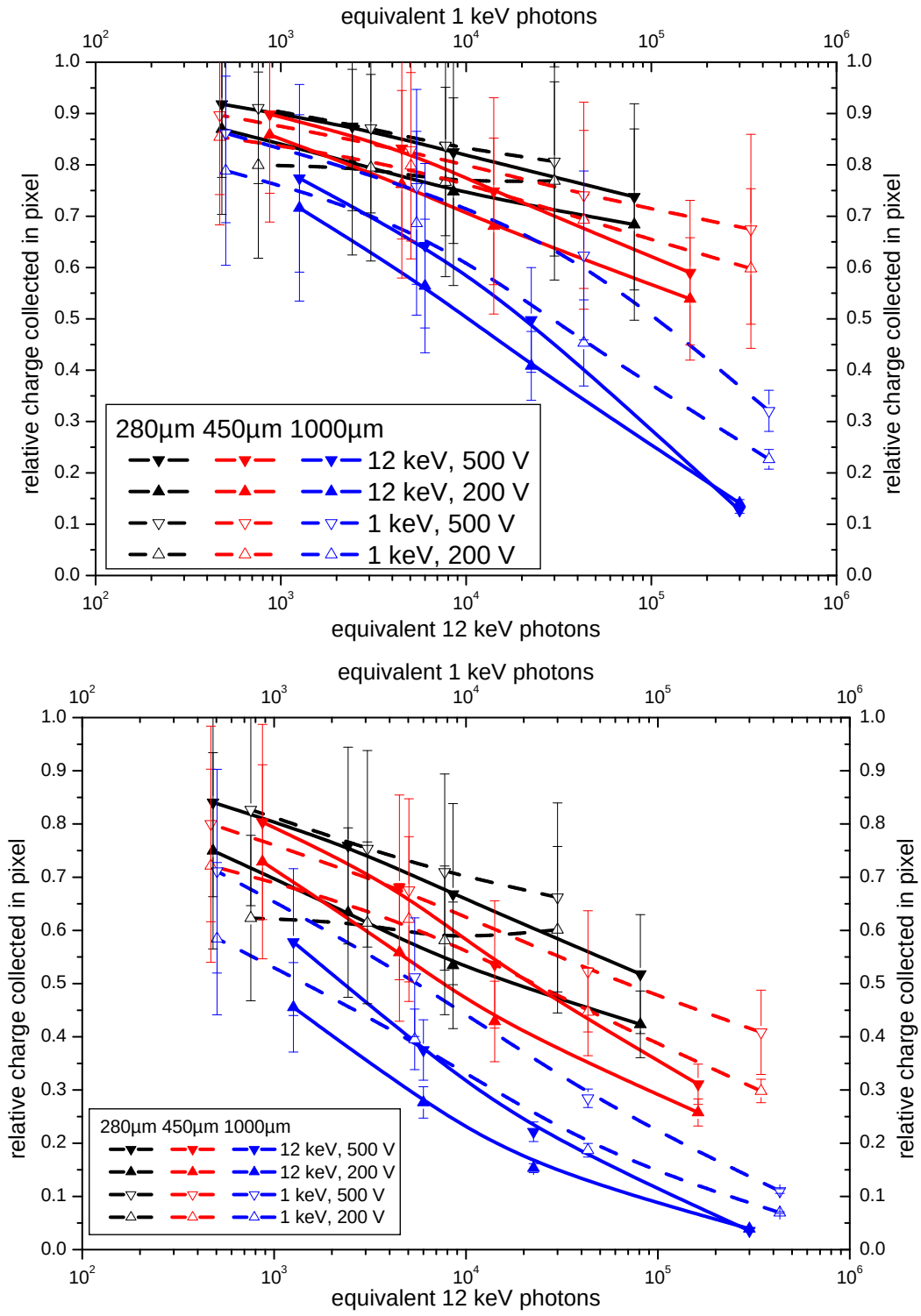

Figure 14.5: Collected charge within a 200 µm pixel (upper graph) and 100 µm pixel (lower graph) for two different wavelengths as function of intensity for all investigated sensors and two different voltages. Markers show the average value for random impact positions, error bars show the spread. The collected charge as function of impact position is shown in Figure 14.3.

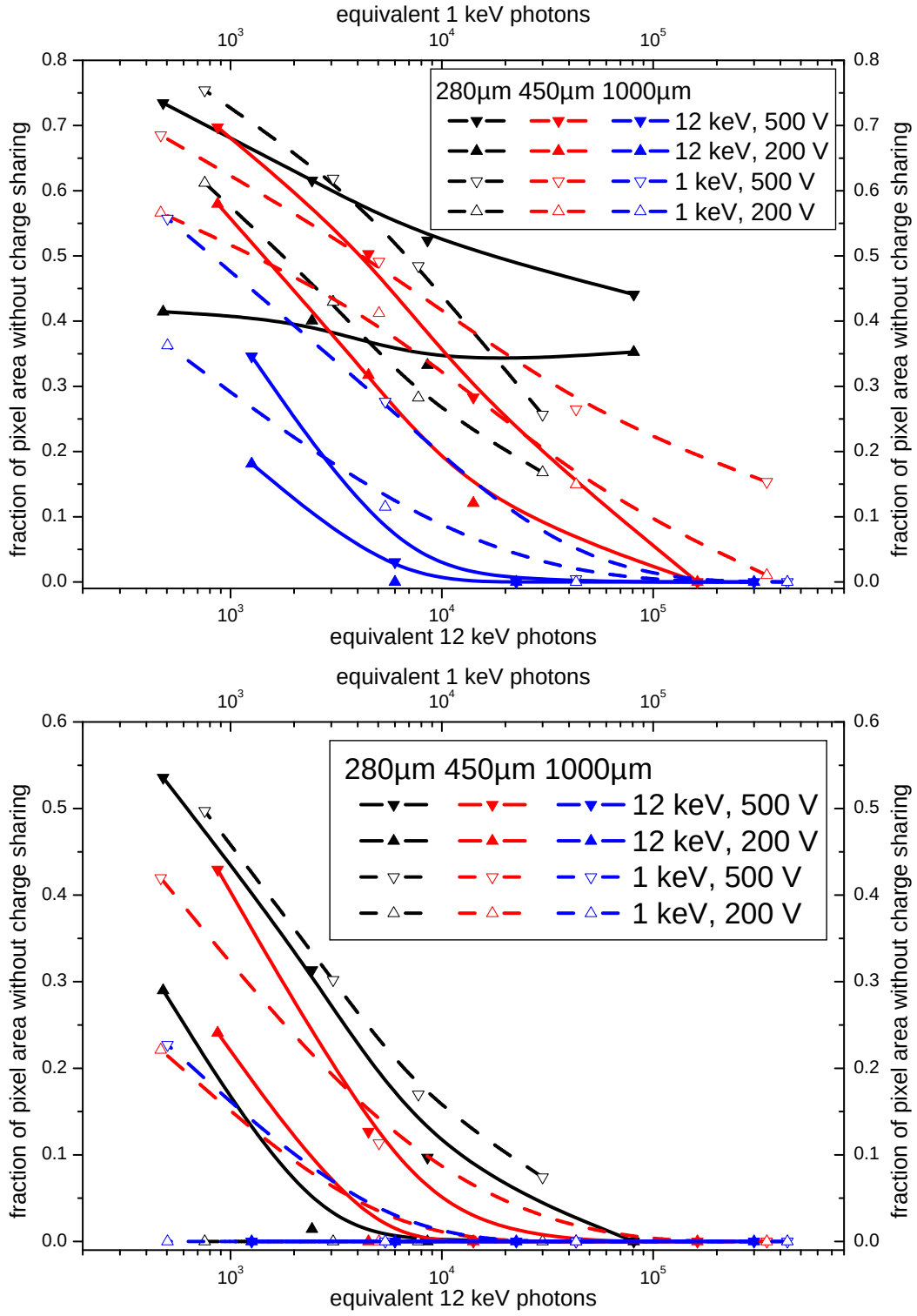

Figure 14.6: Fraction of the pixel area without charge sharing ($\geq$ 90% charge collected in the pixel) for 200 µm pixels (top) and 100 µm pixels (bottom) for two different wavelengths as function of intensity for all investigated sensors and two different voltages.

More charge sharing is observed in smaller pixels, as shown in the lower graph of Figure 14.6. For 10^3 12 keV photons, the area without charge sharing varies strongly with applied voltage and is always below 50%, which is comparable to the situation for 10^4 12 keV photons in 200 µm pixels.

14.8 Summary

The presented results have been used to define sensor parameters of the AGIPD sensor. It was shown that using a conventional p-in-n sensor layout will satisfy the quoted sensor requirements for a detector at the European XFEL. Recommendations for the applied bias voltage ($\geq$ 300 V) and the integration time ($\geq$ 60 ns) were derived from measurements with focused lasers.

The lasers have been used to create charge carrier densities larger than the charge carrier densities expected for the European XFEL. Thus the quoted parameters have been derived from worst case estimations and can be considered safe, taking all possible differences between the simulations and real experiments into account.

It was concluded that the input of the charge integrating amplifier should be protected by current limiting diodes.

It was shown that for bias voltages $\geq$ 300 V pile-up effects at high intensities are avoided. At this voltage an integration time of 60 ns is sufficient to collect up to 10^4 12 keV photons.

The impact of the charge sharing properties of 200 µm and 100 µm pixels was investigated for different intensities and voltages. It was concluded that the increased charge sharing within the range of the dynamic range of the readout circuit can be tolerated for 200 µm pixels. For 100 µm pixels significant increases in the charge sharing are observed already for intensities above 1000 12 keV photons.

15 Summary and Conclusions

In this chapter the results presented in the previous chapters will be summarized and the conclusions drawn from these results will be presented.

15.1 Setup

A multi channel Transient Current Technique (mTCT) setup was built. It provides a versatile way to investigate silicon sensors. It features a laser system with very intense pulses, which allow to create charge clouds with charge carrier densities large enough to study plasma effects.

The created charge carrier density can be varied by using neutral density filters to attenuate the laser beam. The laser beam can be focused to spot sizes of ≈ 3 µm. Three different lasers with different wavelengths are available to simulate 1 keV or 12 keV photons and mips.

A special mounting and substrate were developed allowing light injection from both sides of the sensor. The high voltage is provided to the rear side of the sensor, up to 32 channels can be bonded for readout and the temperature can be controlled in the range from -30°C to +60°C.

15.2 Simulation program

A simulation program for current pulses of silicon sensors has been developed. Assuming no charge carrier interactions (no plasma effects), current pulses for sensors with pad, strip and pixel geometries can be calculated.

The simulation is grid based and allows arbitrary definitions of the initial charge carrier distribution, electric field and weighting potential. The transport code calculates drift and diffusion of both charge carrier types, taking the mobility reduction due to high electric fields, trapping and multiplication into account.

As the simulation code is limited to one dimension, diffusion perpendicular to the drift direction is not taken into account and results for strip and pixel sensors are only approximations.

15.3 Investigations on pad sensors

Pad diodes were investigated to measure basic properties of silicon sensors. Specific measurements and results are summarized below.

15.3.1 Measurements with low charge carrier densities

Using a defocused and attenuated laser beam, current pulses showing no plasma effects were measured. Comparing measurements and simulations a new parameterization of the charge carrier mobilities as function of electric field and temperature was presented for two different crystal orientations.

15.3.2 Comparison of simulations and measurements

Simulations of irradiated epitaxial diodes have been performed. One of the sensors has a thickness of 153 μm and shows a double peak structure and field dependent trapping. It was shown that an agreement between simulation and measurement can be achieved when the parameterizations described in Chapter 9 are used.

The other investigated sensor has a thickness of 75 μm and shows charge multiplication after heavy proton irradiation. Using different parameterizations of the impact ionization coefficient the general behavior of the sensor could be reproduced. The simulation allowed to investigate the charge transport inside the sensor showing that predominantly electron but also hole multiplication play a role in the charge collection process.

15.3.3 Measurements with high charge carrier densities

Plasma effects were created with focused lasers of high intensity. The recorded transients were compared to simulations from WIAS [73]. It was shown that the general behavior can be reproduced by the simulation, but the simulations systematically overestimate the pulse duration for high charge carrier densities.

Using mobility models accepted in literature, it was not possible to reproduce the observed plasma effects.

Two different sets of parameters were used to provide upper and lower bounds of the expected current pulse duration.

15.4 Investigations on strip sensors

Performing position sensitive measurements in order to extract the spatial distributions of the collected charge after high intensity illumination has been a central topic of this work.

15.4.1 Transient measurements

Most of the presented transients have been obtained with very tight focusing ($\sigma \approx 3$ μm). Considering the expected situation at the European XFEL the plasma effects are overestimated. Thus the results presented here should be seen as worst case estimates.

The effect of a relaxed focusing has been investigated for the 450 μm sensor showing that, as expected, plasma effects decrease for reduced densities.

For experiments at the European XFEL spot sizes with $\sigma \approx 140$ µm are expected. It was shown that at these spot sizes plasma effects will be observed.

Transients showing plasma effects were evaluated for all three sensors showing an increase in charge collection time with increased intensity. Using front side illumination the plasma effects expected in n-in-n devices could be estimated, showing that when plasma effects shall be avoided the use of n-in-n devices is favorable.

Peak currents, charge collection times and pile-up effects have been investigated for different intensities and applied voltages with respect to the specifications of the AGIPD for the European XFEL.

15.4.2 Position sensitive measurements

The radial distribution of the collected charge has been determined. As the width of the distribution of initial charge carriers was very small, the charge distribution is identical to the Point Spread Function (PSF). From integrated transients (charge) as function of position the PSF for different wavelengths, intensities and voltages has been determined.

For given operating conditions the PSF is a sensor property, which can be used to estimate the imaging performance of a sensor.

The width of the PSFs was observed to increase strongly with increased intensity and increased sensor thickness. A small decrease was observed when the bias voltage was increased.

Using the PSFs the modulation transfer function has been calculated. At the Nyquist frequency the contrast was above 0.8 for the 280 µm sensor, above 0.6 for the 450 µm sensor and significantly below 0.5 for the 1000 µm sensor. Similar to the observations for the PSFs, it was observed that the contrast at a fixed spatial frequency decreases strongly when the charge carrier density is increased and decreases significantly for thicker sensors. An increase of contrast is observed when the applied voltage is increased, however this effect is small compared to the effect of the increased charge carrier density and the increased thickness.

It should be noted that the modulation transfer function is only an indicator for the imaging performance, as it is usually determined from a line pattern and not individual bright spots.

15.4.3 Comparison of simulations and measurements

Measurements and simulations for one sensor (labeled CG1017) have been compared. The simulations have been performed by WIAS [73]. The general behavior was reproduced, but, especially when comparing the fraction of charge collected on the neighbor strip, discrepancies are observed.

The comparison of transient simulations and measurements reveals the same discrepancies discussed for pad diodes. The strip geometry allows access to additional spatial information by evaluating the fraction of charge collected on the readout strip and its neighbor.

Comparison of the collected charge on readout and neighbor strip reveals strong discrepancies. While for high intensity simulations and measurements are similar, the difference increases with decreasing intensity. Incorrect coupling capacitances, an incorrect sampling of the large displacement currents and incorrect alignment of the laser spot with respect to the strip center have been discussed as possible reasons for the deviations.

As literature data on the diffusion constants perpendicular to the drift direction is sparse it cannot be concluded at this point what the main reasons for the observed discrepancies are. It seems reasonable that the assumptions on the sensor layout for the simulations are not entirely valid, the experimental situation is poorly defined or the experimental errors are too large for comparison with simulations.

15.5 Implications for the AGIPD sensor design

The presented results have been used to define sensor parameters of the AGIPD sensor. It was shown that using a conventional p-in-n sensor layout will satisfy the quoted sensor requirements for a detector at the European XFEL. Recommendations for the applied bias voltage ($\geq$ 300 V) and the integration time ($\geq$ 60 ns) were derived from measurements with focused lasers.

The lasers have been used to create charge carrier densities larger than the charge carrier densities expected for the European XFEL. Thus the quoted parameters have been derived from worst case estimations and can be considered safe, taking all possible differences between the simulations and real experiments into account.

It was concluded that the input of the charge integrating amplifier should be protected by current limiting diodes.

It was shown that for bias voltages $\geq$ 300 V pile-up effects at high intensities are avoided. At this voltage an integration time of 60 ns is sufficient to collect up to 10^4 12 keV photons.

The impact of the charge sharing properties of 200 µm and 100 µm pixels was investigated for different intensities and voltages. It was concluded that the increased charge sharing within the range of the dynamic range of the readout circuit can be tolerated for 200 µm pixels. For 100 µm pixels significant increases in the charge sharing are observed already for intensities above 1000 12 keV photons.

A Appendix

A.1 List of investigated sensors

A list of all sensors investigated in this work is found in Table A.1. The investigation of the sensors CG1233 and CG1234 was discontinued, as their usefulness was limited. The sensor CG1234 has many scratches and a very high guard ring current. In order to avoid problems with microdischarges, which may damage the equipment CG1234 is only used as reference photodiode for simultaneous laser stability measurements, as no bias is applied to the photodiode.

The usability of sensor CG1233 suffered from a sparking around the edges after applying $\approx$ 750 V over a wire bond. The corresponding wire bond was evaporated in the process. The sensor has been manually rebonded with a piece of copper wire, but the investigation of this sensor has been discontinued, as it showed a very high guard current.

The sensors CC1604 and CG1215 where investigated in Chapter 8 and from the investigations a new parameterization of the charge carrier mobilities in bulk silicon was derived. CG1215 was also used in Chapter 10 to investigate electron hole plasmas.

The comparison of simulations and measurements for two irradiated epitaxial silicon sensors, labeled 261636-11-39-1 and 8364-03-50, was presented in Chapter 9. The measurements on these sensors have been performed by T. Poehlsen [37] and J. Lange [1].

Three different strip sensors (CG1017, PSI02 and PSI1mm) have been investigated in Chapter 11 and Chapter 12. The strip sensor labeled PSI1mm was known to have an inhomogeneous bulk doping concentration, which could be confirmed from position sensitive measurements [81].

A.2 Optical components used to build the setup

The optical system has been designed to focus the laser beam to a very small spot. The laser beam can be described as a Gaussian beam and according to the laws of Gaussian optics for diffraction limited performance the spot size on the sensor is

$$\sigma_{sensor} = \frac{M^2 \lambda f}{\pi \sigma_{lens}} \tag{A.1}$$

with σ the corresponding spot sizes, M^2 the 'Gaussianness' of the beam ($M^2 = 1$ is a perfect Gaussian beam), λ the light wavelength and f the focal length of the lens.

Sensor	layout	d [μm]	p [μm]	U_{dep} [V]	N_{eff} [cm^{-3}]	C_{final} [pF]	orientation
CC1604	pad	272	-	63	1.1×10^{12}	9.23	<111>
CG1215	pad	280	-	49	8.2×10^{11}	9.42	<100>
CG1233	pad	≈280	-	49	8.2×10^{11}	9.29	<100>
CG1234	pad	≈280	-	50	8.2×10^{11}	9.20	<100>
CG1017	strip	280	80	≈63	$\approx8\times10^{11}$	0.24	<100>
PSI02	strip	450	50	≈155	$\approx1\times10^{12}$	0.54	<111>
PSI1mm	strip	1000	25	≈150-200	$\approx2\times10^{11}$	≈0.24	unknown
Irrad1[a]	epi	153	-	≈285	1.6×10^{13}	4.4	<100>
Irrad2[b]	epi	≈75	-	≈750	$\approx1.75\times10^{14}$	≈36	<111>

[a]This sensor (261636-11-39-1) has been irradiated with neutrons to a fluence of 2×10^{15} cm^{-2}. It was measured by T. Poehlsen.

[b]This sensor (8364-03-50) has been irradiated with protons to a neutron equivalent fluence of 1×10^{16} cm^{-2}. It was measured by J. Lange.

Table A.1: List of all sensors investigated in this work.

optical element	Thorlabs part number
fiber splitter	FCMM625-90A
fiber collimator	F240APC-B
neutral density filter wheel (use discontinued)	discontinued
neutral density filters	NEK01
beam expander	BE15M-B
iris	SM2D25D
plano-convex lens (use discontinued)	LA1145-B
achromatic doublet	AC508-075-B

Table A.2: List of optical components. There are many holders, adapters, mountings, etc. in the optics system, which are not listed here.

Assuming $M^2 = 1$ and $\sigma_{lens} = D_{iris}/2 = 7.5$ cm yields $\sigma_{sensor} = 2.1$ μm for 660 nm light and 3.2 μm for 1015 nm light, which is close to the measured minimum spot sizes.

The optics system has been improved from the original design. The original design used the neutral density filter wheel and the plano-convex lens listed in Table A.2.

The neutral density filter wheel proved to be mechanically unstable and was replaced by neutral density filters which could be screwed to the optical assembly. The neutral density filters can be stacked. The screwing mechanism is very stable but requires unmounting and remounting the optical fiber in order to exchange the filters.

The stability of the remounting process was investigated and found to be stable.

The plano-convex lens was replaced by an achromatic one as the smallest spot size obtained with the plano-convex lens was ≈ 10 μm for 660 nm light. Additionally the spot profile before and after the focal point differed from each other for the same distance from the focal point and were not described by a Gaussian distribution.

The use of an achromatic lens was motivated by their superior performance, shown in

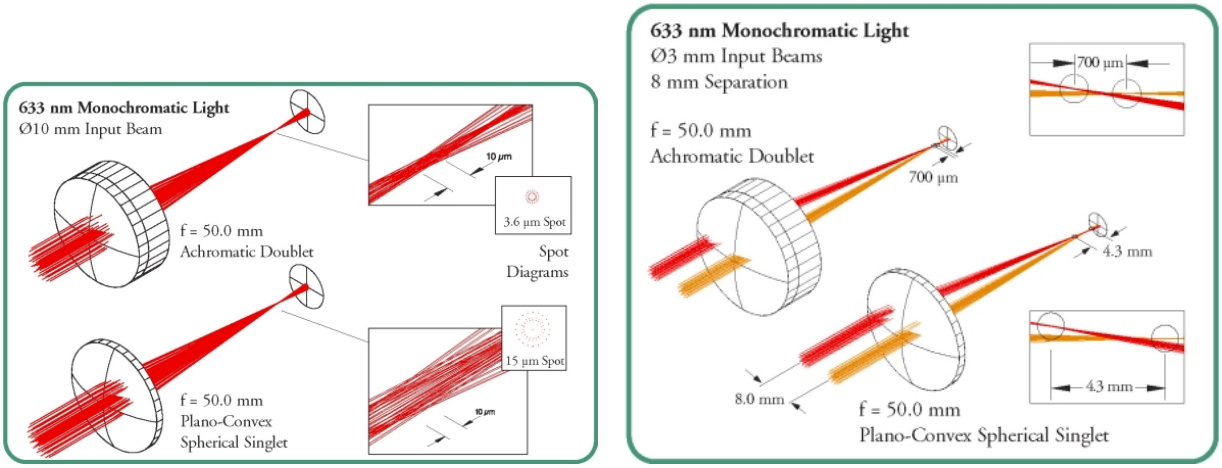

Figure A.1: Performance of plano-convex and achromatic lenses, reproduced from [82].

Figure A.1. Using the achromatic lens produced the laser beam profiles shown in this work. The beam profiles can be described by a Gaussian function at the focal point and away from it. The width of the profiles are approximately the same, for the same distance before and after the focal point.

A.3 Experiments with irradiated strip sensors

In order to investigate the effects of radiation damage on the charge cloud and its properties strip sensors have been irradiated with 24 GeV/c protons.

Three sensors with identical layout were available, the first was not irradiated, the second to a neutron equivalent fluence of 10^{14} cm^{-2}, the third to a neutron equivalent fluence of 10^{15} cm^{-2}.

A break down around 600 V was observed for the non-irradiated sensor, however it is not depleted at this voltage. The irradiated sensors break down around 150 V. Current and capacitance measurements for the devices are shown in Figure A.2. None of the devices could be used to investigate the properties of the charge cloud after irradiation.

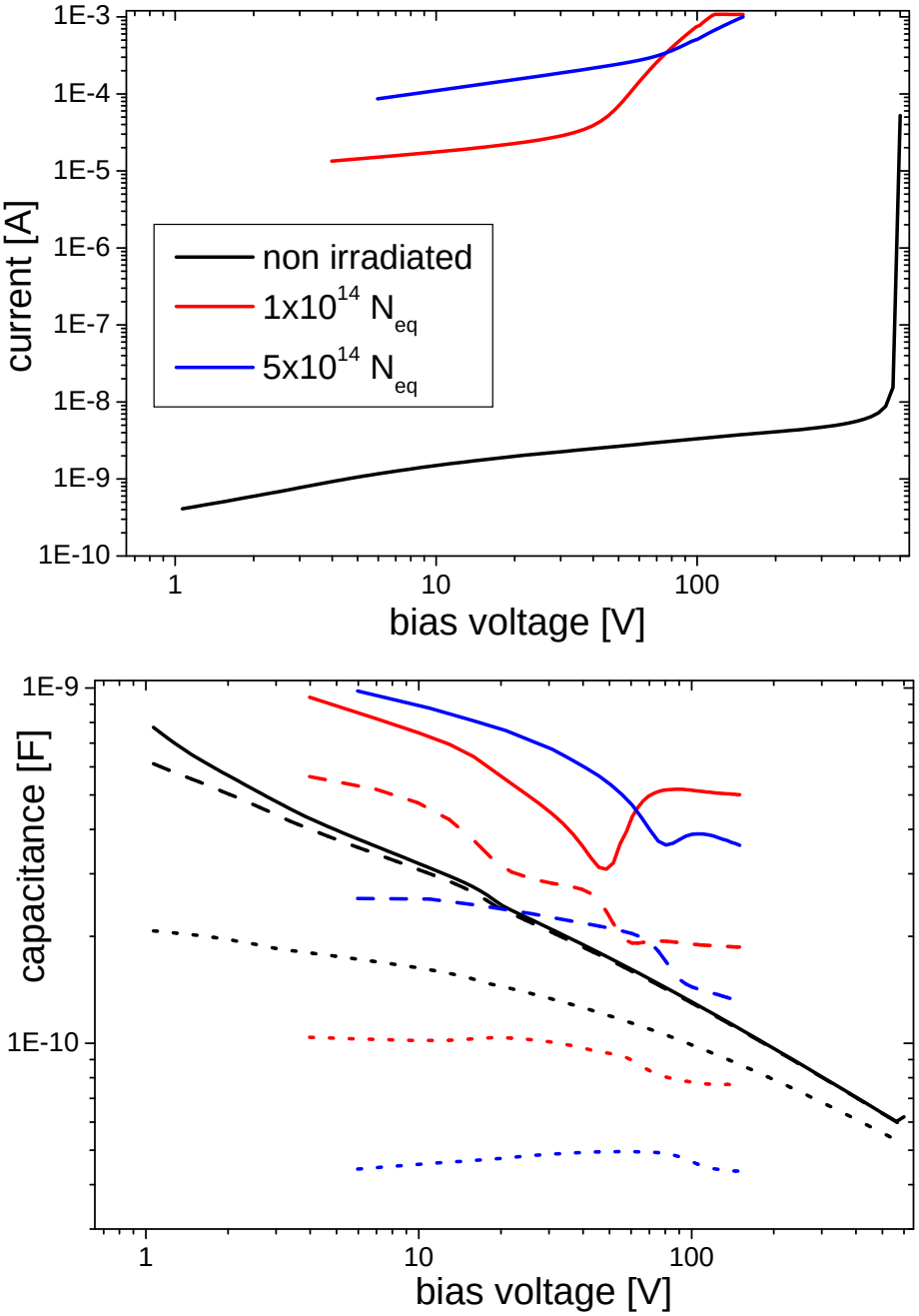

Figure A.2: Current and capacitance measurements on irradiated strip sensors. Breakdown occurs before depletion of the devices. In the lower graph the solid lines represent measurements with 1 kHz frequency, the dashed lines with 10 kHz and the dotted lines with 100 kHz.

B List of publications

During the course of this work several publications have been made, which are listed here:

B.1 List of publications as corresponding author

- J. Becker, D. Eckstein, R. Klanner, G. Steinbrück, Impact of plasma effects on the performance of silicon sensors at an X-ray FEL, Nucl. Inst. Meth. A, 615 (2010) 230-236, DOI:10.1016/j.nima.2010.01.082
- J. Becker, E. Fretwurst, R. Klanner, Measurements of charge carrier mobilities and drift velocity saturation in bulk silicon of <111> and <100> crystal orientation at high electric fields, Solid-State Electronics, 56(1) (2011) 104-110, DOI: 10.1016/j.sse.2010.10.009
- J. Becker, K. Gärtner, R. Klanner, R. Richter, Simulation and Experimental Study of Plasma Effects in Planar Silicon Sensors, submitted to Nucl. Inst. Meth. A 624(3) (2010) 716-727, DOI: 10.1016/j.nima.2010.10.010
- J. Becker, D. Eckstein, R. Klanner, G. Steinbrück, Plasma effects in silicon sensors for the XFEL and impact on imaging performance, Poster Award at the 1st EIROforum School on Instrumentation, CERN 11.05-15.05.09
- J. Becker, D. Eckstein, R. Klanner, G. Steinbrück, Investigation of plasma effects in silicon sensors for the European XFEL, Vienna Conference on Instrumentation, Vienna 15.2-20.02.10

B.2 List of publications as contributing author

- J. Lange, J. Becker, D. Eckstein, E. Fretwurst, R. Klanner, G. Lindstrom, Charge collection studies of proton-irradiated n- and p-type epitaxial silicon detectors, NIM A, DOI: 10.1016/j.nima.2009.11.082
- J. Lange, J. Becker, E. Fretwurst, R. Klanner, G. Lindstrom, Properties of a radiation-induced charge multiplication region in epitaxial silicon diodes, NIM A DOI: 10.1016/j.nima.2010.07.036

Bibliography

[1] J. Lange et al., Properties of a radiation-induced charge multiplication region in epitaxial silicon diodes, submitted to NIM-A

[2] F. Gianotti et al., hep-ph/02004087, April 2002

[3] J. Lange, Radiation Damage in Proton-Irradiated Epitaxial Silicon Detectors, Diploma thesis, University of Hamburg, October 2008, DESY THESIS-2009-022

[4] J. Lange et al., Charge collection studies of proton-irradiated n- and p-type epitaxial silicon detectors, Nucl. Instr. Meth. A, DOI: 10.1016/j.nima.2009.11.082

[5] The European XFEL, `http://www.xfel.eu/en/index.php`

[6] The AGIPD detector, `http://hasylab.desy.de/science/developments/detectors/agipd/index_eng.html`

[7] AGIPD (former HPAD) reply to the Call for Expression of Interest available at `http://xfel.desy.de/project_group/work_packages/photon_beam_systems/wp_75_detector_development/2d_x_ray_detectors/eoi_replies/`

[8] G. Potdevin, U. Trunk, H. Graafsma for the AGIPD Consortium, Performance simulation of a detector for 4th generation photon sources: The AGIPD, Nucl. Instr. Meth. A, Volume 607, Issue 1, Radiation Imaging Detectors 2008 - Proceedings of the 10th International Workshop on Radiation Imaging Detectors, 1 August 2009, Pages 51-54, DOI: 10.1016/j.nima.2009.03.121

[9] B. Henrich et al., Proceedings of the 11th iWoRiD Conference, June 28 - July 2, 2009, Prague, Czech Republic (to be published in Nucl. Instr. Meth. A.)

[10] X. Shi et al., Challenges in chip design for the AGIPD detector, Nucl. Instr. Meth. A, doi:10.1016/j.nima.2010.05.038

[11] Technical Design Report of the European XFEL available at `http://xfel.desy.de/tdr/tdr/`

[12] W. Seibt, K. E. Sundstrom, P. A. Tove, Charge collection in silicon detectors for strongly ionizing particles, Nucl. Instr. and Meth., Volume 113, Issue 3, 1 December 1973, Pages 317-324, DOI: 10.1016/0029-554X(73)90496-5

[13] R. N. Williams, E. M. Lawson, The plasma effect in silicon semiconductor radiation detectors, Nucl. Instr. and Meth., Volume 120, Issue 2, 1 September 1974, Pages 261-268, DOI: 10.1016/0029-554X(74)90044-5

[14] W. Bohne et al., The influence of plasma effects on the timing properties of surface-barrier detectors for heavy ions, Nucl. Instr. Meth. A, Volume 240, Issue 1, 1 October 1985, Pages 145-151, DOI: 10.1016/0168-9002(85)90398-5

[15] M. Campbell et al., Study of the charge sharing in a silicon pixel detector by means of [alpha]-particles interacting with a Medipix2 device, Nucl. Instr. Meth. A, Volume 591, Issue 1, Radiation Imaging Detectors 2007 - Proceedings of the 9th International Workshop on Radiation Imaging Detectors, 11 June 2008, Pages 38-41, DOI: 10.1016/j.nima.2008.03.096

[16] J. Bouchami et al., Study of charge sharing in a silicon pixel detector with heavy ionizing particles interacting with a Medipix2 device, Nucl. Instr. Meth. A, Volume 607, Issue 1, Radiation Imaging Detectors 2008 - Proceedings of the 10th International Workshop on Radiation Imaging Detectors, 1 August 2009, Pages 196-198, DOI: 10.1016/j.nima.2009.03.147

[17] Wikipedia, the free encyclopedia `http://www.wikipedia.org/`

[18] S. M. Sze, Kwok K. Ng, Physics of Semiconductor Devices, Thrid Edition, Wiley-Interscience,New Jersey

[19] A. Junkes, personal communication

[20] G. Lindstrom et al., Radiation hard silicon detectors–developments by the RD48 (ROSE) collaboration, Nucl. Inst. Meth. A, Volume 466, Issue 2, 1 July 2001, Pages 308-326, DOI: 10.1016/S0168-9002(01)00560-5

[21] Gunnar Lindstrom, Radiation damage in silicon detectors, Nucl. Inst. Meth. A, Volume 512, Issues 1-2, Proceedings of the 9th European Symposium on Semiconductor Detectors: New Developments on Radiation Detectors, 11 October 2003, Pages 30-43, DOI: 10.1016/S0168-9002(03)01874-6

[22] Georg Steinbrück, Dieter Horns, Physik V Einführung: Kern und Teilchenphysik, Universität Hamburg Winter-Semester 2007/2008

[23] Georg Steinbrück, Solid State Detectors Lecture for Summer Students at DESY, Hamburg University, August 15, 2008

[24] Jon Geist, Alan Migdall and Henry P. Baltes, Analytic representation of the silicon absorption coefficient in the indirect transition region, Applied Optics, Vol. 27, No. 18, 3777-3778, 1988

[25] NIST (XAAMDI Database) `http://www.nist.gov/physlab/data/xraycoef/index.cfm`

[26] Lothar Strüder, pnCCDs for High Speed X-ray imaging at experiments at FLASH, LCLS and XFEL, presentation at NDIP09, Aix-les-Bains, 16.- 21. 6. 2008 http://ndip.in2p3.fr/ndip08/Presentations/3Tuesday/Matin/204-Struder.pdf

[27] G. Kramberger, Signal development in irradiated silicon detectors, University of Ljubljana, 2001, http://krambi.ijs.si/gregor/papers/dok_eng.pdf

[28] D. Eckstein, Strahlenharte Siliziumsensoren für den SLHC, presentation at the DPG spring meeting, Munich, 2009

[29] The CMS pixel tracker http://cms.web.cern.ch/cms/Detector/Tracker/Pixels.html

[30] N. Meidinger et al., pnCCD for photon detection from near-infrared to X-rays, Nucl. Instr. Meth. A 565, Issue 1, Proceedings of the International Workshop on Semiconductor Pixel Detectors for Particles and Imaging - PIXEL 2005, (2006), 251-257, DOI: 10.1016/j.nima.2006.05.006

[31] L. Andricek et al., The MOS-type DEPFET pixel sensor for the ILC environment, Nucl. Instr. Meth. A, 565, Issue 1, Proceedings of the International Workshop on Semiconductor Pixel Detectors for Particles and Imaging - PIXEL 2005, (2006), 165-171, DOI: 10.1016/j.nima.2006.05.045

[32] Attix, Roesch and Tochilin, "Radiation Dosimetry" Book 1-3, AP (1969)

[33] Data provided by the particle data group, available at http://pdg.lbl.gov/2005/reviews/atomicrpp.pdf

[34] Marko Mikuž, Diamond Pixel Modules for the High Luminosity ATLAS Inner Detector Upgrade, Presentation at ATLAS Tracker Upgrade Workshop, Valencia, December 12-14 2007 http://pi.physik.uni-bonn.de/~eng/talks/Valencia_Mikuz.pdf

[35] H.W. Kraner, Z. Li, E. Fretwurst, The use of the signal current pulse shape to study the internal electric field profile and trapping effects in neutron damaged silicon detectors, Nucl. Instr. Meth. A, Volume 326, Issues 1-2, 1 March 1993, Pages 350-356, DOI: 10.1016/0168-9002(93)90376-S

[36] G. Kramberger et al., Determination of effective trapping times for electrons and holes in irradiated silicon, Nucl. Instr. Meth. A, Volume 476, Issue 3, 11 January 2002, Pages 645-651, DOI: 10.1016/S0168-9002(01)01653-9

[37] T. Pöhlsen, DESY-THESIS-2010-013

[38] CeramTec AG, CeramTec-Platz 1-9, 73207 Plochingen http://www.ceramtec.com/de/

[39] Laird Technologies, Daimlerring 31, 31135 Hildesheim, Germany http://www.lairdtech.com/Products/Thermal-Management-Solutions/Thermoelectric-Assemblies/

[40] Lauda Dr. R. Wobser GmbH & Co. KG, Pfarrstraße 41/43, 97922 Lauda-Königshofen, Deutschland http://www.lauda.de/

[41] Keithley Instruments GmbH, Landsberger Strasse 65, 82110 Germering http://www.keithley.de/

[42] HAMEG Instruments GmbH, Industriestr. 6, 63533 Mainhausen http://www.hameg.de/

[43] Physik Instrumente (PI) GmbH & Co. KG., Auf der Römerstr. 1, 76228 Karlsruhe/Palmbach http://www.physikinstrumente.de/de/index.php

[44] Agilent Technologies Deutschland GmbH, Herrenberger Str. 130, 71034 Böblingen http://www.agilent.de/

[45] MITEQ Inc., 100 Davids Drive, Hauppauge, NY 11788 http://www.miteq.de/

[46] Tektronix UK Ltd. Western Peninsula, Western Road, Bracknell, Berkshire RG12 1RF, United Kingdom http://www.tek.com/de/

[47] Picosecond Pulse Labs, 2500 55th Street, Boulder, Colorado 80301, USA http://www.picosecond.com/

[48] PicoQuant GmbH, Rudower Chaussee 29 (IGZ), 12489 Berlin, Germany http://www.picoquant.de/

[49] S. Ramo, Proc. IRE 27 (1939) 584

[50] L. Rossi, P. Fischer, T. Rohe, N. Wermes, Pixel detectors From Fundamentals to Applications, Springer, Berlin / Heidelberg / New York

[51] J. Schwandt, Detector simulation (with PIXELAV), internal presentation at Hamburg, 23.01.2009

[52] J. Schwandt, personal communication

[53] L. Beattie et al., Carrier lifetimes in heavily irradiated silicon diodes, Nucl. Inst. Meth. A, Volume 421, Issue 3, 1 February 1999, Pages 502-511, DOI: 10.1016/S0168-9002(98)01229-7

[54] C. Canali, G. Ottaviani and A. A. Quaranta, Drift velocity of electrons and holes and associated anisotropic effects in silicon, Chem. Solids 1971, Vol 32 1707-1720

[55] C. Jacoboni et al., A review of some charge transport properties of silicon, Solid State Electronics, 1977, Vol. 20, 77-89

[56] M. A. Omar and L. Reggiani, Drift and diffusion of charge carriers in silicon and their empirical relation to the electric field, Solid-State Electronics Vol. 30 (1987), No. 7 693-697

[57] S. Selberherr et al., The evolution of the MINIMOS mobility model, Solid-State Electronics 1990 Vol. 33, No. 11 1425-1436

[58] S. R. Shukla and M. N. Sen, Analytical expressions for the drift velocity of hot charge carriers in silicon, Solid-State Electronics Vol. 35 (1992), No. 4 593-597

[59] S. N. Mohammad, Unified model for drift velocities of electrons and holes in semiconductors as a function of temperature and electric field, Solid-State Electronics Vol. 35 (1992) No. 10 1391-1396

[60] CiS Forschungsinstitut für Mikrosensorik und Photovoltaik GmbH website `http://www.cismst.de/`

[61] Siltronic AG, Hanns-Seidel-Platz 4, 81737 München `http://www.siltronic.com/`

[62] F. James and M. Ross, Comput. Phys. Commun. 10:343-367,1975

[63] Homepage `http://root.cern.ch/`

[64] M. A. Green, Intrinsic Concentration, Effective Densities of States, and Effective Mass in Silicon, J. Appl. Phys. 67(6) 1990 2944-2954

[65] N. Ahmad and V. K. Arora, IEEE Trans. Electron Devices ED-33, 1075 (1986)

[66] R. Quay et al., A temperature dependent model for the saturation velocity in semiconductor materials, Materials Science in Semiconductor Processing 3 (2000) 149-155

[67] P. M. Smith and J. Frey, High-Field Transport of Holes in Silicon, Appl. Phys. Lett. 39(4) 1981, 332-333

[68] A. Castoldi and P. Rehak, Eelectron-Drift Time in Silicon Drift Detectors - a Technique for High-Precision Measurement of Electron-Drift Mobility, Rev. Sci. Instrum. 66(10) 1995 4989-4995

[69] W. N. Grant, Electron and hole ionization rates in epitaxial silicon at high electric fields, Solid-St. Electron. 16 (1973) 1189

[70] R. Van Overstraeten, H. De Man, Measurement of the ionization rates in diffused silicon p-n junctions, Solid-State Electronics, Volume 13, Issue 5, May 1970, Pages 583-608, DOI: 10.1016/0038-1101(70)90139-5

[71] Thomas Lackner, Avalanche multiplication in semiconductors: A modification of Chynoweth's law, Solid-State Electronics, Volume 34, Issue 1, January 1991, Pages 33-42, DOI: 10.1016/0038-1101(91)90197-7

[72] Y. Okuto and C. R. Crowell, Ionization coefficients in semiconductors: A nonlocalized property, Phys. Rev. B 10, 4284-4296 (1974), DOI: 10.1103/PhysRevB.10.4284

[73] Weierstraß-Institut für Angewandte Analysis und Stochastik, Mohrenstr. 39, 10117 Berlin `http://www.wias-berlin.de`

[74] W. V. van Roosbroeck, Theory of Flow of Electrons and Holes in Germanium and Other Semiconductors, Bell Syst. Techn. J., 29 (1950), 560-607

[75] S. Selberherr, Analysis and Simulation of Semiconductor Devices, Springer, 1984, Wien-New York

[76] V. L. Bonč-Bruevič and S. G. Kalašnikov, Halbleiterphysik, Deutscher Verlag der Wissenschaften, 1982 , Berlin

[77] H. Gajewski, G. Albinus and R. Hünlich, Thermodynamic design of energy models of semiconductor devices, *Nonlinearity*, 15:367–383, 2002

[78] Hamamatsu Photonics `http://www.hamamatsu.com/`

[79] SINTEF `http://www.sintef.no/`

[80] Teubner-Taschenbuch der Mathematik, E. Zeidler (Editor), Teubner-Verlag, 2003, Stuttgart / Leipzig / Wiesbaden

[81] B. Schmidt, personal communication

[82] Thorlabs GmbH, Hans-Boeckler-Str. 6, 85221 Dachau/Munich `http://www.thorlabs.com/`

Acknowledgments

I would like to thank everyone who contributed to this work.

I am grateful to Prof. Dr. Robert Klanner for constant encouragement and supervision. His detailed and elaborate comments have been very helpful and have improved this work.

I am greatly indebted to Dr. Heinz Graafsma for the successful cooperation with the photon science detector group and refereeing this thesis.

I am genuinely thankful to Dr. Erika Garutti for agreeing to referee the defense of this thesis.

Major thanks are not enough to appreciate the help of Dr. Eckart Fretwurst, who was always willing to share his enormous knowledge of silicon sensors with me.

The encouragement an supervision by Dr. Doris Eckstein and Dr. Georg Steinbrück have been very helpful in correlating my work to the sensor applications in high energy physics.

A massive amount of typos in this work was found by Dipl. Phys. Jörn Lange, to whom I am much obliged for insightful discussions about ROOT, transient analysis, charge multiplication and epitaxial silicon.

This work could not have been done without the help of Peter Buhmann, especially without his help with the experimental side of experimental physics.

I am sincerely thankful to the members of the AGIPD collaboration for letting me contribute significantly to the project although I was just a PhD student.

Special thanks to the WIAS, especially Dr. Klaus Gärtner, for the unique experience of cooperating with a different field of science.

I have enjoyed my stay at the working group, the nice atmosphere and the possibility to exchange opinions with so many experts from different fields.

Having had some of the most enjoyable lunchtimes of my life, I salute everyone who boycotts the canteen.

And, most important of all:

I thank my wonderful wife, family and friends for supporting me.